Doctoral Thesis

Mechanisms and stochastic dynamics of transport in Darcy-scale heterogeneous porous media

Author:
Alessandro Comolli

Advisor:
Prof. **Marco Dentz**

Tutor:
Prof. **Daniel Fernández García**

Institute of Enviromental Assessment and Water Research (IDAEA, CSIC)

Department of Civil and Environmental Engineering, Program of Geotechnical Engineering, Universitat Politècnica de Catalunya (UPC)

Hydrogeology Group (GHS)

June, 2018
Barcelona, Spain

This thesis was funded by the European Research Council (ERC) through the Project MHetScale (617511).

Abstract

Solute transport in heterogeneous porous media in general exhibits anomalous behaviors, in the sense that it is characterized by features that cannot be explained in terms of traditional models based on the advection-dispersion equation with constant effective coefficients. Signatures of anomalous transport are the non-linear temporal growth of the variance of solute concentration, non-Gaussian density profiles and heavy-tailed breakthrough curves. Understanding and predicting transport behavior in groundwater systems is crucial for several environmental and industrial applications, including groundwater management and risk assessment for nuclear waste repositories. The complexity of this task lies in the intrinsic multi-scale heterogeneity of geological formations and in the large amount of degrees of freedom. Hence, the predictive description of transport requires a process of upscaling that is based on measurable medium and flow attributes. The time domain random walk (TDRW) and continuous time random walk (CTRW) approaches provide suitable frameworks for transport upscaling.

In this thesis, we identify different mechanisms that induce anomalous transport and we quantify their impact on transport attributes. We propose average transport models that can be parameterized in terms of flow and medium properties. Among the mechanisms that induce non-Fickian behaviors, a pivotal role is played by the heterogeneity of the flow field, which is directly linked to medium disorder. Due to its importance, the impact of advective heterogeneity is studied throughout the thesis, alongside with other mechanisms.

First, we consider solute trapping due to physical or chemical heterogeneity, which we parameterize in terms of a constant trapping rate and a distribution of return times. We observe three distinct transport regimes that are linked to characteristic trapping time scales. At early times, transport is advection-controlled until particles start to get trapped. Then, the increasing distance between mobile and immobile particles gives rise to a superdiffusive regime which finally evolves towards a trapping-controlled regime.

Second, we study transport in correlated porous media. We show that particle motion describes a coupled CTRW that is parameterized in terms of the distribution of flow velocity and length scales. We show that disorder and correlation may lead to similar behaviors in terms of displacement moments, but the difference between these mechanisms is manifest in the distributions of particle positions and arrival times.

Next, we study the relationship between flow and transport properties and the impact of different injection conditions on transport. To this end, the relationship between Eulerian and Lagrangian velocities is investigated. Lagrangian statistics evolves to a steady-state that depends on the injection conditions. We study the velocity organization in Darcy flows and we develop a CTRW model for transport that is parameterized in terms of flow and medium attributes only. This CTRW accounts for non-stationarity through Markovian velocity models. We study the impact of advective heterogeneity by considering different disorder scenarios.

Finally, we quantify the impact of diffusion in layered and fibrous heterogeneous media by considering two disorder scenarios characterized by quenched random velocities and quenched retardation properties, respectively. These mechanisms lead to different, dimension-dependent disorder samplings that give rise to dual transport processes in space and time. Specifically, transport describes correlated Lévy flights in the random velocity model and correlated CTRWs in the random retardation model.

Resumen

El transporte de solutos en medios heterogéneos porosos exhibe comportamientos anómalos, que se caracteriza por rasgos que no pueden ser explicados en términos de modelos tradicionales basados en la ecuación de advección-dispersión con coeficientes efectivos constantes. Las características del transporte anómalo son el crecimiento temporal no lineal de la varianza de la concentración de soluto, los perfiles de densidad no gausianos y la curvas de llegada con colas pronunciadas. Entender y predecir el comportamiento del transporte en hidrología subterránea es crucial para aplicaciones ambientales e industriales, como la gestión de aguas subterráneas o la evaluación de riesgos en repositorios de residuos nucleares. La complejidad de estas tareas se debe a la heterogeneidad intrínseca en múltiples escalas de las formaciones geológicas y del gran número de grados de libertad. Por lo tanto, una descripción predictiva del transporte requiere un proceso de upscaling basado en propiedades medibles del medio y el flujo para el que los modelos time domain random walk (TDRW) y continuous time random walk (CTRW) proporcionan un marco adecuado. En esta tesis, se identifican los mecanismos que inducen transporte anómalo y se cuantifica su impacto en el transporte. Se proponen modelos de transporte parametrizados en términos de las propiedades del medio y el flujo. Entre los mecanismos que inducen comportamientos no fickianos, la heterogeneidad del flujo, relacionada con el desorden del medio, desempeña un papel fundamental. Por lo tanto, su impacto se estudia junto con los de otros mecanismos a lo largo de toda la tesis.

Primero, se considera el atrapamiento de soluto debido a heterogeneidades físicas o químicas parametrizadas en términos de un ratio de atrapamiento constante y una distribución de tiempos de retorno. Se observan tres regímenes de transporte relacionados con las escalas temporales características del atrapamiento. A tiempos pequeños, el transporte está controlado por la advección hasta que las partículas comienzan a ser atrapadas. A continuación el incremento de la distancia entre partículas móviles e inmóviles origina un régimen superdifusivo que finalmente evoluciona hacia un régimen controlado por el atrapamiento.

Después, se estudia el transporte en medios correlacionados en los que el movimiento de las partículas es descrito por un CTRW acoplado parametrizado según la distribución de velocidades del flujo y de las escalas espaciales. El desorden y la correlación generan comportamientos similares en los momentos del desplazamiento de las partículas, pero diferentes en las distribución de posiciones

y de tiempos de llegada.

A continuación, se estudia la relación entre flujo y transporte bajo diferentes condiciones de inyección, a través de las velocidades eulerianas y lagrangianas. La estadística lagrangiana evoluciona hacia un estado estacionario que depende de los modos de inyección. Se estudia la organización de las velocidades en flujos de Darcy y se desarrolla un CTRW para el transporte que se parametriza solo en términos de las propiedades del medio y del flujo. Este CTRW considera la no estacionariedad a través de modelos de velocidad markovianos. El impacto de la heterogeneidad advectiva se estudia considerando diferentes escenarios de desorden.

Finalmente, se cuantifica el impacto de la difusión en medios heterogéneos estratificados considerando dos escenarios de heterogeneidad que se caracterizan respectivamente por velocidades y propiedades de retraso aleatorias. Estos mecanismos originan diferentes muestreos del desorden que generan procesos de transportes duales en tiempo y espacio. El transporte describe un Lévy flight correlacionado en el modelo de velocidades aleatorias y un CTRW correlacionado en el modelo de retraso.

Acknowledgements

I wish to express my sincere gratitude to Marco for the splendid opportunity that this PhD has represented for me, from both the professional and the personal point of view. I am truly thankful for the wise guidance that I received and for the encouraging attitude that he showed me throughout these years. His always reliable advice was crucial to overcome the challenges that I have encountered along the path.

Special acknowledgements go to Juan and Vivien, who have worked with me at part of the thesis. Working with them has been inspiring and I have benefited significantly from their help. I also thank all the other members of the MHetScale team for the stimulating discussions in the weekly meetings and for all the suggestions that helped me improve my presentations. I am grateful to Dani, who accepted to be my UPC tutor for the thesis.

All the reviews that I have received throughout the PhD represented for me an incentive to improve and a stimulating challenge. Thus, I acknowledge Dr. Pietro de Anna and Dr. Anna Russian, who reviewed the thesis, as well as all the anonymous referees who reviewed my publications.

He tenido la suerte de trabajar en un ambiente genial, con personas encantadoras que han hecho que estos años pasaran volando. Por eso les doy las gracias a todos los compañeros del grupo, a los que han estado siempre, a los que ya se han ido y a los que he encontrado durante el camino. Gracias por los momentos de diversión que hemos vivido dentro y fuera de la oficina. Sobre todo gracias a los que han compartido despacho conmigo. Hemos estado juntos varios años, todos los días, durante muchas horas: no sé cómo me han aguantado.

Entre los que han estado a mi lado en el día a día hay algunos que sería simplemente injusto no mencionar. En primer lugar Mar, que con paciencia y diversión corrigió todos y cada uno de mis errores lingüísticos durante años. Una gran parte de lo que sé de Castellano se lo debo a ella. También agradezco de manera especial a Silvia, Sheila y Lázaro, con los que he compartido inolvidables viajes.

Grazie agli amici che ho lasciato in Italia, ma che mi sono sempre stati vicini nonostante la distanza geografica, gli innumerevoli impegni e i limitati tempi

liberi che la vita ci concede. E quindi grazie a Fau, a Gio, a Ricky, ad Eli, a Ste e a Lara. Ringrazio chi ha voluto venire a trovarmi a Barcellona e chi semplicemente, passando di qui, si è ricordato di me.

Infine grazie ai miei genitori. Senza di loro, per ovvi motivi, tutto questo non sarebbe stato possibile. Ma soprattutto grazie a loro, alle nonne e al resto della famiglia per tutto l'affetto incondizionato che ho ricevuto. Il loro amore ha per me un valore inestimabile.

Table of Contents

1 Introduction

1.1 Motivation

A sound understanding of transport processes in complex environments is crucial in several branches of science and engineering. This challenge is, however, anything but trivial. In fact, large-scale transport usually exhibits anomalous features that do not conform to Fickian advection-dispersion models that are parameterized in terms of effective constant drift and dispersion coefficients. The anomalous, or non-Fickian, character emerges at a broad range of scales, from pore to regional scale, and is characterized by the non-linear growth of solute dispersion, non-Gaussian solute distributions with forward and backwards tails (Koch and Brady, 1988; Gelhar et al., 1992; Boggs et al., 1993; Moroni and Cushman, 2001; Levy and Berkowitz, 2003) and heavy-tailed arrival time distributions and breakthrough curves (Hatano and Hatano, 1998; Haggerty et al., 2000; Berkowitz et al., 2001; Gouze et al., 2008a; Willmann et al., 2008).

Non-Fickian behavior is constantly encountered in a wide variety of natural and engineered systems, including charge carriers diffusion in disordered solids (Scher and Lax, 1973; Scher and Montroll, 1975), light diffusion in Lévy glasses (Barthelemy et al., 2008) and in cellulose nanofibrils (Toivonen et al., 2018). In biology, the emergence of anomalous transport features has been observed in animal foraging patterns (Viswanathan et al., 1996; Ramos-Fernández et al., 2004), protein and lipid diffusion in crowded environments (Banks and Fradin, 2005; Jeon et al., 2011), intracellular transport (Caspi et al., 2000) and many others (Metzler and Klafter, 2004).

Evidence of non-Fickian transport in groundwater hydrology has been found in a plethora of studies at the pore (Cortis et al., 2004; Bijeljic and Blunt, 2006; de Anna et al., 2013), Darcy (Koch and Brady, 1988; Levy and Berkowitz, 2003) and field scale (Sudicky, 1986; LeBlanc et al., 1991; Adams and Gelhar, 1992; Boggs et al., 1993), as a consequence of the multi-scale heterogeneity that char-

acterizes geological porous media. The importance of describing these processes in a predictive way concerns environmental issues of public interest such as aquifer contamination, water resources management or geological carbon dioxide sequestration, to cite a few. The direct solution of the ADE is not feasible, since it would require a complete knowledge of the system heterogeneity and huge computational resources. For this reason, several attempts have been made in the last decades to describe non-Fickian transport and to perform the upscaling, based on the knowledge of few transport-independent parameters. In the following section, we summarize the state of the art of the modeling of non-Fickian transport in heterogeneous porous media. More detailed and specific summaries of the state of the art can be found in the introductory sections of each chapter.

1.2 State of the art

In literature, several approaches have been proposed to describe and predict non-Fickian transport. These can be distinguished in Eulerian, which solve the advection-dispersion equation (ADE) directly, and Lagrangian. Eulerian methods include fractional calculus (Meerschaert et al., 1999; Benson et al., 2000, 2013), non-local constitutive theories (Cushman et al., 1994; Guadagnini and Neuman, 1999) and multi-rate mass transfer (MRMT) (Harvey and Gorelick, 1995; Carrera et al., 1998; Willmann et al., 2008; Tecklenburg et al., 2016) . Lagrangian models solve the transport problem in terms of idealized solute particles. Although these classes of models have different approaches to solve transport, it can be shown that every Lagrangian model has its equivalent Eulerian approach. Lagrangian models include, but are not limited to, non-stationary Gaussian noise (Cushman et al., 2009), time domain random walks (TDRW) (Delay et al., 2005; Russian et al., 2016) and continuous time random walks (CTRW) (Berkowitz and Scher, 1997; Berkowitz, 2002; Dentz et al., 2004; Le Borgne et al., 2008a; Cvetkovic et al., 2014; Edery et al., 2014). In this thesis, we use the TDRW and the CTRW approaches and their Eulerian equivalent approaches. In Chapter 2 we present a summary of the TDRW and the CTRW. Both models have been used to describe and predict the expected breakthrough curves of solutes within heterogeneous media (Berkowitz et al., 2001; Cvetkovic et al., 2014; Russian et al., 2016), as well as solute distribution and its spatial moments (Dentz and Berkowitz, 2003; Dentz et al., 2004, 2012; Russian et al., 2016). The CTRW framework also proved to be effective in describing advective transport with sorption in a heterogeneous column experiment (Hatano and Hatano, 1998), as well as in a 3D laboratory experiment (Holzner et al., 2015). Remarkably, the CTRW model represents a valid framework for the description of anomalous transport over a broad range of scales, from pore (Bijeljic and Blunt, 2006; de Anna et al., 2013; Kang et al., 2015a; Holzner et al., 2015), to Darcy (Le Borgne et al., 2008a; Dentz and Castro, 2009) up to catchment scale (Scher et al., 2002). The reason why this is possible is that the dynamic properties underlying non-Fickian transport are scale-independent. The CTRW is a coarse-grained approach that provides new insight on the fundamental effective transport dynamics. It also provides signif-

icant improvement in terms of the reduction of the system's degrees of freedom and of needed computational resources with respect to direct numerical solutions of the ADE.

We discuss now the mechanisms that induce anomalous transport. It is well-known that the non-Fickian character of transport is due to heterogeneity. The latter, manifests itself in different forms and different are the mechanisms underlying. In the following, we summarize the principal processes that are considered in this thesis. We first consider medium disorder, which is the spatial variability of the hydraulic properties, such as hydraulic conductivity. This parameter typically spans several orders of magnitude in aquifers (Gelhar, 1993) and has a pivotal role on flow at the Darcy scale. In literature, the point distribution of hydraulic conductivity is widely considered as a log-normal (Rubin, 1990; Salandin and Fiorotto, 1998; de Dreuzy et al., 2007; Gotovac et al., 2009; Edery et al., 2014). Nevertheless, some authors have considered different distributions (Painter, 1996; Kohlbecker et al., 2006; Haslauer et al., 2012) to account for strong heterogeneity and sharp contrasts. Motivated by these studies, in this thesis we consider both log-normal and power-law distributions for the hydraulic conductivity. We consider spatial correlation as a feature that induces anomalous transport behaviors. Its relevance is evident in stratified (Matheron and de Marsily, 1980) and connected fields (Stanley, 1984), as well as in fractured media (Kang et al., 2015b), where a mean correlation length for velocity transitions is often lacking. These geometric and hydraulic properties of the medium induce heterogeneity of the advective field. This mechanism has a pivotal role for transport and its impact will be studied systematically throughout the thesis. Tracer tests performed at the MAcro Dispersion Experiment (MADE), where heavy-tailed solute concentrations have been observed after injecting the tracers in areas of low conductivity (Adams and Gelhar, 1992; Boggs et al., 1993) seem to suggest that there is a relationship between the injection conditions and large scale transport behavior. Anomalous transport also arises as a consequence of mass transfer between mobile and immobile phases, which occurs in virtue of sorption and desorption of the solutes onto the grains of the porous medium, as well as for dead-end pore dynamics. Although these processes occur at the pore scale, they have a significant impact on transport at the Darcy scale. Finally, diffusion is another important transport mechanism. Longitudinal diffusion has been accounted for in stochastic convective streamtube models (Dagan and Bressler, 1979; Ginn et al., 1995; Cirpka and Kitanidis, 2000). Notice that transverse diffusion also plays a significant role in the faith of longitudinal transport. In fact, diffusion allows particles to move across streamlines, thus shortening the velocity correlation length. This effect is especially relevant in layered formations, since it represents the only mechanism that enables particles to explore the disorder. Transverse diffusion as sampling mechanism is more efficient in high spatial dimensions, since the return probability to a previously visited site decreases.

1.3 Open questions

Despite the remarkable progress in the understanding of non-Fickian transport, some important questions are still open. These refer to

1. the nature and the relative impact of different physical mechanisms that induce anomalous behaviors;

2. the parameterization of the TDRW and CTRW models in terms of few transport-independent quantities that can be related to flow and medium properties;

3. the impact of the injection conditions on the asymptotic behavior of transport observables;

4. the role of diffusion as heterogeneity sampling mechanism.

This thesis, as part of the ERC project MHetScale, aims to address these open issues and to perform the upscaling of Darcy-scale anomalous transport.

1.4 Objectives

Main objective The main objective of the thesis is to derive a framework that allows us to upscale transport in heterogeneous porous media.

While it is well-known that the hydraulic and geometric structure of the medium and the mechanism of advection, diffusion and mass transfer are among the causes of non-Fickian transport, it is still not clear how to distinguish and quantify the relative impact of each process on large-scale transport.

The TDRW and CTRW have proved to be efficient frameworks for the upscaling of anomalous transport, since they require few parameters, thus reducing dramatically the number of degrees of freedom. However, the parameterization of such models in terms of measurable properties of the medium and the flow, i.e. in terms of transport-independent variables, represents still an open challenge. It is also still unknown how to account for diffusive mechanisms and for the non-resident injection conditions in a systematic way.

Specific objectives On the basis of the aforementioned open questions, we set the following specific objectives for this thesis

1. to quantify the impact of the above mentioned mechanisms underlying non-Fickian transport on diagnostic observables such as spatial density profiles, moments of solutes displacement and breakthrough curves;

2. to perform Lagrangian statistics analysis to quantify the effect of heterogeneity and correlation on particle dynamics;

3. to use the knowledge obtained from the previous points to develop TDRW and CTRW models for transport upscaling. These models will be parameterized in terms of transport-independent quantities and have a predictive character;

4. to account for different injection conditions and to quantify their impact on large-scale transport within the proposed stochastic frameworks;

5. to quantify the impact of diffusion as sampling process.

1.5 Thesis outline

To address these objectives, in the following chapters we consider different heterogeneity scenarios. Most of the chapters are based on papers that are published or have been submitted to peer-reviewed journals. These chapters can be read independently and may therefore present differences in notation as well as repeated concepts. Nevertheless, the chapters are interconnected by the common main objective of deriving a framework for transport upscaling. Due to its pivotal role in the faith of solute transport in heterogeneous porous media, heterogeneous advection will be studied throughout the whole thesis alongside with different mechanisms, according to the chapter. Therefore, the thesis is structured as follows.

- In Chapter 3, we study the combined action of advective heterogeneity and trapping, i.e. mass transfer between mobile and immobile phases on transport. To this end, we consider a $d-$dimensional CTRW model in which the advective heterogeneity is mapped onto a distribution of advective transition times and trapping is quantified through a constant trapping rate and the distribution of return times. To quantify the impact of heterogeneous advection and mass transfer, we study different transport diagnostics, such as the spatial moments and the first passage time distributions, for different scenarios of increasing heterogeneity. We observe the occurrence of three distinct temporal regimes that are separated by the characteristic trapping rate and trapping times. We show that in the limit of weak heterogeneity, this model is equivalent to the multi-rate mass transfer.

- In Chapter 4 we study the impact of medium disorder and spatial correlation on anomalous transport at the Darcy scale. The spatial variability of the hydraulic properties gives rise to heterogeneous advective fields in virtue of Darcy's law. We consider purely advective transport in systems characterized by broad distribution of heterogeneity length scales and point values. To model and upscale transport, we use a coupled CTRW model in which disorder is mapped onto a distribution of spatially-sampled Lagrangian velocities and correlation is mapped onto distribution of correlation lengths. We apply the model to different scenarios of increasing disorder and correlation. The analysis of the moments of particle displacements shows that

dispersion is governed by the stronger process. Although similar behaviors of the displacement moments can arise as a consequence of profoundly different mechanisms, it is possible to discriminate the process leading to anomalous behavior by observing the spatial density distribution and the breakthrough curves.

- Chapter 5 deals with the relationship between flow and transport attributes in view of the parameterization of an effective transport model and with the role of the injection conditions. First, we investigate the crucial concepts of Eulerian and Lagrangian velocity statistics and the relationships between them. Velocity time-series in Darcy flows typically exhibit an intermittent behavior due to the persistence of low velocities, which impedes the identification of characteristic time scales. Velocity space-series, on the other hand, show more regular patterns and characteristic correlation lengths emerge. Thus, the velocity space-series represent a Markovian process, for which the CTRW is a natural modeling formalism. Based on this, we develop a CTRW for the dynamics of Lagrangian velocities under both stationary and non-stationary conditions. This CTRW is parameterized in terms of the injection and the steady-state velocity PDF and of the velocity correlation length, i.e. on transport-independent quantities. In the non-stationary case, we make use of a stochastic relaxation process to account for the evolution of Lagrangian velocity statistics. We show that the stationarity of Lagrangian velocities depends on the sampling (isochronal or equidistant sampling), while the transient regime is governed by the injection conditions. The study of the dispersion coefficient, on the other hand, shows that transport attributes keep memory of the initial conditions in the asymptotic regime.

- In Chapter 6 we investigate the velocity organization in Darcian flows. We study the relationship between Eulerian and Lagrangian velocities and their representation using Markovian models. To this end, we perform Eulerian and Lagrangian velocity analysis statistics in Darcian flows obtained by solving flow in randomly-generated multi-Gaussian conductivity fields. These fields are characterized by broad distributions of point values, accounting for strong disorder. The latter gives rise to highly heterogeneous advective fields. We also study the impact of different injection conditions, namely resident (or uniform) and flux-weighted, on the velocity statistics. Here the CTRW approach proposed in Chapter 5 is used to reproduce the results of Lagrangian analysis obtained through direct numerical simulations. In the non-stationary cases, we show that the stochastic relaxation process does not provide the correct convergence to the sampled velocity PDF in the pre-asymptotic regime. This implies biased results for the evolution of the mean and the variance of Lagrangian velocities. Therefore, we use the mean-reverting Ornstein-Uhlenbeck process, which provides a proper convergence of the Lagrangian velocity distribution.

- In Chapter 7 we propose a large-scale transport formulation that is parameterized in terms of flow and medium attributes and thus represents a predictive model for transport in Darcy-scale flows. Specifically, we develop a CTRW with evolving velocity PDFs that we use to upscale transport. This CTRW is parameterized in terms of the injection and the stationary PDF only. The Ornstein-Uhlenbeck process that we used to mimic the velocity transitions is parameterized in terms of the sole velocity correlation length. Hence, the proposed framework has a predictive character. We study the impact of heterogeneous advection and of different injection conditions on transport diagnostics such as spatial density distributions, moments of particles displacement and breakthrough curves and we get excellent agreement with the results of direct numerical simulations.

- In Chapter 8 we investigate the impact of disorder and diffusion on transport in correlated media. In the previous chapters, the only mechanism through which particles were allowed to sample the system heterogeneity is advection. This is a valid approximation for system characterized by high Péclet numbers, as it is often the case for groundwater systems. Nevertheless, in general transport in real porous media is also governed by diffusion, especially at short times and for small Péclet numbers. Diffusion is also crucial for transport in stratified formations, as it is the only mechanism through which particles can explore the heterogeneity. Thus, here we account for both disorder and diffusion in layered and fibrous media characterized by infinite longitudinal correlation, in which particles move by effect of heterogeneous advection and transverse diffusion. We consider two types of quenched disorder characterized by random velocity and random retardation properties, respectively. In absence of diffusion, both models give rise to ballistic behavior, since particles are not allowed to sample the system heterogeneity. The effect of diffusion is to reduce the correlation length, enhancing exploration of the heterogeneity of the advective field. Its impact is different, according to the considered disordered scenario. We upscale transport in these systems by means of a TDRW model, in which spatial disorder is mapped onto a distribution of velocity or retardation coefficients. Because diffusion is isotropic and longitudinal correlation is infinite, subsequent increments in particle trajectories are not independent. In fact, particles are allowed to return to previously visited strata (or channels) and, in virtue of the quenched nature of the medium, they experience the same advective properties. The return probability by diffusion depends on the dimensionality of the system, and so do the transport observables.

- Chapter 9 presents the general conclusions to the thesis and provides some ideas for future work.

2

Basics

2.1 Transport in heterogeneous media

In this section we summarize the main features of transport in heterogeneous porous media. Solute transport in porous media is governed by the advection-dispersion equation for the solute density $c(\mathbf{x}, t)$

$$\phi(\mathbf{x})\frac{\partial c(\mathbf{x},t)}{\partial t} + \nabla \cdot [\mathbf{u}(\mathbf{x})c(\mathbf{x},t)] - \nabla \cdot [\mathbf{D}(\mathbf{x})\nabla c(\mathbf{x},t)] = \mathbf{0}, \tag{2.1}$$

where $\phi(\mathbf{x})$ is the local porosity, $\mathbf{u}(\mathbf{x})$ is the flow velocity and $\mathbf{D}(\mathbf{x})$ the hydrodynamic dispersion tensor. The general ADE does not have any analytical solution and its direct numerical solutions require a detailed knowledge of the medium and the flow, as well as important computational resources. Alternatives to its direct solution include particle-based approaches such as random walk particle tracking (RWPT) and time domain random walk. Both methods are based on the discretization of the particle trajectories $\mathbf{x}(t)$. Solute density in these frameworks is given by

$$c(\mathbf{x}, t) = \frac{\langle \delta[\mathbf{x} - \mathbf{x}(t)] \rangle}{\phi(\mathbf{x})}, \tag{2.2}$$

where $\delta(\cdot)$ is the Dirac delta function and the angular brackets denote noise average over particle trajectories. The basic concepts on these approaches are summarized in the following.

2.1.1 Random walk particle tracking

Lagrangian methods are based on the equivalence of Equation (2.1) and the following Langevin equation (Kinzelbach, 1988)

$$\frac{d\mathbf{x}(t)}{dt} = \frac{\mathbf{u}[\mathbf{x}(t)]}{\phi[\mathbf{x}(t)]} + \frac{\nabla \cdot \mathbf{D}[\mathbf{x}(t)]}{\phi[\mathbf{x}(t)]} + \sqrt{\frac{2\mathbf{D}[\mathbf{x}(t)]}{\phi[\mathbf{x}(t)]}} \cdot \boldsymbol{\zeta}(t), \tag{2.3}$$

where $\boldsymbol{\zeta}(t)$ is a vector of Gaussian white noise. In RWPT, the temporal increments are taken constant, whereas the spatial increments are distributed random variables. The recursive equations using the Ito interpretations are (Gardiner, 1986; Salamon et al., 2006)

$$\mathbf{x}_{n+1} = \mathbf{x}_n + \mathbf{v}_n \Delta t + \mathbf{B}(\mathbf{x}_n)\boldsymbol{\zeta}_n \sqrt{\Delta t}, \tag{2.4}$$

where $\mathbf{v}_n = \mathbf{u}(\mathbf{x}_n)$, $\zeta_n = \zeta(\mathbf{x}_n)$ and the displacement tensor $\mathbf{B}$ is defined through the dispersion tensor as $\mathbf{D} = \mathbf{B}\mathbf{B}^\top$. In the following, we will assume that porosity is homogeneous and we will set $\phi(\mathbf{x}) = 1$ for simplicity. We will further assume isotropy, which implies $\mathbf{D}(\mathbf{x}) = D(\mathbf{x})\mathbb{J}$, where $\mathbb{J}$ is the identity matrix. Under these hypothesis, Eq. (2.4) reduces to the much simple (Salamon et al., 2006)

$$\mathbf{x}_{n+1} = \mathbf{x}_n + \mathbf{v}_n \Delta t + \sqrt{2D(\mathbf{x}_n)\Delta t}\zeta_n \qquad t_{n+1} = t_n + \Delta t. \tag{2.5}$$

This approach has some significant drawbacks. In fact, it requires a detailed knowledge of the flow field and the stability of the solution is assured only for small Δt, which makes numerical simulations particularly demanding in terms of computational times.

2.1.2 Time domain random walk

The time domain random walk is another method to solve the ADE (2.1) in a single realization of disorder. This approach shares the RWPT philosophy of describing transport through discretized particle trajectories. Unlike the previously described model, however, the TDRW assumes that particles move by steps of constant distance, whose direction is determined by local advection and/or diffusion, while temporal increments are randomly distributed. Hence, the recursive relations that define the TDRW are the following

$$\mathbf{x}_{n+1} = \mathbf{x}_n + \ell\boldsymbol{\omega}_n \qquad t_{n+1} = t_n + \tau_n \tag{2.6}$$

where $\boldsymbol{\omega}_n$ is the unit vector aligned with particle's local velocity. If the distribution of transition times is exponential, the TDRW is equivalent to the diffusion equation (Dentz et al., 2012). The TDRW also proved to be an efficient approach for modeling transport in hydrodynamic conditions (Delay et al., 2002; Russian et al., 2016; Noetinger et al., 2016). The discretization of the ADE equation (2.1) in a finite volume scheme yields (Delay et al., 2002)

$$\phi_i \frac{dc_i(t)}{dt} = \sum_{j=i-1}^{i+1} b_{ij} c_j(t) - \sum_{j=i-1}^{i+1} b_{ji} c_i(t) \tag{2.7}$$

where c_i is the discretized concentration at the i-th voxel and the coefficients b depend on advective and diffusive terms as (Gjetvaij et al., 2015; Russian et al., 2016; Noetinger et al., 2016)

$$b_{ij} = \frac{\hat{D}_{ij}}{\epsilon^2} + \frac{|u_{ij}|}{2\epsilon}(\omega_{ij} + 1). \tag{2.8}$$

where the effective dispersion coefficient $\hat{D}$ accounts for the dispersive mass transfer between the voxels i and j. In $d = 1$ dimensions, it is given by the harmonic mean over these voxels, while in $d = 2$ it is the geometric mean (Noetinger and Estebenet, 2000). It has been shown by (Russian et al., 2016) that Equation (2.7) is equivalent to the discrete generalized master equation

$$\frac{dc_i(t)}{dt} = \int_0^t dt' \sum_{j=i-1}^{i+1} [M_{ij}(t-t')c_j(t') - M_{ji}(t-t')c_i(t')], \tag{2.9}$$

where $M_{ij}(t) = M(\mathbf{x}_i - \mathbf{x}_j, t)$ is the discretized memory function. Since it is a coarse-grained method, the TDRW allows to overcome the computational limitations of the particle tracking random walk and it requires less information.

2.2 Continuous time random walk

The continuous time random walk is a general and flexible framework that is used to account for memory effects in non-local and non-Markovian transport. This model is a generalization of the classical random walk (RW) model, for which the Langevin equation is discretized such that particles trajectories are made of subsequent transitions length in fixed temporal intervals. Introduced in 1905 by Pearson (1905), the RW is a valid framework for the description of Brownian motion. However, it fails in reproducing the anomalous features of transport described in the previous section. Numerical random walk simulations require fine temporal discretization, which makes it computationally expensive. To overcome this important drawbacks, the continuous time random walk has been proposed (Montroll and Weiss, 1965). As for classical RW, here the transport process is simulated through a series of random transitions of particles in space and time. The trajectories are defined by the recursive relations

$$\mathbf{x}_{n+1} = \mathbf{x}_n + \boldsymbol{\xi}_n \qquad\qquad t_{n+1} = t_n + \tau_n. \tag{2.10}$$

Notice that, unlike the classic RW, here both the spatial increment $\{\boldsymbol{\xi}_n\}$ and the transition times $\{\tau_n\}$ are stochastic processes that are in general coupled. The model is therefore determined by the joint PDF of transition lengths and times $\psi(\boldsymbol{\xi}, \tau)$. Its parameterization represents the core of the stochastic model. If the distribution of spatial and temporal increments can be decoupled, $\psi(\mathbf{x}, t) = p(\boldsymbol{\xi})\psi(\tau)$, the PDF of spatial increments $p(\boldsymbol{\xi})$ accounts for the geometric properties of the medium. The distances $\{\boldsymbol{\xi}_n\}$ then represent characteristic length scales

over which the dynamic properties are considered constant. The dynamics of particle motion are mapped onto the distribution of transition times $\psi(\tau)$. Thus, the transition times τ represent the amount of time needed to travel the characteristic length scales $\boldsymbol{\xi}$ and explore the heterogeneity of the system. The transition time PDF accounts for different physical processes that govern particle dynamics, such as advection, diffusion and retardation processes. Berkowitz and Scher (1997, 1998) and Painter and Cvetkovic (2005) have modeled transition times in terms of velocities. Painter and Cvetkovic compare their TDRW model to the approach by Berkowitz and Scher. In terms of advective transitions, both models are similar, but these authors' approaches differ in the way retention mechanisms are accounted for. In fact, while in (Berkowitz and Scher, 1997, 1998) retention effects are incorporated in the definition of the waiting time PDF, Painter and Cvetkovic decompose the advective and retention contributions. This provides an improved flexibility in the model parameterization. In Chapter 3 (Section Heterogeneous advection and trapping), we use a similar approach to implement the multi-rate mass transfer model within the CTRW. In this thesis, we will use for this model and for others with different parameterizations the term continuous time random walk in order to distinguish them from the previously presented TDRW, which is a solution method for the direct transport problem.

The density of particle $c(\mathbf{x}, t)$ satisfies the set of equations (Berkowitz et al., 2006)

$$\begin{aligned} c(\mathbf{x}, t) &= \int_0^t dt' R(\mathbf{x}, t') \int_{t-t'}^{\infty} dt'' \psi(\mathbf{x}, t'') \\ R(\mathbf{x}, t) &= c_0(\mathbf{x}) + \int_\Omega d\mathbf{x}' \int_0^t dt' \psi(\mathbf{x} - \mathbf{x}', t - t') c(\mathbf{x}', t'), \end{aligned} \tag{2.11}$$

where $c_0(\mathbf{x})$ is the initial condition, Ω is the spatial domain and $R(\mathbf{x}, t)$ is the probability per time that a particle just arrives at $\mathbf{x}$ at the time t. The system of equations (2.11) is equivalent to the generalized master equation

$$\frac{\partial c(\mathbf{x}, t)}{\partial t} = \int_0^t dt' \int_\Omega d\mathbf{x}' M(\mathbf{x} - \mathbf{x}', t - t')[c(\mathbf{x}', t') - c(\mathbf{x}, t')] \tag{2.12}$$

where $M(\mathbf{x}, t)$ is the so-called memory function, which connects the particles density at $(\mathbf{x}, t)$ to all the previous positions along the trajectory. To show the equivalence, we take the Laplace transform of Equations (2.11) and solve for $R^*(\mathbf{x}, \lambda)$

$$\frac{\lambda c^*(\mathbf{x}, \lambda)}{1 - \psi^*(\lambda)} = c_0(\mathbf{x}) + \int_\Omega d\mathbf{x}' \frac{\lambda \psi^*(\mathbf{x} - \mathbf{x}', \lambda)}{1 - \psi^*(\lambda)} c^*(\mathbf{x}', \lambda), \tag{2.13}$$

where the asterisks denote Laplace-transformed functions and λ is the Laplace variable. We used here

$$\psi(t) = \int_{\Omega} d\mathbf{x}' \psi(\mathbf{x}', t). \tag{2.14}$$

By isolating the term $\lambda c^*(\mathbf{x}, \lambda)$ on the left side and by performing the inverse Laplace transform, we get the generalized master equation (2.12), provided that we define the memory function by its Laplace transform as

$$M^*(\mathbf{x}, \lambda) = \frac{\lambda \psi^*(\mathbf{x}, \lambda)}{1 - \psi^*(\lambda)}. \tag{2.15}$$

If we apply the Fourier transform in space and the Laplace transform in time to Equations (2.11), we find an algebraic solution for the concentration in the transformed space

$$\tilde{c}^*(\mathbf{k}, \lambda) = \tilde{c}_0(\mathbf{k}) \frac{1 - \psi^*(\lambda)}{\lambda[1 - \tilde{\psi}^*(\mathbf{k}, \lambda)]}, \tag{2.16}$$

where the tilde indicates Fourier-transformed quantities in space and $\mathbf{k}$ is the Fourier variable. From the latter expression one can calculate the moments of particle displacement by making use of the well-known relations

$$\mu_i^*(\lambda) = (-i) \frac{\partial \tilde{c}^*(\mathbf{k}, \lambda)}{\partial k_i}\bigg|_{\mathbf{k}=0} \qquad \mu_{ij}^*(\lambda) = - \frac{\partial^2 \tilde{c}^*(\mathbf{k}, \lambda)}{\partial k_i \partial k_j}\bigg|_{\mathbf{k}=0}. \tag{2.17}$$

Notice that in $d = 1$ dimensions, if we consider the uncoupled distribution of transition times and lengths $\psi(x, t) = p(x)\psi(t)$ and we suppose that $\psi(t)$ is an exponential distribution with mean τ, Equation (2.17) leads to (Klafter and Sokolov, 2011)

$$\mu_{11}(t) - \mu_1^2(t) = \frac{\langle \ell \rangle^2}{\tau} t, \tag{2.18}$$

where $\langle \ell \rangle$ is the mean transition length. By defining the dispersion coefficient as $D = \langle \ell \rangle^2 / (2\tau)$ we finally get

$$\mu_{11}(t) - \mu_1^2(t) = 2Dt, \tag{2.19}$$

as expected for Fickian diffusion. Note that in this case the spatial particle density obtained by inverting Equation (2.16) yields the Gaussian distribution

$$c(x, t) = \frac{1}{\sqrt{2\pi\sigma^2 t/\tau}} \exp\left(-\frac{(x - \langle \ell \rangle)^2}{2\sigma^2 t/\tau}\right), \tag{2.20}$$

where σ^2 is the variance of the distribution $p(x)$. If the distribution $\psi(x, t)$ can not be decoupled, or if the moments of the transition times and lengths are not defined, e.g. because $p(x)$ and/or $\psi(t)$ are power-law distributions, these results are no longer valid. Based on results present in the literature and on new derivations, we will show how to address these issues in the thesis.

3

Heterogeneous advection and solute trapping

Abstract

We study the combined impact of heterogeneous advection and trapping on non-Fickian transport using the continuous time random walk (CTRW) approach. The CTRW models solute transport in heterogeneous media as a random walk in space and time. Our study is based on a d–dimensional CTRW model that accounts for both heterogeneous advection and trapping in immobile zones. The flow heterogeneity is mapped into the distribution of advective transition times over a characteristic heterogeneity scale. Trapping due to diffusion into immobile zones is quantified by a trapping rate and the distribution of particle return times. The total particle transition time over a characteristic heterogeneity scale then is given by the advective time and the sum of trapping times over the number of trapping events. We establish explicit integro-partial differential equations for the evolution of the concentration and discuss the relation to the multirate mass transfer (MRMT) approach, specifically the relation between the trapping time distribution and the memory function. We then analyze the signatures of anomalous transport due to advective heterogeneity and trapping in terms of spatial moments and first passage times or breakthrough curves. The behaviors for different disorder scenarios are analyzed analytically and through random walk particle tracking simulations. Assuming that advective mass transfer is faster than diffusive, we identify three regimes of distinct transport behaviors, which are separated by the characteristic trapping rate and trapping times. (1) At early times we identify a preasymptotic time regime that is fully determined by advective heterogeneity and

This chapter is based on the paper " A. Comolli et al. - Non-Fickian transport under heterogeneous advection and solute trapping, Transport in Porous Media (2016)".

which is characterized by superlinear growth of longitudinal dispersion. (2) For longitudinal dispersion, we identify an intermediate regime of strong superlinear diffusion. This regime is determined by the combined effect of advective heterogeneity and trapping. (3) At larger time, the asymptotic trapping-driven regime shows the signatures of diffusion in immobile zones, which leads to both sub and super-linear dispersion. These results shed some new light on the mechanism of non-Fickian transport and their manifestation in spatial and temporal solute distributions.

3.1 Introduction

Solute transport in highly heterogeneous porous media is characterized by features that do not conform to advection-dispersion models characterized by equivalent transport parameters. This has been observed from pore to field-scale under forced and natural flow conditions. The non-Fickian character is manifest for example in non-linear growth of solute dispersion, forward and backward tails in spatial tracer distributions (Koch and Brady, 1988; Adams and Gelhar, 1992; Moroni and Cushman, 2001; Levy and Berkowitz, 2003; Holzner et al., 2015), and in the occurrence of heavy-tailed solute breakthrough curves and first passage time distributions (Hatano and Hatano, 1998; Haggerty et al., 2000, 2001; Berkowitz et al., 2001; Becker and Shapiro, 2003; Cortis and Berkowitz, 2004; Gouze et al., 2008a; Kang et al., 2015b). Methods and models to explain and quantify such anomalous behaviors include moment equations (Neuman and Zhang, 1990; Morales-Casique et al., 2006) and projector methods (Cushman et al., 1994), as well as space and time fractional advection-dispersion equations (Benson et al., 2000; Cushman and Ginn, 2000; Schumer et al., 2003).

In this paper, we focus on the continuous time random walk (CTRW) and multirate mass transfer (MRMT) approaches for the modeling of anomalous transport. Both approaches are similar in nature in the sense that anomalous transport features are related to distributions of characteristic mass transfer time scales which renders the governing equations for solute concentrations non-local in time.

The CTRW approach models transport in heterogeneous media through a random walk in both space and time. The time increment can be related to the advective or diffusive transition times over a characteristic heterogeneity scale as well as to the time a particle is trapped or immobilized. The CTRW framework developed by Scher and Lax (1973) based on the model of Montroll and Weiss (1965) has found broad applications for the modeling of history-dependent dynamics in fluctuating and disordered systems ranging from the dispersion of light in disordered optical media (Barthelemy et al., 2008) to the movement of single molecules in living cells (Barkai et al., 2012), among many others (Klafter and Sokolov, 2005). In the 1990s Harvey Scher and Brian Berkowitz realized that the CTRW provides a natural framework for the understanding and quantification of anomalous transport in heterogeneous fractured and porous media (Berkowitz and Scher, 1995, 1997). Since then the CTRW has been used as an upscaling

and average transport framework to quantitatively understand flow and transport processes in geological media (Berkowitz et al., 2006) and has shed light on the origins and mechanisms of non-Fickian transport from the pore (Bijeljic and Blunt, 2006; Cortis et al., 2004; de Anna et al., 2013; Kang et al., 2014; Holzner et al., 2015) to the Darcy scale (Dentz and Castro, 2009; Le Borgne et al., 2008a; Edery et al., 2014) and catchment scale (Scher et al., 2002).

The MRMT approach is based on a multicontinuum concept (Barenblatt et al., 1960) that represents a highly heterogeneous porous or fractured medium by a mobile continuum and a suite of immobile continua, which communicate through linear mass transfer mechanisms such as diffusion or first-order rate processes (Maloszewski and Zuber, 1985; Roth and Jury, 1993; Haggerty and Gorelick, 1995; Carrera et al., 1998; Haggerty et al., 2000). The medium heterogeneity is encoded in the memory function, which reflects the mass transfer mechanisms, diffusion or slow advection, for example, and the geometry and heterogeneity of the immobile regions (Zinn et al., 2004; Gouze et al., 2008b; Willmann et al., 2008; Zhang et al., 2014). It has been shown that MRMT can be modeled within the CTRW framework through mapping the memory function onto the distribution of transition times (Dentz and Berkowitz, 2003; Schumer et al., 2003; Berkowitz et al., 2008). More specifically, the trapping process can be modeled within the CTRW framework as a compound Poisson process (Margolin et al., 2003; Benson and Meerschaert, 2009; Dentz et al., 2012, 2015a). This means that trapping events occur at constant rate, which renders the number of trapping events during a given time interval a Poisson process. The distribution of trapping times can be related directly to the memory function of MRMT, in fact, it is given by its derivative.

Non-Fickian transport often arises in presence of viscoelastic or fractal media (Meroz and Sokolov, 2015) or geometric constraints (Metzler et al., 2014). In this paper, we will study the impact of advective heterogeneity and solute trapping on transport. In fact, advective heterogeneity and solute trapping into immobile zones represent two mechanisms that can lead to anomalous transport as expressed through non-Gaussian spatial and temporal distributions and nonlinear evolution of spatial moments (Haggerty et al., 2000; Becker and Shapiro, 2003; Kang et al., 2015b). It is often not clear how to separate these mechanisms and their impact on large scale transport because of their similar manifestation. These questions have been approached in Kang et al. (2015b) and Dentz et al. (2015a) in the analysis of solute breakthrough curves in radial tracer tests. Here we set-up a CTRW model that represents explicitly heterogeneous advection and solute trapping in d–dimensional heterogeneous media, in order to systematically study the manifestation of these different mechanisms on spatial and temporal large scale transport characteristics. This allows to discriminate between advective and trapping mechanisms and quantify them from observations of anomalous transport. Furthermore, the formulation of MRMT in terms of CTRW give some new insight in to the relation of the trapping process and the mass transfer processes encoded by the memory function.

The next section describes the general CTRW framework and the specific

implementation of advective heterogeneity and solute trapping. It discusses the equivalence to the MRMT approach and analyzes the relation between memory function, trapping rate and the distribution of trapping times. Section 3.3 defines the observables that are analyzed, namely the center of mass and dispersion of a solute distribution as well as the distribution of first passage times. We also visualize spatial solute distributions in $d = 1$ and $d = 2$ dimensions. Section 3.4 studies the temporal evolution of the spatial concentration moments and the behavior of the first passage time distributions for different heterogeneity scenarios.

3.2 Continuous time random walk

The CTRW models particle movements in a heterogeneous environment as a random walk in space and time such that the particle position $\mathbf{x}_n$ and t_n after n random walk steps are given by the stochastic recursion

$$\mathbf{x}_{n+1} = \mathbf{x}_n + \boldsymbol{\xi}_n, \qquad t_{n+1} = t_n + \tau_n, \tag{3.1}$$

where $\boldsymbol{\xi}_n$ and τ_n are random spatial and temporal increments, respectively. The stochastic dynamics of the heterogeneous system are mapped into the joint probability density function (PDF) of the random space and time increment $\psi(\boldsymbol{\xi}, \tau)$, which is at the heart of the CTRW approach. The particle distribution, or equivalently concentration distribution $c(\mathbf{x}, t)$ is given in terms of the space-time particle trajectories as

$$c(\mathbf{x}, t) = \langle \delta[\mathbf{x} - \mathbf{x}_{n_t}] \rangle, \tag{3.2}$$

where the angular brackets denote the average over all particles; $n_t = \sup(n|t_n \leq t)$ is the number of steps needed to reach time t. In order to derive the governing equations for $c(\mathbf{x}, t)$, we follow Scher and Lax (1973) and consider $R_n(\mathbf{x}, t) = \langle \delta(\mathbf{x}-\mathbf{x}_n)\delta(t-t_n) \rangle$, the joint density of particle position and times after n random walk steps. Note that the space-time random walk (3.1) is a Markov process in the step number n. Thus, its density $R_n(\mathbf{x}, t)$ satisfies the Chapman-Kolmogorov equation

$$R_{n+1}(\mathbf{x}, t) = \int d\mathbf{x}' \int_0^t dt' \psi(\mathbf{x} - \mathbf{x}', t - t') R_n(\mathbf{x}', t'). \tag{3.3}$$

Note that the particle distribution $c(\mathbf{x}, t)$ measures the probability that a particle is at position $\mathbf{x}$ at time t for any number of random walk steps. Thus, we define now the quantity $R(\mathbf{x}, t) = \sum_{n=0}^{\infty} R_n(\mathbf{x}, t)$, which denotes the probability per time that the particle has just arrived at a position $\mathbf{x}$ at time t after any number of steps. It is now evident that $c(\mathbf{x}, t)$ is constituted by the number of particles that have just arrived at position $\mathbf{x}$ and the ones that have arrived at an earlier time t' and have not finished the transition to the next position in space, or in

other words, the transition time to any other position $\mathbf{x}$ is larger than $t-t'$. The latter is given by

$$\Phi(t-t') = \int_{t-t'}^{\infty} d\tau \psi(\tau), \tag{3.4}$$

where $\psi(\tau) = \int d\mathbf{x}\psi(\mathbf{x},\tau)$ is the transition time PDF. Thus, the governing equation for $c(\mathbf{x},t)$ can be written as

$$c(\mathbf{x},t) = \int_0^t dt' R(\mathbf{x},t')\Phi(t-t'), \tag{3.5}$$

which is complemented by the equation for $R(\mathbf{x},t)$ as given by summation of (3.3),

$$R(\mathbf{x},t) = R_0(\mathbf{x},t) + \int d\mathbf{x}' \int_0^t dt' \psi(\mathbf{x}-\mathbf{x}', t-t') R(\mathbf{x}',t'). \tag{3.6}$$

The initial condition of the CTRW is denoted by $R_0(\mathbf{x},t) = \langle\delta(\mathbf{x}-\mathbf{x}_0)\rangle\delta(t-t_0)$. Equations (3.5) and (3.6) can be combined into the generalized Master equation (Kenkre et al., 1973)

$$\frac{dc(\mathbf{x},t)}{dt} = \int d\mathbf{x}' \int_0^t dt' \mathcal{K}(\mathbf{x}-\mathbf{x}', t-t') \left[c(\mathbf{x}',t') - c(\mathbf{x},t')\right], \tag{3.7}$$

where the memory kernel $\mathcal{K}(\mathbf{x},t)$ is defined in Laplace space (Abramowitz and Stegun, 1972) as

$$\mathcal{K}^*(\mathbf{x},\lambda) = \frac{\lambda\psi^*(\mathbf{x},\lambda)}{1-\psi^*(\lambda)}. \tag{3.8}$$

Here and in the following, the Laplace variable is denoted by λ, Laplace transformed quantities are marked by an asterisk.

Scher and Lax (1973) developed this theory based on the CTRW model of Montroll and Weiss (1965) to quantify stochastic transport in disordered solids. Since then, it has found a wide range of applications in the modeling of the history-dependent dynamics in fluctuating and disordered systems (Klafter and Sokolov, 2005). Most notably, the CTRW framework has been used for the understanding and quantification of non-Fickian transport in heterogeneous fractured and porous media in the seminal works of Berkowitz and Scher (1995) and Berkowitz and Scher (1997). In this context the transition time τ of a solute particle is related kinematically to the transition length $\ell = |\xi|$ through the particle velocity v as $\tau = \ell/v$ as discussed in the following.

In the following sections, we will make use of this CTRW framework to model two distinct mechanisms that enhance non-Fickian transport. First, we will consider heterogeneous advection which arises because of the heterogeneity of the

hydraulic conductivity field. The second process that we are going to discuss is the trapping of solutes that describes mass exchange between mobile and immobile phase, as well as sorption/desorption reactions.

3.2.1 Heterogeneous advection

We consider now purely advective transport in a heterogeneous velocity field $\mathbf{u}(\mathbf{x})$. The particle trajectory is described by the advection equation

$$\frac{d\mathbf{x}(t)}{dt} = \mathbf{v}(t), \tag{3.9}$$

where $\mathbf{v}(t) = \mathbf{u}[\mathbf{x}(t)]$ denotes the Lagrangian particle velocity. The distance $s(t)$ and the time $t(s)$ travelled along a streamline can be written as

$$\frac{ds(t)}{dt} = v[s(t)], \qquad \frac{dt(s)}{ds} = \frac{1}{v_s(s)}, \tag{3.10}$$

where $\mathbf{v}_s(s) = \mathbf{v}[t(s)]$ and $v_s(s) = |\mathbf{v}_s(s)|$ is the velocity along the streamline. It has been shown for flow in pore and Darcy scale heterogeneous porous media (Le Borgne et al., 2008a; Kang et al., 2011; de Anna et al., 2013; Kang et al., 2014, 2015b) that particle velocities measured equidistantly in space along trajectories form a Markov process. Particle trajectories are then characterized by a one-step correlation. Therefore, some authors have studied an extension of this model that is known as correlated CTRW (Checkin et al., 2009; Tejedor et al., 2010). For distances larger than the correlation length ℓ_c along the streamline (Kang et al., 2015b), subsequent velocities can be considered independent. Note that subsequent space and time increments in the CTRW (3.1) are independent. Thus, by coarse graining the particle movement on a scale Δs larger or equal to the correlation distance ℓ_c, we can write the equations of motion of solute particle as

$$\mathbf{x}_{n+1} = \mathbf{x}_n + \ell_c \boldsymbol{\omega}_n, \qquad t_{n+1} = t_n + \frac{\ell_c}{v_n}, \tag{3.11}$$

where $\boldsymbol{\omega}_n = \mathbf{v}_n/|\mathbf{v}|$ is the orientation of the streamwise velocity $\mathbf{v}_n = \mathbf{v}_s(s_n)$. We assume that the mean velocity is aligned with the 1–direction of the coordinate system. Thus, we consider $\boldsymbol{\omega}_n$ as a random vector whose average is $\langle \boldsymbol{\omega} \rangle = \mathbf{e}_1$ where $\mathbf{e}_1$ is the unit vector in 1–direction. The streamwise velocities v_n are fully characterized by the one-point PDF $p_v(v)$. Note that the PDF of streamwise velocities is related to the Eulerian velocity PDF through flux weighting. Some authors (Fiori et al., 2007; Cvetkovic et al., 2014) have shown through simulations in random porous media that for low velocities it is possible to establish a linear relation between the conductivity field and the Eulerian advective field. Thus, through flux weighting it is possible to relate the streamwise velocity field to the conductivity field. The transition time is given by $\tau_a = \ell_c/v$. Thus, the joint PDF of transition length and transition time is

$$\psi_a(\boldsymbol{\xi}, \tau) = p_\xi(\boldsymbol{\xi})\psi_a(\tau), \qquad \psi_a(\tau) = \frac{\ell_c}{\tau^2} p_v(\ell_c/\tau). \tag{3.12}$$

It decouples because the constant transition length $|\boldsymbol{\xi}| = \ell_c$ is constant. The PDF $p_\xi(\boldsymbol{\xi})$ of space increments has mean $\langle \boldsymbol{\xi} \rangle = \ell_c \mathbf{e}_1$. In the following, we consider $p_\xi(\boldsymbol{\xi})$ with a mean that is aligned with the 1–direction of the coordinate system, and isotropic variance such that the first and second moments are given by

$$\langle \xi_i \rangle = \delta_{i1} \ell_c, \qquad \langle \xi_i \xi_j \rangle = \ell_c^2 \delta_{i1} \delta_{j1} + \delta_{ij} \sigma^2. \tag{3.13}$$

3.2.2 Heterogeneous advection and trapping

We now consider the trapping of particles in immobile regions as described through the MRMT approach (Haggerty and Gorelick, 1995; Harvey and Gorelick, 1995; Carrera et al., 1998; Dentz and Berkowitz, 2003; Schumer et al., 2003; Silva et al., 2009). MRMT has been used to model different types of retardation properties, from trapping due to sorption/desorption reactions to slow advection. However, here we use the MRMT model as a process that represents trappings only, in order to consider the effects of heterogeneous advection separately. The MRMT model considers solute transport under mass transfer between a single (homogeneous) mobile zone and a suite of immobile zones. Here, we model these processes within the CTRW framework (Margolin et al., 2003; Benson and Meerschaert, 2009; Dentz et al., 2012, 2015a; Gjetvaij et al., 2015). Trapping events occur at a constant rate γ. Thus, the number n_{τ_a} of trapping events during a mobile transition of duration τ_a is Poisson distributed with mean $\langle n_{\tau_a} \rangle = \gamma \tau_a$,

$$P(n, \tau_a) = \frac{(\gamma \tau_a)^n}{n!} \exp\left(-\gamma \tau_a\right). \tag{3.14}$$

Each trapping event is associated with a trapping time τ_f, which is distributed according to $p_f(\tau)$. Thus, for a given mobile time τ_a, the total trapping time during a mobile step is thus given by

$$\tau_{f,t} = \sum_{i=0}^{n_{\tau_a}} \tau_{f,i}. \tag{3.15}$$

It is a compound Poisson process whose density can be written in Laplace space as (Margolin et al., 2003)

$$\psi_f^*(\lambda|\tau_a) = \exp\left(-\left\{\lambda + \gamma[1 - p_f^*(\lambda)]\right\} \tau_a\right). \tag{3.16}$$

Thus, the total transition time is given by

$$\tau = \tau_a + \tau_{f,t}. \tag{3.17}$$

Its density reads in Laplace space as

$$\psi^*(\lambda) = \psi_a^*\left(\lambda + \gamma[1 - p_f^*(\lambda)]\right). \tag{3.18}$$

Note that the probability that the particle is trapped for a time longer than t is given by

$$\varphi(t) = \int_t^\infty dt' p_f(t'). \tag{3.19}$$

As we will see in the following, the latter is equal to the memory function of the MRMT approach (Haggerty and Gorelick, 1995; Carrera et al., 1998). Equivalently, the trapping time PDF is obtained for a given memory function as

$$p_f(t) = -\frac{d\varphi(t)}{dt}. \tag{3.20}$$

We divide now the total concentration into a mobile and an immobile concentration,

$$c(\mathbf{x}, t) = c_m(\mathbf{x}, t) + c_{im}(\mathbf{x}, t). \tag{3.21}$$

The immobile and mobile concentrations are related as

$$c_{im}(\mathbf{x}, t) = \gamma \int_0^t dt' \varphi(t - t') c_m(\mathbf{x}, t'). \tag{3.22}$$

The right hand side expresses the density of immobile particles by the probability per time that mobile particles get trapped at a given time t', $\gamma c_m(r, t')$, times the probability that the residence time in the immobile region is larger than $t - t'$. Thus, at asymptotically long times, the ratio of the time averaged immobile and mobile concentrations is given by

$$\lim_{t\to\infty} \frac{\overline{c}_{im}(\mathbf{x}, t)}{\overline{c}_m(\mathbf{x}, t)} = \lim_{\lambda\to 0} \gamma\lambda^{-1}[1 - p_f^*(\lambda)] = \gamma\langle\tau_f\rangle \tag{3.23}$$

where $\langle\tau_f\rangle$ is the mean immobile time, if it exists, and the overline denotes the time average $\overline{c}(\mathbf{x}, t) = t^{-1}\int_0^t dt' c(\mathbf{x}, t')$.

We can now express the Laplace transform of the total concentration $c(\mathbf{x}, t)$ in terms of the mobile and immobile concentrations as

$$c_m^*(\mathbf{x}, \lambda) = [1 + \gamma\varphi^*(\lambda)]c^*(\mathbf{x}, \lambda). \tag{3.24}$$

Using the latter in the Laplace transform of (3.7) and using (3.18) in the definition of the memory kernel, we can write down the following governing equation for $c^*(\mathbf{x}, \lambda)$,

$$\begin{aligned}\lambda c_m^*(\mathbf{x}, \lambda) + \gamma\lambda\varphi^*(\lambda)c_m^*(\mathbf{x}, \lambda) &= c(\mathbf{x}, 0)\\ + \int d\mathbf{x}' p_\xi(\mathbf{x}')\mathcal{K}_a^*(\lambda[1 + \gamma\varphi^*(\lambda)])\left[c_m^*(\mathbf{x} - \mathbf{x}', \lambda) - c_m^*(\mathbf{x}, \lambda)\right],\end{aligned} \tag{3.25}$$

where the purely advective memory kernel $\mathcal{K}_a^*(\lambda)$ is defined by (3.8) with $\psi^*(\lambda)$ replaced by $\psi_a^*(\lambda)$. Inverse Laplace transform of (3.25) gives

$$\frac{dc_m(\mathbf{x},t)}{dt} + \frac{d}{dt}\gamma \int_0^t dt' \varphi(t-t') c_m(\mathbf{x},t') = \int d\mathbf{x}' p_\xi(\mathbf{x}') \times$$
$$\int_0^t dt' \int_0^{t-t'} d\tau \mathcal{K}_a(\tau) \psi_f(t-t'-\tau|\tau) \left[c_m(\mathbf{x}-\mathbf{x}',t') - c_m(\mathbf{x},t')\right]. \tag{3.26}$$

The right side can be read as follows. The flux towards x is given by the probability that particles make a transition from $\mathbf{x}'$ to $\mathbf{x}$ times the probability that during the time interval $(t-t')$ there is a mobile episode of duration τ and a trapping episode of duration $t-t'-\tau$.

Weak advective heterogeneity

Although MRMT models have been used to model several retardation processes, ranging from sorption/desorption reactions to slow advection, in this work we will apply the MRMT model to the trapping process only. By doing so, we will consider the processes of heterogeneous advection and solute trapping separately. Most MRMT approches in the literature consider a homogeneous mobile zone, which is characterized in the CTRW frame by the exponential transition time

$$\psi_0(t) = \frac{\exp(-t/\tau_0)}{\tau_0}. \tag{3.27}$$

This implies that the memory kernel (3.8) reduces to a Dirac delta

$$\mathcal{K}_a(t) = \frac{\delta(t)}{\tau_0} \tag{3.28}$$

where τ_0 is the characteristic mobile transition time. Using this kernel in (3.26), we obtain directly

$$\frac{dc_m(\mathbf{x},t)}{dt} + \frac{d}{dt}\int_0^t dt' \varphi(t-t') c_m(\mathbf{x},t') =$$
$$\int d\mathbf{x}' p_\xi(\mathbf{x}') \left[c_m(\mathbf{x}-\mathbf{x}',t) - c_m(\mathbf{x},t)\right], \tag{3.29}$$

because $\psi_f(t-t'|0) = \delta(t-t')$. In order to obtain the advective-dispersive MRMT formulation, we specify the mean and mean squared displacement as $\langle \xi_i \rangle = v\tau_0\delta_{i1}$ and $\langle \xi_i \xi_j \rangle = v^2\tau_0^2\delta_{i1}\delta_{j1} + 2D\tau_0\delta_{ij}$, respectively, where v is the transport velocity and D is the dispersion coefficient. In the limit of $\tau_0 \to 0$, the displacement distribution is sharply peaked about 0 such that we can expand $c_m(\mathbf{x}-\mathbf{x}',t)$ into

a Taylor series for small $|\mathbf{x}'|$. Thus, we obtain from (3.29)

$$\frac{\partial c_m(\mathbf{x},t)}{\partial t} + \frac{\partial}{\partial t}\gamma \int_0^t dt' \varphi(t-t') c_m(\mathbf{x},t') = -\left(v\frac{\partial}{\partial x_1} - D\nabla^2\right) c_m(\mathbf{x},t) \quad (3.30)$$

Note terms of order higher than second in the Taylor expansion disappear in the limit $\tau_0 \to 0$. Equation (3.30) represents the MRMT model as often used in literature (Carrera et al., 1998; Haggerty and Gorelick, 1995). However, it is possible to consider a more general framework in which the MRMT is applied to transport in flow fields (Fernàndez-Garcia et al., 2009; Russian et al., 2016).

Trapping time distributions

The memory function $\varphi(t)$ encodes the mass transfer between mobile and immobile zones (Haggerty and Gorelick, 1995; Harvey and Gorelick, 1995; Carrera et al., 1998; Dentz and Berkowitz, 2003; Dentz et al., 2011). For linear first-order mass exchange it reflects the distribution of transfer rates between mobile and immobile regions (Haggerty and Gorelick, 1995). For diffusive mass transfer it is related to the PDF of particle return times to the immobile zone boundaries (Gouze et al., 2008b). Thus it is determined by the geometries and the characteristic diffusion scales of the immobile regions. The formulation of MRMT in terms of the CTRW framework sheds some new light on the meaning of the memory function and its relation to the residence time PDF $p_f(\tau)$. As outlined above, the memory function $\varphi(t)$ as defined in (3.19), is in fact the probability that a particle is trapped longer than a time t. The memory function here has the property $\varphi(0) = 1$. Note that $\varphi(t)$ is often defined differently, namely such that its integral is normalized to 1. Thus, in terms of the trapping time PDF, an alternative $\varphi_a(t)$ reads in terms of $p_f(\tau)$ as

$$\varphi_a(t) = \frac{1}{\langle \tau_f \rangle} \int_t^\infty d\tau p_f(\tau), \quad (3.31)$$

which requires the existence of the mean residence time $\langle \tau_f \rangle < \infty$.

For first-order mass transfer, the memory function is given by the exponential

$$\varphi(t) = \exp(-\alpha t), \quad (3.32)$$

with α the release rate, and equivalently α^{-1} the characteristic trapping time. The corresponding trapping time PDF is given by

$$p_f(t) = \alpha \exp(-\alpha t). \quad (3.33)$$

For diffusive trapping in slab-shaped semi-infinite immobile regions, the trapping time distribution is equivalent to the distribution of return times to the origin for a pulse input at the boundary. It is known that the return time PDF is

not well-defined in continuous space (Weiss, 1994) but needs to be determined on a lattice, which here has the characteristic length ℓ_g. In this case, the return time PDF, or equivalently the trapping time PDF is given by the inverse Gaussian

$$p_f(t) = \frac{\exp\left(-\frac{\tau_g}{4t}\right)}{t\sqrt{4t/\tau_g}} \tag{3.34}$$

where τ_g is a characteristic trapping time. It estimates the time that particles need to travel a distance ℓ_g by diffusion. Note that the trapping time PDF $p_f(t)$ decays for $t \gg \tau_g$ as $t^{-3/2}$. The PDF (3.34) is also termed Lévy distribution. The corresponding memory function is given by

$$\varphi(t) = 1 - \frac{\Gamma\left(\frac{1}{2}\frac{\tau_g}{4t}\right)}{\sqrt{\pi}}, \tag{3.35}$$

with $\Gamma(\beta, t)$ the incomplete Gamma function (Abramowitz and Stegun, 1972). It behaves as $t^{-1/2}$ for $t \gg \tau_g$.

For diffusive trapping in slab-shaped immobile regions of finite size, on the other hand, the memory function can be written in Laplace space as (Harvey and Gorelick, 1995; Carrera et al., 1998)

$$\varphi_a^*(\lambda) = \frac{1}{\sqrt{\lambda\tau_D}} \tanh(\sqrt{\lambda\tau_D}), \tag{3.36}$$

where τ_D is the characteristic diffusion scale. It is normalized to 1 and has an integrable singularity at $t = 0$. It behaves as $\varphi(t) \propto t^{-1/2}$ for $t \ll \tau_D$. This means, however, that $\langle \tau_f \rangle = \varphi_a(0)^{-1}$ cannot be defined in terms of this memory function, for the reasons outlined above. Nevertheless, from the behavior of the memory function at times $t \ll \tau_D$, we deduce that the PDF of trapping times behaves as $p_f(t) \propto t^{-3/2}$, as in the case of the semi-infinite medium. For $t \gg \tau_D$, $p_f(t)$ is cut-off exponentially in the same way as the memory function $\varphi_a(t)$. In the following, our focus is on the pre-asymptotic behavior when the immobile zone has not yet equilibrated with the mobile zone, this means at times $t \ll \tau_D$. Thus, we will employ the trapping time PDF (3.34). It has been shown in Gouze et al. (2008b) that the memory function $\varphi(t)$ may display behaviors that are different from the characteristic $t^{-1/2}$ if the immobile regions are heterogeneous. Thus, in order to account for diffusive trapping in heterogeneous immobile regions, we employ the more general Lévy stable distributions

$$p_f^*(\lambda) = \exp\left[-(\tau_g\lambda)^\delta\right], \tag{3.37}$$

where $0 < \delta < 1$. It behaves for $t \gg \tau_g$ as $p_f^*(t) \propto t^{-1-\delta}$. Note that τ_g is approximately the median time of the trapping time PDF. Note also that for $\delta = 1/2$ (3.37) is the Laplace transform of the inverse Gaussian (3.34).

3.3 Observables

In the following, we define the spatial distribution and moments of the concentration distribution as well as first passage time distributions and present expressions for their quantification in the CTRW framework reported in the previous section.

3.3.1 Spatial moments

The evolution of the spatial particle distribution is given by the generalized Master equation (3.7). In Fourier-Laplace space, we obtain the compact expression (Scher and Lax, 1973)

$$\tilde{c}^*(\mathbf{k},\lambda) = \frac{1-\psi^*(\lambda)}{\lambda[1-\tilde{p}_\xi(\mathbf{k})\psi^*(\lambda)]}, \tag{3.38}$$

where we used that the PDF of transition length and time decouples into $\psi(\mathbf{x},t) = p_\xi(\mathbf{x})\psi(t)$.

The Fourier transform is defined here by

$$\tilde{c}(\mathbf{k},t) = \int\limits_{\mathbb{R}^d} d\mathbf{x}\exp(i\mathbf{k}\cdot\mathbf{x})c(\mathbf{x},t), \tag{3.39}$$

$$c(\mathbf{x},t) = \int\limits_{\mathbb{R}^d} \frac{d\mathbf{k}}{(2\pi)^d}\exp(-i\mathbf{k}\cdot\mathbf{x})\tilde{c}(\mathbf{k},t). \tag{3.40}$$

Fourier transformed quantities are marked by a tilde, the wave vector is denoted by $\mathbf{k}$; the imaginary unit is denoted by i.

The first and second moments $m_j(t)$ and $m_{ij}(t)$ of the particle density $c(\mathbf{x},t)$ can be expressed in Laplace space by using (3.38) as

$$m_i^*(\lambda) = -i\left.\frac{\partial\tilde{c}^*(\mathbf{k},\lambda)}{\partial k_i}\right|_{\mathbf{k}=0}, \qquad m_{ij}^*(\lambda) = -\left.\frac{\partial^2\tilde{c}^*(\mathbf{k},\lambda)}{\partial k_i\partial k_j}\right|_{\mathbf{k}=0} \tag{3.41}$$

The center of mass of the particle distribution is measured by $m_i(t)$ while its dispersion is quantified by the second centered moments

$$\kappa_{ij}(t) = m_{ij}(t) - m_i(t)m_j(t). \tag{3.42}$$

By inserting (3.38) into (3.41) and using (3.13) one obtains for $m_i^*(\lambda)$ (Dentz et al., 2004)

$$m_i^*(\lambda) = \delta_{i1}\frac{\ell\psi^*(\lambda)}{\lambda[1-\psi^*(\lambda)]}. \tag{3.43}$$

For the second moments, one obtains analogously

$$m_{ii}^*(\lambda) = \frac{(\delta_{i1}\ell^2+\sigma^2)\psi^*(\lambda)}{\lambda[1-\psi^*(\lambda)]} + \lambda m_i^*(\lambda)^2\delta_{i1}. \tag{3.44}$$

The off-diagonal components are zero by definition. These expressions form the basis for the calculation of the evolution of the spatial moments in the following.

3.3.2 First passage time distribution

The first passage times of solute particles at a plane located at $x_1 = x_c$ is defined here by

$$\tau(x_c) = t_{n_c}, \qquad n_c = \inf\left(n | x_{1,n} \geq x_c\right). \tag{3.45}$$

We consider here pulse injections at $\mathbf{x} = 0$ at the time $t = 0$. The generalization to different injection conditions is immediate, since it simply requires the superposition of the responses to pulses. The first passage time distribution (FPTD) is defined by

$$f(t, x_c) = \langle \delta[t - \tau(x_c)] \rangle. \tag{3.46}$$

Using (3.45), this expression can be expanded as

$$f(t, x_c) = \sum_{n=0}^{\infty} f_0(n, x_c) p_n(t), \tag{3.47}$$

where $f_0(n, x_c) = \langle \delta_{n,n_c} \rangle$ is the distribution of the numbers of steps needed to reach x_c and $p_n(t) = \langle \delta(t - t_n) \rangle$ is the distribution of times t_n after n CTRW steps. For large values of n, $f_0(n, x_c)$ converges to an inverse Gaussian distribution that is well-peaked about the mean value $\langle n_c \rangle = \lceil x_c/\ell \rceil$, where the upper brackets denote the ceiling function. Therefore, we approximate

$$f(t, x_c) \approx p_{\langle n_c \rangle}(t). \tag{3.48}$$

Thus, we can develop explicit expressions for $f(t, x_c)$ along the lines of Dentz et al. (2015a). In Laplace space $p_{\langle n_c \rangle}(t)$ can be written as

$$p^*_{\langle n_c \rangle}(\lambda) = \psi^*(\lambda)^{\langle n_c \rangle}. \tag{3.49}$$

We define now $\psi^*(\lambda) = 1 - \Delta\psi^*(\lambda)$ in order to write

$$p^*_{\langle n_c \rangle}(\lambda) = \exp\left(\langle n_c \rangle \ln\left[1 - \Delta\psi^*(\lambda)\right]\right) \approx \exp\left[-\langle n_c \rangle \Delta\psi^*(\lambda)\right]. \tag{3.50}$$

This expression is the basis for the derivation of the asymptotic behaviors of the FPTD under advective heterogeneity and solute trapping investigated in the following.

3.4 Transport under heterogeneous advection and trapping

Here we study transport under the combined action of heterogeneous advection and solute trapping in the framework of the CTRW model described in Section 3.2. We analyze the transport behavior for scenarios that correspond to different degrees of heterogeneity of the advective field and of the mass transfer

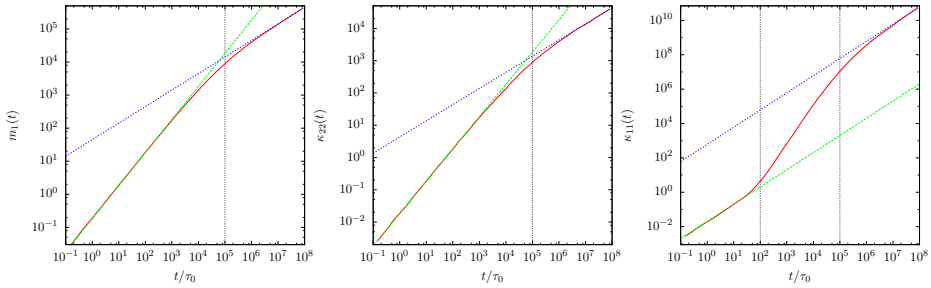

Figure 3.1: (Left) Center of mass position $m_1(t)$, (center) transverse variance $\kappa_{22}(t)$, and (right) longitudinal variance $\kappa_{11}(t)$, for $\delta = 1/2$, $\gamma = 10^{-2}\tau_0^{-1}$.

processes. Namely, we will first present the case in which the mobile transition times follow an exponential distribution, which corresponds to a condition of weak advective heterogeneity as discussed in Section 3.2.2, while the distribution of trapping times is characterized by strong tailing characteristic for pre-asymptotic diffusive mass transfer. Secondly, we will consider the case of heterogeneous advection characterized by a strong tailing in the PDF $\psi_a(t)$ of the advective transition time PDF together with a broad distribution of trapping times $p_f(t)$, for which we employ the stable distributions (3.37).

Before proceeding to the analysis of the transport behaviors, we briefly discuss the characteristic time scales of the trapping process. The first time scale is represented by the inverse of the trapping rate $\tau_\gamma = \gamma^{-1}$. It has a double meaning. On one hand, it represents the time at which, on average, particles undergo the first trapping event. On the other hand, it is the average time particles spend in the mobile phase. The second characteristic scale is given by the time at which the average time spent mobile τ_γ is equal to the average time spent immobile. A characteristic average trapping time after n trapping events is given by $\langle \tau_f(n) \rangle \approx \tau_g n^{\frac{1-\delta}{\delta}}$, see Appendix A, while the average number of trapping events after time t is given by $\langle n_{f,t} \rangle = \gamma t$. This means that the mean trapping time after time t is given by

$$\langle \tau_f(t) \rangle \approx \tau_g (\gamma t)^{\frac{1-\delta}{\delta}}. \tag{3.51}$$

The mean trapping time increases as a power law of the overall travel time, which is a characteristic of a fractal process (Bouchaud and Georges, 1990). By setting $\tau_\gamma = \langle \tau_f(\tau_e) \rangle$, we obtain for the time scale τ_e

$$\tau_e = \tau_\gamma \left(\gamma \tau_g\right)^{\frac{\delta}{1-\delta}}. \tag{3.52}$$

In the following, we investigate the temporal evolution of the spatial moments and the first-passage time distributions in the light of these characteristic time trapping time scales.

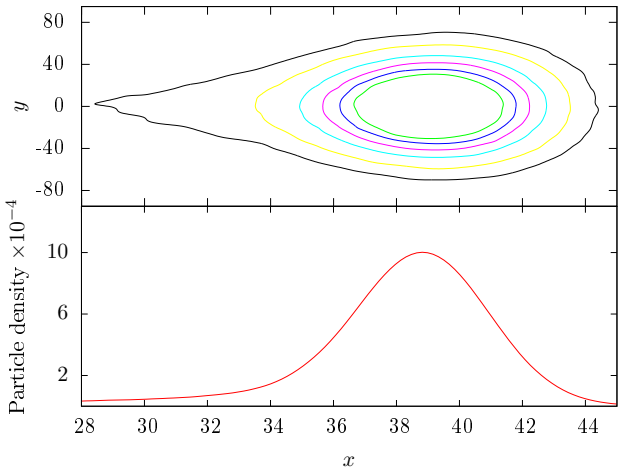

Figure 3.2: (Top panel) Spatial particle density and (bottom panel) vertically integrated particle density at $t = 4 \times 10^2 \tau_0$ for $\delta = 1/2$, $\gamma = 10^{-2}\tau_0^{-1}$.

3.4.1 Weak advective heterogeneity–multirate mass transfer

The MRMT model has been extensively studied in the literature in terms of first passage times and breakthrough curves. Here we analyze the spatial aspects of the model in terms of the evolution of the spatial moments with respect to the characteristic trapping times discussed previously. For completeness, we also discuss the first passage time distributions in the light of the parameters of the trapping model, specifically, the role of the trapping rate γ. The PDF $p_f(t)$ of trapping times is given by the Lévy distribution (3.34), while the distribution of advection times is given by the exponential (3.27). The advection scale τ_0 represents the time at which particles have sampled full advective heterogeneity. Here we set $\tau_0 \ll \tau_\gamma \ll \tau_e$. Thus, we identify three time regimes, the *pre-asymptotic time regime* defined by $\tau_0 \ll t \ll \tau_\gamma$, the *intermediate time regime* $\tau_\gamma \ll t \ll \tau_e$ and the *asymptotic time regime* $t \gg \tau_e$.

Spatial moments

Figure 3.1 shows the behavior of the center of mass and the spatial variance of the particle distribution in the longitudinal and transverse directions obtained through numerical particle tracking simulations in $d = 2$ spatial dimensions. We have studied the system under the condition of point-like injection at position $\mathbf{x} = 0$ at time $t = 0$. We observe that the mean in the longitudinal direction and the variance in the transverse direction exhibit very similar behaviors. In contrast, the behavior of the variance in the longitudinal direction is rather different as discussed in the following.

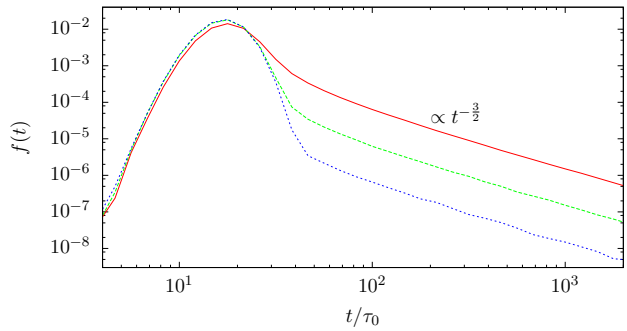

Figure 3.3: First passage time distributions at $x_c = 20\ell_c$ for $\delta = 1/2$ for (red solid line) $\gamma = 10^{-1}\tau_0^{-1}$, (green dashed line) $\gamma = 10^{-2}\tau_v^{-1}$ and (blue dotted line) $\gamma = 10^{-3}\tau_v^{-1}$.

Pre-asymptotic regime $\tau_0 \ll t \ll \tau_e$ For times $t > \tau_0$, particles have sampled the full advective heterogeneity and advection is homogeneous. Thus, the center of mass and the spatial variances scale linearly with time. While this behavior persists until the time scale τ_e for the center of mass and transverse dispersion, we observe an additional intermediate regime for the spatial variance in flow direction.

Intermediate regime $\tau_\gamma \ll t \ll \tau_e$ Due to the separation of trapped and advected particles, the solute distribution is elongated in flow direction, as illustrated in the Figure 3.2. In fact, we observe a strong increase of the longitudinal plume extension due to this chromatographic mechanism. This behavior sets on at the time τ_γ when the first particles get trapped and lasts until τ_e, where the slope of $\kappa_{11}(t)$ starts decreasing.

Asymptotic regime $t \gg \tau_e$ At times larger than τ_e, the time particles spend trapped is in average larger than the time mobile, which leads to a slowing down of particle motion. Trapping is the limiting process. As illustrated in Figure 3.1, $m_1(t)$ and $\kappa_{22}(t)$ cross-over to their asymptotic subdiffusive behavior $t^{-1/2}$. The spatial variance in the longitudinal direction $\kappa_{11}(t) \propto t$ evolves linearly with time, which may suggest normal diffusive behavior. However, we have here rather an equilibrium between trapping and chromatographic stretching due to the fact that here the average time spent in the immobile zone given by (3.51) scales linearly with time. This means that the ratio between time spent in the mobile region and immobile traps is constant.

First passage time distribution

Figure 3.3 shows first passage time distributions for three different values of the trapping rate γ recorded at a control plane at $x_c = 20\ell_c$. These behaviors have

been well known in the literature. We observe a characteristic advective peak at approximately $\tau_p = x_c/v$ with $v = \langle\xi\rangle/\tau_0$. At the peak time, the average time spent immobile is according to (3.51) $\langle\tau_f(t_p)\rangle \approx \tau_g\gamma t_c$. This explains the observation of slight retardation of the peak behavior for larger trapping rate $\gamma = 10^{-1}$ compared to the smaller rates. At times larger than the peak time, the FPTD first decays exponentially fast before it shows the characteristic $t^{-3/2}$ tailing typical for matrix diffusion, see also Appendix C. The tailing is exclusively caused by particle release from the immobile traps. and it depends on the proportion of trapped versus mobile particles during the peak arrival times, which is approximately γ, see (3.22). Thus the onset of the power-law tail the FPTD is approximately γ times the peak value of the FPTD as illustrated in Figure 3.3.

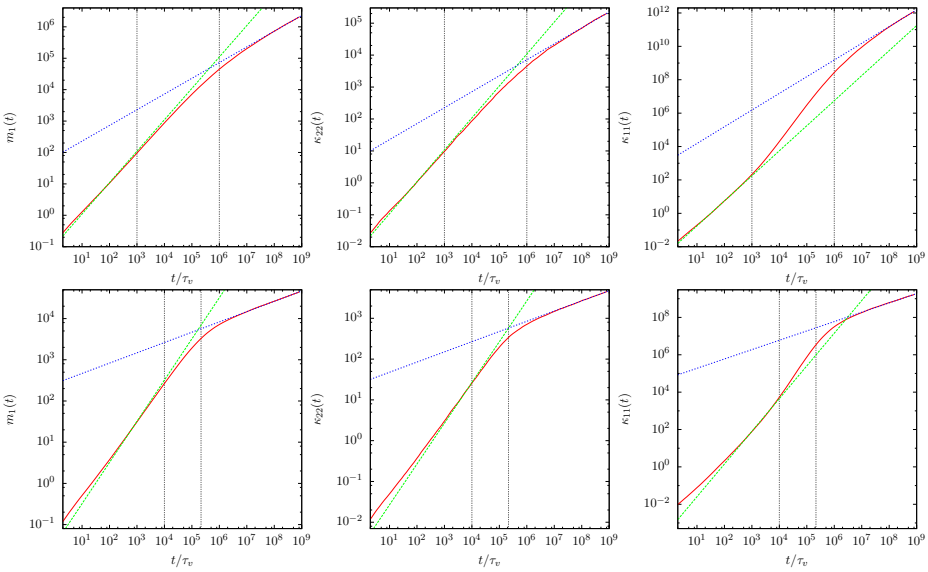

Figure 3.4: (Left) Center of mass position $m_1(t)$, (center) transverse variance $\kappa_{22}(t)$, and (right) longitudinal variance $\kappa_{11}(t)$, for (top row) $\beta = 3/2$, $\delta = 1/2$, $\gamma = 10^{-3}\tau_v^{-1}$, and (bottom row) $\beta = 5/4$, $\delta = 1/4$, $\gamma = 10^{-4}\tau_v^{-1}$. The vertical dashed lines denote (left to right) the corresponding τ_γ and τ_e.

3.4.2 Heterogeneous advection

We study the combined impact of advective heterogeneity and solute trapping on the spatial particle distribution and first passage times. Velocity PDFs in highly heterogeneous porous media may be characterized by power-law behaviors at small velocities, while high velocities are rather unlikely (Berkowitz et al., 2006; Le Borgne et al., 2007; Edery et al., 2014). In order to account for these

characteristics, we employ a Gamma distribution of transport velocities

$$\psi_v(v) = \left(\frac{v}{v_0}\right)^{\beta-1} \frac{\exp\left(-\frac{v}{v_0}\right)}{v_0\Gamma(\beta)}. \tag{3.53}$$

We limit the range of the exponent to $1 < \beta < 2$ because advection is here the mobile transport mechanism and thus faster than trapping in immobile zones, which is characterized by the Lévy stable distribution (3.37). The advective transition time then is given by $\tau_a = \ell_c/v$. It is given by the inverse Gamma PDF

$$\psi_a(t) = \left(\frac{t}{\tau_v}\right)^{-1-\beta} \frac{\exp\left(-\frac{\tau_v}{t}\right)}{\tau_v\Gamma(\beta)} \tag{3.54}$$

where the scale $\tau_v = \ell_c/v_0$ marks the time after which particles start experiencing the spectrum of advective heterogeneity. It corresponds to the characteristic advection time over one correlation length. In the following, we analyze the evolution of the spatial moments and the behavior of the first passage times in the light of the characteristic advection and trapping time scales.

Spatial moments

Figure 3.4 shows the evolution of the center of mass as well as transverse and longitudinal spatial variances. We distinguish a preasymptotic regime set by τ_v and τ_γ, a cross-over regime between τ_γ and τ_e and asymptotic regime for $t \gg \tau_e$ characterized by distinct temporal behaviors for all observables.

Pre-asymptotic regime $\tau_v \ll t \ll \tau_\gamma$ In this time regime transport is dominated by advective heterogeneity. Particles sample the velocity variability, but the average number of trapping events is smaller than 1. Thus, $m_1(t) \propto t$ and $\kappa_2(t) \propto t$ evolve linearly with time, while the longitudinal variance scales as $\kappa_{11} \propto t^{3-\beta}$ (Dentz et al., 2004), see also Appendix B.2.

Cross-over regime $\tau_\gamma \ll t \ll \tau_e$ Particles start experiencing the first trapping events. Thus, the center of mass position and transverse variance start deviating from the linear behavior and cross-over to their asymptotic behavior. As in the previous scenario, we observe a the strong increase of the longitudinal variance $\kappa_{11}(t)$ due to the separation of mobile and immobile particles in flow direction. This chromatographic plume elongation illustrated in the spatial particle distribution shown in Figure 3.5. We observe for both plumes a characteristic drop shaped form, while for $\beta = 5/4$ and $\delta = 1/4$ we observe a double peak behavior. This is a consequence of stronger particle trapping for decreasing δ.

Asymptotic regime $t \gg \tau_e$ In this regime the average time that particles spend in the immobile phase becomes larger than their average mobile times. Thus, the trapping process governs the transport behavior. While the center

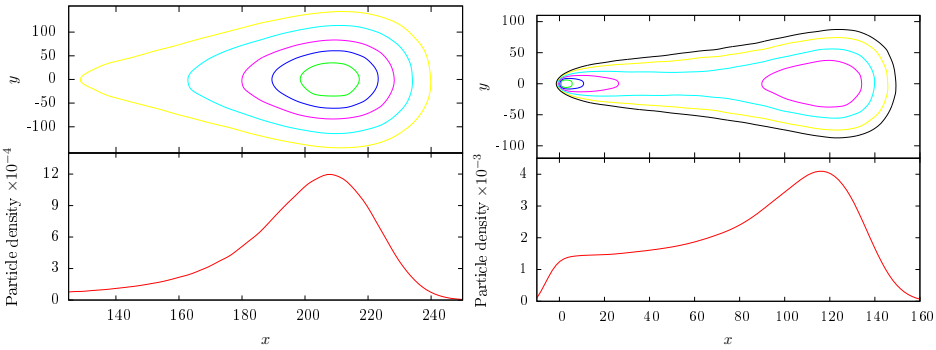

Figure 3.5: (Top) spatial particle density and (bottom) vertically integrated particle densities at $t = 4 \times 10^3 \tau_v$ for $\gamma = 10^{-3}\tau_v^{-1}$ and (left) $\beta = 3/2$, $\delta = 1/2$ and (right) $\beta = 5/4$, $\delta = 1/4$.

of mass position and transverse variance always show both subdiffusive growth as $\propto t^{\delta}$, the longitudinal variance scales as $\kappa_{11} \propto t^{2\delta}$, see Appendix B.2. This means that for $\delta = 1/4$ the longitudinal variance scales as $\kappa_{11} \propto t^{1/2}$. The behavior is subdiffusive in flow direction because of the strong trapping. The average trapping time (3.51) increases here as $\langle \tau_f(t) \rangle \approx \tau_g(\gamma t)^3$, this means that the ratio of the total time spent mobile versus the average trapping time decreases as $\gamma t / \langle \tau_f(t) \rangle \propto t^{-2}$. The particles will eventually localize, which gives rise to the subdiffusive behavior. For increasing δ this is different. As discussed previously for $\delta = 1/2$, $\langle \tau_f(t) \rangle \approx \tau_g(\gamma t)$. Thus, the ratio of total mobile time to average trapping time is constant, which here implies a linear growth of the longitudinal variance. For increasing $\delta > 1/2$, the average immobile time decreases with increasing time. Thus $\kappa_{11}(t)$ evolves superlinearly, again due to the increasing distance between mobile and trapped particles.

First passage time distribution

Figure 3.6 shows first passage time distributions for two different values of β and δ and varying trapping rates γ. The peak arrival time is related to the mode of the Gamma velocity PDF, i.e., the most probable value of $v_m = v_0/(\beta - 1)$ such that $\tau_p \approx x_c/v_m$. We distinguish again two time regimes. The early time regime is set by the peak time τ_p and characteristic time τ_γ for the first trapping event to occur. For $\tau_p \ll \tau_\gamma$, the first passage time behavior in the regime $\tau_p \ll t \ll \tau_\gamma$ is dominated by the advective heterogeneity. The FPTD here scale as $f(t, x_c) \propto t^{-1-\beta}$ (Berkowitz and Scher, 1997), see also Appendix C.2. For increasing time particle start experiencing trapping event and the breakthrough curves crosses over from the advective scaling toward the asymptotic scale $f(t, x_c) \propto t^{-1-\delta}$ in the asymptotic regime $t \gg \tau_e$.

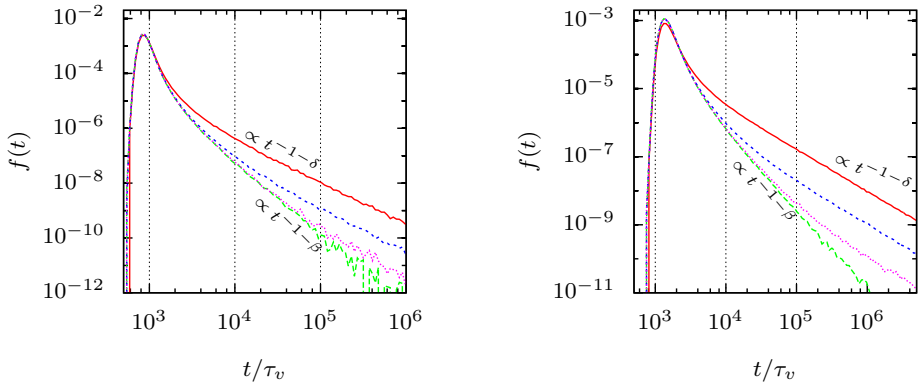

Figure 3.6: First passage time distributions at $x_c = 5 \times 10^2 \ell_c$ for (left panel) $\beta = 3/2$, $\delta = 1/2$, and (right panel) $\beta = 5/4$ and $\delta = 1/4$ for (red solid line) $\gamma = 10^{-3}\tau_v^{-1}$, (blue short dashed) $\gamma = 10^{-4}\tau_v^{-1}$, (pink dotted) $\gamma = 10^{-5}\tau_v^{-1}$ and (green long-dashed) $\gamma = 0$. The advection time scale is $\tau_v = 10^{-1}$. The black vertical dashed lines mark (left to right) $\tau_\gamma = 10^3\tau_v$, $10^4\tau_v$ and $10^5\tau_v$.

3.5 Summary and conclusions

We investigate the signatures of anomalous transport caused by heterogeneous advection and solute trapping. To this end we use a CTRW model that distinguishes between the two disorder mechanisms. In this approach the particle displacement is given by a characteristic velocity correlation scale. The transition time is composed of the advection time over this characteristic length and the total time particles spend trapped in immobile zones. The trapping process is modeled as a compound Poisson process. This means that trapping events are assumed to occur at a constant rate such that the number of trapping events during an advective transition is Poisson distributed. The total trapping time per step then is given by the sum of the trapping times over the number of trapping events. The distribution of trapping times can be related to the derivative of the memory function of the MRMT approach, or directly derived as the distribution of return times to the boundaries of the immobile region. We derive the integro-differential equation governing the evolution of the total concentration as well as the mobile concentration for this scenario of coupled heterogeneous advection and solute trapping. For weak heterogeneity we discuss the equivalence with the MRMT approach and study the relation between the memory function of MRMT and the distribution of trapping times. The CTRW model is formulated for d–spatial dimensions, our analysis of the transport behaviors is for illustration in $d = 2$.

In order to identify the signatures of advective heterogeneity and solute trapping on large scale transport, we study the temporal evolution of the center of mass and dispersion of the particle distribution as well as the distributions of first

passage times for different disorder scenarios. As we focus on aspects of anomalous transport, we consider stable distributions for the trapping times such that $p_f(t) \propto t^{-1-\delta}$ with $0 < \delta < 1$ and Gamma distributions of velocities which behave at small velocities as $p_v(v) \propto v^{\beta-1}$ with $1 < \beta < 2$. This gives rise to a distribution of advective transition times $\psi_a(t) \propto t^{-1-\beta}$.

We identify two characteristic time scales related to the trapping process, which set regimes of distinct transport behaviors. The first time scale is given by the inverse trapping rate, $\tau_\gamma = \gamma^{-1}$. It denotes the characteristic time after which a particle is trapped for the first time, as well as the mean time the particle is mobile. The second characteristic scale τ_e measures the time at which the particle has spend in average more time trapped than mobile. This means, for times larger than τ_e the transport behavior is dominated by the particle traps rather than by advection in the mobile zones. This time scale is given by $\tau_e = \tau_\gamma(\tau_g\gamma)^{\frac{\delta}{1-\delta}}$ with τ_g the median trapping time.

For weak heterogeneity, transport is Gaussian both in terms of spatial and temporal distributions for times smaller than τ_γ and larger than the characteristic advection time scale. For times larger than τ_γ, the spatial distribution takes on a clearly non-Gaussian elongated drop shape as a consequence of the separation of mobile and trapped particles. This is reflected quantitatively in the evolution of the longitudinal cumulant, which increases superlinearly until the begin of the asymptotic time regime in which solute trapping starts dominating and slows down the rapid particle separation. The center of mass position and transverse cumulant are not effected by this chromatographic separation and evolve linearly until trapping dominated from where on the behaviors become subdiffusive due to strong particle retention. These behaviors are also reflected by the first passage time distributions, characterized by an advective peak and a heavy tail due to particle trapping.

For strong heterogeneity, which is characterized by a high probability of low velocities, or long advective transition times, the behavior is qualitatively similar. Here we observe anomalous advection-dominated transport behavior for times that are larger than the characteristic advection, which is the time after which particle start sampling the advective heterogeneity. For times $t > \tau_\gamma$ we observe a similar chromatographic elongation due to the separation of mobile and immobile particles, which gives rise to a superlinear increase of the longitudinal cumulant. The increase is less drastic than in the case of weak heterogeneity because particles have in average lower velocities, which weakens the chromatographic effect. In fact, for decreasing δ, this means stronger trapping, a secondary peak in the tail of the particle distribution forms because advection is efficient in the separation of trapped and advected particles. For times larger than τ_e, trapping dominates and the longitudinal dispersion behavior is the same as in the case of weak heterogeneity. Again advective particle separation is not affecting the evolution of the center of mass position and transverse spreading. They both evolve linearly in time until they cross over to their asymptotic behavior on the time scale τ_e, from which on trapping dominates. The first passage time distributions are characterized by two regimes which are set by the peak arrival time

τ_p and the characteristic time τ_γ from the first trapping event. If both scales are well separate, we observe advection controlled taling behavior for $t \gg \tau_p$ and a cross-over to the trapping controlled long time behavior for $t \gg \tau_e$.

In conclusion, we have identified and quantified characteristic behaviors of spatial and temporal particle distributions as a response to advective heterogeneity and solute trapping. These results shed some new light on the manifestations of different heterogeneity mechanisms on large scale transport, which may aid in the their identification from large scale data and for the quantification of the pertinent heterogeneity parameters.

4

Heterogeneous advection and correlation

Abstract

We study the causes of anomalous dispersion in Darcy-scale porous media characterized by spatially heterogeneous hydraulic properties. Spatial variability in hydraulic conductivity leads to spatial variability in the flow properties through Darcy's law and thus impacts on solute and particle transport. We consider purely advective transport in heterogeneity scenarios characterized by broad distributions of heterogeneity length scales and point values. Particle transport is characterized in terms of the stochastic properties of equidistantly sampled Lagrangian velocities, which are determined by the flow and conductivity statistics. The persistence length scales of flow and transport velocities are imprinted in the spatial disorder and reflect the distribution of heterogeneity length scales. Particle transitions over the velocity length scales are kinematically coupled with the transition time through velocity. We show that the average particle motion follows a coupled continuous time random walk (CTRW), which is fully parameterized by the distribution of flow velocities and the medium geometry in terms of the heterogeneity length scales. The coupled CTRW provides a systematic framework for the investigation of the origins of anomalous dispersion in terms of heterogeneity correlation and the distribution of heterogeneity point values. We derive analytical expressions for the asymptotic scaling of the moments of the spatial particle distribution and first arrival time distribution (FATD), and perform numerical particle tracking simulations of the coupled CTRW to capture the full average transport behavior. Broad distributions of heterogeneity point values and lengths scales may lead to

This chapter is based on the paper " A. Comolli & M. Dentz - Anomalous dispersion in correlated porous media: A coupled continuous time random walk approach, European Physical Journal B (2017)".

very similar dispersion behaviors in terms of the spatial variance. Their mechanisms, however are very different, which manifests in the distributions of particle positions and arrival times, which plays a central role for the prediction of the fate of dissolved substances in heterogeneous natural and engineered porous materials.

4.1 Introduction

Large scale transport in disordered media generally exhibits non-Fickian features that cannot be captured by models based on the advection-dispersion equation (ADE) with constant drift and dispersion coefficients. Non-Fickian or anomalous transport characteristics have indeed been found ubiquitously in natural and engineered systems (Bouchaud and Georges, 1990; Klafter and Sokolov, 2005), including transport of charge carriers in amorphous solids (Scher and Lax, 1973; Scher and Montroll, 1975), photon transport in atomic vapors (Chevrollier et al., 2010) and in Lévy glasses (Barthelemy et al., 2008), animal foraging patterns (Viswanathan et al., 1996) and human motion (Brown et al., 2006), diffusion in living cells (Yu et al., 2009; Jeon et al., 2016; Massignan et al., 2014), and contaminant transport in geological formations (Berkowitz et al., 2006).

In this paper, we focus on solute and particle transport in Darcy-scale heterogeneous porous media, whose applications range from solute transport in fractured and porous geological media (Bear, 1972) to chromatography and chemical engineering (Brenner and Edwards, 1993). Spatial heterogeneity in the physical and chemical medium properties lead to anomalous transport behaviors characterized by non-linear growth of variance of particle displacements, non-Gaussian particle distributions and early and late particle arrivals (Gelhar et al., 1992; Cushman and Ginn, 1993; Haggerty and Gorelick, 1995; Berkowitz and Scher, 1995; Cvetkovic et al., 1996; Berkowitz and Scher, 1997; Carrera et al., 1998; Haggerty et al., 2000; Willmann et al., 2008; Berkowitz et al., 2006; Le Borgne et al., 2008a; Cvetkovic et al., 2014). The sound understanding of these phenomena is of crucial importance for applications ranging from geological storage of nuclear waste, carbon dioxide sequestration in geological formations, geothermal energy exploration, to name a few. The heterogeneity impact on large scale transport through heterogeneous media has been quantified using stochastic-perturbative approaches to quantify macrodispersion coefficients (Dagan, 1984; Gelhar and Axness, 1983; Rubin, 2003), as well as non-local constitutive theories (Cushman et al., 1994; Guadagnini and Neuman, 1999), fractional advection-dispersion equations (Meerschaert et al., 1999; Benson et al., 2000; Zhang and Benson, 2008; Benson et al., 2013), multi-rate mass transfer models (Haggerty and Gorelick, 1995; Carrera et al., 1998; Willmann et al., 2008), time domain random walks (Cvetkovic et al., 1996; Delay et al., 2005; Benke and Painter, 2003; Fiori et al., 2007; Cvetkovic et al., 2014; Russian et al., 2016; Noetinger et al., 2016) and continuous time random walks (CTRW) (Berkowitz and Scher, 1997; Hatano and Hatano, 1998; Dentz et al., 2004; Berkowitz et al., 2006; Le Borgne et al., 2008a) to account for anomalous transport features in spatial distributions

and arrival times.

Continuous time random walks (Montroll and Weiss, 1965) provide a natural approach to dispersion in disordered media, for which transport properties such as particle velocities and retention are persistent in space. Thus, particle motion can be characterized through a series of spatial and temporal transitions, which are determined by the statistical medium properties. Independence of subsequent space and time increments requires that the spatial disorder is sampled efficiently by the microscopic particle motion, this means, particles should in average explore ever new aspects of the disorder (Bouchaud and Georges, 1990). This is the case for purely diffusive motion in $d > 2$ dimensional disordered media (Bouchaud and Georges, 1990; Dentz et al., 2016c), and for biased motion in random media in any dimension. Thus, the CTRW approach has been used for the modeling of anomalous dispersion for a broad range of particle motions in random media (Metzler and Klafter, 2000a; Klafter and Sokolov, 2005; Berkowitz et al., 2006; Barkai et al., 2012; Kutner and Masoliver, 2017; Shlesinger, 2017) starting with the pioneering work of *Scher and Lax* (Scher and Lax, 1973) that quantifies the anomalous motion of charge carriers in amorphous solids.

Here we focus on solute and particle transport in heterogeneous porous media. *Saffman* (Saffman, 1959) used an approach very similar to CTRW for the quantification of pore-scale particle motion and the derivation for dispersion coefficients. Anomalous transport due to pore scale flow heterogeneity has been modeled with CTRW approaches based on detailed numerical simulations (Bijeljic and Blunt, 2006; Le Borgne et al., 2011; Bijeljic et al., 2011a, 2013; de Anna et al., 2013; Kang et al., 2014; Gjetvaij et al., 2015) and laboratory scale experiments (Holzner et al., 2015). These approaches are based on the property that particle velocities are persistent over a characteristic pore scale such that the transition time is given kinematically by the transition length and the flow velocity (Dentz et al., 2016a). The work of *Berkowitz and Scher* (Berkowitz and Scher, 1997) has used the CTRW approach for the characterization of anomalous solute dispersion in fractured media, the work by *Hatano and Hatano* (Hatano and Hatano, 1998) for the interpretation of solute breakthrough curves in laboratory scale flow and transport experiments through columns filled with porous material. The CTRW and the related time-domain random walk (TDRW) approach (Cvetkovic et al., 2014; Noetinger et al., 2016) have been used to model non-Fickian and anomalous transport features in Darcy-scale heterogeneous porous media (Berkowitz et al., 2006; Noetinger et al., 2016) under uniform and non-uniform flow conditions (Kang et al., 2015b; Dentz et al., 2015a). Again, the impact of advective heterogeneity is quantified through kinematic coupling of the transition length and time via the flow velocity. In this context, the CTRW has been coupled with spatial Markov models for the evolution of particle velocities along streamlines (Le Borgne et al., 2008b,a; Kang et al., 2011) in order to capture correlation effects of subsequent velocities and to model the impact of the initial velocity distributions on solute transport (Dentz et al., 2016a; Kang et al., 2017). Also the impact of solute retention due to mass transfer between mobile and immobile zones owing to physical or chemical interactions between the transported particle

and the medium has been modeled by different CTRW approaches (Dentz and Berkowitz, 2003; Margolin et al., 2003; Dentz and Berkowitz, 2005; Dentz and Castro, 2009; Benson and Meerschaert, 2009; Dentz et al., 2012; Gjetvaij et al., 2015; Comolli et al., 2016).

We investigate here two particular aspects of transport through heterogeneous porous media, namely disorder correlation and disorder distribution, which both can give rise to anomalous dispersion in disordered media (Bouchaud and Georges, 1990). Distribution versus correlation induced anomalous transport was studied for biased particle motion in $d = 1$ dimensional media characterized by spatially varying retention properties (Dentz and Bolster, 2010). Here we focus on advective particle motion through Darcy scale porous media characterized by spatially variable hydraulic conductivity. Hydraulic conductivity is the central material property for the understanding of flow and transport in porous media. It varies in natural media over up to 12 orders of magnitude (Bear, 1972). For Darcy scale porous and fractured media, the distribution of hydraulic conductivity is mapped onto the flow velocity via the Darcy equation (Bear, 1972). For low hydraulic conductivities, which are of particular relevance for the occurrence of anomalous transport, the conductivity has been shown to be proportional to the magnitude of the Eulerian flow velocities (Fiori et al., 2007; Tyukhova et al., 2016), which in turn can be related to the particle velocities (Dentz et al., 2016a). We consider porous media characterized by strong spatial correlation of hydraulic conductivity and thus flow velocity, expressed by a distribution of characteristic persistence scale, as well as broad heterogeneity point distributions. The objective is to derive the governing equation for the average particle motion and investigate and quantify the impacts of heterogeneity distribution and heterogeneity correlation on average particle transport in terms of spatial particle distributions, arrival times and dispersion.

This paper is organized as follows. The flow and transport model as well as the porous media model are discussed in Sect. 4.2. Section 4.3 derives a coupled CTRW model for average particle motion based on coarse-graining of the microscopic equations of motion and ensemble averaging. Section 4.4 uses the derived model to investigate the transport behavior in three different disorder scenarios that are characterized by distribution-induced anomalous transport, correlation-induced anomalous transport and anomalous transport induced by both distribution and correlation. For each scenario, we derive the asymptotic scalings of the moments and the first arrival time distributions and we perform numerical simulations.

4.2 Physical model

In the following, we present the basics of flow and advective transport in Darcy scale heterogeneous porous media and specify the statistical properties of the heterogeneous media model under consideration.

4.2.1 Flow and transport in porous media

Flow through heterogeneous porous media is described by the Darcy equation (Bear, 1972) for the Eulerian flow field $\mathbf{u}(\mathbf{x})$

$$\mathbf{u}(\mathbf{x}) = -K(\mathbf{x})\nabla h(\mathbf{x}), \tag{4.1}$$

where $K(\mathbf{x})$ is hydraulic conductivity and $h(\mathbf{x})$ is hydraulic head. We assume that both medium and fluid are incompressible and thus $\nabla \cdot \mathbf{u}(\mathbf{x}) = 0$, which implies

$$\nabla K(\mathbf{x}) \cdot \nabla h(\mathbf{x}) + K(\mathbf{x})\nabla^2 h(\mathbf{x}) = 0. \tag{4.2}$$

The position vector here is where $\mathbf{x} = (x, y, z)^\top$. The absolute Eulerian velocity is denoted by $v_e(\mathbf{x}) = \|\mathbf{u}(\mathbf{x})\|$, where $\|\cdot\|$ denotes the ℓ^2 norm. The spatially varying hydraulic conductivity depends both on the medium and fluid properties. The fluid properties are constant here, thus it expresses the permeability of the porous medium. The hydraulic conductivity is modeled as a stationary and ergodic spatial random field (Christakos, 1992; Rubin, 2003), whose statistical properties are discussed in the next section. The stochasticity of $K(\mathbf{x})$ is mapped onto the flow velocity through Eq. (4.1). Ergodicity implies that the probability density function (PDF) $p_e(v)$ of velocity point values $v_e(\mathbf{x})$ sampled in space is equal to ensemble sampling, $p_e(v) = \langle \delta[v - v_e(\mathbf{x})] \rangle$, where the angular brackets denote the disorder average and $\delta(\cdot)$ denotes the Dirac delta-distribution. We consider in the following a global hydraulic head gradient aligned with the x-direction, which drives the flow through the porous medium.

We consider here purely advective transport, which is described by the advection equation

$$\frac{d\mathbf{x}(t)}{dt} = \mathbf{u}[\mathbf{x}(t)]. \tag{4.3}$$

For steady flows, streamlines and particle trajectories are identical. The distance $s(t)$ a particle covers along a streamline is given by

$$\frac{ds(t)}{dt} = v_t(t), \qquad v_t(t) = \|\mathbf{u}[\mathbf{x}(t)]\|. \tag{4.4}$$

We perform now a change of variables from $t \to s$ according to (Dentz and Bolster, 2010; Comolli et al., 2016; Dentz et al., 2016a)

$$dt = \frac{ds}{v_s(s)}, \qquad v_s(s) = \|\mathbf{u}[\mathbf{x}(s)]\| \tag{4.5a}$$

such that the advection equation (4.3) transforms to

$$\frac{d\mathbf{x}(s)}{ds} = \frac{\mathbf{v}_s(s)}{v_s(s)}, \qquad \mathbf{v}_s(s) = \mathbf{u}[\mathbf{x}(s)]. \tag{4.5b}$$

The particle velocities $v_s(s)$ are sampled equidistantly along streamlines as opposed to the classical definition of Lagrangian velocities given by v_t which are

sampled isochronally along streamlines (Dentz et al., 2016a). We refer to the point probability density function (PDF) $p_s(v)$ of velocities $v_s(s)$ along streamlines as the s-Lagrangian velocity PDF. It is related to the Eulerian velocity PDF $p_e(v)$ through flux-weighting as (Dentz et al., 2016a)

$$p_s(v) = \frac{v}{\langle v_e \rangle} p_e(v), \tag{4.6}$$

where $\langle v_e \rangle$ is the mean Eulerian velocity, see also Appendix D. As initial condition, we consider here a flux-weighted particle injection, this means the number of particles is proportional to flow velocity at the injection point. Thus, the initial distribution of particle velocities is equal to (4.6).

4.2.2 Disorder model

We consider random media in which the hydraulic conductivity is spatially distributed in a geometry of bins or voxels of constant height h_0 and width d_0 and variable length ℓ. We assume that the properties of the medium are constant within a bin. Thus, we assign to the i-th bin the conductivity K_i, which is distributed according to $p_K(K)$. The bin length ℓ is distributed according to $p_\ell(\ell)$. Figure 4.1 illustrates the heterogeneity organization and the distribution of the velocity magnitude $v_e(\mathbf{x})$. We observe that the spatial organization of $v_e(\mathbf{x})$ is similar to the distribution of $K(\mathbf{x})$. In fact the relation between velocity magnitude and hydraulic conductivity is obtained from (4.1) as

$$v_e(\mathbf{x}) = K(\mathbf{x}) \|\nabla h(\mathbf{x})\|. \tag{4.7}$$

This means that, for an approximately constant hydraulic head gradient, velocity magnitude and hydraulic conductivity are directly proportional. In fact, for stratified media, this means media characterized by infinitely long bins, the head gradient is constant and the streamlines are parallel. Here, the streamlines are not parallel because of fluid mass conservation as expressed by $\nabla \cdot \mathbf{u}(\mathbf{x}) = 0$. Nevertheless, within a bin of constant conductivity, the streamlines are approximately parallel as illustrated in Fig. 4.1. Locally, within a bin, conductivity is constant and thus, the flow equation (4.2) implies that the head gradient is constant. In fact, the flow field inside a bin can be approximated by the solution for an isolated inclusion (Eames and Bush, 1999; Fiori et al., 2007; Cvetkovic et al., 2014). This implies specifically that for small conductivities $v_e(\mathbf{x}) \propto K(\mathbf{x})$, which is what we see in Fig. 4.1. It has been observed in numerical simulations of Darcy scale flow that the PDF of the velocity magnitude and the PDF of hydraulic conductivity are proportional at small values (Edery et al., 2014; Tyukhova et al., 2016; Hakoun et al., 2018). Note that this local relation does not violate fluid mass conservation because it concerns the velocity magnitude $v_e(\mathbf{x})$ and not $\mathbf{u}(\mathbf{x})$. Furthermore, the flux-weighting relation (4.6) between the PDF of the Eulerian velocity magnitude and the PDF of the s-Lagrangian velocity is a direct consequence of the fact that the flow field is divergence-free. Thus, fluid mass conservation is accounted for in this sense.

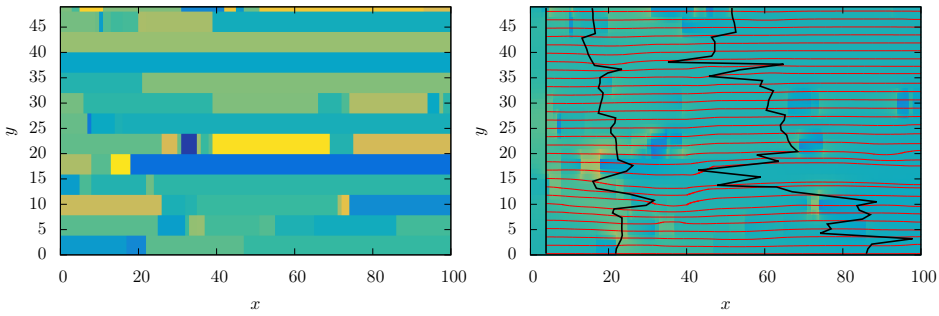

Figure 4.1: (Top panel) Spatial distribution of hydraulic conductivity $K(\mathbf{x})$. (Bottom panel) Spatial distribution of the corresponding Eulerian velocity $v_e(\mathbf{x})$. Dark blue denotes the lowest, yellow the highest values of conductivity and velocity magnitude, respectively. Red lines represent the streamlines and the black line shows the dispersion of particles at different times, which are injected along a line. The velocity field is obtained by solving 4.1 using finite volumes with a prescribed head gradient at the vertical boundaries and no-flow conditions at the bottom and top boundaries.

In summary, geometry and distribution of the K-field are imprinted, at least for small values, in the distribution of Eulerian velocity magnitudes. Based on these observations, we make the following simplifying assumptions. We consider the spatial distribution of the Eulerian velocity $v_e(\mathbf{x})$ rather than $K(\mathbf{x})$ as our starting point. We note that the small values of velocity magnitude and thus conductivity dominate the asymptotic transport behavior. Thus, this simplification allows to study the mechanisms of anomalous transport in correlated porous media, while the early time behavior is in general not captured. Thus, we now assume that the Eulerian velocity field $v_e(\mathbf{x})$ is organized in bins of variable horizontal and constant vertical extensions as described above. In the following, we specify the heterogeneity and correlation scenarios in terms of the PDF $p_e(v)$ of Eulerian velocities and $p_\ell(\ell)$ of horizontal bin sizes.

Heterogeneity

We consider two different distributions of v_e. The weak heterogeneity scenario is defined by the log-normal velocity PDF

$$p_e(v) = \frac{1}{v\sqrt{2\pi\sigma_e^2}} \exp\left\{-\frac{[\ln(v) - \mu_e]^2}{2\sigma_e^2}\right\}. \tag{4.8}$$

where μ_e is the geometric mean of v_e and σ_e the variance of $\ln(v_e)$. Note that the point distribution of hydraulic conductivity is often modeled as a log-normal distribution (Rubin, 2003). We consider moderate heterogeneity characterized by $\sigma_e^2 = 1$. The corresponding PDF of the s-Lagrangian velocities v_s is obtained

from (4.6) by flux-weighting as

$$p_s(v) = \frac{1}{v\sqrt{2\pi\sigma_e^2}} \exp\left\{-\frac{(\ln(v) - \mu_s]^2}{2\sigma_e^2}\right\}, \tag{4.9}$$

where $\mu_s = \mu_e + \sigma_e^2$.

In order to investigate the impact of strong heterogeneity of velocity point values, we consider a velocity distribution that is characterized by power-law behavior at low velocities (Dentz et al., 2016b; Tyukhova et al., 2016)

$$p_e(v) \propto \frac{1}{v_0}\left(\frac{v}{v_0}\right)^{\gamma-1}, \tag{4.10}$$

and a sharp cut-off for $v \gg v_0$. We consider exponents $0 < \gamma < 1$ and also $-1 < \gamma < 0$. In the latter case, it is understood that the Eulerian velocity PDF has another cut-off at low velocity values, otherwise it is not normalizable. The corresponding PDF of s-Lagrangian velocities is again obtain from (4.6) and behaves at small values as

$$p_s(v) \propto \frac{1}{v_0}\left(\frac{v}{v_0}\right)^{\beta-1}, \tag{4.11}$$

where $\beta = \gamma + 1$ is between 0 and 2. Note that no lower cut-off is needed for values of β between 1 and 2. For the numerical simulations and detailed analytical calculations, we employ a Gamma-distribution of velocities, which is characterized by the same properties at small v as (4.11) and an exponential cut-off for $v \gg v_0$.

Correlation

The covariance function of the velocity fluctuations $v_e'(\mathbf{x}) = v_e(\mathbf{x}) - \langle v_e\rangle$ is defined by

$$\mathcal{C}(\mathbf{x} - \mathbf{x}') = \langle v_e'(\mathbf{x}) v_e'(\mathbf{x}')\rangle. \tag{4.12}$$

The velocity variance is $\sigma_v^2 = \mathcal{C}(\mathbf{0})$. The correlation function is defined by $\mathscr{C}(\mathbf{x}) = \mathcal{C}(\mathbf{x})/\sigma_v^2$. For the disorder scenarios under consideration it factorizes into

$$\mathscr{C}(\mathbf{x}) = \mathscr{X}(x)\mathscr{Y}(y)\mathscr{Z}(z), \tag{4.13}$$

where $\mathscr{X}(x)$ denotes the correlation function in x-direction and $\mathscr{Y}(y)$ and $\mathscr{Z}(z)$, the correlation function in y and z-directions, see Appendix E. The constant bin size d_0 in y-direction gives rise to the linear correlation function

$$\mathscr{Y}(y) = \left(1 - \frac{|y|}{d_0}\right) H(d_0 - |y|). \tag{4.14}$$

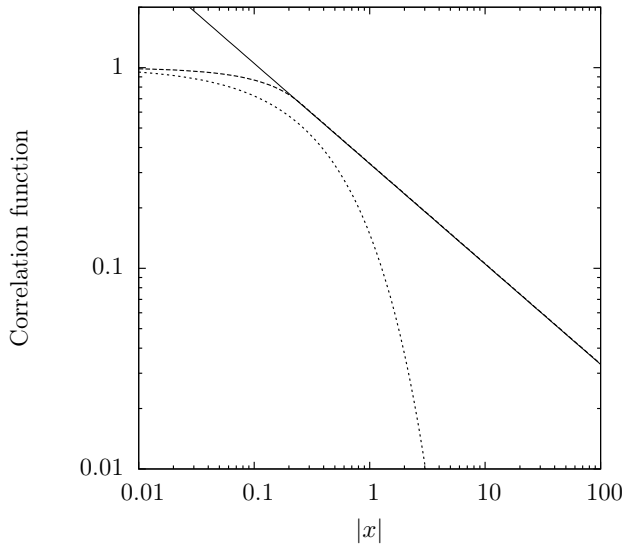

Figure 4.2: 1D correlation function. Comparison between a weakly correlated (dotted line) and a strongly correlated (dashed line) medium. The solid line is $x^{-\frac{1}{2}}$. Results for the case $\ell_0 = \frac{1}{2}$ and $\alpha = \frac{1}{2}$, respectively.

The same holds for the z-direction. For a general distribution $p_\ell(\ell)$ of bin lengths, we obtain for the correlation function in x-direction

$$\mathscr{X}(x) = \int_{|x|}^{\infty} d\ell p_\ell(\ell) \left(1 - \frac{|x|}{\ell}\right), \tag{4.15}$$

as detailed in Appendix E.

The weakly-correlated scenario is characterized by an exponential distribution of bins sizes

$$p_\ell(\ell) = \frac{e^{-\ell/\ell_0}}{\ell_0}, \tag{4.16}$$

with ℓ_0 a characteristic scale. The correlation function in x-direction is then obtained from (E.3) as

$$\mathscr{X}(x) = e^{-|x|/\ell_0} + \frac{|x|}{\ell_0} \mathrm{E}_1(-|x|/\ell_0), \tag{4.17}$$

where $\mathrm{E}_1(\cdot)$ denotes the exponential integral (Abramowitz and Stegun, 1972). Note that the correlation function decays exponentially at large distance, as shown in Fig. 4.2.

The strongly correlated scenario is characterized by a Pareto distribution of bin sizes

$$p_\ell(\ell) = \frac{\alpha}{\ell_0}\left(\frac{\ell}{\ell_0}\right)^{-1-\alpha} \tag{4.18}$$

for $\ell > \ell_0$. We consider $0 < \alpha < 2$. Thus, we obtain from (E.3) the correlation function

$$\mathscr{X}(x) = \begin{cases} \left(\frac{|x|}{\ell_0}\right)^{-\alpha}\left(1 - \frac{\alpha}{\alpha+1}\right) & |x| \geq \ell_0 \\ 1 - \frac{\alpha|x|}{\ell_0(\alpha+1)} & |x| < \ell_0. \end{cases} \tag{4.19}$$

It decays slowly as a power-law for $\ell \geq \ell_0$ as shown in Fig. 4.2.

Ergodicity

We shortly discuss here the ergodicity of the media model under consideration, this means the equivalence of spatial and ensemble sampling of the velocity point values. It is clear that sampling along the y-direction is equivalent to ensemble sampling by construction of the random medium. Also, it is clear that spatial sampling along x is equivalent to ensemble sampling for distributions $p_\ell(\ell)$ for which $\langle\ell\rangle < \infty$. Here we briefly discuss the case of $\langle\ell\rangle = \infty$, which is the case for $0 < \alpha < 1$ in (4.18). The velocity PDF $\hat{p}_e(v)$ is defined through spatial sampling along the x-direction as

$$\hat{p}_e(v) = \lim_{L\to\infty} \frac{1}{L} \int_{-L/2}^{L/2} dx \delta[v - v_e(x)]. \tag{4.20}$$

Because of the geometry of the medium, it can be written as

$$\hat{p}_s(v) = \lim_{L\to\infty} \frac{1}{L} \sum_{i=0}^{n_L} \ell_i \delta(v - v_i), \tag{4.21}$$

where n_L is the number of bins needed to cover the distance L. It is given by

$$n_L = \max(n|x_n \leq L), \qquad x_n = \sum_{i=0}^{n} \ell_i. \tag{4.22}$$

For $0 < \alpha < 1$, the average bin size out of a sample of n scales as $\langle\ell\rangle_n \propto n^{1/\alpha-1}$, while the average number of bins to cover the distance L is $\langle n_L\rangle \propto L^\alpha$ (Bouchaud and Georges, 1990). Thus, we obtain

$$\hat{p}_s(v) = \lim_{n\to\infty} \frac{1}{n} \sum_{i=0}^{n} \delta(v - v_i) = p_e(v), \tag{4.23}$$

this means spatial and ensemble sampling are equivalent.

4.3 Average particle motion

We derive the average particle dynamics based on the streamwise formulation (4.5) of particle motion. To this end, we disregard particle displacements perpendicular to the mean flow direction, which implies that $\mathbf{v}_s(s)/v_s(s)$ is aligned with the x-direction. This is justified because the streamline tortuosity is small due to the medium geometry and flow boundary conditions as discussed in Sect. 4.2.2. Furthermore, it has been demonstrated that transverse dispersion is asymptotically zero for purely advective transport in $d = 2$ dimensional porous media (Attinger et al., 2004). We use the geometric structure of the Eulerian velocity to coarse grain the particle motion in time and space. Flow velocities in different bins here are statistically independent. Thus, we coarse grain the distance s along streamlines using the longitudinal bin size as

$$s_n = \sum_{i=1}^{n} \ell_i. \tag{4.24}$$

Thus, we obtain for the space-time particle motion the recursion relations

$$x_{n+1} = x_n + \ell_n, \qquad t_{n+1} = t_n + \frac{\ell_n}{v_n}, \tag{4.25}$$

where we defined $x_n = x(s_n)$, $t_n = t(s_n)$ and $v_n = v_s(s_n)$. The transition time is defined by $\tau_n = \ell_n/v_n$. We consider a flux weighted extended particle injection at $x = 0$ whose extension is much larger than the bin size perpendicular to the flow direction. Thus, the PDF of particle velocities is given by $p_s(v)$ at all steps. The impact of different initial conditions is discussed in (Dentz et al., 2016a).

The relations (4.25) define a coupled CTRW (Scher and Lax, 1973). Transition time and length are kinematically coupled through velocity, which itself is distributed (Dentz et al., 2008b; Dentz and Bolster, 2010). This type of coupled CTRW is similar to Lévy walks (Shlesinger et al., 1987; Klafter et al., 1990; Meerschaert et al., 2009; Rebenshtok et al., 2014; Zaburdaev et al., 2015; Dentz et al., 2015b) in that transition time and length are kinematically coupled. The Lévy walk, however, prescribes a transition time PDF $\psi(t)$ and determines the transition length for a constant or distributed velocity kinematically (Zaburdaev et al., 2015). Here, the distribution of transition lengths is dictated by the medium geometry, and the distribution of velocities by the medium heterogeneity and flow equation as discussed in Sect. 4.2.2. Thus, here the joint PDF $\psi(x,t)$ of transition lengths and times is given in terms of the PDF of transition length and velocities as

$$\psi(x,t) = \int_0^\infty dv \psi(t|x,v) p_\ell(x) p_s(v), \tag{4.26}$$

where the conditional PDF of transition time given the transition length and velocity is $\psi(t|x,v) = \delta(t - x/v)$. Evaluating the integral gives for $\psi(x,t)$ the

expression

$$\psi(x,t) = \frac{x}{t^2} p_\ell(x) p_s\left(\frac{x}{t}\right). \tag{4.27}$$

The marginal PDF of transition times is denoted by $\psi(t)$. The coarse-grained particle position at a given time t is x_{n_t} where $n_t = \sup(n|t_n \leq t)$. Its PDF is given by $P(x,t) = \langle \delta(x - x_{n_t}) \rangle$ where the angular brackets denote the average over all particles in a single realization and the average over the disorder realizations. The evolution of $P(x,t)$ is determined by the following set of equations (Scher and Lax, 1973; Berkowitz et al., 2006)

$$P(x,t) = \int_0^t dt' R(x,t') \int_{t-t'}^{\infty} dt'' \psi(t'') \tag{4.28a}$$

$$R(x,t) = \delta(x)\delta(t) + \int dx' \int_0^{\infty} dt' R(x',t') \psi(x - x', t - t'), \tag{4.28b}$$

where $R(x,t)$ is the probability per time that a particle arrives at a turning point at (x,t). Thus, the right side of Eq. (4.28a) denotes the probability that a particle just arrives at x at time t' times the probability that the next transition takes longer than $t - t'$. Equation (4.28b) is an expression of particle conservation in (x,t)-space.

Note that x_{n_t} denotes the coarse grained particle position at a turning point of the CTRW. In order to obtain the actual particle position at time t, we interpolate by the velocity in the bin such that (Dentz et al., 2008b; Dentz and Bolster, 2010)

$$x(t) = x_{n_t} + v_{n_t}(t - t_{n_t}), \tag{4.29}$$

where t_{n_t} is the arrival time at the turning point right before t. The average particle density is now given by

$$c(x,t) = \langle \delta[x - x_{n_t} - v_{n_t}(t - t_{n_t})] \rangle. \tag{4.30}$$

This expression can be expanded to

$$c(x,t) = \int_0^t dt' \int dx' R(x',t') \Phi(x - x', t - t'), \tag{4.31}$$

where $\Phi(x,t)dx$ is the joint probability that the particle makes an advective displacement of a length in $[x, x + dx]$ during time t and that t is smaller than the time for a transition

$$\Phi(x,t) = \langle \delta[x - v_s t] \mathbb{I}(0 \leq t < \ell/v_s) \rangle. \tag{4.32}$$

The average can be executed explicitly by noting that $\tau = \ell/v_s$ and using the joint PDF $\psi(x,t)$ of transition length and time. This gives

$$\Phi(x,t) = \int_t^\infty d\tau \frac{\tau}{t} \psi\left(\frac{\tau}{t}x, \tau\right). \tag{4.33}$$

The system (4.28) can be combined into the generalized Master equation for $P(x,t)$ (Berkowitz et al., 2002; Klafter and Silbey, 1980)

$$\frac{\partial P(x,t)}{\partial t} = \int dx' \int_0^t dt' \mathcal{K}(x-x', t-t') \times [P(x',t') - P(x,t')], \tag{4.34}$$

where the memory kernel $\mathcal{K}(x,t)$ is defined through its Laplace transform (Abramowitz and Stegun, 1972)

$$\mathcal{K}^*(x,\lambda) = \frac{\lambda\psi^*(x,\lambda)}{1-\psi^*(\lambda)}. \tag{4.35}$$

Laplace transformed quantities are marked by an asterisk in the following, the Laplace variable is denoted by λ. We solve for $P(x,t)$ and the particle density $c(x,t)$ in Fourier-Laplace space. We employ here the following definition of the Fourier transform,

$$\tilde{c}(k,t) = \int dx\, c(x,t) \exp(ikx), \tag{4.36}$$

$$c(x,t) = \int \frac{dk}{2\pi} \tilde{c}(k,t) \exp(-ikx). \tag{4.37}$$

Fourier transformed quantities are marked by a tilde, the wave number is denoted by k. Thus, we obtain from (4.28) for $\tilde{P}^*(k,\lambda)$

$$\tilde{P}^*(k,\lambda) = \frac{1}{\lambda} \frac{1-\psi^*(\lambda)}{1-\tilde{\psi}^*(k,\lambda)}. \tag{4.38}$$

Combining (4.28) and (4.31) gives for $\tilde{c}^*(k,\lambda)$

$$\tilde{c}^*(k,\lambda) = \frac{\lambda\tilde{\Phi}^*(k,\lambda)\tilde{P}^*(k,\lambda)}{1-\psi^*(\lambda)}. \tag{4.39}$$

Equations (4.38) and (4.39) form the basis for the derivation of the behaviors of the mean and variance of the particle displacements.

4.3.1 Spatial moments

We study the first and the second centered moment of the particle density $c(x,t)$. While the first moment describes the position of the center of mass, the second

centered moment provides a measure of the particle dispersion. Moreover, the temporal scaling of the mean squared displacement is commonly used to discriminate the nature of transport, with non-linear growth being considered a signature of non-Fickian transport. The jth moment of $x(t)$ is given by

$$m_j(t) = \langle x(t)^j \rangle = \int dx\, x^j c(x,t). \tag{4.40}$$

The second centered moment, or in other words, the variance of $x(t)$ is defined by

$$\kappa(t) = m_2(t) - m_1(t)^2. \tag{4.41}$$

In order to calculate the moments, we make use of the following identity in Fourier-Laplace space (Shlesinger et al., 1982)

$$m_j^*(\lambda) = (-i)^j \frac{\partial^j \tilde{c}^*(k,\lambda)}{\partial k^j}\bigg|_{k=0}. \tag{4.42}$$

By substituting (4.39) into (4.42) we can express the moments of the particle density $c(x,t)$ in terms of the spatial moments of $P(x,t)$ and $\Phi(x,t)$. In Appendix F we derive the following Laplace space expressions for the first and second displacement moments

$$m_1^*(\lambda) = \int_0^\lambda d\lambda' \frac{\mu_1^*(\lambda')}{\lambda^2[1-\psi^*(\lambda)]} \tag{4.43}$$

$$m_2^*(\lambda) = \int_0^\lambda d\lambda' \frac{2\lambda'\mu_2^*(\lambda')}{\lambda^3[1-\psi^*(\lambda)]} + \frac{2\mu_1^*(\lambda)m_1^*(\lambda)}{1-\psi^*(\lambda)}, \tag{4.44}$$

where the ith spatial moment of $\psi(x,t)$ is denoted by

$$\mu_i(t) = \int dx\, x^i \psi(x,t). \tag{4.45}$$

4.3.2 First arrival time distribution

The time of first arrival of a particle at a position x is defined by

$$t_a(x) = \sup\,[t | x(t) \leq x], \tag{4.46}$$

where $x(t)$ is given by (4.29). The arrival time PDF is defined by

$$f(t,x) = \langle \delta[t - t_a(x)] \rangle. \tag{4.47}$$

Using (4.25) and (4.29), the arrival time can be written as

$$t_a(x) = \sum_{i=0}^{n_x-1} \tau_i + \frac{x - x_{n_x}}{v_{n_x}}, \tag{4.48}$$

where x_n is given by (4.25) and $n_x = \sup(n|x_n \leq x)$. The first arrival time PDF satisfies a similar equation as $c(x,t)$ and is given by

$$f(t,x) = \int_0^x dx' \int_0^t dt' R(x',t')\Theta(x-x',t-t'), \tag{4.49}$$

where $\Theta(x,t)dt$ is the joint probability that the particle makes an advective displacement of length x in a time in the interval $[t, t+dt]$ and that x is smaller than a transition length

$$\Theta(x,t) = \left\langle \delta\left(t - \frac{x}{v}\right) \mathbb{I}(0 \leq x < \ell) \right\rangle. \tag{4.50}$$

In analogy with $\Phi(x,t)$, we can relate this joint probability to the joint PDF of transition lengths and times without interpolation as follows

$$\Theta(x,t) = x^{-1} \int_x^\infty d\ell\, \ell\psi\left(\ell, \frac{\ell t}{x}\right). \tag{4.51}$$

4.4 Transport behavior

In the following, we study particle dynamics in terms of the variance of particle displacements and first arrival time distributions. In order to probe the impact of heterogeneity and spatial correlation on large scale transport, we study three scenarios. The first one is characterized by strong heterogeneity and weak correlation, the second by strong correlation and weak disorder. Although driven by different causes, transport in both scenarios is non-Fickian and it exhibits similar behaviors. The third scenario is characterized by both strong heterogeneity and strong correlation. For each scenario, the transport behavior is investigated through numerical random walk particle tracking simulations of the coarse-grained equations of motion (4.25), and analytical expressions for the scalings of the moments and the first arrival time distributions.

4.4.1 Distribution-induced anomalous diffusion

We first consider the case of anomalous diffusion induced by a broad distribution of velocity point values characterized by the power-law distribution (4.11), $p_s(v) \propto v^{\beta-1}$ for $0 < \beta < 2$, and short-range correlation characterized by the exponential distribution of transition lengths (4.16). This scenario accounts for frequent changes in the particle velocities along trajectories, characterized by the characteristic correlation scale ℓ_0.

Dispersion behavior

The temporal evolution of the mean squared displacement is shown in Fig. 4.3 for two different values of β that correspond to different degrees of heterogeneity.

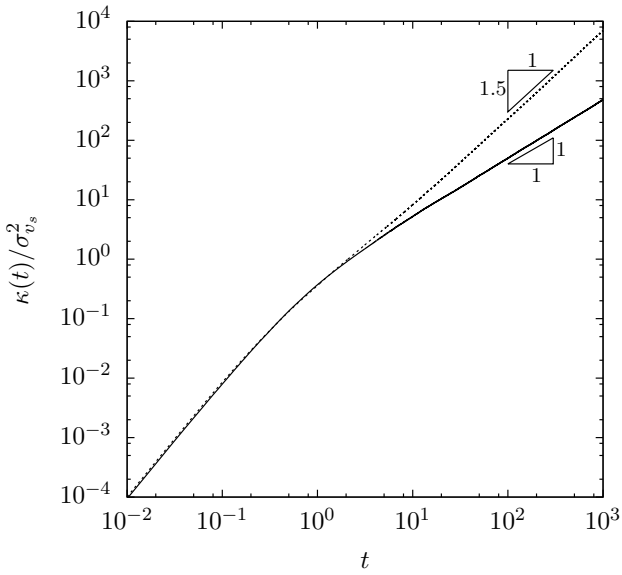

Figure 4.3: Temporal evolution of the variance in case of distribution-induced anomalous transport for $\beta = \frac{1}{2}$ (solid line) and $\beta = \frac{3}{2}$ (dashed line). The second centered moments are normalized by the variance of v_s.

At short times particles move, on average, within a correlation length, where they maintain a constant velocity. As a result, the mean squared displacement exhibits a ballistic growth as $\kappa(t) = \sigma^2_{v_s} t^2$ with $\sigma^2_{v_s}$ the variance of the s-Lagrangian velocity v_s. The sub ballistic asymptotic behavior depends on the velocity and thus transition time distribution. It arises when the particles have traveled several correlation lengths, thus exploring the heterogeneity of the spatially variable velocity. We observe the same behavior as for an uncoupled CTRW in line with (Dentz et al., 2008b). The explicit expressions for the mean and variance of the particle displacement are derived in Appendix F.2.1. For $0 < \beta < 1$, we find that

$$m_1(t) \propto t^\beta \qquad \kappa(t) \propto t^{2\beta}. \tag{4.52}$$

The behavior for $\kappa(t)$ is illustrated in Fig. 4.3 for $\beta = 1/2$. Note that, as discussed in Sect. 4.2.2, this behavior has to be understood in a preasymptotic sense because the Eulerian velocity PDF $p_e(v)$ needs a cut-off at low velocities to be normalizable. For $1 < \beta < 2$, we derive for the displacement mean and variance the scalings

$$m_1(t) \propto t \qquad \kappa(t) \propto t^{3-\beta}. \tag{4.53}$$

The behavior for $\kappa(t)$ is illustrated in Fig. 4.3 for $\beta = 3/2$. These results are consistent with those for uncoupled CTRW (Shlesinger, 1974; Margolin and Berkowitz, 2002; Dentz et al., 2004).

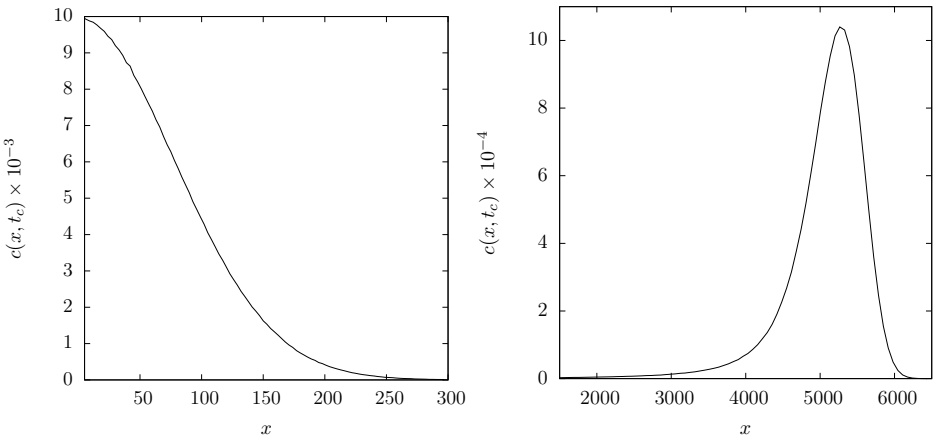

Figure 4.4: Particle density at time $t_c = 10^4$ for $\beta = \frac{1}{2}$ (upper panel) and $\beta = \frac{3}{2}$ (lower panel). The results are obtained by a CTRW simulation with 10^7 particles . Injection occurs point-wise and impulsively at $x = 0$ and $t = 0$.

Figure 4.4 shows the particle distributions for $\beta = 1/2$ and $\beta = 3/2$. Due to the high probability of low velocities, $c(x,t)$ has a forward tail and strong localization at the origin. For $\beta = 3/2$, particles are more mobile, which manifests in a leading front and a trailing tail.

First arrival time distribution

Figure 4.5 shows the first arrival time distributions for the exponents $\beta = 1/2$ and $\beta = 3/2$ at a distance of $x_c = 10^2\ell_0$ from the injection point. Again the case $0 < \beta < 1$ needs to be understood in a preasymptotic sense. The peak of the arrival time distribution for $\beta = 1/2$ is strongly delayed compared to the one for $\beta = 3/2$ due to the higher probability of low velocities. The tailing behavior is characterized by $f(t, x_c) \propto t^{-1-\beta}$ characteristic for an uncoupled CTRW. This behavior can be readily understood as follows. The average number of steps n_c needed to arrive at the control point is x_c/ℓ_0. The transition time may be approximated by $\tau \approx \ell_0/v_s$, so that the transition time PDF is approximately

$$\psi(t) \approx \frac{\ell_0}{t^2} p_s(\ell_0/t) \propto t^{-1-\beta} \tag{4.54}$$

for $t \gg \ell_0/v_0$. We used (4.11) for $p_s(v)$. The tailing behavior of $f(t, x_c)$ follows for $0 < \beta < 2$ from the generalized central limit theorem.

4.4.2 Correlation-induced anomalous diffusion

Here we study the case of anomalous diffusion induced by correlation. To this end we consider the power-law distribution of transition lengths (4.18), $p_\ell(\ell) \propto$

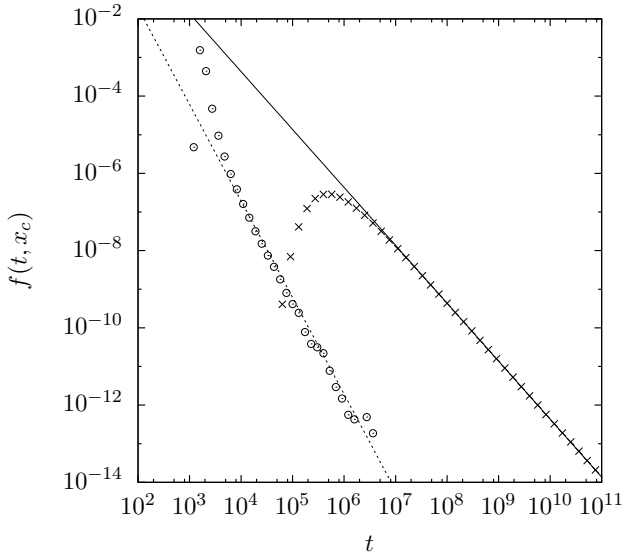

Figure 4.5: First arrival time distribution for the cases $\beta = \frac{1}{2}$ (crosses) and $\beta = \frac{3}{2}$ (circles). The results are obtained by CTRW simulations using 10^7 particles. The solid line is $t^{-\frac{3}{2}}$, while the dashed line is $t^{-\frac{5}{2}}$. Particle injection occurs instantaneously at the origin of space and time and the detection is performed at $x_c = 100\ell_0$.

$\ell^{-1-\alpha}$ for $0 < \alpha < 2$, and the log-normal distribution of velocities (4.9) for $\sigma_2^2 = 1$ and $\mu_e = 0$. Following the path of the previous section, we study the temporal evolution of the spatial moments and the first arrival time distribution to understand the impact of correlation on the average transport.

Dispersion behavior

Figure 4.6 shows the temporal evolution of $\kappa(t)$ for two different values of $0 < \alpha < 1$ and $1 < \alpha < 2$. The degree of correlation is determined by the exponent α. At early times, most of the particles have traveled less than a correlation length and, as a consequence, they have maintained their initial velocity. The early time behavior of $\kappa(t)$ is ballistic. The asymptotic scaling behaviors are derived in Appendix F.2.2.

For very strong correlation, this means $0 < \alpha < 1$, we obtain

$$m_1(t) \propto t \qquad\qquad \kappa(t) \propto t^2. \tag{4.55}$$

While the center of mass position increases linearly with time, the variance shows still ballistic behavior. This is a consequence of the broad distribution of correlation scales. While a given proportion of particles have changed velocities at

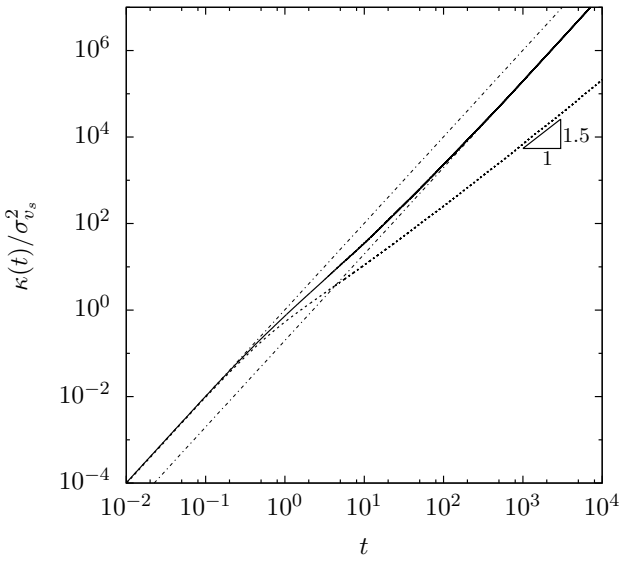

Figure 4.6: Temporal evolution of the variance in case of correlation-induced anomalous transport for $\alpha = \frac{1}{2}$ (solid line) and $\alpha = \frac{3}{2}$ (dashed line). Dashed-dotted lines indicate ballistic growth.

asymptotically long time, a large proportion still persists in the initial velocity. In fact, for $0 < \alpha < 1$, the mean transition length is infinite and the number of velocity changes increase sublinearly with distance x as x^α, see also the discussion in Sect. 4.2.2. The number of velocity changes corresponds to the number of bins needed to cover the distance x. The resulting ballistic behavior of the persistent particles dominates over the dispersion of the particle that have experienced several velocity transitions. The spatial particle distribution for $\alpha = 1/2$ is shown in Fig. 4.7. Initial difference in the particle velocities are amplified with time due to their persistence. The spatial distribution reflects the distribution of velocities $p_s(v)$.

For values of α between 1 and 2, correlation is still strong, but here the mean transition length is finite. We obtain the following scalings for the mean and variance of the particle displacements

$$m_1(t) \propto t \qquad\qquad \kappa(t) \propto t^{3-\alpha}. \tag{4.56}$$

Because of the strong correlation, those particles that experience low velocities as they move through regions of low conductivity are efficiently separated from those that move fast. Although the heterogeneity is weak and the velocities show small variability, those velocities are kept for a long distance. The resulting separation of particles gives rise to the superdiffusive behavior. The corresponding particle density for $\alpha = 3/2$ is shown in Fig. 4.7. Unlike for disorder dominated

superdiffusion, see Fig. 4.4, here the particle distribution does not show a dominant backward tail. Superdiffusion is due to persistent velocity contrast and not to slow velocities.

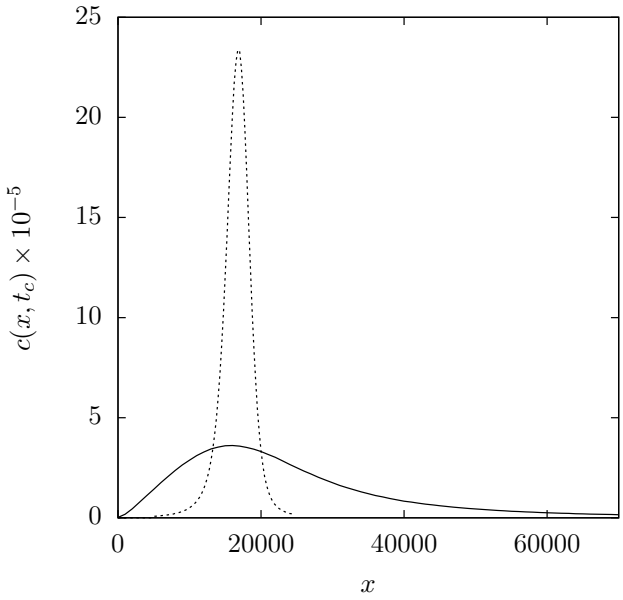

Figure 4.7: Particle density at time $t_c = 10^4$ for $\alpha = \frac{1}{2}$ (solid line) and $\alpha = \frac{3}{2}$ (dotted line). The results are obtained by CTRW simulations with 10^7 particles . Injection occurs point-wise and impulsively at $x = 0$ and $t = 0$.

First arrival time distribution

Figure 4.8 shows the first arrival time distributions for $\alpha = \frac{1}{2}$ and $\alpha = \frac{3}{2}$ at a detection plane located at a distance $x_c = 10^2\ell_0$ from the inlet. We observe an earlier peak for the case $\alpha = \frac{1}{2}$, which is due to those particles that maintain a high velocity for a long distance, since this case corresponds to the higher correlation. At late times, both curves show log-normal tailings. This kind of behavior is particularly interesting if compared to the results of dispersion. In fact, although the variance exhibits a super-linear growth in time, no anomalous behavior is observed in the first arrival time distribution. In order to explain this character, we recall that, due to the high variability of bins lengths, a significant proportion of particles travels until the detection plane x_c without performing any transition, i.e. by keeping the same initial velocity. This proportion of particles is given by

$$P_0(x_c) = \int_{x_c}^{\infty} d\ell\, p_\ell(\ell). \tag{4.57}$$

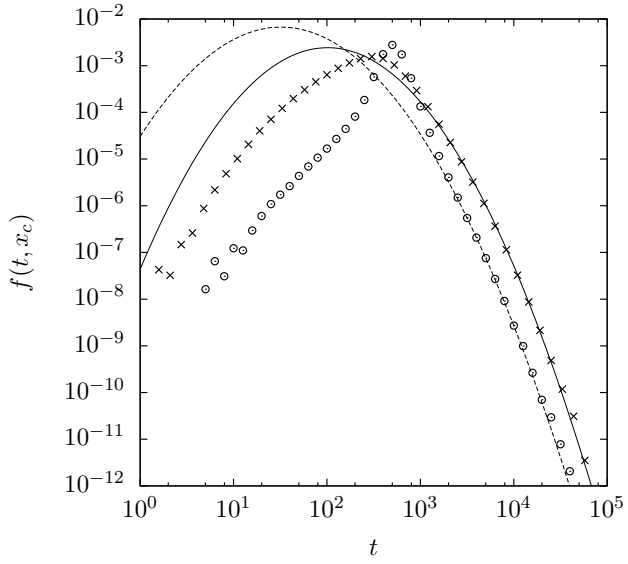

Figure 4.8: First arrival time distribution for the cases $\alpha = \frac{1}{2}$ (crosses) and $\alpha = \frac{3}{2}$ (circles). The solid and the dashed lines are log-normal distributions fitted to the data. The results are obtained by CTRW simulations using 10^8 particles. injection occurs instantaneously at the origin of space and time and the detection is performed at $x_c = 100\ell_0$.

For the distribution of Eq. (4.18) we obtain $P_0(x_c) = \left(\frac{\ell_0}{x_c}\right)^{\alpha}$. For these particles, the arrival time at x_c is given by the kinematic relationship $t_a = x_c/v$. Thus, the first arrival time distribution can be written as

$$f(t, x_c) = P_0(x_c)\frac{x_c}{t^2} p_s\left(\frac{x_c}{t}\right) + ..., \tag{4.58}$$

where the dots indicate the contribution by particles undergoing transitions. Since the distribution of velocities is log-normal, $f(t, x_c)$ is asymptotically also log-normal and this explains the tails that we observe in Fig. 4.8. Because for $\alpha = \frac{1}{2}$ the proportion of particles that undergo no transitions is larger than for $\alpha = \frac{3}{2}$, the log-normal tailing arises earlier.

4.4.3 Anomalous diffusion induced by distribution and correlation

In this last scenario, we study anomalous diffusion induced by both distribution and correlation. In order to do so, we consider distributions with power-law tails for both the transition lengths (4.18) for $0 < \alpha < 2$ and the velocities (4.11) for $0 < \beta < 2$. As we discussed, the case $0 < \beta < 1$ has to be intended in a

preasymptotic sense. As we did in the previous sections, we analyze the behavior of the spatial moments and the first arrival time distribution to quantify the impact of strong correlation and strong distribution on transport.

Dispersion behavior

Figure 4.9 shows the temporal evolution of the mean squared displacement for two different choices of the shape parameters $\alpha \in (1,2)$ and $\beta \in (1,2)$. In particular, the cases $\alpha < \beta$ and $\alpha > \beta$ are considered in order to understand the relative impact of each process. At early times, particles have traveled less than a correlation length. Thus, the variance exhibits a ballistic behavior, as particles have maintained their initial velocity. In the large time limit, we observe a convergence to the asymptotic regimes that are derived analytically in Appendix F.2. We obtain for this case

$$m_1(t) \propto t \qquad\qquad \kappa(t) \propto t^{3-\omega}, \tag{4.59}$$

where $\omega = \min(\alpha, \beta)$. This means that the asymptotic behavior is determined by the stronger between disorder and correlation. Thus, for $\alpha < \beta$ the superdiffusive behavior is due to the persistent contrast of velocities, rather than on the retention of particles with slow velocities. Conversely, for $\alpha > \beta$, the impact of slow velocities becomes more important than the persistence of different velocities.

Figure 4.10 shows the spatial particles density for the two considered cases. We observe that the peak position depends on the value of β, since smaller values correspond to an higher probability of low velocities and, thus, to a retarded peak. We also observe that the curves are tailed towards the same direction, but the processes that lead to this phenomenon are opposite. For $\alpha < \beta$, correlation is stronger than distribution and the tail develops itself towards low values, in analogy to what we observed in Sect. 4.4.2. For $\alpha > \beta$, distribution dominates over correlation. We observe that the same tailing as for the case of distribution-induced anomalous diffusion (see Fig. 4.4, lower panel).

Until here we have considered the case in which both α and β are between 1 and 2. Nevertheless, a variety of different cases may arise. In the following, we discuss different scenarios related to different choices of the exponents α and β, which means different degrees of correlation and disorder. The scalings of the moments are derived in Appendix F.2.

Case $\boldsymbol{\alpha \in (0,1)}$, $\boldsymbol{\beta \in (1,2)}$ In this case, we derive that the first moment and the variance scale as

$$m_1(t) \propto t \qquad\qquad \kappa(t) \propto t^2. \tag{4.60}$$

This scenario is tantamount to the case of correlation-induced anomalous diffusion with $0 < \alpha < 1$ described in Sect. 4.4.2. Since no mean transition length exists, transport behavior is fully determined by the longest bins and, consequently, dispersion is ballistic. The net effect is that the process (4.25) is decoupled.

Case $\boldsymbol{\alpha} \in (\mathbf{1},\mathbf{2})$, $\boldsymbol{\beta} \in (\mathbf{0},\mathbf{1})$ We derive the following scalings for the first moment and the variance of particles displacement

$$m_1(t) \propto t^{\beta} \qquad\qquad \kappa(t) \propto t^{2\beta}. \tag{4.61}$$

Notice that these scalings are the same that we observed in Sect. 4.4.1 for $0 < \beta < 1$. The reason for this fact is that this case is dual to the previous. In fact, while on one hand a mean transition length can be defined, on the other no mean transition time exists. Thus, transport is dominated by disorder and it exhibits a non-Fickian behavior $\kappa(t) \propto t^{2\beta}$ that is due to the retention of particles moving with low velocities. The strength of retention depends on the exponent β. In particular, we observe subdiffusive behavior for $0 < \beta < 1$ and superdiffusive growth for $1 < \beta < 2$.

Case $\boldsymbol{\alpha},\boldsymbol{\beta} \in (\mathbf{0},\mathbf{1})$ In this case, the scalings of the moments depend on the relationship between α and β. In particular, we get that the mean and the variance of particles displacement scale as

$$m_1(t) \propto t^{\nu} \qquad\qquad \kappa(t) \propto t^{\epsilon}, \tag{4.62}$$

where $\nu = \min(1, \beta - \alpha + 1)$ and $\epsilon = \min(2, 2 + \beta - \alpha)$. This means that for $\alpha < \beta$ we get ballistic growth of the variance, which is analogous to the behavior that we observed in Sect. 4.4.2 for $0 < \alpha < 1$. It is interesting to observe that for $\alpha > \beta$, a superballistic behavior arises. This very anomalous behavior is due to the combined action of very low velocities and the high persistence of the velocity contrast. However, we recall that the case $0 < \beta < 1$ has to be understood in a preasymptotic sense.

First arrival time distribution

Figure 4.11 shows the first arrival time distribution for two combinations of α and β between 1 and 2. We distinguish the cases $\alpha < \beta$ and $\alpha > \beta$, as they correspond to the cases in which the dominating processes are correlation and disorder, respectively. The positions of the peaks appear shifted. This is due to the fact that for smaller values of β the probability of encountering very low velocities is higher. In both the considered cases, the first arrival time distribution behaves asymptotically as

$$f(t, x_c) \propto t^{-1-\beta}. \tag{4.63}$$

As we discussed in Sect. 4.4.2, the tails of the distribution are determined by those particles that undergo no velocity transitions. The relative proportion of these particles is given by Eq. (4.57). Thus, the first arrival time distribution is given by Eq. (4.58). Since the distribution of velocities scales as $v^{\beta-1}$, the distribution of arrival times scales as $t^{-1-\beta}$ due to the kinematic relationship $t_a = x_c/v$.

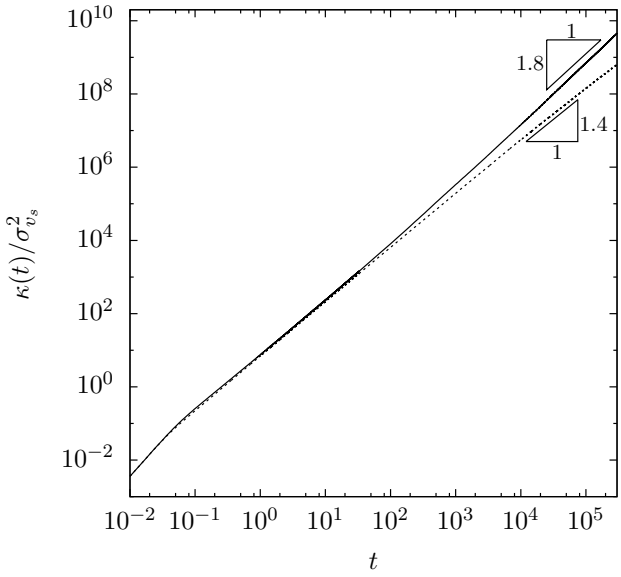

Figure 4.9: Temporal evolution of the variance in case of anomalous transport induced by both distribution and correlation for $\alpha = 1.4, \beta = 1.2$ (solid line) and for $\alpha = 1.6, \beta = 1.9$ (dashed line).

4.5 Summary and conclusions

We investigate the origins of anomalous transport in the flow through correlated porous media focusing on the impact of disorder and correlation. We consider quenched d-dimensional random hydraulic conductivity fields, in which the correlation structure is determined by a distribution of length scales of regions of equal hydraulic conductivity K. The spatial variability in K is mapped onto a distribution of Eulerian velocities through the Darcy equation. Particle transport is characterized by the series of Lagrangian velocities sampled equidistantly along the streamlines, whose statistics are related to the Eulerian velocity PDF by flux-weighting. We show that average particle follows a coupled CTRW characterized by the PDF of characteristic length scales and the PDF of Eulerian velocities. Within this framework, we derive analytical expressions for the asymptotic scaling of the moments of particle displacements and the first arrival time distributions or breakthrough curves. In order to quantify the impact of disorder and correlation on average transport, we consider three different scenarios, in which the anomalous behaviors are induced by disorder, correlation or both.

In the first scenario, we use an exponential distribution of bin sizes and a Gamma distribution of velocities $p_v(v) \propto v^{\beta-1}$. Since the transition length PDF is sharply peaked, in the long time limit this case is equivalent to an uncoupled CTRW. Thus, we get that the mean squared displacement evolves in time as

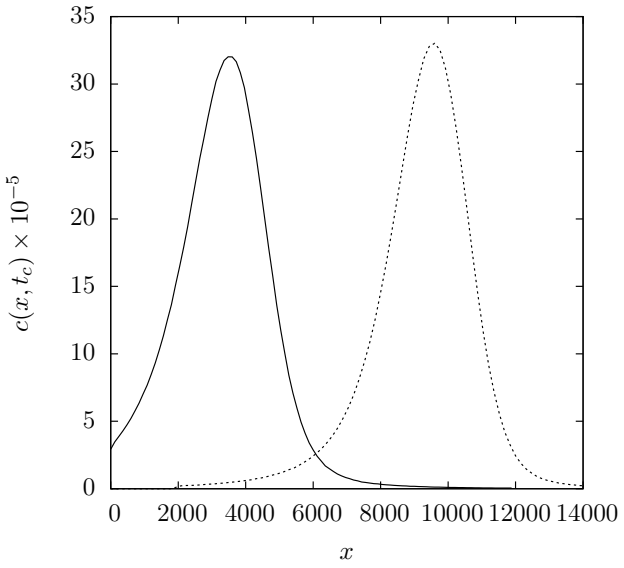

Figure 4.10: Particle density at time $t_c = 10^4$ for $\alpha = 1.4, \beta = 1.2$ (solid line) and for $\alpha = 1.6, \beta = 1.9$ (dotted line). The results are obtained by CTRW simulations with 10^7 particles . Injection occurs point- wise and impulsively at $x = 0$ and $t = 0$.

$\kappa(t) \propto t^{2\beta}$ for $\beta \in (0,1)$ and $\kappa(t) \propto t^{3-\beta}$ for $\beta \in (1,2)$. The first arrival time distribution exhibits retarded peaks for smaller values of β that are due to the higher probability of having lower velocities and a tail proportional to $t^{-1-\beta}$ which is a consequence of the generalized central limit theorem.

The second scenario accounts for the effects of strong correlation, which is modeled through a power-law distribution of bin sizes $p_\ell(\ell) \propto \ell^{-1-\alpha}$. For $\alpha \in (0,1)$, because the mean correlation length is infinite, transport is dominated by those particles that undergo no transition. This reflects itself into the observation of a ballistic growth of the mean squared displacement and breakthrough curves that behave asymptotically as the distribution of the inverse of velocities. For $\alpha \in (1,2)$, because a mean correlation length can be defined, particles undergo velocity transitions in a finite time. Nevertheless, some very long bins with low velocities may be encountered, which gives rise to an efficient retention of particles that manifests itself in the stretching of the spatial density distribution and in the superlinear growth of the mean squared displacement $\kappa(t) \propto t^{3-\alpha}$. In this case, the anomalous character is not determined by low velocities, but by the persistence of velocity contrasts for long distances.

In the last scenario that we consider, power-law distributed bin sizes and velocities are used. We distinguish a variety of asymptotic behaviors that depend on the exponents α and β and thus on the relative importance of correlation ver-

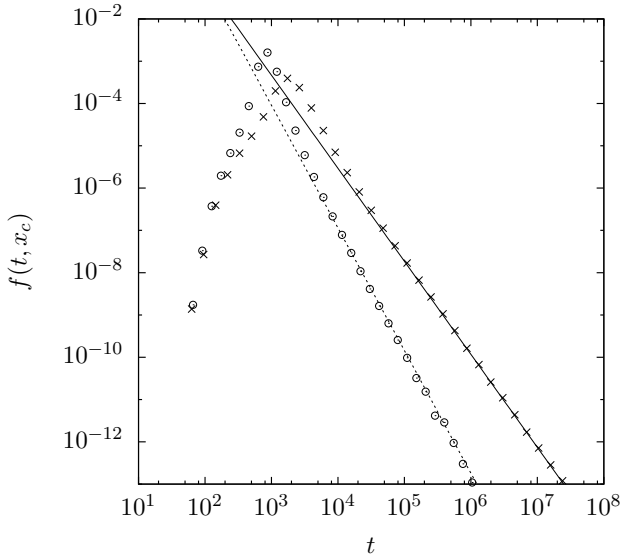

Figure 4.11: First arrival time distribution for $\alpha = 1.4, \beta = 1.2$ (crosses) and for $\alpha = 1.6, \beta = 1.9$ (circles). The results are obtained by CTRW simulations with 10^8 particles. The solid line is $t^{-2.2}$, while the dashed line is $t^{-2.9}$. The injection occurs instantaneously at $x = 0$ and $t = 0$ and the detection is performed at $x_c = 100\ell_0$.

sus disorder distribution. The transport behavior is in general governed by the process characterized by the heavier tails. For example, for α and β between 1 and 2, the velocity distribution dominates for $\beta < \alpha$, while for $\alpha < \beta$ correlation determines the asymptotic behavior of the displacement variance. The long time behavior of the particle arrival times is again dominated by particles with persistent velocities, this means, particles that have not made a velocity transition until the sampling position. The arrival time distribution thus scales as the PDF of inverse velocities.

In conclusion, we have characterized anomalous behaviors of transport in correlated porous media. These non-Fickian behaviors are induced by heterogeneity and correlation. We show that in some cases it is not possible to decouple the effects of these processes, even though in general the stronger process determines the nature of transport. This work sheds some new light on th mechanisms underlying anomalous transport in porous media, which may aid in identifying their footprints from experimental data. Future work will address the generalization of the derived approach in presence of diffusion and local scale dispersion.

5

Lagrangian velocities evolution

Abstract

We develop a continuous time random walk (CTRW) approach for the evolution of Lagrangian velocities in steady heterogeneous flows based on a stochastic relaxation process for the streamwise particle velocities. This approach describes persistence of velocities over a characteristic spatial scale, unlike classical random walk methods, which model persistence over a characteristic time scale. We first establish the relation between Eulerian and Lagrangian velocities for both equidistant and isochrone sampling along streamlines, under transient and stationary conditions. Based on this, we develop a space continuous CTRW approach for the spatial and temporal dynamics of Lagrangian velocities. While classical CTRW formulations have non-stationary Lagrangian velocity statistics, the proposed approach quantifies the evolution of the Lagrangian velocity statistics under both stationary and non-stationary conditions. We provide explicit expressions for the Lagrangian velocity statistics, and determine the behaviors of the mean particle velocity, velocity covariance and particle dispersion. We find strong Lagrangian correlation and anomalous dispersion for velocity distributions which are tailed toward low velocities as well as marked differences depending on the initial conditions. The developed CTRW approach predicts the Lagrangian particle dynamics from an arbitrary initial condition based on the Eulerian velocity distribution and a characteristic correlation scale.

This chapter is based on the paper "M. Dentz et al. - Continuous time random walks for the evolution of Lagrangian velocities, Physical Review Fluids (2016)".

5.1 Introduction

The dynamics of Lagrangian velocities in fluid flows are fundamental for the understanding of tracer dispersion, anomalous transport behaviors, but also pair-dispersion and intermittent particle velocity and acceleration time series, as well as fluid stretching and mixing. A classical stochastic view-point on particle velocities in heterogeneous flows is their representation in terms of Langevin models for the particle velocities (Pope, 2000), which accounts for temporal persistence, and the random nature of velocity through a Gaussian white noise. Such approaches assume that velocity time series form a Markov process when measured isochronically along a particle trajectory (Meyer and Saggini, 2016).

The observation of intermittency in Lagrangian velocity and acceleration time series in steady heterogeneous flow (de Anna et al., 2013; Kang et al., 2014; Holzner et al., 2015) questions the assumptions that underly the representation of Lagrangian velocity in terms of a classical random walk. Observed intermittency patterns manifest themselves in long episodes of low velocities and relatively short episodes of high velocity. This indicates an organizational principle of Lagrangian velocities that is different from the one implied in a temporal Markov processes, which assumes that velocities are persistent for a constant time interval of characteristic duration τ_c. Observed intermittency for flow through disordered media (de Anna et al., 2013; Kang et al., 2014; Holzner et al., 2015) suggests that particle velocities are persistent along a characteristic length scale ℓ_c along streamlines. Approaches that model particle velocities as Markov processes in space, assign to particle transitions a random transition time, which is given kinematically by the transition distance divided by the transition velocity. Thus, such approaches are termed continuous time random walks (CTRW) (Montroll and Weiss, 1965; Scher and Lax, 1973; Metzler and Klafter, 2000b; Berkowitz et al., 2006). They are different from classical random walk approaches, which employ a constant discrete transition time.

Particle motion and particle dispersion have been shown to follow CTRW dynamics for flow through pore and Darcy-scale heterogeneous porous and fractured media (Berkowitz and Scher, 1997; Benke and Painter, 2003; Painter and Cvetkovic, 2005; Le Borgne et al., 2008b,a; Kang et al., 2011; Bijeljic et al., 2011b; Edery et al., 2014), as well as turbulent flows (Shlesinger et al., 1987; Thalabard et al., 2014). While CTRW provides an efficient framework for the quantification of anomalous dispersion and intermittency in heterogeneous flows, some key questions remain open regarding the relation of particle velocities and Eulerian flow statistics, and the stationarity of Lagrangian velocity statistics.

In classical CTRW formulations, particle velocities are non-stationary. This means, for example that the velocity mean and covariance evolve in time. This property is termed aging (Sokolov, 2012). However, for steady divergence-free random flows, such as flow through porous media, it has been found that particle velocities may in fact be stationary Dagan (1989); specifically the Lagrangian mean velocity may be independent of time. Furthermore, it has been found for flow through random fracture networks that the Lagrangian velocity statistics

depends on the initial particle distribution (Hyman et al., 2015; Frampton and Cvetkovic, 2009; Kang et al., 2016). Hence, in general, Lagrangian velocities are expected to evolve from an arbitrary initial distribution toward an asymptotic stationary distribution. Quantifying this property, which is not described in current CTRW frameworks, is critical for upscaling transport dynamics through disordered media, whose transport properties are sensitive to the initial velocity distribution.

In this paper, we study the evolution of Lagrangian velocities and their relation with the Eulerian velocity statistics. To this end, we discuss in the following section the concepts of Lagrangian velocities determined isochronically and equidistantly along streamlines and their relation to the Eulerian velocity. Furthermore, we recall some fundamental properties that elucidate the conditions under which they are transient or stationary. In Section 5.3, we derive the Lagrangian velocity statistics in the classical CTRW and develops a Markov-chain CTRW approach that models the evolution of equidistant streamwise Lagrangian velocities as a stochastic relaxation process. In this framework, we derive explicit expressions for the one and two-point statistics of Lagrangian velocities, and analyze the evolution of the mean particle velocity, its covariance as well as particle dispersion in Section 5.4.

5.2 Lagrangian Velocities

We consider purely advective transport in a heterogeneous stationary velocity field $\mathbf{u}(\mathbf{x})$. Particle trajectories are described by the advection equation

$$\frac{d\mathbf{x}(t,\mathbf{a})}{dt} = \mathbf{v}(t,\mathbf{a}), \tag{5.1}$$

where $\mathbf{v}(t,\mathbf{a}) = \mathbf{u}[\mathbf{x}(t,\mathbf{a})]$ denotes the Lagrangian particle velocity. The initial particle position is given by $\mathbf{x}(t=0,\mathbf{a}) = \mathbf{a}$. The particle motion can be described in terms of the distance $s(t,\mathbf{a})$ traveled along a trajectory, which is given by

$$\frac{ds(t,\mathbf{a})}{dt} = v_t(t,\mathbf{a}), \qquad \frac{dt(s,\mathbf{a})}{ds} = \frac{1}{v_s(s,\mathbf{a})}, \tag{5.2}$$

We define the t-Lagrangian particle velocity as $v_t(t,\mathbf{a}) = |\mathbf{v}(t,\mathbf{a})|$, the s-Lagrangian velocity $v_s(s,\mathbf{a}) = v_t[t(s,\mathbf{a}),\mathbf{a}]$. The initial velocities are denoted by $v_0(\mathbf{a}) \equiv v_t(t=0,\mathbf{a}) \equiv v_s(s=0,\mathbf{a})$.

The absolute Eulerian velocities are defined by $v_e(\mathbf{x}) = |\mathbf{u}(\mathbf{x})|$. Their probability density function (PDF) is defined through spatial sampling as

$$p_e(v) = \lim_{V\to\infty} \frac{1}{V} \int_{\Omega} d\mathbf{x}\delta[v - v_e(\mathbf{x})], \tag{5.3}$$

where Ω is the sampling domain and V its volume. We assume here Eulerian ergodicity, this means that spatial sampling is equal to ensemble sampling such

that

$$p_e(v) = \overline{\delta[v - v_e(\mathbf{x})]}, \tag{5.4}$$

where the overbar denotes the ensemble average. In the following, we discuss the t-Lagrangian velocities $v_t(t, \mathbf{a})$, which are sampled isochronally along particle trajectories, and the s-Lagrangian velocities $v_s(s, \mathbf{a})$, which are sampled equidistantly along particle trajectories. Here and in the following, we assume both Eulerian and Lagrangian ergodicity. As outlined below, Lagrangian ergodicity implies that the statistics of particle velocities $v_t(t, \mathbf{a})$ sampled in time along a trajectory coincide with the statistics obtained by sampling between particles.

5.2.1 Steady Lagrangian Velocity Distributions

The PDF of the t-Lagrangian velocity is defined by isochrone sampling along a particle trajectory as

$$p_t(v, \mathbf{a}) = \lim_{T\to\infty} \frac{1}{T} \int_0^T dt \delta \left[v - v_t(t, \mathbf{a})\right], \tag{5.5}$$

Under Lagrangian ergodic conditions, it is independent of the initial particle position $\mathbf{a}$ and equal to the average over an ensemble of particles

$$p_t(v) = \lim_{V_0\to\infty} \frac{1}{V_0} \int_{\Omega_0} d\mathbf{a} \delta[v - v_t(t, \mathbf{a})]. \tag{5.6}$$

The latter is equal to the Eulerian velocity PDF due to volume conservation,

$$p_t(v) = \lim_{V_0\to\infty} \frac{1}{V_0} \int_{\Omega(t)} d\mathbf{x} \delta[v - v_e(\mathbf{x})] \equiv p_e(v), \tag{5.7}$$

which can be seen by performing a change of variables according to the flow map $\mathbf{a} \to \mathbf{x}(t, \mathbf{a})$ and recalling that the Jacobian is one due to the incompressibility of the flow field.

The PDF of the s-Lagrangian velocity is defined in analogy to (5.5) by equidistant sampling along a particle trajectory as

$$p_s(v, \mathbf{a}) = \lim_{L\to\infty} \frac{1}{L} \int_0^L ds \delta[v - v_s(s, \mathbf{a})]. \tag{5.8}$$

Changing variables under the integral according to the kinematic relationship (5.2) between t and s gives immediately

$$p_s(v, \mathbf{a}) = \frac{v p_t(v, \mathbf{a})}{\langle v_t \rangle}, \tag{5.9}$$

this means the s-Lagrangian velocity PDF is equal to the flux weighted t-Lagrangian velocity PDF. This can also be understood intuitively by the fact that isochrone sampling as expressed through $p_t(v)$ gives a higher weight to low velocities because particles spend more time at low velocities, while equidistant sampling assigns the same weight to high and low velocities.

Under conditions of Lagrangian ergodicity, we thus have that (i) $p_s(v, \mathbf{a}) = p_s(v)$ is independent of the particle trajectory and equal to the average over an ensemble of particles and (ii) that the s-Lagrangian velocity PDF is related to the Eulerian velocity PDF through flux weighting as

$$p_s(v) = \frac{v p_e(v)}{\langle v_e \rangle}. \tag{5.10}$$

The latter establishes the relation between s-Lagrangian and Eulerian velocity distributions.

5.2.2 Transient Lagrangian Velocity Distributions

In the previous sections, we considered the PDFs of t- and s-Lagrangian velocities under stationary conditions. Here we focus on their transient counterparts, which are defined through a spatial average over an arbitrary normalized initial particle distribution $\rho(\mathbf{a})$.

The PDF of t-Lagrangian velocities then is defined by

$$\hat{p}_t(v, t) = \int d\mathbf{a} \rho(\mathbf{a}) \delta[v - v_t(t, \mathbf{a})]. \tag{5.11}$$

Its temporal average is given by

$$\lim_{T \to \infty} \frac{1}{T} \int_0^T dt \hat{p}_t(v, t) = p_t(v) = p_e(v), \tag{5.12}$$

and thus its steady state PDF is of course given by the Eulerian velocity PDF. In analogy, we consider the PDF of s-Lagrangian velocities for an arbitrary initial PDF

$$\hat{p}_s(v, s) = \int d\mathbf{a} \rho(\mathbf{a}) \delta[v - v_s(s, \mathbf{a})]. \tag{5.13}$$

Its average along a streamline is given by

$$\lim_{L \to \infty} \frac{1}{L} \int_0^L ds \hat{p}_t(v, s) = p_s(v) = \frac{v p_e(v)}{\langle v_e \rangle}. \tag{5.14}$$

The initial conditions for both the t-Lagrangian and s-Lagrangian velocity PDFs are identical,

$$\hat{p}_s(v, s = 0) = \hat{p}_t(v, t = 0) = p_0(v) \tag{5.15}$$

Thus, as their respective steady state PDFs are different, either one or both of them need to evolve, depending on whether the initial PDF is the flux weighted Eulerian PDF, (the steady state PDF for $\hat{p}_s(v,s)$), the Eulerian PDF (the steady state PDF for $\hat{p}_t(v,t)$), or neither of the two.

The initial velocity PDF depends on the particle injection mode. For example, a uniform in space particle injection corresponds here to an initial velocity PDF equal to the Eulerian PDF,

$$p_0(v) = \lim_{V_0\to\infty} \frac{1}{V_0} \int\limits_{\Omega_0} d\mathbf{a}\delta[v - v_0(\mathbf{a})] \equiv p_e(v) \tag{5.16}$$

because of Eulerian ergodicity. As this initial distribution is equal to the asymptotic steady t-Lagrangian velocity distribution, the $\hat{p}_t(v,t) = p_e(v)$ is independent of time for this initial injection condition, while the $\hat{p}_s(v)$ evolves with distance from the injection.

A flux weighted particle injection mode corresponds to an initial velocity PDF equal to the flux weighted Eulerian PDF

$$p_0(v) = \lim_{V_0\to\infty} \frac{1}{V_0} \int\limits_{\Omega_0} d\mathbf{a}\frac{v_0(\mathbf{a})}{\langle v_e\rangle}\delta[v - v_0(\mathbf{a})] \equiv \frac{vp_e(v)}{\langle v_e\rangle} \tag{5.17}$$

again because of Eulerian ergodicity. As this initial distribution is equal to the asymptotic steady s-Lagrangian velocity distribution, $\hat{p}_s(v,s) \equiv p_s(v)$ is independent of s for this initial injection condition, while $\hat{p}_t(v,t)$ evolves with time.

A point-like injection at the initial position $\mathbf{x}(t=0|\mathbf{a}) = \mathbf{a}$ corresponds to the delta initial PDF

$$p_0(v) = \delta[v - v_0(\mathbf{a})]. \tag{5.18}$$

For this initial condition, both the t-Lagrangian and s-Lagrangian velocities are unsteady.

The evolution of Lagrangian velocities may be very slow and thus have a strong impact on the transport dynamics. This is the case in particular for heavy-tailed (towards low velocities) velocity distributions that induce long-range temporal correlations of particle velocities. In the following, we study the quantification of the evolution of the Lagrangian velocity PDFs in a Markov model in s, this means distance along streamline.

5.2.3 Lagrangian Velocity Series

We have established that the Lagrangian velocity PDFs evolve with travel time or travel distance along a streamline, unless the initial velocity distribution coincides with the respective steady state PDF. In order to quantify this evolution, we need to model the Lagrangian velocity series. As mentioned in the Introduction, a classical approach is to model the t-Lagrangian velocity as a Markov process,

based on the assumption, or observation that velocities decorrelate on a characteristic time scale τ_c. Thus, the equations of motion (5.2) may be discretized isochronically as

$$t_{n+1} = t_n + \Delta t, \qquad s(t_{n+1}) = s(t_n) + v_t(t_n)\Delta t. \tag{5.19}$$

Velocity time series have been modeled by Langevin equations of the type (Pope, 2000)

$$\tilde{v}_t(t_{n+1}) = \tilde{v}_t(t_n) - \frac{\Delta t}{\tau_c}\tilde{v}_t(t_n) + \sqrt{\frac{2\sigma_v^2\Delta t}{\tau_c}}\xi(t_n), \tag{5.20}$$

which describes an Ornstein-Uhlenbeck process for the velocity fluctuation $\tilde{v}_t(t_n) = v_t(t_n) - \langle v_t\rangle$. The noise $\xi(t_n)$ is Gaussian distributed with zero mean and unit variance. The steady state distribution $p_t(v)$ here is Gaussian with mean $\langle v_t\rangle$ variance σ_v^2. Under stationary conditions, the velocity correlation is exponential with correlation time τ_c. Evidently, this modeling framework is limited to Gaussian statistics and short range correlation in time.

Here, we consider a different modeling approach. As pointed out in the Introduction, there has been ample evidence that particle motion in the flow through random porous and fractured media may be quantified by a CTRW (Berkowitz et al., 2006). In fact, as a consequence of the existence of a spatial correlation length scale for, e.g., the hydraulic conductivity or pore-structure, flow velocities are expected to vary over a characteristic length scale ℓ_c. This implies for t-Lagrangian velocities that a given velocity v_t persists for a duration of ℓ_c/v_t, and specifically that small velocities are more strongly correlated in time than high velocities (Cvetkovic et al., 1991, 1996). This characteristic can explain intermittency in velocity and acceleration time series (de Anna et al., 2013; Kang et al., 2014; Holzner et al., 2015). The existence of a characteristic length scale ℓ_c suggests discretizing the equations of motion (5.2) along a particle trajectory equidistantly such that

$$s_{n+1} = s_n + \Delta s, \qquad t(s_n) = t(s_{n+1}) + \frac{\Delta s}{v_s(s_n)}. \tag{5.21}$$

Here, the s-Lagrangian velocity series $v_s(s_n)$ is modeled as Markov process, which renders the equations of motion (5.21) a CTRW. In the following, we analyze the evolution of the Lagrangian velocity statistics in the setup of a classical CTRW characterized by independent s-Lagrangian velocities, and a CTRW in which the velocity series is modeled as a Markov process through a stochastic relaxation.

5.3 Continuous Time Random Walk

We study now the evolution of space and time Lagrangian velocities in the CTRW framework. The classical approach assigns to each particle transition a transit time τ that is sampled at each step from its PDF $\psi(t)$. The transition times are

related to the characteristic transition length ℓ_c and s-Lagrangian velocities v_s as $\tau = \ell_c/v_s$. Thus, independence of subsequent transit times implies indepence of subsequent s-Lagrangian velocities. In the following, we first consider the evolution of t-Lagrangian velocities in this classical CTRW formulation. The velocity statistics turn out to be non-stationary at finite times. We then study a CTRW formulation that is based on a Markov process for the s-Lagrangian velocities that allows for an evolution of both the s- and t-Lagrangian velocities.

5.3.1 Independent s-Lagrangian Velocities

Particle motion along a particle trajectory is quantified in the framework of a classical CTRW by the recursion relations

$$s_{n+1} = s_n + \ell_c, \qquad t_{n+1} = t_n + \tau_n, \tag{5.22}$$

where the transition length ℓ_c denotes a characteristic length scale on which streamwise velocities $v_n \equiv v_s(s_n)$ decorrelate. In this framework, the particle velocity is constant between turning points. Thus, the transition times $\tau_n = \ell_c/v_n$ are independent identically distributed random variables. Their PDF is given by $\psi(\tau)$. It is related to the distributions of s-Lagrangian and Eulerian velocities by

$$\psi(\tau) = \frac{\ell_c}{\tau^2} p_s(\ell_c/\tau) = \frac{\ell_c \tau_v}{\tau^3} p_e(\ell_c/\tau), \tag{5.23}$$

where we defined the advection time scale $\tau_v = \ell_c/\langle v_e \rangle$. Note that the mean transit time $\langle \tau \rangle = \tau_v$ is equal to the characteristic advection time.

In this framework, the t-Lagragian velocity is given by

$$v_t(t) = v_{n_t}, \tag{5.24}$$

where the renewal process $n_t = \sup(n|t_n \leq t)$ denotes the number of steps needed to arrive at time t. The PDF of the t-Lagrangian velocity is given by

$$\hat{p}_t(v,t) = \langle \delta[v - v_{n_t}] \rangle. \tag{5.25}$$

This expression can be expanded as

$$\hat{p}_t(v,t) = p_s(v) \int_0^{\ell_c/v} dz R(t-z), \tag{5.26}$$

for $t > \ell_c/v$ and $\hat{p}_t(v,t) = p_s(v)$ for $0 < t \leq \ell_c/v$; $R(t)$ is the probability per time that a particle arrives at a turning point at time t, see Appendix G. Thus, the t-Lagrangian velocity PDF is determined by the sampling of the steady s-Lagrangian PDF $p_s(v)$ between turning points. The right side of (5.26) expresses the probability $p_s(v)$ of encountering velocity v at a turning point times the probability that the particle has arrived within an interval of length ℓ_c/v before

the observation time. The arrival time frequency $R(t)$ at a turning point satisfies the Kolmogorov-type equation

$$R(t) = \delta(t) + \int_0^t dt' R(t')\psi(t - t'). \tag{5.27}$$

The probability per time to just arrive at a turning point is equal to the probability to be at a turning point at any time t' times the probability to make a transition of duration $t - t'$ to arrive at the next turning point. The t-Lagrangian velocity PDF (5.26) is non-stationary.

From (5.27), the Laplace space solution for $R^*(\lambda)$ is

$$R^*(\lambda) = \frac{1}{1 - \psi^*(\lambda)}. \tag{5.28}$$

In the limit $\lambda\tau_v \ll 1$, it can be approximated by $R^*(\lambda) = (\lambda\tau_v)^{-1} + \dots$ and therefore for $t \gg \tau_v$, we approximate $R(t) = \tau_v^{-1} + \dots$. Thus, in the limit in the limit of $t \gg \tau_v$, we obtain from (5.26)

$$\hat{p}_t(v, t) = p_e(v) + \dots. \tag{5.29}$$

Thus asymptotically, $\hat{p}_t(v, t)$ converges toward the Eulerian velocity PDF $p_e(v)$.

Similarly, we obtain for the two-point PDF of the t-Lagrangian velocity the equation

$$\hat{p}_t(v, t; v', t') = p_s(v')\times \int_0^{\ell_c/v'} dz' \hat{p}_t(v, t - t' + z')R(t' - z'), \tag{5.30}$$

where $t > t'$, see Appendix G. It is non-stationary as indicated by its explicit dependence on t'. Again, in the limit $t, t' \gg \tau_v$, we approximate

$$\hat{p}_t(v, t; v', t') = p_e(v')\hat{p}_t(v, t - t'). \tag{5.31}$$

It is therefore asymptotically stationary.

In summary, the classical CTRW describes the evolution of the t-Lagrangian velocity PDF from the flux weighted Eulerian to the Eulerian velocity PDF. The t-Lagrangian velocities are non-stationary (Baule and Friedrich, 2005). This property is also called aging in the literature (Sokolov, 2012). In the following, we analyze a CTRW formulation that allows for stationary t-Lagrangian statistics and accounts for the evolutions of the t- and s-Lagrangian velocity PDFs from any initial distribution.

5.3.2 Markov Process of s-Lagrangian Velocities

In order to introduce correlations between subsequent particle velocities, and thus quantify the evolution of Lagrangian velocity statistics, we describe the velocity series $v_s(s)$ measured equidistantly along a streamline as a Markov process (Le Borgne et al., 2008b; Kang et al., 2011, 2015a; Meyer and Saggini, 2016). The evolution of the s-Lagrangian velocity PDF is now given by the Chapman-Kolmogorov equation

$$\hat{p}_s(v, s + \Delta s) = \int_0^\infty dv' r(v, \Delta s|v')\hat{p}_s(v', s), \tag{5.32}$$

where we assume that the transition PDF $r(v, s|v, s') \equiv r(v, s-s'|v')$ is stationary in s. The evolution of particle time in this CTRW is given by

$$t(s + \Delta s) = t(s) + \frac{\Delta s}{v_s(s)}. \tag{5.33a}$$

The joint Markov process $[v_s(s), t(s)]$ of streamwise velocity and time is characterized by the joint transition density

$$\psi(v, t - t', \Delta s|v') = r(v, s|v')\delta(t - t' - \Delta s/v'). \tag{5.33b}$$

Note that a Markov-chain may be characterized by the convergence rate of the transition PDF $r(v, n\Delta s|v')$ toward its steady state, which here is given by

$$\lim_{n\to\infty} r(v, n\Delta s|v') = p_s(v). \tag{5.33c}$$

The (spatial) convergence rate is given by the inverse of the correlation distance ℓ_c along the streamline. We consider now a process that is uniquely characterized by the steady state PDF $p_s(v)$ and the streamwise correlation distance ℓ_c, and model the s-Lagrangian velocity series by the stochastic relaxation process

$$v_s(s + \Delta s) = [1 - \xi(s)]v(s) + \xi(s)\nu(s). \tag{5.33d}$$

The random velocities $\nu(s)$ are identical independently distributed according to the steady s-Lagrangian velocity PDF $p_s(\nu)$. The $\xi(s)$ are identical independently distributed Bernoulli variables that take the value 1 with probability $1 - \exp(-\Delta s/\ell_c)$ and 0 with probability $\exp(-\Delta s/\ell_c)$. Thus, its PDF is

$$\begin{aligned} p_\xi(\xi) = {} & \exp(-\Delta s/\ell_c)\delta(\xi) \\ & + [1 - \exp(-\Delta s/\ell_c)]\delta(\xi - 1). \end{aligned} \tag{5.33e}$$

The initial velocity distribution is given by $p_0(v)$. The transition probability $r(v, s|v')$ for the process (5.33d) is given by

$$\begin{aligned} r(v, s|v') = {} & \exp(-s/\ell_c)\delta(v - v') \\ & + [1 - \exp(-s/\ell_c)]p_s(v). \end{aligned} \tag{5.33f}$$

The velocity process is fully defined by the transition PDF (5.33f) and the PDF $p_0(v)$ of initial velocities.

Space-Lagrangian Velocity Statistics

Using the explicit expression (5.33f) in (5.32) and performing the continuum limit $\Delta s \to 0$, we obtain the following Master equation for the streamwise evolution of $\hat{p}_s(v,s)$,

$$\frac{\partial \hat{p}_s(v,s)}{\partial s} = \ell_c^{-1}\left[p_s(v) - \hat{p}_s(v,s)\right] \tag{5.34}$$

subject to the initial condition $\hat{p}_s(v, s=0) = p_0(v)$. Its solution

$$\hat{p}_s(v,s) = p_s(v) + \exp(-s/\ell_c)\left[p_0(v) - p_s(v)\right] \tag{5.35}$$

converges exponentially from $p_0(v)$ toward the steady state distribution $p_s(v)$, and for $p_0(v) = p_s(v)$ it is stationary. The mean s-Lagrangian velocity is defined by

$$\langle v_s(s)\rangle = \int_0^\infty dv v \hat{p}_s(v,s), \tag{5.36}$$

and from (5.35) we obtain the explicit expression

$$\langle v_s(s)\rangle = \langle v_s\rangle + \exp(-s/\ell_c)\left[\langle v_0\rangle - \langle v_s\rangle\right], \tag{5.37}$$

Under stationary conditions, this means for $v_0 = v_s$, it is constant equal to $\langle v_s\rangle$.

The velocity covariance is then defined by

$$C_s(s,s') = \langle v_s(s)v_s(s')\rangle - \langle v_s(s)\rangle\langle v_s(s')\rangle, \tag{5.38}$$

where the velocity cross-moment is

$$\langle v_s(s)v_s(s')\rangle = \int_0^\infty dv \int_0^\infty dv' v v' r(v, s-s'|v') p_s(v', s'), \tag{5.39}$$

for $s > s'$. Using (5.34) and (5.33f), we obtain for $s > s'$ the explicit expression

$$\begin{aligned} C_s(s,s') &= \left(\langle v_0\rangle - \langle v_s\rangle\right)^2 \exp(-s/\ell_c)\left[1 - \exp(-s'/\ell_c)\right] \\ &+ \sigma_{v_s}^2 \exp[-(s-s')/\ell_c] + \left(\sigma_{v_0}^2 - \sigma_{v_s}^2\right)\exp(-s/\ell_c). \end{aligned} \tag{5.40}$$

For stationary initial velocities $v_0 = v_s$, it reduces to $C_s(s,s') \equiv C_s(s-s') = \sigma_{v_s}^2 \exp[-(s-s')/\ell_c]$.

Time-Lagrangian Velocity Statistics

Here we quantify the temporal evolution of the Lagrangian velocity distribution. The existence of a spatial correlation length entails short range correlation in

space and long range correlation in time for the Lagrangian velocities, which we quantify in the following.

In the continuum limit of $\Delta s \to 0$, the time process (5.33a) becomes

$$\frac{dt(s)}{ds} = \frac{1}{v_s(s)}. \tag{5.41}$$

The conjugate process $s(t)$, which is the distance traveled along the streamline until time t is defined by $s(t) = \sup\{s|t(s) \leq t\}$. The t-Lagragian velocities $v_t(t)$ are now given in terms of $v_s(s)$ as

$$v_t(t) = v_s[s(t)], \tag{5.42}$$

One-Point Statistics Thus, the t-Lagrangian velocity PDF reads now as

$$\hat{p}_t(v,t) = \langle \delta\left(v - v_s[s(t)]\right)\rangle. \tag{5.43}$$

Using the properties of the Dirac-delta, we can expand this equation into

$$\hat{p}_t(v,t) = \int_0^\infty ds v^{-1} R(v,t,s), \tag{5.44}$$

where we defined the probability density $R(v,t,s)$ that a particle has the velocity v and the time t at a distance s along the trajectory as

$$R(v,t,s) = \langle \delta[v - v(s)]\delta[t - t(s)]\rangle. \tag{5.45}$$

Note that $R(v,t,s)$ is the density of the joint Markov process (5.33) for $[v_s(s), t(s)]$. Thus, it satisfies the Chapman-Kolmogorov equation

$$R(v,t,s+\Delta s) = \int_0^\infty dv' \int_0^t dz \psi(v, t-z, \Delta s|v') R(v',z,s). \tag{5.46}$$

Inserting (5.33b) and (5.33f) into the right side of (5.46) and taking the limit $\Delta s \to 0$ gives the Master equation (see Appendix H)

$$\frac{\partial R(v,t,s)}{\partial s} = -\ell_c^{-1} R(v,t,s) - v^{-1}\frac{\partial R(v,t,s)}{\partial t} + \ell_c^{-1} p_s(v) \int_0^\infty dv' R(v',t,s), \tag{5.47}$$

with the initial condition $R(v,t,s=0) = p_0(v)\delta(t)$. Integrating this equation over s according to (5.44) gives for the t-Lagrangian velocity PDF the integro-differential equation

$$\frac{\partial \hat{p}_t(v,t)}{\partial t} = -\frac{v}{\ell_c}\hat{p}_t(v,t) + p_s(v)\int_0^\infty dv' \frac{v'}{\ell_c}\hat{p}_t(v',t) \tag{5.48}$$

with the initial condition $\hat{p}_t(v, t = 0) = p_0(v)$. Its solution in Laplace space is given by (see Appendix H)

$$\hat{p}_t^*(v,\lambda) = p_0(v) g_0^*(v,\lambda) + \frac{v}{\langle v_e \rangle} \frac{p_e(v) g_0^*(v,\lambda) \psi_0^*(\lambda)}{1 - \psi_s^*(\lambda)}, \tag{5.49}$$

where we defined the propagator

$$g_0(v,t) = \exp(-tv/\ell_c), \tag{5.50}$$

whose Laplace transform is given by $g_0^*(v,\lambda) = (\lambda + v/\ell_c)^{-1}$. We define the transit time distributions $\psi_0(t)$, $\psi_s(t)$, and $\psi_e(t)$ through

$$\psi_i(t) = \tau_v^{-1} \int_0^\infty dv g_0(v,t) \frac{v p_i(v)}{\langle v_e \rangle} \tag{5.51}$$

with $i = 0, s, e$. Note that its initial value is $\psi_i(t = 0) = \langle v_i \rangle / \ell_s$. Its Laplace transform is given by

$$\psi_i^*(\lambda) = \tau_v^{-1} \int_0^\infty dv \frac{v p_i(v)}{(\lambda + v/\ell_c)\langle v_e \rangle}. \tag{5.52}$$

It can be seen from (5.49) that $\hat{p}_t(v,t)$ is steady for the initial condition $p_0(v) = p_e(v)$ and is unsteady for any other initial condition by noting that $1 - \psi_s^*(\lambda) = \lambda \tau_v \psi_e^*(\lambda)$.

Expression (5.49) quantifies the evolution of the t-Lagrangian velocity distribution through potentially long-range temporal correlations reflected by the transit time distributions (5.51). Note that the transition time PDFs (5.51) are different from definition (5.23) for the classical s–discrete CTRW framework discussed in Section 5.3.1.

Two-Point Statistics The two-point velocity density is defined here by

$$\hat{p}_t(v,t;v',t') = \langle \delta(v - v[s(t)]) \delta(v' - v[s(t')]) \rangle. \tag{5.53}$$

Along the same lines as above, we derive by using the properties of the Dirac-delta

$$\hat{p}_t(v,t;v',t') = \int_0^\infty ds \int_0^\infty ds' v^{-1} R(v, t - t', s - s'|v') \times v'^{-1} R(v', t', s'). \tag{5.54}$$

The conditional PDF $R(v, t - t', s - s'|v')$ describes the joint distribution of $[v_s(s), t(s)]$ conditional to $v_s(s') = v'$ and $t(s') = t'$. It satisfies the Master

equation (5.47) with the initial condition $R(v,t,s=0|v') = \delta(v-v')\delta(t)$. Note that $R(v,t-t',s-s'|v')$ is stationary in t and s due to the stationarity of the velocity and time processes as expressed by the transition PDF (5.33b). Using definition (5.44), we can now write (5.54) as

$$\hat{p}_t(v,t;v',t') = \hat{p}_t(v,t-t'|v')\hat{p}_t(v',t'). \tag{5.55}$$

where we defined

$$\hat{p}_t(v,t|v') = v^{-1}\int_0^\infty ds R(v,t,s|v'). \tag{5.56}$$

It satisfies the integro-differential equation (5.48) for the initial condition $\hat{p}_t(v,t=0|v') = \delta(v-v')$. Its Laplace space solution is obtained from (5.49) by setting $p_0(v) = \delta(v-v')$ as

$$\begin{aligned}\hat{p}_t^*(v,\lambda|v') &= g_0^*(v,\lambda)\delta(v-v') \\ &+ \frac{vv'}{\langle v_e\rangle^2\tau_c}\frac{p_e(v)g_0^*(v,\lambda)g_0^*(v',\lambda)}{1-\psi_s^*(\lambda)},\end{aligned} \tag{5.57}$$

where we note that here $\psi_0^*(\lambda) = g_0^*(v',\lambda)v'/\ell_c$. Recall that the one-point PDF $\hat{p}_t(v,t)$ is stationary and equal to $p_e(v)$ for the initial condition $p_0(v) = p_e(v)$. Under these conditions, the two-point density (5.55) is then

$$\hat{p}_t(v,t;v',t') \equiv \hat{p}_t(v,t-t',v') = \hat{p}_t(v,t-t'|v')p_e(v'), \tag{5.58}$$

and so is stationary. In the following, we determine the mean and covariance of the t-Lagrangian velocities as well as the corresponding particle dispersion.

5.4 Velocity Mean, Covariance and Dispersion

We study here the t-Lagrangian mean velocity, its covariance and the particle dispersion for the CTRW model presented in Section 5.3.2. We investigate these quantities for the following Γ–distribution of Eulerian velocities

$$p_e(v) = \frac{(v/v_0)^{\alpha-1}\exp(-v/v_0)}{v_0\Gamma(\alpha)} \tag{5.59}$$

for $\alpha > 0$, which provides a parametric model for the low end of Eulerian velocity distributions in porous media both on the pore and on the Darcy scale (Berkowitz et al., 2006; Holzner et al., 2015). As initial conditions we consider either the Eulerian (5.59) or steady s-Lagrangian velocity PDF (5.10), which is obtained from the Eulerian velocity PDF through flux weighting

$$p_s(v) = \frac{(v/v_0)^{\alpha}\exp(-v/v_0)}{v_0\Gamma(\alpha+1)}. \tag{5.60}$$

Note that the Eulerian and flux-weighted mean and mean square velocities are

$$\langle v_e \rangle = \alpha v_0, \qquad \langle v_e^2 \rangle = \alpha(\alpha+1)v_0^2 \tag{5.61}$$

$$\langle v_s \rangle = v_0(\alpha+1), \qquad \langle v_s^2 \rangle = v_0^2(\alpha+1)(\alpha+2). \tag{5.62}$$

Inserting (5.59) into (5.51), we obtain for the transit time distribution $\psi_e(t)$

$$\psi_e(t) = \frac{\alpha}{\tau_0(1+t/\tau_0)^{1+\alpha}}. \tag{5.63}$$

where $\tau_0 = \ell_c/v_0$. For the transit time distribution $\psi_s(t)$, we obtain analogously

$$\psi_s(t) = \frac{\alpha+1}{\tau_0(1+t/\tau_0)^{2+\alpha}}. \tag{5.64}$$

The Laplace transforms of $\psi_e(t)$ and $\psi_s(t)$ can be expanded by using Tauberian theorems. For $0 < \alpha < 1$, $\psi_e^*(\lambda)$ is

$$\psi_e^*(\lambda) = 1 - a_\alpha(\lambda\tau_0)^\alpha, \tag{5.65}$$

where $a_\alpha = \Gamma(1-\alpha)$. For $\alpha = 1$, we have

$$\psi_e^*(\lambda) = 1 + \lambda\tau_0 \ln(\lambda\tau_0). \tag{5.66}$$

In the range $0 < \alpha < 1$, we obtain for $\psi_s^*(\lambda)$ the expansion

$$\psi_s^*(\lambda) = 1 - \lambda\tau_v + b_\alpha(\lambda\tau_0)^{1+\alpha}, \tag{5.67}$$

where $\tau_v = \ell_c/(\alpha v_0)$ and $b_\alpha = \Gamma(2-\alpha)$. For $\alpha = 1$, one obtains

$$\psi_s^*(\lambda) = 1 - \lambda\tau_0 - (\lambda\tau_0)^2 \ln(\lambda\tau_0). \tag{5.68}$$

Note that the case $\alpha = 1$ corresponds to an exponential distribution of Eulerian velocities.

For $\alpha > 1$, both the first and second moments of $\psi_s(t)$ exist, such that $\psi_s^*(\lambda)$ can be expanded as

$$\psi_s^*(\lambda) = 1 - \lambda\tau_v + \frac{\langle \tau_s^2 \rangle}{2}\lambda^2. \tag{5.69}$$

In the following, we will discuss the mean t-Lagrangian velocity, the velocity covariance and particle dispersion. We present general Laplace space expressions based on the explicit expressions for the one- and two point velocity PDFs derived in Section 5.3.2, and study their temporal behavior for the Eulerian velocity PDF given by the Γ–distribution (5.59). To this end, we perform random walk particle tracking simulations based on (5.33) and derive explicit expressions for the early and late time behaviors using the expansions (5.67)–(5.69) of the Laplace transform of the streamwise transition time PDF $\psi_s(t)$.

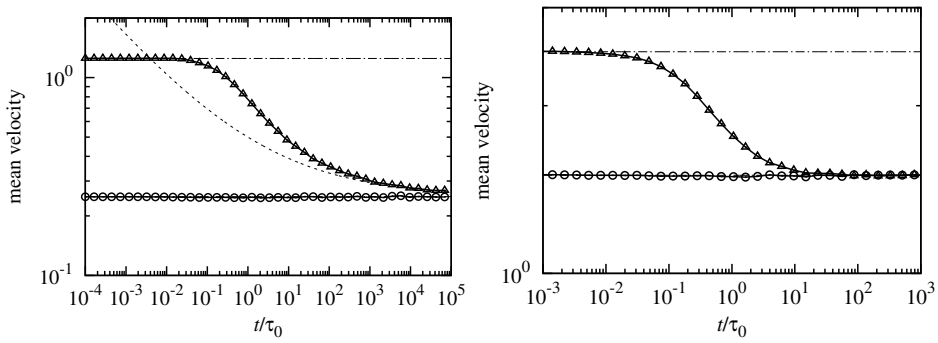

Figure 5.1: Evolution of the mean velocity under stationary and non-stationary conditions for (circles) $p_0(v) = p_e(v)$ and (triangles) $p_0(v) = p_s(v)$ for (top panel) $\alpha = 1/4$ and (bottom panel) $\alpha = 3/2$. The dashed line in the top panel indicates the asymptotic behavior (5.75). The dash-dotted lines indicate the average stationary s-Lagrangian and Eulerian velocities. The numerical random walk simulation to produce these data are based on (5.33) for $\Delta s = 10^{-2}\ell_c$ for 10^5 particles.

5.4.1 Mean Velocity

The mean particle velocity is equal to the one-point t-Lagrangian velocity moment

$$m_1(t) = \int_0^\infty dv v \hat{p}_t(v,t). \tag{5.70}$$

Using (5.49), we obtain for the Laplace transform of $m_1(t)$

$$m_1^*(\lambda) = \ell_c \psi_0^*(\lambda) + \int_0^\infty dv \frac{v^2}{\langle v_e \rangle} \frac{p_e(v) g_0^*(v,\lambda)\psi_0^*(\lambda)}{1-\psi_s^*(\lambda)}. \tag{5.71}$$

For the stationary initial conditions, $p_0(v) = p_e(v)$, the particle velocity is constant, $m_1(t) = \langle v_e \rangle$ and equal to the mean Eulerian velocity.

For the non-stationary initial conditions $p_0(v) = p_s(v)$ we obtain at short times $t \ll \tau_v$

$$m_1(t) = \ell_c \psi_s(t). \tag{5.72}$$

This means it decreases from its initial value $\langle v_s \rangle$ as $\psi_s(t)$. For times $t \gg \tau_v$ and $0 < \alpha < 1$, we use the expansion (5.67) in (5.71), which gives in leading order

$$m_1^*(\lambda) = \frac{\langle v_e \rangle}{\lambda} + \frac{\langle v_e \rangle \tau_0 b_\alpha}{b_1} (\lambda \tau_0)^{\alpha-1}. \tag{5.73}$$

For $\alpha = 1$ we obtain

$$m_1^*(\lambda) = \frac{\langle v_e \rangle}{\lambda} - \ell_c \ln(\lambda \tau_0). \tag{5.74}$$

Thus, the long-time behavior of $m_1(t)$ for $0 < \alpha \leq 1$ is

$$m_1(t) = \langle v_e \rangle + c \langle v_e \rangle (t/\tau_0)^{-\alpha}, \tag{5.75}$$

where we defined $c = b_\alpha / [\Gamma(1-\alpha) b_1]$ for $0 < \alpha < 1$ and $c = 1$ for $\alpha = 1$. This means, the mean velocity converges as a power-law toward its asymptotic value, which is given by the Eulerian mean velocity.

For $\alpha > 1$, we use (5.69) in order to obtain in leading order for $\lambda \ll \tau_0$

$$m_1^*(\lambda) = \frac{\langle v_e \rangle}{\lambda} + \ell_c + \langle v_e \rangle \frac{\langle \tau_s^2 \rangle}{2\tau_v}. \tag{5.76}$$

This means, for $t \gg \tau_v$, $m_1(t)$ can be written as

$$m_1(t) = \langle v_e \rangle + \left(\ell_c + \langle v_e \rangle \frac{\langle \tau_s^2 \rangle}{2\tau_v} \right) \delta(t). \tag{5.77}$$

Note that the Dirac-delta indicates that the convergence toward its asymptotic value is faster than $1/t$. These behaviors are illustrated in Figure 5.1, which shows the evolution of the t-Lagrangian mean velocity with time under Eulerian and flux-weighted Eulerian initial conditions for $\alpha = 1/4$ and $\alpha = 3/2$.

5.4.2 Velocity Covariance

The t-Lagrangian velocity covariance is given by

$$C_t(t, t') = m_2(t, t') - m_1(t) m_1(t'), \tag{5.78}$$

where we defined the two-point velocity moment by

$$m_2(t, t') = \int_0^\infty dv \int_0^\infty dv' v v' \hat{p}_t(v, t; v', t'), \tag{5.79}$$

which can be written in terms of (5.55) for the two-point velocity PDF as

$$m_2(t, t') = \int_0^\infty dv' m_1(t - t' | v') v' \hat{p}_t(v', t'), \tag{5.80}$$

where we defined the conditional velocity moment as

$$m_1(t | v') = \int_0^\infty dv v \hat{p}_t(v, t | v'). \tag{5.81}$$

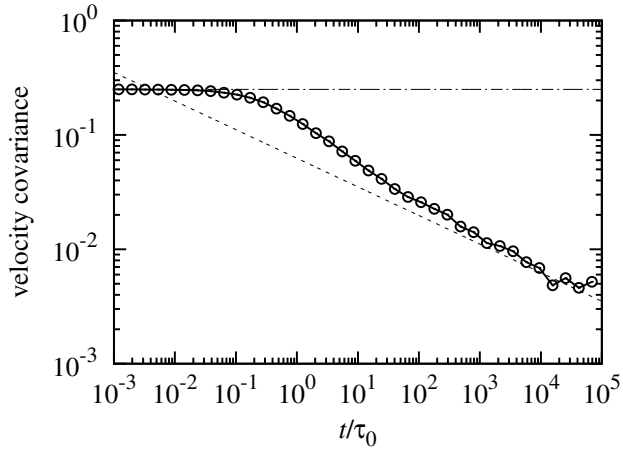

Figure 5.2: Covariance of the t-Lagrangian velocity under the stationary condition $p_0(v) = p_e(v)$ for $\alpha = 1/4$. The dashed line indicates the asymptotic behavior (5.85). The dash-dotted lines indicates the velocity variance. The numerical random walk simulation to produce these data are based on (5.33) for $\Delta s = 10^{-2}\ell_c$ for 10^5 particles.

The Laplace transform of (5.81) is then obtained from (5.57) as

$$m_1^*(\lambda|v') = v' g_0^*(v', \lambda) + \int_0^\infty dv \frac{v^2 v'}{\langle v_e\rangle^2 \tau_v} \frac{p_e(v) g_0^*(v,\lambda) g_0^*(v',\lambda)}{1 - \psi_s^*(\lambda)}. \tag{5.82}$$

We first consider the case $0 < \alpha \leq 1$. For times $t \gg \tau_v$, this means for $\lambda\tau_v \ll 1$, we find by using (5.67) and (5.68) in (5.82) that the leading order of $m_1^*(\lambda|v')$ is given by (5.73) for $0 < \alpha < 1$ and (5.74) for $\alpha = 1$. Specifically, this implies that $m_1(t|v')$ is independent of v'. Using (5.75) in (5.80), we obtain

$$m_2(t,t') = \left[\langle v_e\rangle + \frac{c\langle v_e\rangle \tau_0^\alpha}{(t-t')^\alpha}\right] m_1(t'). \tag{5.83}$$

Under stationary conditions, $p_0(v) = p_e(v)$, $m_1(t) = \langle v_e\rangle$ and $m_2(t,t') \equiv m_2(t - t')$, hence

$$m_2(t-t') = \langle v_e\rangle^2 + \frac{c\langle v_e\rangle^2 \tau_0^\alpha}{(t-t')^\alpha}. \tag{5.84}$$

Thus, the velocity covariance is stationary and behaves for $(t - t') \gg \tau_v$ and $0 < \alpha \leq 1$ as

$$C_t(t-t') = \frac{c\langle v_e\rangle^2 \tau_0^\alpha}{(t-t')^\alpha}. \tag{5.85}$$

This behavior is illustrated in Figure 5.2.

Under the non-stationary condition with $p_0(v) = p_s(v)$, we use the fact that $m_1(t|v') = m_1(t)$ in the limit $t \gg \tau_v$ in order to write

$$m_2(t,t') = m_1(t-t')m_1(t'). \tag{5.86}$$

Accordingly, we obtain for the covariance in the limit $(t-t') \gg \tau_v$

$$C_t(t,t') = m_1(t')\left[m_1(t-t') - m_1(t)\right]. \tag{5.87}$$

We now consider the case $\alpha > 1$. For $\lambda\tau_v \ll 1$, we expand (5.82) by using (5.69) to leading order, which gives

$$m_1(\lambda|v') = \frac{\langle v_e\rangle}{\lambda} + \frac{\langle v_e\rangle\langle\tau_s^2\rangle}{2\tau_v} - \frac{\langle v_2\rangle\ell_c}{v'}. \tag{5.88}$$

Thus, we obtain for $m_2(t,t')$

$$\begin{aligned} m_2(t,t') = &\left[\langle v_e\rangle + \frac{\langle v_e\rangle\langle\tau_s^2\rangle}{2\tau_v}\delta(t-t')\right] m_1(t') \\ &- \ell_c\langle v_e\rangle\delta(t-t'). \end{aligned} \tag{5.89}$$

For $t - t' \gg \tau_v$, we obtain for the covariance under both stationary and non-stationary conditions the expression

$$C_t(t-t') = \ell_c\langle v_e\rangle\left(\frac{\langle\tau_s^2\rangle}{2\tau_v^2} - 1\right)\delta(t-t'). \tag{5.90}$$

Again note that the Dirac-delta indicates here that the covariance decays faster than $1/t$. These expression allow studying the dynamics of dispersion as a function of the Eulerian velocity distribution and the initial injection, as discussed in the following.

5.4.3 Dispersion

The time-dependent dispersion coefficient $\mathcal{D}(t)$ is obtained from the Green-Kubo relation (Kubo et al., 1991) as the integral of the t-Lagragian velocity correlation as

$$\mathcal{D}(t) = \int_0^t dt' C_t(t,t'). \tag{5.91}$$

At time $t \ll \tau_v$, particle velocities are strongly correlated. As a consequence, the dispersion coefficient grows ballistically as

$$\mathcal{D}(t) = \langle(v_0 - \langle v_0\rangle)^2\rangle t. \tag{5.92}$$

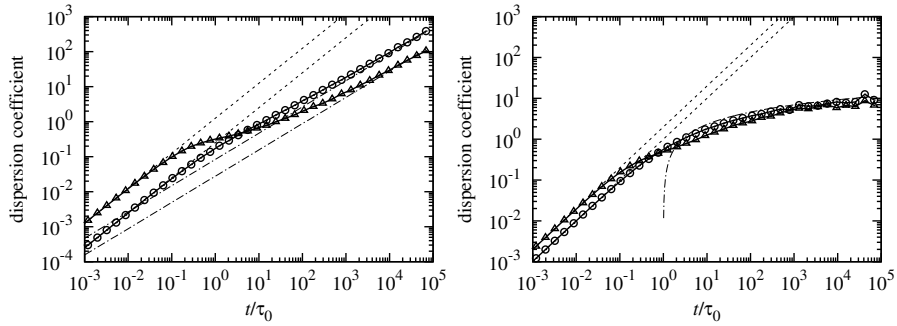

Figure 5.3: Evolution of the dispersion coefficient under stationary and non-stationary conditions for (circles) $p_0(v) = p_e(v)$ and (triangles) $p_0(v) = p_s(v)$ for (top panel) $\alpha = 1/4$, (bottom panel) $\alpha = 1$. The dashed lines indicate the ballistic behaviors (5.92) at short times, dash-dotted lines the asymptotic power-law behaviors (5.93) and (5.94) for $\alpha = 1/4$, and the logarithmic behavior (5.95) for $\alpha = 1$. The numerical random walk simulation to produce these data are based on (5.33) for $\Delta s = 10^{-2}\ell_c$ for 10^5 particles.

Thus, for the initial condition $p_0(v) = p_s(v)$ the ballistic initial growth is faster than for the stationary condition $p_0(v) = p_e(v)$, because the variance of the flux weighted $p_s(v)$ is larger than the variance of the Eulerian $p_e(v)$. For times $t > \tau_v$, particle velocities decorrelate from their initial values. High velocities decorrelate faster than low velocities because the characteristic time at which a particle of velocity v makes a velocity transition is given by ℓ_c/v. Thus, at time τ_v most of the particles with $v > \langle v_e \rangle$ have experienced a velocity transition, which particles with $v < \langle v_e \rangle$ persist in their initial velocities. The dispersion coefficient $\mathcal{D}(t)$ then crosses over to its asymptotic long time behavior, which we study in the following.

We first consider the case $0 < \alpha \leq 1$. Under stationary conditions, this means for $p_0(v) = p_e(v)$, we obtain from (5.85) for $t \gg \tau_v$ and $0 < \alpha < 1$

$$\mathcal{D}(t) = \langle v_e \rangle \ell_c \frac{c\alpha}{1-\alpha} (t/\tau_0)^{1-\alpha}. \tag{5.93}$$

Thus, the dispersion behavior is superdiffusive. In the non-stationary case, for $p_0(v) = p_s(v)$, we obtain from (5.87) and (5.75) at $t \gg \tau_v$

$$\mathcal{D}(t) = \langle v_e \rangle^2 \tau_0^\alpha \frac{c\alpha}{1-\alpha} t^{1-\alpha}. \tag{5.94}$$

It grows asymptotically with the same power-law, but slower then in the stationary case. Thus, while the growth rate of particle dispersion is initially larger for the non-stationary initial condition, asymptotically its growth is slower than for the stationary initial velocity PDF. For $\alpha = 1$, we obtain for both stationary and

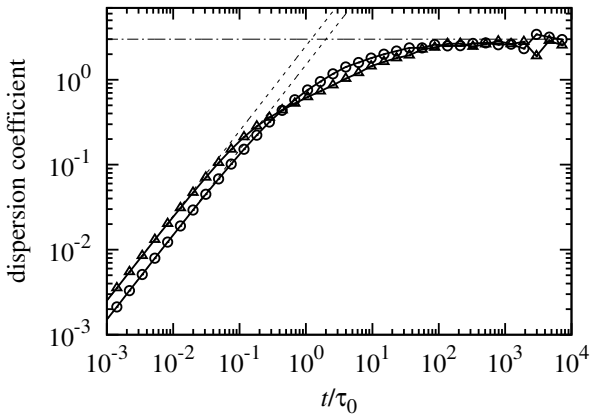

Figure 5.4: Evolution of the dispersion coefficient for (circles) steady and (triangles) unsteady initial velocity PDFs for $\alpha = 3/2$. The dashed lines indicate the ballistic behaviors (5.92) at short times, dash-dotted lines the asymptotic long time value (5.96). The numerical random walk simulation to produce these data are based on (5.33) for $\Delta s = 10^{-2}\ell_c$ with 10^5 particles.

non-stationary intial conditions the behavior

$$\mathcal{D}(t) = \langle v_e \rangle \ell_c \ln(t/\tau_0). \tag{5.95}$$

Figure 5.3 illustrates the evolution of $\mathcal{D}(t)$ for $\alpha = 1/4$ and $\alpha = 1$ under stationary and non-stationary initial conditions. For times $t \ll \tau_v$, we observe the ballistic behavior (5.92), which persists until particle velocities start decorrelating from their initial velocity. Then an intermediate time regime develops which marks the cross-over to the super-diffusive long-time behavior. In this regime, the $\mathcal{D}(t)$ for the non-stationary initial velocity distribution grows slower than for stationary. The dispersion behavior here is due to the fluctuations of fast velocities, which have already decorrelated, and low velocity particles that persist in the ballistic mode. The stationary, Eulerian initial distribution $p_e(v)$ has a stronger weight on low velocities than the flux-weighted $p_s(v)$. Thus, dispersion for the former is higher in the intermediate time regime than for the latter. The end of the intermediate regime is characterized by the decorrelation of most particles from their initial velocities. In the long time regime, we observe for $0 < \alpha < 1$ the power-law behaviors (5.93) and (5.94), for stationary and non-stationary initial conditions. The difference persists and the dispersion coefficient for stationary initial conditions is larger than for non-stationary. The power-law scalings (5.93) and (5.94) are consistent with the ones observed in the CTRW for uncorrelated particle velocities (Margolin and Berkowitz, 2002; Dentz et al., 2004). For $\alpha = 1$, we observe the logarithmic behavior (5.95) for both stationary and non-stationary initial conditions.

For $\alpha > 1$, the dispersion coefficient converges for $t \gg \tau_v$ both for stationary

and non-stationary initial conditions towards the constant asymptotic long-time value

$$\mathcal{D}^e = \langle v_e \rangle \ell_c \left(\frac{\langle \tau_s^2 \rangle}{2\tau_v^2} - 1 \right). \tag{5.96}$$

Figure 5.4 illustrates the evolution of the dispersion coefficient toward the asymptotic value for $\alpha = 3/2$. At short times $t \ll \tau_v$, both dispersion coefficients evolve ballistically, again, the one for the non-stationary initial condition evolves faster. Then for $t > \tau_v$, the dispersion coefficient for stationary initial conditions grows faster than for non-stationary. As pointed out above, the dispersion behavior is due to the fluctuations of decorrelated fast velocities, and persistent low velocity. As the stationary, Eulerian initial velocity distribution gives a higher probability to low velocities than the flux-weighted, the contrast between particle positions increases faster. The asymptotic regime is reached as the particle velocities fully decorrelate from their initial values. For times $t \gg \tau_v$ the dispersion coefficients for both stationary and non-stationary initial conditions converge to the same asymptotic long-time value (5.96).

5.5 Summary and Conclusions

We develop a CTRW approach for the evolution of Lagrangian velocities based on a Markov model for the streamwise equidistant Lagrangian velocities in the form of a stochastic relaxation process. The CTRW framework provides a natural formalism to quantify the impact of the persistence of particle velocities in space on the Lagrangian velocity statistics in time. It has been used to quantify intermittent particle velocities and accelerations for flow through pore- and Darcy-scale porous media, in which flow velocities vary on a characteristic length scale. The velocity statistics in CTRW formulations based on independent successive particle velocities are in general non-stationary. This however, is not necessarily the case for particle motion through heterogeneous flow fields. Specifically, under Eulerian and Lagrangian ergodicity, the stationarity of the Lagrangian velocity series depends on the initial velocity distribution.

In order to shed light on these dynamics, we first discuss the relation between the Eulerian flow properties and the t-Lagrangian and s-Lagrangian velocities. The t-Lagrangian velocities are defined as the particle velocities sampled isochrone along a streamline, the s-Lagrangian velocities accordingly through equidistant sampling. We find that the PDFs of s- and t-Lagrangian velocities are related through flux weighting. This can be understood by the fact that isochrone sampling gives a higher weight to low velocities because particles spend more time at low velocities, while equidistant sampling assigns the same weight to high and low velocities. Under Eulerian and Lagrangian ergodicity and for volume conserving flows, the Eulerian velocity PDF is equal to the t-Lagrangian PDF. This gives a direct relation between the s-Lagrangian velocity PDF, a transport property, to the Eulerian PDF, a flow property, via flux weighting. We then show that t-Lagrangian velocities are stationary if their initial distribution is

equal to the Eulerian, while s-Lagrangian velocities are stationary if their initial distribution is given by the flux-weighted Eulerian distribution.

Based on these considerations, we first analyze the t-Lagrangian velocity statistics in the s-discrete CTRW characterized by independent velocities with a unique velocity distribution. In classical CTRW approaches, the velocity statistics are in general non-stationary. Thus, we introduce a CTRW that is defined through a Markovian velocity process, for which we use a stochastic relaxation relation that is characterized by the steady state s-Lagrangian velocity PDF and the correlation length along the streamlines. Based on this we define a CTRW approach that models the evolution of Lagrangian velocities from arbitrary initial conditions and yields stationary and non-stationary s- and t-Lagrangian velocity series. Specifically, this CTRW is s-continuous, this means the streamwise s-Lagrangian velocity is defined at any point along the streamline and its distribution evolves continuously in s. We determine the evolution equations and solutions for the Lagrangian one-and two-point statistics and discuss the evolution of the mean particle velocity, covariance and dispersion under stationary and non-stationary initial conditions. We apply these results to a Γ-distribution of Eulerian velocities, which serves as a model for heavy-tailed flow-statistics through porous media. The low-end of the velocity spectrum here scales as $p_e(v) \propto v^{\alpha-1}$. For $0 < \alpha \leq 1$ we find strong velocity correlations and anomalous dispersion, this means here a power-law or logarithmic evolution of the dispersion coefficient with time, while for $\alpha > 1$ it evolves toward a constant. These behaviors are fully determined by the Eulerian velocity PDF and the streamwise correlation length. The asymptotic scalings for dispersion are similar as the ones obtained in a corresponding discrete CTRW, as they are attained when particle velocities decorrelate. Their evolution, however, depends on the initial velocity distributions and can be quite different under stationary and non-stationary conditions.

The developed approach sheds light on the modeling and understanding of Lagrangian velocity series in heterogeneous flows, and their evolution under stationary and non-stationary conditions. It provides a bridge between CTRW based modeling approaches of particle transport, and stochastic transport approaches that start from the representation of the Eulerian velocity field, or the medium structure as spatial random fields. The developed CTRW is fully characterized in terms of the Eulerian velocity PDF and the streamwise correlation length, which allows to predict Lagrangian particle dynamics based on the flow or medium properties.

6

Eulerian and Lagrangian analyses in Darcy flows

Abstract

In this study we analyze the relationships between heterogeneous hydraulic conductivity ($K-$) fields, Eulerian and Lagrangian statistics to shed light on processes affecting solute transport in porous media. Here, we show how Lagrangian velocity distributions evolve from an initial distribution to a stationary distribution, in space and/or time. We study this evolution in steady flows in $K-$fields characterized by two distinct point distributions, a log-normal and a gamma distribution, over a broad range of heterogeneity degrees. In addition, we show that the evolution of Lagrangian velocity distributions is heterogeneity dependent. To quantify the evolution of particle velocities sampled equidistantly along trajectories, we propose two stochastic models, namely the Bernoulli and the Ornstein-Uhlenbeck model. These models use 1) an arbitrary initial velocity distribution that stems from the injection mode, 2) the stationary Lagrangian velocity distribution, that stems from the Eulerian velocity distribution and 3) the (space-Lagrangian) velocity correlation length, that stems from the degree of heterogeneity (i.e. variance) of the $\ln_K$ field.

6.1 Introduction

Improving the knowledge on solute transport mechanisms in heterogeneous porous media is crucial for applications such as understanding and predicting groundwater contamination, remediation or carbon dioxide storage in shallow and deep aquifers.

This chapter is the backbone of the paper "V. Hakoun, A. Comolli and M. Dentz, Eulerian and Lagrangian velocities in heterogeneous Darcy flow, *in preparation*".

Predictions of transport in heterogeneous porous media should lie on medium and flow properties. Indeed, the interplay between these properties controls solute transport in heterogeneous porous media. In particular, solute transport is affected by fluctuations of flow velocities, that are in turn driven by the pressure gradient and the hydraulic properties of the medium –spatial structure (i.e. correlation) and hydraulic conductivity K. Solute dispersion is affected by the time particles spend in different velocity zones; long and short times for low and high velocities respectively which induce intermittency of solute velocity. Intermittency has been widely observed at the pore scale (de Anna et al., 2013; Kang et al., 2014; Holzner et al., 2015; Morales et al., 2017; Puyguiraud et al., 2017) but overlooked at the Darcy scale with one example (Le Borgne et al., 2007). Here, we study this feature (see Figure 6.1) and how it combines with stationarity. Dispersion mechanisms depend on initial conditions, that is the injection mode, or in other words the local velocity where the solute particles enter the system. To date, only few works have investigated this dependence (Dentz et al., 2016a; Dagan, 2017).

In the last decades, field (Mackay et al., 1986; LeBlanc et al., 1991; Boggs et al., 1993; Zheng et al., 2011) and theoretical investigations allowed to broaden the community's knowledge on transport processes. Based on experimental results, it has been seen that traditional methods based on the advection dispersion equation (ADE) with constant drift and diffusion coefficients are limited and cannot capture the non-Fickian features of transport. Hence, alternative approaches have been proposed, including multi-rate mass transfer (Haggerty and Gorelick, 1995; Carrera et al., 1998; Sanchez-Vila and Carrera, 2004; Wang et al., 2005; Willmann et al., 2008), fractional-oder ADE methods (Meerschaert et al., 1999; Cushman and Ginn, 2000; Benson et al., 2001; Schumer et al., 2003), non-local constitutive theories (Guadagnini and Neuman, 1999, 2001), time domain random walks (Cvetkovic et al., 1996; Delay et al., 2005; Benke and Painter, 2003; Russian et al., 2016) and continuous time random walk (Berkowitz and Scher, 1997; Dentz et al., 2004; Le Borgne et al., 2008a). Numerical simulations focused on transport in K-fields following a log-normal distribution ($\ln_K$-fields). The first- and second-order theory allows to link the heterogeneity of the medium ($\sigma^2_{\ln_K}$) to Eulerian velocity statistics (Dagan, 1994; Hsu et al., 1996). These theories provide an envelope for the Eulerian statistics (variance of the longitudinal velocity component) (Gotovac et al., 2009). Note that first-order approach provide accurate prediction of solute transport in $\ln_K$-fields with low heterogeneity ($\sigma^2_{\ln_K} < 1$). However, it is inaccurate for higher degrees of heterogeneity. Performing accurate predictions of solute transport in heterogeneous porous medium at all scales of interest remains a challenge.

In this work, we study the statistics of K and Eulerian velocity distributions and the stochastic dynamics of Lagrangian velocities for solute transport in Darcy flow in heterogeneous porous media. Our aim is 1) to shed light on the relationships between flow properties and transport properties (i.e. the Eulerian and Lagrangian velocity distributions), 2) to quantify the impact of different injection conditions on the evolution of Lagrangian velocities and 3) to propose an

effective Markov model that describes and predicts such evolution in terms of transport-independent quantities. The results that we obtain while addressing these issues will pave the way for the derivation of a large-scale transport formulation for the description and the prediction of anomalous behaviors in the Darcian flow fields (Chapter 7).

6.2 Flow and transport in heterogeneous porous media

6.2.1 Flow and Eulerian velocity distribution

Groundwater flow through porous media follows Darcy's law (de Marsily, 1986)

$$\mathbf{q}(\mathbf{x}) = -\mathbf{K}(\mathbf{x})\nabla h, \tag{6.1}$$

where $\mathbf{q}$ is a seepage (Eulerian) velocity vector, $\mathbf{x}$ is a vector of space coordinates, h is hydraulic head and $\mathbf{K}$ is the hydraulic conductivity tensor. Here, we will assume isotropy, so that we can treat the hydraulic conductivity as a scalar K. For incompressible flow, $\nabla \cdot \mathbf{q}(\mathbf{x}) = 0$, Equation (6.1) reduces to

$$\nabla K(\mathbf{x}) \cdot \nabla h(\mathbf{x}) + K(\mathbf{x})\nabla^2 h(\mathbf{x}) = 0\,. \tag{6.2}$$

A classic hydraulic conductivity distribution is the log-normal, $Y = \ln(K)$. Often, it is correlated with the exponential model that is characterized by the correlation function

$$C_Y(\mathbf{r}) = \sigma_Y^2 \exp(-\mathbf{r}/\lambda), \tag{6.3}$$

where σ_Y^2 is the variance of the log-hydraulic conductivity, $\mathbf{r}$ is the lag distance ($\mathbf{r} = \mathbf{x}' - \mathbf{x}''$) and λ is the correlation length of the K-field. Matheron (1967) showed that for a $\ln_K$-field, the theoretical mean Eulerian velocity is $u_0 = K_G h/\phi$, where K_G is the geometric mean of the hydraulic conductivity and ϕ is the porosity. For natural aquifers, heterogeneity is mainly described by the variance of the $\ln_K$-field which spans the 0.1–5 range (Gelhar, 1993). For example Rehfeldt et al. (1992) reports $\sigma^2_{\ln_K} \approx 5$ for the Columbus site (US). Despite its wide use, the log-normal distribution of K has been challenged for heterogeneous sedimentary formations (Painter, 1996; Sanchez-Vila et al., 2006). Other authors have considered different distributions of hydraulic conductivity to account for different disorder properties (Painter, 1996; Kohlbecker et al., 2006). In particular, Haslauer et al. (2012) have used a Weibull distribution to describe the distribution of hydraulic conductivity in the Borden aquifer (Sudicky, 1986), since this PDF fitted best the experimental data in a maximum-likelihood sense among a variety of distributions. The Weibull distribution is characterized by a power-law behavior for small values of K. Thus, we consider a truncated Gamma distribution which, like the Weibull distribution, exhibits power-law tails at low values. Moreover, it relaxes the assumption that the mean and the variance of the distribution are independent, as for the log-normal.

Groundwater flow in heterogeneous porous media can be described by a distribution of Eulerian velocities. Local backward flow may occur due to contrasting

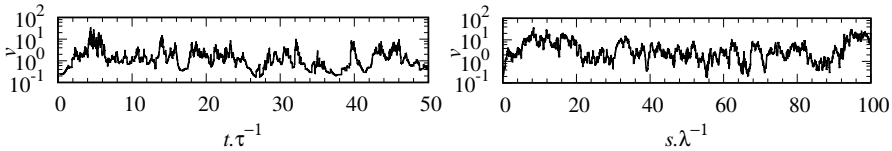

(a) time-Lagrangian velocity series (b) space-Lagrangian velocity series

Figure 6.1: Lagrangian velocity time (left) and space (right) series along a particle trajectory flowing in a Darcy flow field in a $\ln_K$-field with $\sigma^2_{\ln_K} = 7$. The time series exhibits intermittent behavior, as long periods of low velocity and short periods of high velocity arise. No intermittent behavior is observed in the space series.

adjacent K values, for instance in very heterogeneous K-fields. To avoid negative statistics, we use the magnitude of Eulerian velocities $|v_e(\mathbf{x})|$. In the sequel, Eulerian velocity magnitude shall be referred to as Eulerian velocities. The probability density function (PDF) of Eulerian velocities is given by

$$p_e(v) = \lim_{v\to\infty} \frac{1}{V} \int_{\Omega} d\mathbf{x}\delta[v - v_e(\mathbf{x})], \tag{6.4}$$

where Ω is the sampling domain and V is its volume.

6.2.2 Particle motion and Lagrangian velocity distributions

In the absence of diffusion, a particle moves from its initial position $\mathbf{x}(t = 0, \mathbf{a}) = \mathbf{a}$ on a trajectory described by the advection equation

$$\frac{d\mathbf{x}(t, \mathbf{a})}{dt} = \mathbf{v}(t, \mathbf{a}), \tag{6.5}$$

where $\mathbf{v}(t, \mathbf{a}) = \mathbf{u}[\mathbf{x}(t, \mathbf{a})]$ denotes the Lagrangian particle velocity. The spatial motion of a particle along a trajectory is

$$\frac{ds(t, \mathbf{a})}{dt} = v_t(t, \mathbf{a}), \quad \frac{dt(s, \mathbf{a})}{ds} = \frac{1}{v_s(s, \mathbf{a})}. \tag{6.6}$$

Lagrangian velocity distributions

Lagrangian distributions are sampled over particles and along trajectories. Depending on the dimension, two Lagrangian velocity distributions can be defined: t(ime)-Lagrangian and s(pace)-Lagrangian. The t-Lagrangian velocity is given by $v_t(t, \mathbf{a}) = |v_t(t, \mathbf{a})|$ and it follows the PDF

$$p_t(v, \mathbf{a}) = \lim_{T\to\infty} \frac{1}{T} \int_0^T dt\delta[v - v_t(t, \mathbf{a})]. \tag{6.7}$$

Assuming Lagrangian ergodicity, the PDF is independent of the initial position. It equals the average over an ensemble of particles

$$p_t(v) = \lim_{V_0 \to \infty} \frac{1}{V_0} \int_{V_0} d\mathbf{a} \delta[v - v_t(t, \mathbf{a})]. \tag{6.8}$$

The second, s-Lagrangian, distribution is given by $v_s(s, \mathbf{a}) = v_t[t(s, \mathbf{a}), \mathbf{a}]$ it is

$$p_s(v, \mathbf{a}) = \lim_{L \to \infty} \frac{1}{L} \int_0^L ds \delta[v - v_s(s, \mathbf{a})]. \tag{6.9}$$

Assuming ergodicity, the s-Lagrangian velocity distribution is independent of the initial position. It equals the average over an ensemble of particles

$$p_s(v) = \lim_{V_0 \to \infty} \frac{1}{V_0} \int_{V_0} d\mathbf{a} \delta[v - v_s(s, \mathbf{a})]. \tag{6.10}$$

Relationships between Eulerian and Lagrangian velocity distributions

Eulerian and t-Lagrangian velocity PDFs are related due to volume conservation. The average t-Lagrangian velocity PDF (Eq. 6.8) equals the Eulerian velocity PDF (Eq.6.4):

$$p_t(v) = \lim_{V_0 \to \infty} \frac{1}{V_0} \int_{\Omega(t)} d\mathbf{x} \delta[v - v_e(\mathbf{x})] \equiv p_e(v). \tag{6.11}$$

Eulerian and s-Lagrangian velocity PDFs are related due to volume conservation and the kinematic relationship. The s-Lagrangian velocity PDF $p_s(v)$ relates to the Eulerian velocity PDF $p_e(v)$ through flux-weighting (Dentz et al., 2016a)

$$p_s(v) = \frac{v}{\langle v_e \rangle} p_e(v), \tag{6.12}$$

where $\langle v_e \rangle$ is the mean Eulerian velocity.

Both t- and s-Lagrangian velocity PDFs are related through flux-weighting. By performing a change of variables under the integral with the kinematic relationship (6.6) between t and s, the s-Lagrangian velocity PDF equals the flux-weighted t-Lagrangian velocity PDF:

$$p_s(v, \mathbf{a}) = \frac{v}{\langle v_t \rangle} p_t(v, \mathbf{a}), \tag{6.13}$$

where $\langle v_t \rangle$ denotes the ensemble average, i.e. over realizations.

The s-Lagrangian velocity PDF relates to the Eulerian PDF through flux-weighting as seen above. The assumption of Lagrangian ergodicity makes $p_s(v, \mathbf{a}) = p_s$ independent of the particle trajectory and equal to the average over an ensemble of particles. The s-Lagrangian velocity PDF is:

$$p_s(v, \mathbf{a}) = \frac{v}{\langle v_e \rangle} p_e(v, \mathbf{a}). \tag{6.14}$$

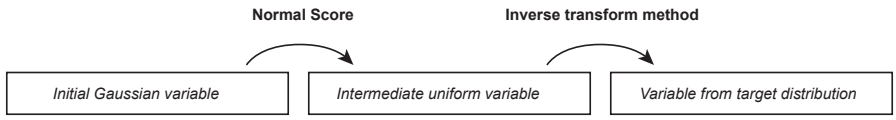

Figure 6.2: Steps to map a random variable from a Gaussian distribution to a target distribution. These steps are used to generate the random K fields with the gamma distribution (6.15)

6.3 Numerical simulations

In this section we describe the direct numerical simulations (DNS) of flow and transport in virtual 2 dimensional heterogeneous porous media. First we describe the methods used to generate random multi-Gaussian fields and the mapping to $\ln_K$- and γ_K-fields. Then, we explain the hydraulic setting for the flow simulations. Last, we explain the particle tracking method used for transport simulations.

6.3.1 Random multi-Gaussian fields

We generate isotropic multi-Gaussian fields of a random variable X on a regular grid in two dimensions. The random variable is mapped to two one-point distributions for the hydraulic conductivity K: a log-normal $\ln_K$ and a Gamma γ_K. The first map is done by taking the exponential of the Gaussian variable, $Y = \exp(X)$. The second map is done using the inverse transform method (or Smirnov transform) that we recall below. As discussed above, alongside with the log-normal distribution, we consider the following truncated γ_K distribution

$$p(K;\alpha,\beta,\eta) = N\frac{\beta^\alpha}{\Gamma(\alpha)}K^{\alpha-1}\exp\left[-\beta K - \frac{\eta}{K}\right] \tag{6.15}$$

where α controls the slope (rate $K^{\alpha-1}$) of the power law decrease of the probability, and η is a cutoff at low K values, N is a normalization constant. The reason for this cutoff is to avoid numerical issues with the flow solver, without cutoff low velocities are on the order of the divergence in a cell.

Figure 6.3 shows one realization of a $\ln_K$- and a γ_K-field. For these $\ln_K$- and γ_K-fields, we consider the exponential correlation model (6.3) and stationary statistics (i.e. constant mean and variance). Regarding log-normal fields, we use the Random Fields package (Schlather et al., 2015) in R (RCoreTeam et al., 2013) to simulate the multi-Gaussian correlated random field. Notice that the same package could be used for the generation of truncated Gamma fields. Nevertheless, here we use a home-made alternative C++ code that is based on the Fourier harmonics decomposition

$$K_G(\mathbf{x}) = \sqrt{\frac{2\sigma^2_{\ln K}}{N}}\sum_{n=1}^{N}\cos\left(\mathbf{k}_n\cdot\mathbf{x}+\phi_n\right), \tag{6.16}$$

where $\mathbf{k}_n$s are the first N Fourier harmonics, $\sigma^2_{\ln K}$ is the desired variance and the ϕ_ns are random phases that are uniformly distributed in $[-\pi, \pi]$. The subscript G stands for Gaussian, meaning that the point values K_G follow a normal distribution. The exponential spatial covariance is obtained by choosing the harmonics components from the Cauchy distribution

$$p_C(k_i) = \frac{\lambda_c}{\pi\left[1 + (k_i\lambda_c)^2\right]}, \tag{6.17}$$

where λ_c is the desired correlation length. In order to map it onto a target distribution ψ_K, we use inverse transform sampling (or Smirnov transform) (Gentle, 2006)(page. 102). This robust method, which is sketched in Figure 6.2 can be used when the inverse cumulative distribution function of a distribution does not have a closed-form analytical solution, as for the case of the γ_K PDF. To do so, we first map the Gaussian field K_G onto a field K_U whose values follow a uniform distribution in $[0, 1]$. This is done by using Gaussian cumulative density function (CDF)

$$K_U(\mathbf{x}) = \frac{1}{2}\,\mathrm{erf}\left[1 + \frac{K_G(\mathbf{x})}{\sqrt{2}}\right], \tag{6.18}$$

where $\mathrm{erf}(\cdot)$ denotes the error function (Abramowitz and Stegun, 1972). By applying the inverse Smirnov transform, we get the desired random multi-Gaussian field

$$K(\mathbf{x}) = \Psi_K^{-1}[K_U(\mathbf{x})], \tag{6.19}$$

where $\Psi_K(K) = \int_0^K \psi_K(K')\,dK'$ is the CDF of the target distribution of conductivity values. The inverse Smirnov transform is performed numerically by making use of the binary search algorithm implemented in the GNU Scientific Library (Galassi et al., 2015).

For both the disorder scenarios that we have presented, the correlation length of the K field, λ, is discretized by ten grid cells. For the $\ln_K$-fields, the mean is $\mu_{\ln_K} = 0$ and the variance $\sigma^2_{\ln_K}$ is in the $0.1 - 7$ range. This set of parameters compares to reference studies (de Dreuzy et al., 2007; Gotovac et al., 2009; Salandin and Fiorotto, 1998). For the γ_K-fields, the mean is constant $\mu_{\gamma_K} = 0.1$ and the variance $(\sigma^2_{\ln_K})$ is in the 0.38–0.74 range. Since the mean is constant, increasing the variance is achieved by lowering the parameter α which is in the 0.1–0.9 range.

6.3.2 Groundwater flow

Direct numerical simulations (DNS) of saturated Darcy flow are performed in steady-state with a reference permeameter-like setting (Bellin et al., 1992; de Dreuzy et al., 2007; Gotovac et al., 2009). We impose the pressure to the upstream (left) and downstream (right) faces of the domain with a unit head drop; no-flow conditions are set along the top and bottom faces. For the $\ln_K$-field, the mean head gradient H is set to unity ($H = 1$), while we take $H = 1/L_d$ for the truncated

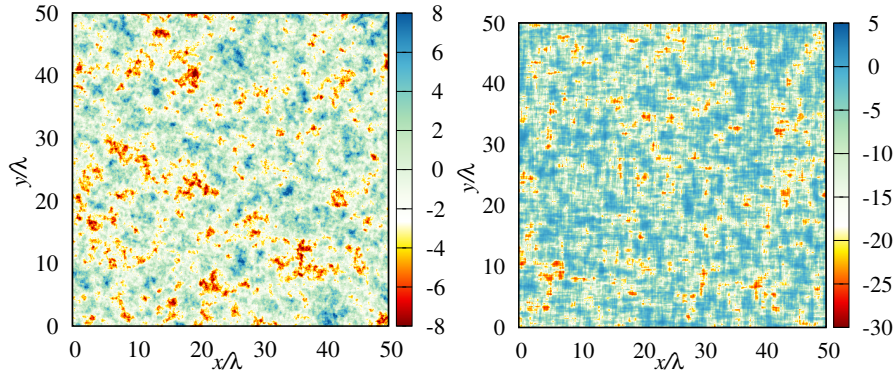

(a) $\ln_K$-field (b) γ_K-field

Figure 6.3: Individual sub-domain realizations of a $\ln_K$-field ($\sigma^2_{\ln_K} = 7$) and a γ_K-field ($\alpha = 0.1$).

Gamma field. We indicate with L_d the length of the domain along the mean flow direction.

We perform Monte Carlo simulations (100 realizations) for each level of heterogeneity which allow us to investigate the impact of heterogeneity on transport behaviors. The level of heterogeneity is set by the value of $\sigma^2_{\ln_K}$ and $\sigma^2_{\gamma_K}$. Porosity is set to unity ($\phi = 1$) because our study focuses on the variability of K. Darcy's equation (Eq. 6.1) is solved numerically with finite differences with FV-Tool (Eftekhari, 2015) for the log-normal fields, while for Gamma fields we use a finite-volume code adapted for the mentioned boundary conditions from(Aarnes et al., 2007). The code is written and used in Octave (Eaton, 2002). Both methods are equivalent.

The flow domain is 600λ long and 150λ wide (9.10^6 cells). We use harmonic inter-cell hydraulic conductivity. The Eulerian velocity field is described by $\mathbf{u}(\mathbf{x}) = \mathbf{q}(\mathbf{x})/n(\mathbf{x})$, it is divergence free. To ensure stationary Eulerian velocity statistics, an inner domain bounded by a biased belt is used for the transport simulations. The belt has a width of 25λ for all simulations in log-normal fields, which is proved sufficient for the most heterogeneous case of $\sigma^2_{\ln_K} = 7$ (see Appendix J). For Gamma fields, we use a belt that has a width of 15λ. To assess the accuracy of our flow simulations, the variance of the Eulerian velocity component along the mean flow direction was compared to reference simulations (de Dreuzy et al., 2007; Gotovac et al., 2009). We found a perfect agreement for our flow simulations.

6.3.3 Particle tracking

We simulate solute transport by random walk particle tracking (RWPT) simulations in each flow realization. Pore scale dispersion is neglected, which is

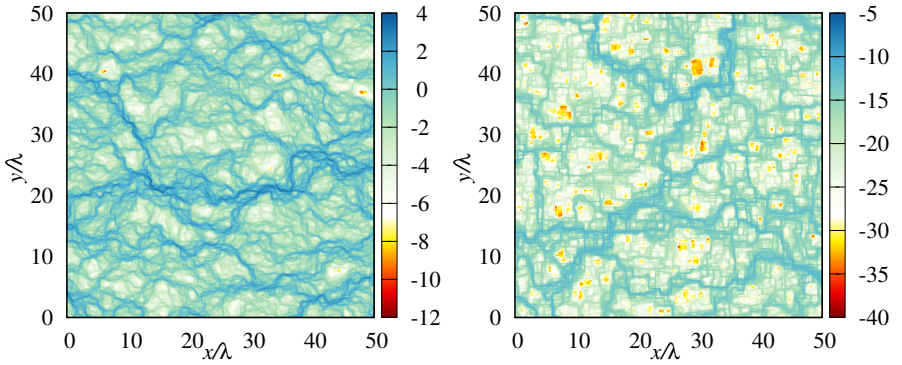

(a) $\ln_K$-field (b) γ_K-field

Figure 6.4: Individual realization of the log of the velocity magnitude for flow in heterogeneous media for a $\ln_K$-field ($\sigma^2_{\ln_K} = 7$) and for a γ_K-field ($\alpha = 0.1$).

equivalent to the limit of infinite Péclet number. Particle tracking is performed either isochronally (t-Lagrangian approach) or equidistantly along streamlines (s-Lagrangian approach). In the t-Lagrangian approach, the equations of motion are obtained through the discretization of Equation (6.5) as

$$\mathbf{x}_{n+1} = \mathbf{x}_n + \mathbf{v}_n \Delta t \qquad t_{n+1} = t_n + \Delta t \tag{6.20}$$

where $\mathbf{v}_n = \mathbf{u}[\mathbf{x}_n]$ is the local Eulerian velocity in $\mathbf{x}_n$ and Δt is a constant temporal increment. In the s-Lagrangian approach, the equation of motion are given by

$$\mathbf{x}_{n+1} = \mathbf{x}_n + \boldsymbol{\Delta}\mathbf{x}_n \qquad t_{n+1} = t_n + \frac{\Delta x}{v_n}, \tag{6.21}$$

where $\boldsymbol{\Delta}\mathbf{x}_n = (v_{x,n}\Delta x/v_n, v_{y,n}\Delta x/v_n)^\top$ and Δx is a constant spatial increment along particle trajectories. Since the flow solver provides the Eulerian velocities at the faces of the cells, the $\mathbf{u}[\mathbf{x}_n]$ are obtained by interpolation. Within a cell, we make use of the bi-linear interpolation scheme (Pollock, 1988)

$$v_x(\mathbf{x}) = A_x(x - x_L) + v_x(x_L) \tag{6.22}$$
$$v_y(\mathbf{x}) = A_y(y - y_B) + v_y(y_B), \tag{6.23}$$

where

$$A_x = [v_x(x_R) - v_x(x_L)]/\Delta \tag{6.24}$$
$$A_y = [v_y(y_T) - v_y(y_B)]/\Delta \tag{6.25}$$

where x_L, x_R, y_B and y_T are the positions of the left, right, bottom and top boundaries of the cell, respectively and Δ is the cell size.

6.4 Lagrangian velocity statistics

In this section we study the statistics of the Lagrangian velocities and their relationship with the Eulerian velocity statistics. In particular, we relate the Eulerian velocity PDF, a flow attribute, to the space- and time-Lagrangian velocity PDF, transport attributes. We quantify how space- and time-Lagrangian velocity PDFs and the respective first moment evolve when the initial velocity PDF differs from the respective steady-state velocity PDF.

6.4.1 Evolution of space Lagrangian velocities

The space-Lagrangian velocity PDF shall evolve if solute particles are injected with a distribution different than its steady-state, the flux-weighted Eulerian velocity PDF (Eq. 6.12). Figure 6.5 shows the evolution of the s-Lagrangian velocity PDF for a uniform injection. For this injection mode, the main features of the evolution are decreasing probabilities for low velocities and increasing probabilities for high velocities. These respective evolutions are in line with a convergence towards the flux-weighted Eulerian velocity velocity PDF for which high velocities have high probabilities. Note that for the larger travel distance, $s = 10\lambda$, there is a singular difference between transport in the $\ln_K$ and γ_K-fields: the Lagrangian velocity PDF does not overlap the steady-state velocity PDF for the $\ln_K$-field, while for the γ_K-field this overlap exists. As we shall discuss below, this difference suggests that for a similar degree of heterogeneity, the correlation of space-Lagrangian velocities is greater in the $\ln_K$-field than in the γ_K-field. Now, we discuss the evolution of the first centered moment of the s-Lagrangian velocity PDF.

Figure 6.5 shows the evolution of the mean s-Lagrangian distribution for a uniform injection. As expected, the mean of the s-Lagrangian velocity evolves between the Eulerian and flux-weighted Eulerian mean at short and long distances respectively. For a uniform injection, the mean of the initial s-Lagrangian velocity PDF is the arithmetic mean of the Eulerian velocity PDF. When the injection distribution differs from the steady-state distribution, the mean of the s-Lagrangian velocity PDF also evolves toward the mean of the steady-state s-Lagrangian velocity PDF. The initial value would be determined by the initial velocity distribution.

6.4.2 Evolution of time-Lagrangian velocities

In Section 6.2.2 we saw that the steady-state t-Lagrangian velocity PDF is the Eulerian velocity PDF (6.11), which is equal to the PDF obtained for a uniform distribution if the ergodic assumption is verified. Thus, if the initial t-Lagrangian velocity PDF differs from uniform injection, the t-Lagrangian velocity PDF shall converge to the steady-state velocity PDF with time.

Figure 6.6 shows the temporal evolution of a t-Lagrangian velocity PDF to its steady-state for flow in both a $\ln_K$- and a γ_K-field. The PDF evolves from an initial flux-weighted velocity PDF to the steady-state velocity PDF. According

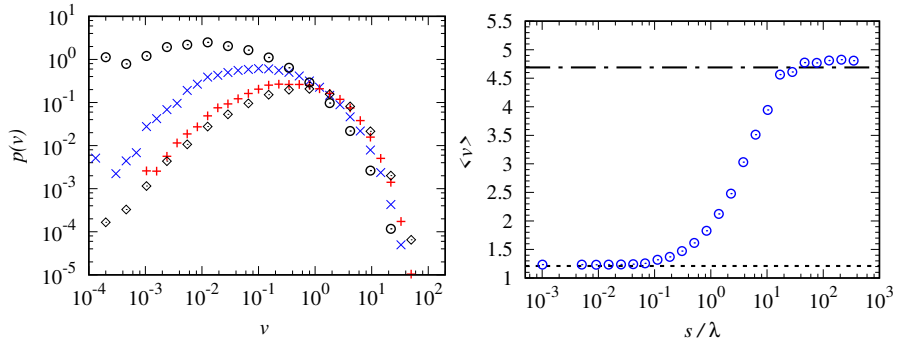

(a) velocity PDF in $\ln_K$-field

(b) mean velocity in $\ln_K$-field

(c) velocity PDF in γ_K-field

(d) mean velocity in γ_K-field

Figure 6.5: Evolution of the space-Lagrangian velocity PDF and mean from an initial velocity PDF (top black circles, Eulerian velocity PDF) to the flux-weighted Eulerian velocity PDF (bottom black diamonds). The intermediate s-Lagrangian velocity PDFs are sampled after a distance along trajectory of $s = 2\lambda$ (blue crosses) and $s = 10\lambda$ (red crosses). The mean increases from the mean of the Eulerian velocity (lower dotted line) to the mean of the flux-weighted Eulerian velocity (upper dashed dotted line).

to the flux-weighted injection for which particles are injected proportional to the local flow, the initial ($t = 0$) velocity distribution has low and high probabilities for the low and high velocities respectively. At an intermediate time $t = 20\tau$, probabilities of low velocities persist close to the initial values. For high velocities, the probabilities overlap those of the steady-state velocity PDF. This difference suggests that probabilities of high velocities reach their steady-state value faster than the probabilities of low velocities. Indeed, particles persist long times at low velocities which gives rise to long correlation times. Long correlation times results in memory effects and intermittency. At $t = 200\tau$, the convergence of probabilities for very low velocities remains incomplete further illustrating the memory of the initial velocity. This memory effect appears simpler when the spatial evolution of the Lagrangian velocity PDF is considered.

These evolutions of Lagrangian velocity PDFs shed light on the fact that accurate interpretations of tracer experiments in heterogeneous porous media require to account for the injection mode. For instance, if a solute is injected in a high velocity zone only (e.g. a preferential flow channel), its mean velocity will decrease at early times, until the steady-state Lagrangian velocity PDF is reached. Thus, assuming a constant mean velocity for the solute particles would be wrong. As far as continuous time random walk models are concerned, they currently lack the ability to reproduce the feature of evolving Lagrangian velocities PDFs. This feature may be reproduced by correlated-CTRW models based on velocity transitions (Le Borgne et al., 2008b), but these transitions are complex to obtain from field experiments. To include the velocity evolution feature in effective stochastic models, one needs to quantify how velocity transitions occur. We shall do so with two parsimonious models.

6.5 Markov models for the evolution of Lagrangian velocities

In this section we quantify the evolution of Lagrangian velocity using two stochastic models of increasing complexity, namely a Bernoulli model (also stochastic relaxation process) and a Ornstein-Uhlenbeck model.

6.5.1 Bernoulli model

To quantify the evolution of Lagrangian velocity distribution we follow the approach based on an exponential relaxation model (Dentz et al., 2016a):

$$\hat{p}_s(v, s) = p_s(v) + \exp(-s/\ell_c)\left[p_0(v) - p_s(v)\right] \tag{6.26}$$

in which the unique parameter ℓ_c is the correlation length of velocities along the trajectory. The decay from an initial Lagrangian velocity distribution $p_0(v)$ to a steady-state distribution $p_s(v)$ is exponential. There is no decay when $p_0(v) = p_s(v)$ and it is infinitesimal when $s \gg \ell_c$. Specifically, the constant decay rate $\exp(-s/\ell_c)$ is velocity-independent. This independence sheds light on

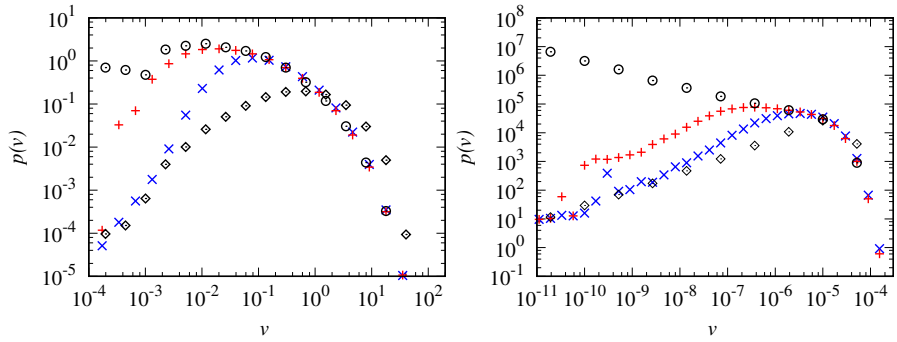

(a) $\ln_K$-field (b) γ_K-field

Figure 6.6: Evolution of the time-Lagrangian velocity PDF. The PDF evolves from the flux-weighted Eulerian velocity PDF (bottom black diamonds) to the Eulerian velocity PDF (top black circles). For the $\ln_K$-field (left panel), the two intermediate velocity PDFs are at $t = 20\tau$ (blue crosses) and $t = 200\tau$ (red crosses). For the γ_K-field (right panel) the two intermediate velocity PDFs are sampled at $t = 5.5\tau$ (blue crosses) and $t = 33\tau$ (red crosses).

a new finding related to the nature of the evolution of Lagrangian velocity PDF, we shall discuss it below.

The evolution of the mean and of the variance of the velocity distribution is obtained from Equation (6.26). For the mean we obtain:

$$\langle v_s(s)\rangle = \langle v_s\rangle + \exp(-s/\ell_c)\,[\langle v_0\rangle - \langle v_s\rangle] \tag{6.27}$$

For the variance we obtain:

$$\langle v_s^2(s)\rangle = \langle v_s^2\rangle + \exp(-s/\ell_c)\,[\langle v_0^2\rangle - \langle v_s^2\rangle] \tag{6.28}$$

Figure 6.7 (insets) shows the evolution of the mean s-Lagrangian velocity obtained by DNS and a fit of the Bernoulli model, for the two kinds of K-fields. The mean s-Lagrangian velocity starts from the mean of the Eulerian velocity (uniform injection) and evolves to the arithmetic mean of the flux-weighted Eulerian velocity PDF (the steady-state s-Lagrangian velocity PDF). The Bernoulli model reproduces the evolution obtained by direct numerical simulations. This relaxation model quantifies the evolution of the mean of the s-Lagrangian velocity distributions. The unique parameter ℓ_c quantifies a characteristic correlation length scale for s-Lagrangian velocities. We shall now check if the Bernoulli model predicts the evolution of the s-Lagrangian and t-Lagrangian velocity PDF.

To test if the Bernoulli model could predict the evolution of the s-Lagrangian velocity PDF, we compared DNS based s-Lagrangian velocity PDFs against Bernoulli model based simulations. Figure 6.5 shows a comparison for two intermediate distances. The modeled probabilities for high s-Lagrangian velocities

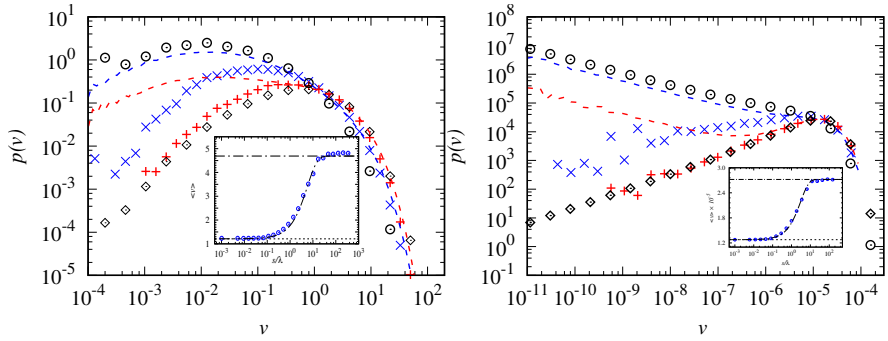

(a) $\ln_K$-field (b) γ_K-field

Figure 6.7: Comparison between DNS and the Bernoulli model for the evolutions of the space-Lagrangian velocity PDF and mean (inset). The PDF evolves from its initial PDF –the Eulerian velocity PDF, black circles– to its steady-state PDF –flux-weighted (FW) Eulerian velocity PDF, black diamonds. Blue and red crosses are DNS s-Lagrangian velocity PDFs at two intermediate distances. The Bernoulli model (dashed lines) underestimates the convergence rate for the probabilities of low velocities. The mean increases from the Eulerian mean (lower dashed line) to the flux-weighted mean (upper dashed line). The black dashed line is a fit of the Bernoulli model.

are in agreement. However for low velocities, the probabilities from the model are overestimated compared to those from DNS. This overestimation suggests that the convergence to the steady-state velocity PDF is too slow, for the low velocities. This result sheds light on a new finding. Since in the Bernoulli model the convergence rate is constant (i.e. $\exp(\Delta s/\ell_c)$), the difference between model and DNS suggests that the convergence rate of the s-Lagrangian velocity PDF is velocity dependent. In the next chapter, whose focus is on transport, we shall see that overestimating probabilities of low velocities leads to overestimating the tails of breakthrough curves. The difference between the s-Lagrangian velocity PDFs from DNS and from the Bernoulli model contrasts with the agreement found for the evolution of the mean s-Lagrangian velocity described above. The Bernoulli model is limited to reproduce the evolution of the s-Lagrangian velocity PDF.

Figure 6.8 shows a comparison between the evolution of the t-Lagrangian velocity PDF from DNS and the prediction made with the Bernoulli model. We observe that, as for the evolution of the s-Lagrangian distribution, the Bernoulli model fails in predicting the PDF convergence rate. At early times, the model reproduces the velocity PDF correctly, but we observe a slower convergence in time, which here manifests itself in underestimating the low velocities contribution.

In order to solve the issue regarding the slow converge of the PDF with the Bernoulli model, in the following we will consider a slightly more complex process, namely the Ornstein-Uhlenbeck process.

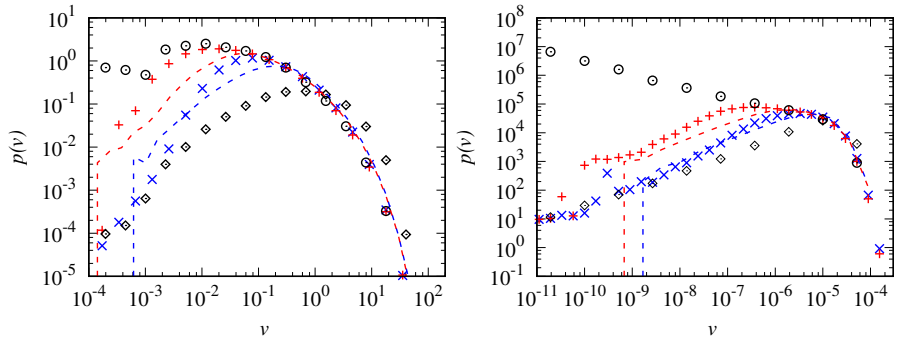

(a) $\ln_K$-field (b) γ_K-field

Figure 6.8: Comparison between DNS and the Bernoulli model for the evolution of the time-Lagrangian velocity PDF. The PDF evolves from its initial PDF – the flux-weighted Eulerian velocity PDF (black diamonds)–, to the steady-state PDF –the Eulerian velocity PDF (black circles). For the $\ln_K$-field, the two intermediate velocity PDFs are at $t = 20\tau$ (blue crosses) and $t = 200\tau$ (red crosses). For the γ_K-field, the two intermediate velocity PDFs are at $t = 5.5\tau$ (blue crosses) and $t = 33\tau$ (red crosses). The dashed lines represent the prediction of the Bernoulli model.

6.5.2 Ornstein-Uhlenbeck model

We propose an alternative mean-reverting model (Gardiner, 1986) to account for the velocity dependence in the evolution of s-Lagrangian velocity PDF. The s-Lagrangian velocity is obtained according to the bijective map

$$v(s) = F[w(s)] \tag{6.29}$$

from the Gaussian process $w(s)$, which evolves according to the Langevin equation

$$\frac{dw(s)}{ds} = -\gamma[w(s) - \mu] + \sqrt{2\kappa}\xi(s). \tag{6.30}$$

in which γ and κ are parameters and $\xi(s)$ is a Gaussian white noise with zero mean and unit variance. This stochastic Ornstein-Uhlenbeck (OU) process has this solution:

$$w(s) = (w_0 - \mu)\exp(-\gamma s) + \mu + \sqrt{2\kappa}\int_0^s ds' \exp[-\gamma(s - s')]\xi(s') \tag{6.31}$$

The characteristic correlation length is given by $\ell_c = \gamma^{-1}$ and the covariance of $w_s(s)$ decay as $\exp(-\gamma/s)$. The PDF $p_w(w, s)$ satisfies the Smoluchowski equation (see Appendix K)

$$\frac{\partial p_w(w,s)}{\partial s} = \frac{\partial}{\partial w}\gamma(w - \mu)p_w(w,s) + \kappa\frac{\partial^2}{\partial w^2}p_w(w,s). \tag{6.32}$$

In steady state it reads as

$$\gamma \frac{\partial}{\partial w}(w-\mu)p_w^\infty(w) = -\kappa \frac{\partial^2}{\partial w^2} p_w^\infty(w). \tag{6.33}$$

Integrating Equation (6.33) we obtain the stationary PDF $p_w^\infty(w)$ subject to the normalization condition

$$\int_{-\infty}^{\infty} dw p_w^\infty(w) = 1. \tag{6.34}$$

It is given by the Gaussian

$$p_w^\infty(w) = \frac{\exp\left(-\frac{(w-\mu)^2}{2\kappa\gamma^{-1}}\right)}{\sqrt{2\pi\kappa\gamma^{-1}}}. \tag{6.35}$$

In order to map $w(s)$ onto a velocity process with a certain stationary streamwise PDF $p_s(v)$, we consider the generic process characterized by $\mu = 0$, whose stationary mean and variance are 0 and 1, respectively and set $\kappa = \gamma^{-1}$, thus reducing the number of parameters to one. Under this condition, the map $F(w)$ of Equation (6.29) is such that

$$\int dv p_s(v) F^{-1}(v) = \mu = 0, \qquad = \int dv p_s(v) F^{-1}(v)^2 = \kappa\gamma^{-1} = 1 \tag{6.36}$$

Alternatively, we can consider the OU process characterized by stationary mean and variance, which correspond to $v(s)$ for a generic functional map $F(w)$ such that

$$\mu = \int dv p_s(v) F^{-1}(v), \qquad \kappa\gamma^{-1} = \int dv p_s(v) F^{-1}(v)^2 - \mu^2 \tag{6.37}$$

Figure 6.9 shows a comparison of the evolution of s-Lagrangian velocity PDF obtained by DNS and simulated with the OU model. The simulated velocity PDF plots closer to the PDF obtained by DNS at high and low velocities. This is an improvement compared to the Bernoulli model which was not able to reproduce the velocity dependent convergence rate at low velocities (compare with Figure 6.7). The reason why the OU model captures this convergence rate lies in the way velocities change at subsequent step. At each step, the velocity changes because of the noise term. In the Bernoulli model, however, a velocity may persist for several steps. Further insights on the shape and strength on the dependence between subsequent jumps may be gained with conditional probability distributions and copulas. This is ongoing work. For now, we note that the OU model is able to capture the velocity dependent rate of change for the evolution of the s-Lagrangian velocity PDF.

For the evolution of the mean of the s-Lagrangian velocity PDF, the OU model relaxes over a length ℓ_c too. This parameter is estimated by fitting the

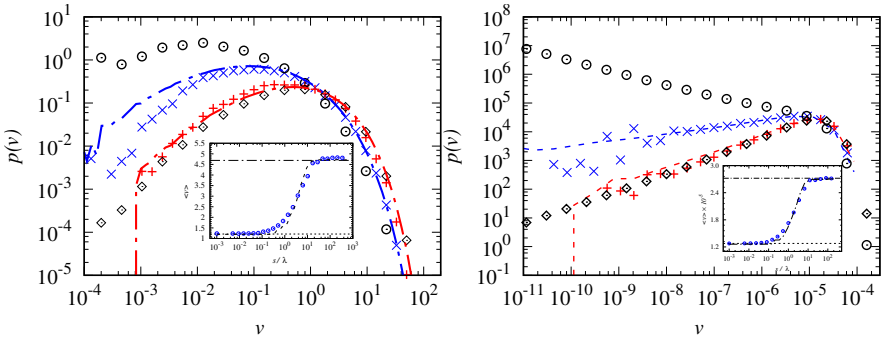

(a) $\ln_K$-field (b) γ_K-field

Figure 6.9: Comparison between DNS and the Ornstein-Uhlenbeck (OU) model for the evolutions of the space-Lagrangian velocity PDF and mean (inset). The PDF evolves from its initial PDF –the Eulerian velocity PDF, black circles– to its steady-state PDF –flux-weighted (FW) Eulerian velocity PDF, black diamonds. Blue and red crosses are DNS s-Lagrangian velocity PDF at two intermediate distances. The OU model (dashed lines) reproduces the velocity dependent rate of convergence for the probabilities of low velocities. Inset: As it evolves from the Eulerian mean (lower dashed line) to the flux-weighted mean (upper dashed line), the mean velocity obtained by DNS (blue dots) is reproduced by the model (black dashed line).

analytical solution that describes the evolution of w, i.e. after the map of the s-Lagrangian velocity to w. Figure 6.9 (inset) shows the prediction made by the OU model for the mean s-Lagrangian velocity, which is in agreement with the DNS. It appears that the parameter ℓ_c of the OU model is smaller than in the Bernoulli model. This difference may be related to the shape of the correlation function in between subsequent jumps and it remains to be investigated. To link the medium property to the transport attribute, we shall explore an empirical relationship between this parameter and the level of heterogeneity of the K field in the next section.

Figure 6.10 shows a comparison between the temporal evolution of the t-Lagrangian velocity PDF from DNS and the prediction made with the Ornstein-Uhlenbeck model. Unlike the results obtained for the Bernoulli model, we observe excellent agreement for the log-normal case. For gamma-distributions of hydraulic conductivity, even though the agreement is not perfect, we observe an improvement for high values of velocities, while the tails at low velocity, which are characterized by very low probabilities, are not reproduced properly.

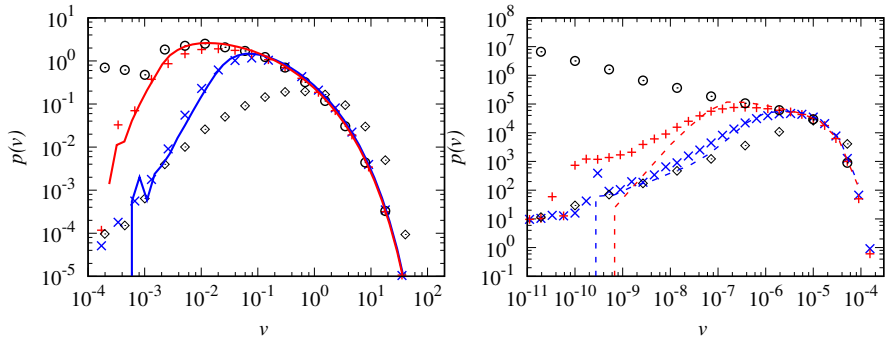

(a) $\ln_K$-field (b) γ_K-field

Figure 6.10: Comparison between DNS and the Ornstein-Uhlenbeck (OU) model for the evolutions of the time-Lagrangian velocity PDF. The PDF evolves from its initial PDF –the Eulerian flux-weighted velocity PDF, black circles– to its steady-state PDF –Eulerian velocity PDF, black diamonds. Blue and red crosses are DNS s-Lagrangian velocity PDF at two intermediate times. The OU model (dashed lines) better predicts the velocity dependent rate of convergence for the probabilities of low velocities.

6.5.3 Spatial correlation of space-Lagrangian velocities

To conclude this chapter, we investigate the relationship between medium and transport properties. To study if and how disorder impacts the fundamental parameter of our CTRW model, i.e. the correlation length along trajectory, ℓ_c, we explored its dependence on $\sigma^2 \ln_K$. The correlation length of the K-field (λ_K) and the level of heterogeneity ($\sigma^2_{\ln_K}$) of the K-field can be estimated from field experiments. Relating medium properties to transport properties is of interest for prediction purposes. Below we shall discuss a correlation length ℓ_c normalized by the correlation length of the K-field λ_K. For $0.1 \leq \sigma^2_{\ln K} \leq 7$ in the $\ln_K$-fields, ℓ_c from the Bernoulli and Ornstein-Uhlenbeck models was estimated with the evolution of the mean velocity and of the w process respectively.

Figure 6.11 shows the positive dependence of ℓ_c on $\sigma^2_{\ln_K}$. This dependence concurs previous work of Cvetkovic et al. (1996), that explored the dependence between the correlation length of Lagrangian velocity projected on the longitudinal direction of the mean flow for $\ln_K$-fields and $\sigma^2_{\ln_K}$ up to 4. The authors provided an empirical relationship to predict the correlation length of the velocities based on the value of $\sigma^2_{\ln_K}$. We note that this relationship may predict ℓ_c values for the Bernoulli model too. For this model, ℓ_c of this study 1) are in close agreement with those of Cvetkovic et al. (1996) and 2) extend to higher $\sigma^2_{\ln_K}$. In contrast, ℓ_c is always smaller when it is estimated with the OU model and the previous relationship can not be applied. Hence, we propose a new empirical relationship to describe the dependence between ℓ_c from the OU model and $\sigma^2_{\ln_K}$.

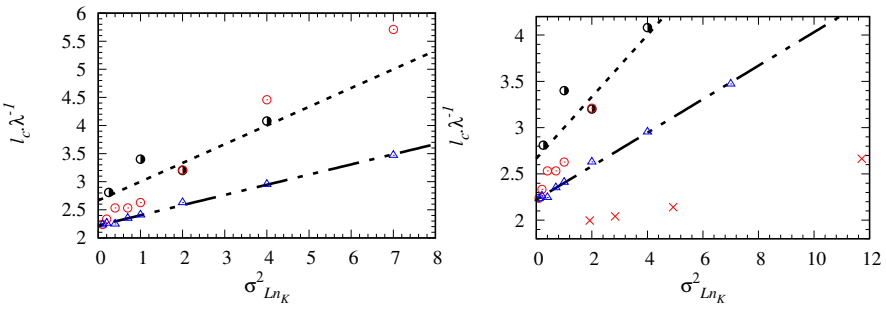

(a) $\ln_K$-field (b) $\ln_K$- and γ_K-field

Figure 6.11: Comparison between the correlation length of Lagrangian velocities along trajectories estimated with the Bernoulli model (red circles), the Ornstein-Ulhenbeck model (blue triangles) and reference values (Cvetkovic et al., 1996) (black circles) and empirical relationship (dash line). The double dash line shows a linear regression ($y = 0.180984 \times x + 2.22144$) for the OU model. The length ℓ_C is obtained by fitting the evolution of the mean Lagrangian velocity for the Bernoulli model and the mean w for the Ornstein-Ulhenbeck model has discussed in the text. The correlation length of Lagrangian velocities increases with increasing heterogeneity of the K field. The figure on the left shows ℓ_c estimated with w for the γ_K-fields (red crosses).

The new relationship has a smaller slope (1/3 vs ≈1/5). These shorter length and smaller slope may be related to the mapping of the mean s-Lagrangian velocity to the w process. This map contains information on the correlation of subsequent velocities and the study of these transitions is on going. In summary, we confirm the existence of a characteristic length scale for the s-Lagrangian velocity distribution. This length is longer than the correlation length of the $\ln_K$-field, it depends on the heterogeneity of the $\ln_K$-field and it is model dependent. Note that the new empirical relationship we proposed is valid for $\sigma^2_{\ln_K} > 0$ and the OU model.

In this study, we consider multi-Gaussian K-fields with the same correlation structure but different point distributions. Using the same structure allow us to inspect the effect of contrasting point K distributions on Lagrangian properties such as the characteristic correlation length scale of the s-Lagrangian velocity, and the impact of this length on transport. However, the structure of the hydraulic conductivity field may change (e.g. connected fields or stratified media) and this change can impact transport properties and the effective associated models (Le Borgne et al., 2008b).

6.6 Summary and Conclusions

In this chapter, we have investigated the velocity organization in Darcian heterogeneous flows and we have studied the relationship between flow properties and transport dynamics attributes. We have studied different configurations of medium disorder by considering random multi-Gaussian hydraulic conductivity fields characterized by broad distributions of point values. Specifically, we have considered log-normal fields characterized by high values of $\sigma^2_{\ln_K}$, as well as truncated Gamma-distributed conductivities. While the first choice represents a standard approach, the power-law distribution is motivated by the necessity to explore different scenarios and quantify the impact of disorder on Eulerian and Lagrangian velocities. As we recalled previously, these distributions appeared to be relevant for real systems (Haslauer et al., 2012).

Regardless the specific choice of the distribution of K, we have shown how flow and transport attributes are related. To this end, we have considered the statistics of Eulerian and Lagrangian velocities and we have studied the relationship between them. We have pointed out the importance of the sampling mode of Lagrangian velocities by distinguishing between t-Lagrangian velocities, sampled isochronally, and s-Lagrangian velocities, sampled equidistantly. We have found that the statistics of t-Lagrangian velocities is the same as for the Eulerian velocities. In contrast, s-Lagrangian velocities follow a different statistics, as their PDF is obtained from the Eulerian PDF through flux-weighting. We have proven that this result is valid for Darcy flows under in the hypotheses of incompressibility and ergodicity.

Next, we have investigated the impact of different injection conditions on Lagrangian velocities. To this end, we have considered two different injection modes, namely resident (uniform) injection and flux-weighted injection. We have seen that Lagrangian velocities are stationary in time for uniform injection, while the steady state for s-Lagrangian velocities is represented by flux-weighted conditions. We have studied the non-stationary scenarios for t- and s-Lagrangian velocities and we have observed the corresponding evolutions towards the steady-state in terms of both Lagrangian velocities PDF and its moments. We have showed that the Bernoulli model, based on stochastic relaxation with constant rate, can capture the evolution of the mean and the variance of s-Lagrangian velocities, but the estimated evolution of the Lagrangian PDFs is too slow. Hence, we have proposed an Ornstein-Uhlenbeck process to describe the velocity transitions. This mean-reverting approach has allowed us to describe and predict the evolution of Lagrangian velocity statistics in terms of the sole correlation length of s-Lagrangian velocities.

In order to estimate this parameter, which is crucial for the parameterization of both the Bernoulli and the OU model, we have studied its relationship with the variance of $\ln_K$, i.e. a medium attribute. We have showed that ℓ_c is model-dependent. In fact, for the Bernoulli model the correlation length grows with increasing log-variance in a way that appears to be consistent with literature results (Cvetkovic et al., 1996). In contrast, for the OU model, the correlation

length relates to $\sigma^2_{\ln_K}$ through a different linear behavior that we have empirically determined.

This work sheds new light on fundamental issues for the description of transport attributes in Darcian heterogeneous flow fields and it paves the way for the definition of a large-scale predictive transport formulation, as we will show in the next chapter.

7

Transport in heterogeneous Darcy flows

7.1 Introduction

Understanding transport in porous media is important to perform predictions of contaminant dispersion in groundwater among others. In nature, flow and transport in porous medium is in general complex. For instance variations in sedimentation sequences or geological history lead to structural heterogeneity, which impact the hydraulic conductivity tensor. At Darcy's scale, heterogeneous hydraulic conductivity fields and groundwater flow velocities vary over length scales (Gelhar, 1993). Velocity variations affect particle dispersion, which may not be described by effective advective dispersive (Fickian) model that use constant drift and diffusion parameters. An alternative and effective framework to model transport in porous media is the Continuous Time Random Walk (CTRW). It has been used to model transport from the pore (Bijeljic and Blunt, 2006; de Anna et al., 2013; Kang et al., 2015a; Holzner et al., 2015) to Darcy (Le Borgne et al., 2008b; Dentz and Castro, 2009) and field scales (Scher et al., 2002) and showed to be suitable to model non-Fickian transport. CTRW may overcome some limitations of other modeling frameworks, such as perturbative theory, which impedes describing dispersion processes in very heterogeneous porous media ($\sigma^2_{\ln_K} \geq 4$). Temporal velocity series in heterogeneous flows are characterized by intermittent behavior (de Anna et al., 2013; Kang et al., 2014; Puyguiraud et al., 2017), which can be described with correlated CTRW models based on transition probabilities (Le Borgne et al., 2008a). Recent theoretical advances extended this CTRW models to include the evolution of the velocity distribution (Dentz et al., 2016a).

As we showed in Chapters 5 and 6, velocity correlation is described through spatial Markov models that are parameterized in terms of the streamwise correlation length. These models account for the evolution of the Lagrangian velocity

PDFs in non-stationary conditions. Velocity stationarity is determined by the injection and detection modes. The flux-weighted Eulerian distribution is the steady-state velocity PDF for equidistantly-sampled Lagrangian velocities. The Eulerian PDF represents the steady-state for isochronally-sampled Lagrangian velocities. As we showed in Chapter 6, we have investigated the velocity organization in Darcy flows through heterogeneous porous media characterized by random disorder configurations. By considering two Markov velocity models, the Bernoulli and the Ornstein-Uhlenbeck (OU) models, for the evolution of t- and s-Lagrangian velocities PDFs. The Bernoulli model fails in predicting the evolution rate of the Lagrangian velocity PDF. This issue will impact on transport features, such as the spatial density profiles and the breakthrough curves. To address this issue, we have developed the Ornstein-Uhlenbeck model that provides more accurate predictions for the velocity evolution and consequently for transport description.

This Chapter focuses on proposing a correlated CTRW model for the upscaling of transport in heterogeneous Darcian flow fields. This model is parameterized in terms of the streamwise correlation length, the velocity PDF at the injection. It makes use of the Bernoulli and the OU models to describe velocity evolution. This represents a novelty in comparison with previous approaches that were based on velocity transition probabilities which are complicated to obtain (they are obtained by solving the transport problem). We investigate the impact of disorder and injection modes on transport observables, including the spatial density of particles, the moments of particle displacements and first passage time distributions at a plane. To this end, we consider Darcy flows in random hydraulic conductivity fields characterized by multi-Gaussian structure and broad distributions of point values. Alongside with the traditionally used log-normal distribution, we also consider conductivity PDFs that are characterized by power-law tails towards low values. This choice is motivated by the observation that real aquifers may exhibit this kind of disorder properties (Haslauer et al., 2012). In our CTRW, disorder is mapped onto the distribution of transition times through the Eulerian and the flux-weighted Eulerian velocity PDF. The results that we obtain are tested against direct numerical simulations performed as in Chapter 6 and excellent agreement is found.

7.2 Methodology

In this section, we present the methodology that we will adopt in the paper. This methodology is composed of two phases. First we perform direct numerical simulations that provide us with the statistical information of the dynamic properties of the flow that we need to parameterize our continuous time random walk model. For this stage, which includes random hydraulic conductivity field generation, flow solution in steady conditions, particle tracking and Eulerian and Lagrangian velocity statistics, we refer to Chapter 6. In this chapter, we will use

the following distributions of hydraulic conductivity

$$\psi_K(K) = \begin{cases} \psi_L(K) = \frac{1}{\sqrt{2\pi\sigma^2_{\ln K}}K} \exp\left\{-\frac{[\ln(K)-\mu]^2}{2\sigma^2_{\ln K}}\right\} \\ \psi_\Gamma(K) = A(\alpha, K_1, K_2)K^{\alpha-1}\exp\left[-K_2K - \frac{K_1}{K}\right], \end{cases} \tag{7.1}$$

where μ is the geometric mean, K_1 and K_2 are the lower and upper cut-off, respectively, α is the shape parameter of the truncated Gamma distribution and $A(\alpha, K_1, K_2)$ is a normalization factor which is calculated numerically. In this work we will take $K_2 = 10^{-11}$. Notice that the degree of heterogeneity is given by the variance of $\ln(K)$ in the former case and by the exponent of the power-law distribution in the latter. The second part of our methodology include the definition and parameterization of a CTRW model.

7.2.1 CTRW model

In order to model dispersion in the presented Darcy fields, we make use of a CTRW approach. In Chapter 5 we show that under the condition of ergodicity the PDFs of Lagrangian velocities evolve from the injection conditions towards a steady-state distribution that depends on the sampling. Namely, the t-Lagrangian steady-state PDF is $p_{t,ss}(v) = p_e(v)$, while the s-Lagrangian steady-state PDF equals the flux-weighted Eulerian (5.10). Thus, our model has to be correlated and account for ageing, i.e. the evolution of the joint transition lengths and times PDFs. Particle motion along streamlines are given by

$$x(t) = x[s(t)] \qquad\qquad v(t) = v_s[s(t)], \tag{7.2}$$

where

$$\frac{dx(s)}{ds} = \overline{T}^{-1} \qquad \frac{ds(t)}{dt} = v(t) \qquad \frac{dt(s)}{ds} = \frac{1}{v_s(s)}, \tag{7.3}$$

where $\overline{T}$ is the average tortuosity. The joint distribution of positions and velocities at a given time is defined as

$$p(x, v; t) = \int_0^\infty ds \langle \delta[s - s(t)]\delta[x - x(s)]\delta[v - v(s)]\rangle. \tag{7.4}$$

We use now the following property of Dirac's delta

$$\delta[s - s(t)] = \frac{\delta[t - t(s)]}{ds(t)/dt}, \tag{7.5}$$

which, in virtue of the equivalence $ds(t)/dt = v(t) = v_s[s(t)]$, reads

$$\delta[s - s(t)] = \frac{\delta[t - t(s)]}{v_s(s)}. \tag{7.6}$$

By substituting the latter into Equation (7.4), we get

$$p(x,v;t) = \int_0^\infty ds v^{-1} R(x,v,t;s) \tag{7.7}$$

where we defined

$$R(x,v,t;s) = \langle \delta[t-t(s)]\delta[x-x(s)]\delta[v-v(s)]\rangle. \tag{7.8}$$

By considering an increment of length Δs, we can write

$$R(x,v,t;s+\Delta s) = \int_0^\infty dv' r(v,\Delta s|v') R(x-\Delta s/\overline{T}, v', t-\Delta s/v'; s). \tag{7.9}$$

We consider the limit $\Delta s \to 0$ and perform the Taylor expansion

$$\begin{aligned} R(x-\Delta s/\overline{T}, v, t-\Delta s/v; s) = R(x,v,t;s) + -\frac{\Delta s}{\overline{T}}\frac{\partial}{\partial x}R(x,v,t;s) \\ - \frac{\Delta s}{v}\frac{\partial}{\partial t}R(x,v,t;s) + ... \end{aligned} \tag{7.10}$$

so that Equation (7.9) reduces to

$$\begin{aligned} R(x,v,t;s+\Delta s) = \int_0^\infty dv' r(v,\Delta s|v') R(x,v',t;s) \\ - \int_0^\infty dv' r(v,\Delta s|v') \Delta s \left[\frac{1}{\overline{T}}\frac{\partial}{\partial x} + \frac{1}{v'}\frac{\partial}{\partial t}\right] R(x,v',t;s). \end{aligned} \tag{7.11}$$

Since $\Delta s \to 0$, we further obtain

$$\begin{aligned} \frac{\partial R(x,v,t;s)}{\partial s} = \int_0^\infty dv' \frac{r(v,\Delta s|v')}{\Delta s}[R(x,v',t;s) - R(x,v,t;s)] \\ - \left[\frac{1}{\overline{T}}\frac{\partial}{\partial x} + \frac{1}{v}\frac{\partial}{\partial t}\right] R(x,v,t;s). \end{aligned} \tag{7.12}$$

Note that $\lim_{\Delta s\to 0} r(v,\Delta s|v') = \delta(v-v')$. By substituting Equation (7.12) into Equation (7.7) we get

$$\frac{\partial p(x,v;t)}{\partial t} + \frac{v}{\overline{T}}\frac{\partial p(x,v;t)}{\partial x} = -vp(x,v;t) + \int_0^\infty dv' \frac{vr(v,\Delta s|v')}{\Delta s} p(x,v';t). \tag{7.13}$$

In the CTRW framework, particle motion along their trajectories is described by the following recursive relations

$$x_{n+1} = x_n + \zeta \qquad t_{n+1} = t_n + \frac{\ell_c}{v_n} \qquad v_{n+1} = v_n' \tag{7.14}$$

where $\zeta = \ell_c/\overline{T}$ represents a characteristic length over which the s-Lagrangian velocity $v_n = v_s(x_n)$ de-correlates, since ℓ_c is the correlation length of the Lagrangian velocity along the streamline. The velocities v' are drawn from an evolving PDF, as we discuss in Section 7.2.2. Particle velocities are constant within this distance, so subsequent transition times $\tau_n = \ell_c/v_n$ are independent identically distributed random variables. Thus, the joint PDF of transition times and lengths is given by

$$\psi(x,t) = \delta\left(x-\zeta\right)\psi(t), \tag{7.15}$$

where $\psi(t) = \frac{\ell_c}{t^2} p_s(\ell_c/t) = \frac{\ell_c^2}{\langle v_e\rangle t^3} p_e(\ell_c/t)$ (Dentz et al., 2016a).

7.2.2 Velocity transition model

As we showed in Chapter 6, the velocity statistics evolves towards the stationary conditions, which depend on the sampling method. For equidistant sampling, the steady-state is represented by the flux-weighted velocity distribution. In order to account for this evolution, we use and compare two models that we present ordered by increasing complexity.

Bernoulli model

First, we consider the Bernoulli model based on a stochastic relaxation process

$$v_s(s+\Delta s) = [1-\xi(s)]v(s) + \xi(s)\nu(s), \tag{7.16}$$

where the $\nu(s)$ are distributed according to the steady-state velocity PDF and the $\xi(s)$ are independent identically-distributed Bernoulli variables, which take the value 1 with probability $1-\exp[-\Delta s/\ell_c]$ and 0 with probability $\exp[-\Delta s/\ell_c]$. Their PDF is given by (5.33e) and the transition probability $r(v,s|v')$ is given by (5.33f). This velocity process is fully determined by Equation (7.16) and by the initial velocity distribution. The Bernoulli model represents the simplest model for velocity evolution.

Ornstein-Uhlenbeck model

As we have shown in Chapter 6, stochastic relaxation enables us to capture the velocity statistics in the asymptotic regime, but the convergence to the steady-state is too slow. Thus, we make use of the mean-reverting Ornstein-Uhlenbeck (OU) process, where the velocity is given by the bijective map

$$v(x) = F[w(x)] \tag{7.17}$$

of the Gaussian process $w(x)$ that evolves according to the Langevin equation

$$\frac{dw(x)}{dx} = -\ell_c^{-1}[w(x)-\mu_w] + \sqrt{2\ell_c}\eta(x), \tag{7.18}$$

where $\eta(x)$ is Gaussian white noise and

$$\mu_w = \int dv p_s(v) F^{-1}(v). \tag{7.19}$$

The solution of (7.18) is given by

$$\begin{aligned} w(x) = (w_0 - \mu_w)\exp(-x/\ell_c) + \mu_w + \sqrt{2\ell_c} \\ + \sqrt{2\ell_c}\int_0^x dx' \exp\left[-\frac{(x-x')}{\ell_c}\right]\eta(x'). \end{aligned} \tag{7.20}$$

The distribution $p_w(w,x)$ of the stochastic process $w(x)$ satisfies the Smoluchowski equation (see Appendix J)

$$\frac{\partial p_w(w,x)}{\partial x} = \ell_c^{-1}\frac{\partial}{\partial w}(w-\mu_w)p_w(w,x) + \ell_c\frac{\partial^2}{\partial w^2}p_w(w,x), \tag{7.21}$$

which in stationarity conditions reduces to

$$\ell_c^{-1}\frac{\partial}{\partial w}(w-\mu_w)p_w^\infty(w) = -\ell_c\frac{\partial^2}{\partial w^2}p_w^\infty(w), \tag{7.22}$$

where $p_w^\infty(w)$ is the stationary PDF. By solving Equation (7.22) and because the steady PDF must be normalized to 1, we get the Gaussian PDF

$$p_w^\infty(w) = \frac{\exp\left(-\frac{(w-\mu_w)^2}{2\ell_c^2}\right)}{\sqrt{2\pi\ell_c^2}}. \tag{7.23}$$

In $x+\Delta x$, the solution (7.20) reads

$$\begin{aligned} w(x+\Delta x) = [w(x)-\mu_w]\exp(-\Delta x/\ell_c) + \mu_w \\ + \sqrt{2\ell_c}\int_x^{x+\Delta x} dx'\eta(x')\exp[-(x-x')/\ell_c]. \end{aligned} \tag{7.24}$$

Hence, the transition probability is given by

$$p_w(w,\Delta x|w') = \frac{\exp\left(-\frac{\left[w-\mu_w-(w'-\mu_w)\exp(-\Delta x/\ell_c)\right]^2}{2\ell_c^2[1-\exp(-2\Delta x/\ell_c)]}\right)}{\sqrt{2\pi\ell_c^2[1-\exp(-2\Delta x/\ell_c)]}} \tag{7.25}$$

Finally, the PDF of the stochastic process w evolving from the initial condition $p_w(w,0)$ is given by

$$p_w(w,x) = \int_0^\infty dw' p_w(w,x|w')p_w(w',0). \tag{7.26}$$

In the numerical simulations, the evolution of w is performed through the discrete Kolmogorov equation for the process (7.18)

$$w(x + \Delta x) = w(x)[1 - \Delta x/\ell_c] + \sqrt{2\ell_c \Delta x}\eta(x), \tag{7.27}$$

The new velocity is given by inverse mapping $v(x + \Delta x) = F[w(x + \Delta x)]$.

7.3 Transport behavior

In this section we present the results of the CTRW model presented in Section 7.2. We consider both the relaxation and the Ornstein-Uhlenbeck (OU) model for the description of the velocity PDF evolution and we study the impact of different injection conditions. We compare the transport observables obtained from the CTRW model to direct numerical simulations. In the following, the results from DNS are intended as ensemble-averaged over 100 realizations of the conductivity field. We consider as diagnostic measures of transport the spatial density $c(x, t)$ and its moments, as well as the breakthrough curves $f(t, x)$.

7.3.1 Spatial particle density

Here we consider the spatial density integrated along the mean flow direction. We present results for fields characterized by the log-normal distribution $\psi_L(K)$ and the power-law distribution $\psi_\Gamma(K)$ (7.1)of hydraulic conductivities. Figure 7.1 shows the particle concentration obtained through direct numerical simulations (100 realizations, 10^4 particles/realization) and CTRW numerical simulations with a) the stochastic relaxation process and b) the Ornstein-Uhlenbeck model for the evolution of the velocity PDF. We observe that the relaxation-based CTRW model does not provide the correct results. This is due to the fact that the stochastic relaxation process does not describe accurately the velocity PDF evolution (see Chapter 6). In particular, we observe that for uniform injection low velocities are over-sampled and the concentration of particles trapped at the inlet is overestimated. This is more evident in the log-normal case, for which $\sigma^2_{\ln K}$ is much higher. The OU-CTRW, on the other hand, guarantees a better convergence towards the steady-state velocity PDF. Thus, the agreement with the Monte Carlo simulation is improved. In particular, we find the peak at the correct position $x_p = \langle v_e \rangle t$ for both the log-normal and the truncated Gamma cases. On the basis of these considerations, in the following we will make use of the OU model. A different injection condition, other than uniform or flux-weighted is now considered. It consists in injecting particles in regions of low velocity. This choice is motivated by the MADE site experiment, where the tracer injection was performed in low permeability regions. In our simulations, injection of particles is performed along a line, but only the velocities belonging to the first 10 percentiles of the Eulerian velocity PDF are taken into account. Figure 7.2 shows the spatial density profile at $t^* = 47.1\tau_v$ obtained by Monte Carlo and by CTRW-OU numerical simulations. Because the initial velocities are very low, particles travel on average less distance than in the uniform and

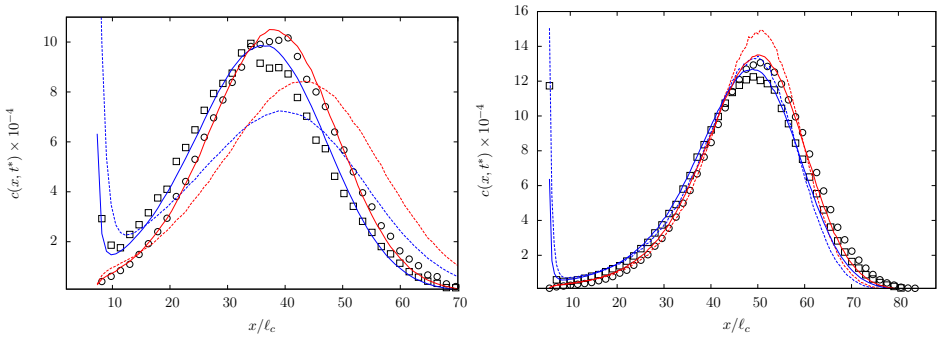

Figure 7.1: Ensemble-averaged spatial density profile obtained by Monte Carlo simulations (100 realizations, 10^4 particles/realization) for uniform (squares) and flux-weighted (circles) injection. Results for the K distribution ψ_L with $\sigma^2_{\ln K} = 7$ at $t^* = 35.6\tau_v$ (left panel) and ψ_Γ with $\alpha = 1/2$ at time $t^* = 47.1\tau_v$ (right panel). Results are compared with CTRW numerical simulations with stochastic relaxation (dashed) and the Ornstein-Uhlenbeck model (solid). In CTRW simulations we use 10^7 particles. Blue lines are for uniform injection, red lines for flux-weighted injection.

flux-weighted injection cases. Moreover, a significant amount of particles are so slow that they travel less than a correlation length by the control time t^*.

7.3.2 Moments of particle displacements

Now we consider the temporal evolution of the moments of particle displacements. The mean displacement grows linearly as

$$\mu_x(t) = \begin{cases} \langle v_i \rangle / \overline{T} t & t \ll \tau_v \\ \langle v_e \rangle / \overline{T} t & t \gg \tau_v, \end{cases} \tag{7.28}$$

where $\langle v_i \rangle$ is the mean velocity at the injection and $\tau_v = \ell_c / \langle v_e \rangle$. In the early time regime the linear behavior is governed by the mean velocity at the inlet, which depends on the injection conditions. Notice that for uniform injection it is given by the mean Eulerian velocity, for flux-weighted injection it is the mean of the flux-weighted velocity PDF $p_{s,ss}(v)$. In the asymptotic time regime, as the velocity PDF evolves towards the steady-state $p_{t,ss}(v) = p_e(v)$, the mean displacement behaves as $\mu_x(t) = \langle v_e \rangle / \overline{T} t$, regardless the injection conditions.

In Section 5.4 we derived the dispersion coefficient for steady-state and transient injection conditions. The variance of particle displacements is given by the Kubo's formula

$$\kappa_x(t) = 2 \int_0^t dt' \mathcal{D}(t') \tag{7.29}$$

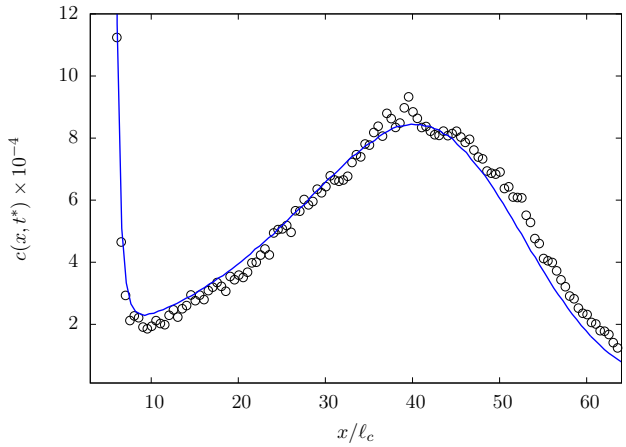

Figure 7.2: Ensemble-averaged spatial density profile at time $t^* = 47.1\tau_v$ obtained by Monte Carlo simulations (100 realizations, 10^4 particles/realization) for injection in low velocity regions (circles). We use the K distribution ψ_Γ with $\alpha = 1/2$. Results are compared with CTRW-OU numerical simulations (blue solid line). In CTRW simulations we use 10^7 particles.

At early times, the dispersion coefficient $\mathcal{D}(t)$ is given by Equation (5.92). Here, we divide by $\overline{T}^2$ because we look at the projection along the main flow direction. By substituting this expression into (7.29), we get for $t \ll \tau_v$

$$\kappa_x(t) = \langle (v_0 - \langle v_0 \rangle)^2 \rangle t^2 / \overline{T}^2. \tag{7.30}$$

The ballistic behavior at early times arises for every injection condition as a consequence of the fact that particles are still moving within one correlation length and thus keep their initial velocity. The multiplicative factors depend on the injection condition. As expected, for flux-weighted injection, the variance is initially larger. The behavior of the dispersion coefficient in the long-time regime depends on the disorder configuration. We will now distinguish between log-normal and truncated-Gamma distributions.

Log-normal K fields

In Chapter (6) we showed that for low conductivity values, we can approximate the velocity PDF with a log-normal distribution. This means, the distribution of Eulerian velocities $p_e(v)$ has finite moments. Thus, the solution for the dispersion coefficient (5.96) holds. By substituting this expression into Equation (7.29), we get the linear growth

$$\kappa_x(t) = 2\mathcal{D}^e t. \tag{7.31}$$

However, in Figure 7.3 we observe a power-law scaling $\sim t^{1.3}$. Indeed, this is not a real power-law, but a pre-asymptotic regime since, due to the finite size of the domain, we couldn't reach the asymptotic regime. This kind of behavior arises as a consequence of the fact that log-normal distributions with large variances can be fitted with a power-law over up to one order of magnitude.

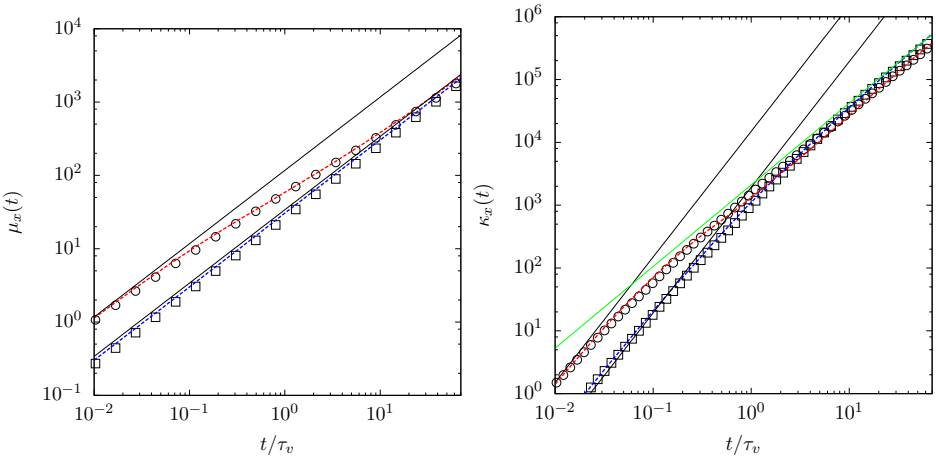

Figure 7.3: Moments of the spatial distribution from Monte Carlo simulations (100 realizations, 10^4 particles/realization) for uniform (squares) and flux-weighted (circles) injection. We use the log-normal K distribution (7.1) with $\sigma^2_{\ln_K} = 7$. Comparison with the CTRW-OU model with 10^4 particles. Blue dashed line is for uniform injection, red dashed line is for flux-weighted injection. (Left) Mean displacement. Black lines indicate the early-time behavior (7.28). (Right) Variance of particle displacement. Black lines show early-time behavior (7.30), the green line is the asymptotic behavior $t^{1.3}$.

Truncated Gamma K fields

We assume here that the sampled Eulerian PDF can be approximated by the Gamma PDF Eq. (5.59) (see Figure 7.4). This approximation is valid for times shorter than the cut-off time $\tau_c = \ell_c/v_c$, where v_c is the cut-off velocity of the sampled Eulerian PDF. Thus, in Equation (5.59) we set $v_0 = \langle v_e \rangle$ and the exponent β is obtained by fitting the Gamma distribution to the sampled PDF. For $\alpha = 1/2$, we get $\beta = 0.58$. With this hypothesis, the dispersion coefficient in the long time regime is given by Equation (5.93) for stationary conditions and (5.94) for the non-stationary case. By inserting these expressions into Equation (7.29) we get for $t \gg \tau_v$

$$\kappa_x(t) = \begin{cases} 2c_\beta \langle v_e \rangle \ell_c \tau_0^{\beta-1} t^{2-\beta} & \text{steady} \\ 2c_\beta \langle v_e \rangle^2 \tau_0^{\beta} t^{2-\beta} & \text{non-steady,} \end{cases} \tag{7.32}$$

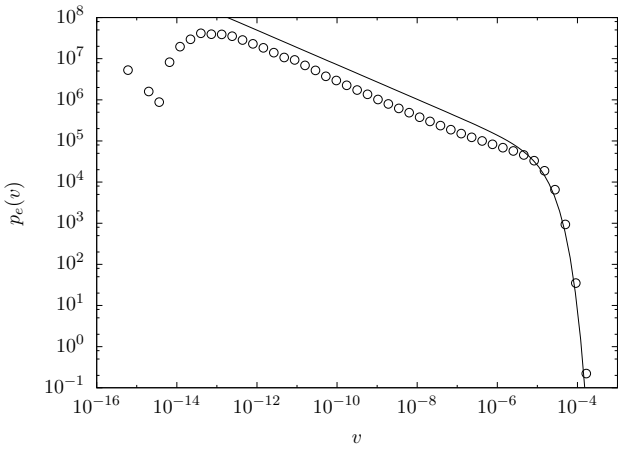

Figure 7.4: Sampled Eulerian velocity PDF (circles) from Monte Carlo simulations and fitted Gamma velocity PDF (5.59) with exponent $\beta = 0.58$ (solid line).

where $c_\beta = c\beta[(1-\beta)(2-\beta)\overline{T}^2]^{-1}$ and c is defined in Section 5.4. Notice that for both stationary and non-stationary injection conditions the variance of particle displacements scales with the same power $t^{2-\beta}$. The exact behavior depends on the initial conditions. As for the dispersion coefficient, while the variance grows faster for stationary conditions at early times, it increases more slowly in the long time regime.

The full behavior of the mean displacement obtained by Monte Carlo and CTRW-OU numerical simulations is shown in Figure 7.5 for the velocity PDF $\psi_\Gamma(v)$ with $\alpha = 1/2$. Good agreement between direct simulations and our model is found.

7.3.3 Breakthrough curves

Here we consider the breakthrough curves at the control plane $x = x^*$. We compare the results from Monte Carlo simulations to those of the CTRW based on the stochastic relaxation for the velocity PDF evolution and with the CTRW-OU. Figure 7.6 shows the first passage time distributions obtained by Monte Carlo simulations for log-normal and power-law K fields. In the case of flux-weighted injection, the initial velocity PDF is the steady-state. Thus, the peak of the FPTD is given by those particles that move with average velocity $\langle v_s \rangle$ at it is located at

$$t_p = x^*/\langle v_s \rangle. \tag{7.33}$$

If the control plane is located at a large distance, at which the velocity PDF is already stationary, the peak time is given by (7.33), regardless the injection

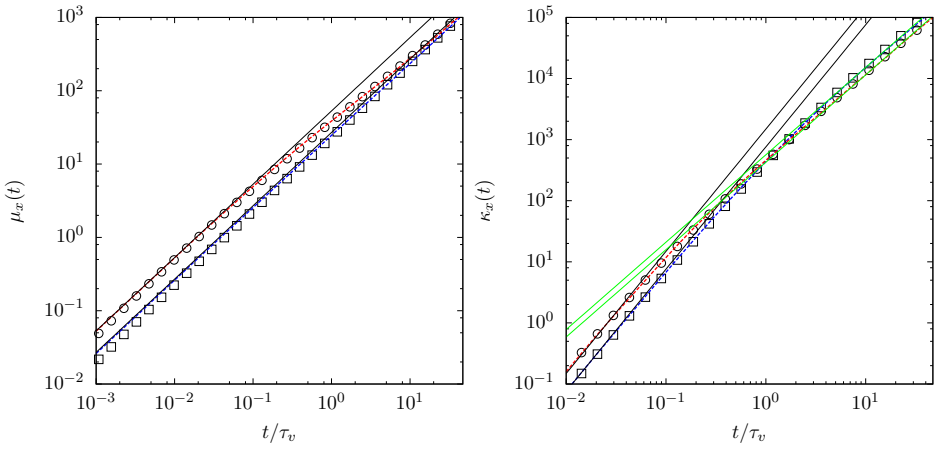

Figure 7.5: Moments of the spatial distribution from Monte Carlo simulations (100 realizations, 10^4 particles/realization) for uniform (squares) and flux-weighted (circles) injection. We use the K distribution ψ_Γ with $\alpha = 1/2$. Comparison with the CTRW-OU model with 10^4 particles. Blue dashed line is for uniform injection, red dashed line is for flux-weighted injection. (Left) Mean displacement. Black lines indicate the early-time behavior (7.28). (Right) Variance of particle displacement. Black lines show early-time behavior (7.30), green lines are the asymptotic behavior (7.32).

conditions. In contrast, at intermediate distances this is not the case, since the mean velocity evolves with the traveled distance, as we showed in Section 5.4. The first passage time distribution is given by

$$f(t,x) = \langle \delta[t - t_{n_x}] \rangle, \tag{7.34}$$

where $n_x = \max[n | t_n \leq t(x)]$ is the number of steps needed to arrive at x. Because the spatial increments are constant, it is given by $n_x = x/\zeta$. In the asymptotic regime, i.e. for $t \gg \tau_s$, the FPTD behavior is governed by the statistics of slowest particles. Thus, for log-normal fields we observe log-normal tails which originates from the PDF of the inverse velocities

$$f(t,x) \propto \begin{cases} xt^{-2} \exp\left[-\frac{(\ln(x/t)-\langle v_e \rangle)^2}{2\sigma_e^2}\right] & \text{steady} \\ t^{-1} \exp\left[-\frac{(\ln(x/t)-\langle v_e \rangle)^2}{2\sigma_e^2}\right] & \text{uniform injection,} \end{cases} \tag{7.35}$$

where σ_e^2 is the Eulerian velocity variance. For the power-law distribution of velocities (5.59), the first passage time distribution scales as a power-law, whose exponent depend on the injection conditions

$$f(t,x) \propto \begin{cases} x^{1+\beta} t^{-2-\beta} & \text{steady} \\ x^\beta t^{-1-\beta} & \text{uniform injection.} \end{cases} \tag{7.36}$$

The full behavior of the FPTD obtained from Monte Carlo simulation is shown in

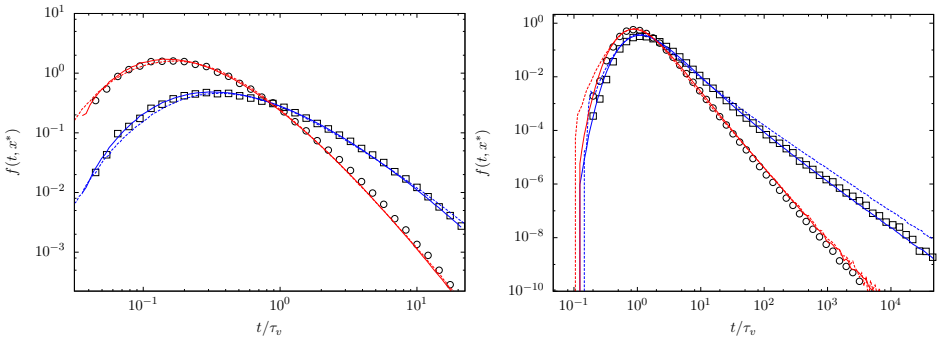

Figure 7.6: First passage time distributions at the control plane $x^* = 2\lambda_c$ from Monte Carlo simulations with uniform (squares) and flux-weighted (circles) injection. Comparison with relaxation-based CTRW (dashed) and OU-CTRW (solid). Blue lines are for uniform injection, red lines are for flux-weighted injection. (Left panel) Results from log-normal K fields. (Right panel) Results from power-law K fields.

Figure 7.6 together with the predicted results from the relaxation-based CTRW and the CTRW-OU. Under flux-weighted injection conditions, because of stationarity the two models provide similar results and they both are in good agreement with direct numerical simulations. When different injection conditions occur, the stochastic relaxation process does not capture the velocity PDF transition towards steady-state properly. For uniform injection, we observe that the first arrivals are delayed and that the tails are too heavy. This is a consequence of the persistence of low velocities sampled from the Eulerian PDF.

7.4 Summary and conclusions

We have studied the impact of disorder on non-Fickian transport in Darcy flows by considering different heterogeneity scenarios characterized by broad distributions of the hydraulic conductivity. Based on the Eulerian and Lagrangian statistics analysis of the previous chapter, we have proposed a CTRW model that is parameterized in terms of transport-independent quantities, which provides it with a predictive character. This CTRW accounts for velocity transitions through a mean-reverting process whose parameterization depends only on the streamwise correlation length. The transition time PDF contains the dynamical information relative to the distribution of Eulerian and steady-state velocities. The proposed model can correctly describe and predict the spatial particle density for different K distributions and different injection conditions, as well as the temporal evolution of the moments of particle displacements. We observe that the characteristic time scale of advection induces the formation of two distinct

time regimes, which arise for both stationary and non-stationary velocity PDFs. In the early-time regime, particles are, on average, moving within a correlation length from injection. This means, they have not experienced the heterogeneity of the flow field. Thus, transport behavior in this regime is ballistic. In the asymptotic regime, we observe different behaviors for log-normal and truncated Gamma fields, which are related to the details of the distributions. We observe that the variance of mean squared displacement scales as $t^{2-\beta}$ for truncated-Gamma fields, while we observe a $t^{1.3}$ scaling for log-normal fields. The latter behavior is not a real power-law regime, but it is a pre-asymptotic effect which is due to the finite size of the domain. This effect is related to the fact that log-normal distributions with high variances can be fitted with power-laws for up to an order of magnitude. The observed is a pre-asymptotic regime that represents a transition from the early-time ballistic to the predicted asymptotic linear behavior. Remarkably, for all the disorder configurations, we observe faster growth in case of non-stationary injection conditions. This is due to the fact that for uniform injection a larger amount of particle gets retained in low velocity zones. The contrast between these very slow particles and those that move with average velocity provokes a stretching of the particle density plume and, consequently, a faster grow rate of the variance. We have derived analytical expressions for both the early-time and the asymptotic behaviors of the moments. Next, we have studied the response of the first passage time distributions to different disorder and injection conditions. Resident injection gives rise to delayed arrivals due to the higher weight attributed to low velocities. The tails of the breakthrough curves are determined by the low velocities. For log-normal fields, the velocity distribution can be approximated with a log-normal for small values of K and v. Hence, the FPTD also exhibits a log-normal behavior at long times. For truncated Gamma fields, the tails of the FPTD are fully determined by the Eulerian velocity PDF for stationary injection conditions. In transient conditions, the tails are determined by the velocity PDF at the injection, since the behavior is governed by the slowest particles according to the big jump principle for the sum of independent random variables that follow an heavy-tailed distribution.

In conclusion, the proposed CTRW model, based on the Ornstein-Uhlenbeck velocity transition process can describe and predict normal and anomalous transport behaviors on the basis of transport-independent attributes. This work provides a large-scale transport formulation which can serve as a starting point for the modeling of laboratory and field experimental results.

8

Diffusion in structured disordered media

Abstract

We elucidate the impact of diffusive motion on the nature of anomalous dispersion in layered and fibrous disordered media. We consider two types of disorder characterized by quenched random velocities and quenched random retardation properties. Purely advective particle motion is ballistic in both disorder models. This changes dramatically in the presence of transverse diffusion, which leads to dimension-dependent disorder sampling. For $d \leq 3$ dimensions, heavy-tailed velocity distributions render large scale particle motion a correlated Lévy flight, while transport in the quenched random retardation model behaves as a biased continuous time random walk with correlated time increments.

8.1 Introduction

Anomalous dispersion can be seen as the result of the interaction of microscopic advective-diffusive mass transfer and spatial disorder, which may hinder or facilitate transport. Subdiffusive transport may be induced by crowdedness, randomly distributed traps and retardation properties, which quantify physical and chemical interactions between the transported substance and the medium. Superdiffusion on the other hand may be induced by strong disorder correlation (Bouchaud and Georges, 1990; Szymanski and Weiss, 2009; Dentz and Bolster,

This chapter is based on the paper "A. Comolli & M. Dentz - Impact of diffusion on anomalous dispersion in structured disordered media: from correlated Lévy flights to continuous time random walks, PRE, *Accepted*".

2010; Sokolov, 2012). Anomalous dispersion as manifested for example in heavy-tailed first-passage time distributions, and non-linear evolution of particle displacement variance has been ubiquitously observed across spatial and temporal scales ranging from natural and engineered porous media (Scher and Lax, 1973; Matheron and de Marsily, 1980; Berkowitz and Scher, 1997; Cushman and Ginn, 2000; Seymour et al., 2004; Berkowitz et al., 2006; Le Borgne et al., 2008a; Bijeljic et al., 2011b; Holzner et al., 2015), biological tissue (Caspi et al., 2000; Swanson et al., 2003; Barkai et al., 2012; Manzo et al., 2015), optical media (Barthelemy et al., 2008, 2010), turbulence (Shlesinger et al., 1987) and other physical systems (Klafter and Sokolov, 2005). Anomalous dispersive behaviors in disordered media have been modeled using stochastic approaches such as Lévy flights (Benson et al., 2000; Brockmann and Geisel, 2003), Lévy walks (Zaburdaev et al., 2015), continuous time random walk (CTRW) (Bouchaud and Georges, 1990; Metzler and Klafter, 2000b, 2004; Berkowitz et al., 2006; Sokolov, 2012), fractional Brownian motion and generalized Langevin equations (Cushman et al., 1994; Kou and Sunney Xie, 2004; Magdziarz et al., 2009), Brownian motion with non-stationary increments (Cushman et al., 2009).

Key questions we address in this paper refer to the origins of anomalous dispersion in terms of medium geometry, disorder properties and microscopic mass transfer mechanisms. The latter play a pivotal role for the way disorder is sampled, which determines the large scale particle motion and its ergodic and self-averaging properties. For diffusive motion in unstructured disordered media characterized by independent quenched random traps, for example, the nature of the (CTRW-type) average particle motion and self-averaging properties of sub-diffusion depend on the dimensionality of space (Bouchaud and Georges, 1990; Miyaguchi and Akimoto, 2011; Manzo et al., 2015; Dentz et al., 2016c; Akimoto et al., 2016; Russian et al., 2017) as a consequence of the diffusive disorder sampling. For biased, purely advective particle motion in unstructured media with random retardation or random conductivity, large scale transport follows (coupled) CTRW dynamics (Berkowitz and Scher, 1997; Le Borgne et al., 2008a; Dentz and Castro, 2009; Dentz and Bolster, 2010; Kang et al., 2011; Cvetkovic et al., 2014; Tyukhova et al., 2016; Comolli and Dentz, 2017). Advective-diffusive transport in stratified media, on the other hand, leads to average particle dynamics that can be described as a fractional Brownian motion (Matheron and de Marsily, 1980; Bouchaud et al., 1990; Zumofen et al., 1991; Dentz et al., 2008a), while purely advective motion in such media is the prototype of ballistic dispersion.

In this paper, we study the impact of diffusion on advective transport in structured disordered media. We consider media organized in channels ($d \geq 3$ dimensions) or strata ($d = 2$ dimensions) as illustrated in Figure 8.1. This type of stratified or fibrous medium geometries can be found in geological media (e.g., sedimentary formations), engineered materials (e.g., capillary bundles, filters) and biological media (e.g., neuronal fiber pathways). We consider advection-driven microscopic transport of a scalar $c(\mathbf{x}, t)$ given by the Fokker-Planck equa-

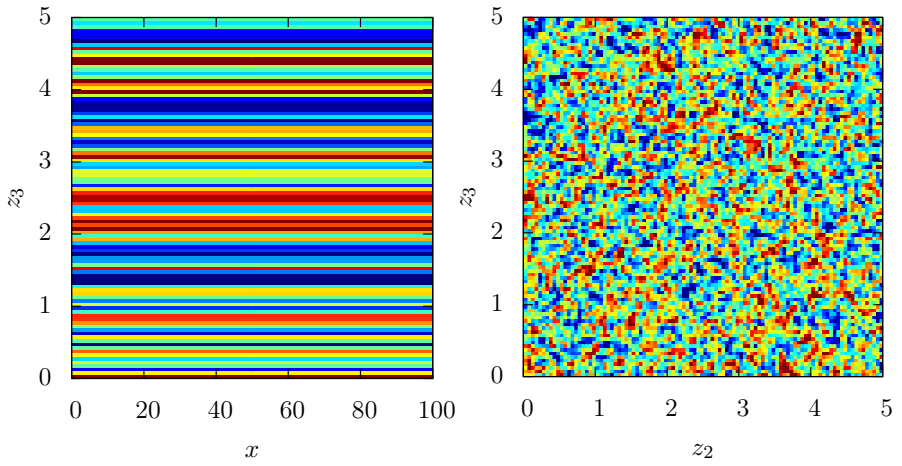

Figure 8.1: (Left) Lateral and (right) frontal view of a $d = 3$ dimensional disordered medium composed of channels of equal size ℓ. The colors represent different medium properties.

tion

$$\frac{\partial c(\mathbf{x},t)}{\partial t} + u(\mathbf{z})\frac{\partial c(\mathbf{x},t)}{\partial x} - \nabla_z^2 \mathcal{D}(\mathbf{z}) c(\mathbf{x},t) = 0, \tag{8.1}$$

where $u(\mathbf{z})$ and $\mathcal{D}(\mathbf{z})$ are drift and diffusion coefficients that vary randomly between the channels or strata. The coordinate vector is denoted by $\mathbf{x} = (x, \mathbf{z})^\top$ with $\mathbf{z} = (z_2, \ldots, z_d)^\top$. Diffusion along the channels is disregarded because it is subleading compared to the disorder impact on longitudinal motion. The Fokker-Planck equation (8.1) is equivalent to the Langevin equations

$$dx(t) = u[\mathbf{z}(t)]dt, \qquad d\mathbf{z}(t) = \sqrt{2D dt}\boldsymbol{\zeta}(t), \tag{8.2}$$

where $\boldsymbol{\zeta}(t)$ is a $d_w = (d-1)$-dimensional white noise, which models the transverse diffusive motion between the strata or fibers. Here and throughout the paper the noise average is indicated by angular brackets while disorder-averaged quantities are marked by an overbar. In the absence of transverse diffusion, this means without noise, the trajectory of a particle originating in $\mathbf{z}_0 = \mathbf{z}(t = 0)$ is simply $x(t) = u(\mathbf{z}_0)t$. Thus, the ensemble averaged particle density in flow direction is $c(x,t) = \overline{\delta[x - u(\mathbf{z}_0)t]}$, and more explicitly

$$c(x,t) = \frac{1}{t} p_u(x/t), \tag{8.3}$$

where $p_u(u)$ is the velocity distribution between the channels or strata. The first passage time distribution $f(t,x) = \overline{\delta[t - x/u(\mathbf{z}_0)]}$ is

$$f(t,x) = \frac{x}{t^2} p_u(x/t). \tag{8.4}$$

This type of models, sometimes including longitudinal diffusion, have been known as stochastic convective streamtube models in the literature (Dagan and Bressler, 1979; Ginn et al., 1995; Cirpka and Kitanidis, 2000). In this paper we focus on the decisive role of transverse diffusion for large scale transport.

We first consider the Matheron-de Marsily random velocity model (Matheron and de Marsily, 1980), which assigns a random velocity to each layer or channel such that $u(\mathbf{z}) = v(\mathbf{z})$ and $\mathcal{D}(\mathbf{z}) = D$, where D is the diffusion coefficient. For flow in porous media, Darcy's law (Bear, 1972) relates the flow velocity $v(\mathbf{z})$ to hydraulic conductivity $k(\mathbf{z})$. Secondly, we consider a random retardation model, which accounts for particle retention due to physical or chemical interaction with the medium such a fast linear adsorption reactions. The drift and diffusion coefficients in this model read as $u(\mathbf{z}) = v_0/\theta(\mathbf{z})$ and $\mathcal{D}(\mathbf{z}) = D/\theta(\mathbf{z})$, where v_0 is a constant flow velocity and $\theta(\mathbf{z})$ the random retardation coefficient. In the absence of diffusion, this means for $D = 0$, both disorder models give ballistic motion. Notice that the presence of transverse diffusion has a significant impact on longitudinal transport. Diffusion shortens the velocity correlation length, which would be otherwise infinite. Thus, it enables particles to explore the disorder. The efficiency of transverse diffusion as a sampling mechanism grows with increasing spatial dimension because the return probability to a previously visited channel decreases. In the following, we study these mechanisms and the consequences for average transport in the two disorder models in detail.

8.2 Matheron-de Marsily model

We start our analysis with the Langevin equation equivalent to (8.1) for the random velocity model, which reads as

$$dx(t) = v[\mathbf{z}(t)]dt, \qquad d\mathbf{z}(t) = \sqrt{2Ddt}\boldsymbol{\zeta}(t). \tag{8.5}$$

The random velocities $v \geq 0$ are distributed between channels according to $p_v(v)$. Note that particle motion in transverse direction describes a $d_w = (d-1)$ dimensional random walk such that $\langle \mathbf{z}(t) \rangle = \mathbf{0}$ and $\langle \mathbf{z}(t)^2 \rangle = 2d_w Dt$.

In order to quantify the average particle motion, we discretize (8.5) such that $\Delta\mathbf{z}(t)$ is oriented along the coordinate axes and $\|\Delta\mathbf{z}(t)\| = \ell$, which implies that particles change channels at each random walk step. The time required is equal to the first passage time τ across the distance ℓ by pure diffusion, which is approximated here by an exponential random variable τ with mean $\tau_D = \ell^2/d_w D$ (Delay et al., 2002; Dentz et al., 2012). The resulting time-domain random walk is given by

$$x_{n+1} = x_n + v_n\tau_n, \qquad t_{n+1} = t_n + \tau_n, \tag{8.6}$$

where we defined $v_n \equiv v(\mathbf{z}_n)$. In the transverse directions, particles perform a random walk on a d_w–dimensional hyperlattice according to $\mathbf{z}_{n+1} = \mathbf{z}_n + \ell\boldsymbol{\zeta}_n$, where the random vector $\boldsymbol{\zeta}$ has unit length and points into the direction of any of the transverse coordinate axes with equal probability. The numerical simulations

reported in the following are based on this time-domain random walk (TDRW) scheme. The TDRW has been used in the literature for the efficient solution of diffusion and advection-diffusion transport problems in heterogeneous porous and fractured media (Delay et al., 2005; Painter et al., 2008; Noetinger et al., 2016).

For the derivation of the large scale transport behaviors, we approximate the transition time τ_n for a single step by its mean τ_D. The space increments $\Delta x = v\tau_D$ in (8.8) thus are distributed according to

$$\psi_\Delta(x) = \frac{1}{\tau_D} p_v(x/\tau_D). \tag{8.7}$$

In order to understand the large scale transport behavior, it is important to note that the series of random velocities v_n and thus space increments Δx_n depends on the transverse random walk process. Thus subsequent v_n are in general not independent because particles may visit the same site repeatedly according to Polya's theorem. This notion is quantified by the average number S_n of distinct sites visited by a random walker on a d_w–dimensional hyperlattice (Vineyard, 1963; Bouchaud and Georges, 1990). For diffusion in $d_w < 2$ transverse dimensions, S_n increases as the volume swept by an ensemble of random walkers $\sim n^{d_w/2}$, for $d_w = 2$, S_n increases sublinearly as $\sim n/\ln(n)$, and for $d_w > 2$, S_n increases proportional to the number of random walk steps $\sim n$. This means that after n steps a particle has seen in average $\gamma_n = n/S_n$ times the same channel. Thus, the particle trajectory along the channels can be renormalized in terms of independent increments as (Bouchaud and Georges, 1990)

$$x_n = \gamma_n \sum_{i=1}^{S_n} v_i \tau_D. \tag{8.8}$$

This means, the impact of transverse noise on particle motion is accounted for through the random sampling of flow velocities and the renormalization with S_n, see also Ref. Russian et al. (2017).

8.2.1 Spatial density and moments

The coarse-grained longitudinal particle position at time t is given by $x(t) = x_{n_t}$, where $n_t = t/\tau_D$ denotes the average number of steps needed to reach t by the time process in (8.6). The average particle distribution is

$$c(x,t) = \overline{\delta(x - x_{n_t})}, \tag{8.9}$$

In the absence of transverse diffusion, the particle distribution is given by (8.3), this means it is obtained by a direct map from the velocity distribution. Here this is different. The particle position (8.8) is given by the sum of S_n independent increments. Thus, $c(x,t)$ is given by the S_{n_t}-fold convolution of the increment distribution (8.7). Note that the disorder average in (8.9) removes the dependence on the noise realizations (Russian et al., 2017).

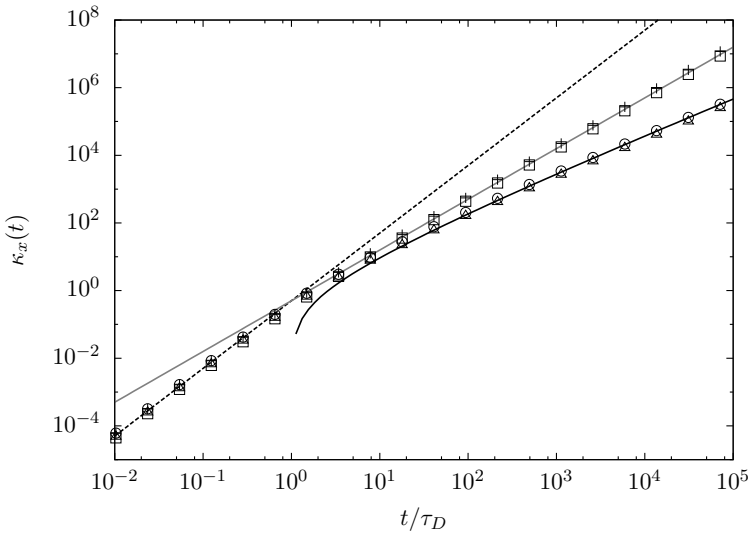

Figure 8.2: Displacement variance for $\delta = 1/2$ (crosses for $d = 2$ and circles for $d = 3$) and $\delta = 3/2$ (squares for $d = 2$ and triangles for $d = 3$). The solid lines represent the asymptotic scalings (8.13), the dashed line the ballistic behavior.

In the following, we study the spatial particle distributions and the displacement moments if they exist. Specifically, the mean displacement $\mu_x(t)$ and the displacement variance $\kappa_x(t)$ are defined by

$$\mu_x(t) = \overline{x_{n_t}} \tag{8.10a}$$

$$\kappa_x(t) = \overline{[x_{n_t} - \mu_x(t)]^2}. \tag{8.10b}$$

We first consider the case of velocity distributions characterized by finite velocity variance, then the case of heavy-tailed velocity distributions.

Finite velocity variance

For $S_{n_t} \gg 1$, this means for $t \gg \tau_D$, the central limit theorem implies that the particle distribution is given by the Gaussian distribution

$$c(x,t) = \frac{\exp\left[-\frac{(x-\overline{v}t)^2}{2\kappa_x(t)}\right]}{\sqrt{2\pi\kappa_x(t)}}. \tag{8.11}$$

The displacement variance $\kappa_x(t)$ obtained by using (8.8) in (8.10) as

$$\kappa_x(t) = \sigma_v^2 \tau_D^2 \frac{(t/\tau_D)^2}{S_{n_t}}. \tag{8.12}$$

Recall that the scaling of the number of distinct visited sites S_n depends on the transverse dimension d_w. This gives the following well-known long-time scalings for $\kappa_x(t)$ (Matheron and de Marsily, 1980; Zumofen et al., 1991)

$$\kappa_x(t) = \sigma_v^2 \tau_D t \begin{cases} \left(\frac{t}{\tau_D}\right)^{1/2} & d = 2 \\ \ln\left(\frac{t}{\tau_D}\right) & d = 3 \\ 1 & d > 3, \end{cases} \tag{8.13}$$

see Appendix I.

Figure 8.2 shows the temporal evolution of the displacement variance $\kappa_x(t)$. For times smaller than the diffusion time $\tau_D = \ell^2/d_w D$ the behavior is ballistic and $\kappa_x(t) = \sigma_v^2 t^2$. For times $t > \tau_D$, we observe the scalings (8.13). Note that the asymptotic scaling of the mean and the variance is not affected by the velocity distribution, but fully determined by correlation, this means by the fact that particles may return to the same channel or fiber. Here particles change velocities at constant rate τ_D^{-1}. This means particularly that low velocities do not persist and thus cannot lead to particle retention and phenomena of intermittency as observed in highly heterogeneous steady random velocity fields (Berkowitz and Scher, 1997; Fiori et al., 2007; Le Borgne et al., 2008a; Dentz et al., 2016a). The numerical simulations employ the truncated power-law velocity distribution

$$p_v(v) = \frac{\alpha}{v_c}\left(\frac{v}{v_c}\right)^{\delta-1} \tag{8.14}$$

with $v < v_c$ and $\delta > 0$. The smaller δ, the higher is the probability of encountering low velocities. The mean and the variance of (8.14) are given by $\overline{v} = \delta v_c/(\delta+1)$ and $\sigma_v^2 = \delta v_c^2/[(\delta+2)(\delta+1)^2]$.

Heavy-tailed velocity distribution

If the velocity distribution is heavy-tailed, this means $p_v(v) \sim v^{-1-\alpha}$ with $0 < \alpha < 2$, so is the distribution $\psi_\Delta(x)$ of space increments $\Delta x = v\tau_D$ in (8.8), which scale as $\psi_\Delta(x) \sim x^{-1-\alpha}$. Thus, the resulting average particle motion constitutes a Lévy flight. However, unlike in classical Lévy flights, subsequent spatial increments Δx_n are not independent due to the finite probability to return to the same velocity. Thus, we call the average particle motion here a correlated Lévy flight.

The renormalization of the particle position according to (8.8) renders x_{n_t} a sum of S_{n_t} independent random increments. Thus, the generalized central limit theorem implies that $c(x,t)$ given by (8.9) converges to a one-sided stable density for $0 < \alpha < 1$ and an extreme stable density for $1 < \alpha < 2$ (Uchaikin and Zolotarev, 1999). This means that

$$c(x,t) = \begin{cases} g_\alpha[x/\eta(t)]/\eta(t) & 0 < \alpha < 1 \\ g_\alpha[(x-\overline{v}t)/\eta(t)]/\eta(t) & 1 < \alpha < 2, \end{cases} \tag{8.15}$$

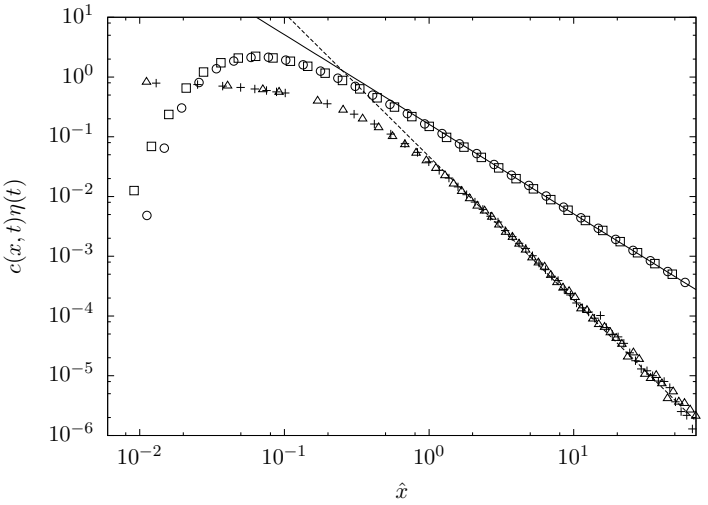

Figure 8.3: Particle density for (squares and circles) $\alpha = 1/2$ and (triangles and crosses) $\alpha = 1.4$ (circles) in $d = 2$ dimensions at times $t = 20\tau_D$ and $100\tau_D$ rescaled by $\eta(t)$ versus $\hat{x} = x/\eta(t)$ for $\alpha < 1$ and $\hat{x} = (x - \overline{v}t)/\eta(t)$ for $1 < \alpha < 2$. The dashed and solid lines show the asymptotic scalings as $x^{-1-\alpha}$. The simulations use the velocity distribution (8.18).

where we defined the scaling variable

$$\eta(t) = \gamma_{n_t} S_{n_t}^{1/\alpha}. \tag{8.16}$$

The function $g_\alpha(x)$ is a stable distribution of order α, which scales as $g_\alpha(x) \propto x^{-1-\alpha}$ for $x \gg 1$. The scaling variable $\eta(t)$ behaves as

$$\eta(t) = \left(\frac{t}{\tau_D}\right)^{1/\alpha} \begin{cases} \left(\frac{t}{\tau_D}\right)^{\frac{\alpha-1}{2\alpha}} & d = 2 \\ \ln\left(\frac{t}{\tau_D}\right)^{\frac{\alpha-1}{\alpha}} & d = 3 \\ 1 & d > 3. \end{cases} \tag{8.17}$$

For $0 < \alpha < 1$, the maximum of the particle distribution moves superlinearly, its velocity increases with increasing dimension. This behavior can be explained by the persistence of low velocities in $d < 4$.

Figure 8.3 shows the density profiles obtained from numerical simulations and the analytical scalings (8.15). The numerical simulations use the Pareto distribution

$$p_v(v) = \frac{\alpha}{v_c}\left(\frac{v}{v_c}\right)^{-1-\alpha}, \tag{8.18}$$

with $v > v_c$ and $0 < \alpha < 2$.

8.2.2 First passage times

We now consider the distribution of first passage times $t(x) = \min(t|x_{n_t} \geq x)$ at a plane at a longitudinal position x, which is defined by

$$f(t,x) = \overline{\delta[t - t(x)]}. \tag{8.19}$$

In the TDRW framework employed here, $t(x) = n_x \tau_D$, where $n_x = \max(n|x_n \leq x)$. Note that we set the transition time $\tau = \tau_D$ for the analytical derivations. Thus, we can write $f(t,x)$ as

$$f(t,x) = \sum_{n=0}^{\infty} \overline{\delta(t - n\tau_D)\delta_{n,n_x}}. \tag{8.20}$$

Furthermore, mass conservation gives the following relation between $f(t,x)$ and $c(x,t)$,

$$\int_0^t dt' f(t',x) = \int_x^{\infty} dx' c(x',t). \tag{8.21}$$

This relationship expresses that the number of particles that have passed the position x at time t is equal to the number of particles that are to the right of the position x. It implies that

$$f(t,x) = \frac{\partial}{\partial t} \int_x^{\infty} dx' c(x',t). \tag{8.22}$$

The mean first passage time $\mu_t(x)$ and its variance $\kappa_t(x)$ are defined by

$$\mu_t(x) = \int_0^{\infty} dt t f(t,x) = \tau_D \overline{n_x} \tag{8.23}$$

$$\kappa_t(x) = \int_0^{\infty} dt [t - \mu_t(x)]^2 f(t,x) = \tau_D^2 \left(\overline{n_x^2} - \overline{n_x}^2 \right). \tag{8.24}$$

In the following, we discuss the first-passage time distribution for velocity distributions with finite variance and heavy-tailed velocity distributions.

Finite velocity variance

In the case of finite velocity variance, the particle distribution $c(x,t)$ is given by (8.11). Thus, Eq. (8.22) implies for $f(t,x)$ the inverse Gaussian-type first passage time distributions

$$f(t,x) = \frac{[\kappa_x(t)\overline{v} + \mathcal{D}_x(t)(x - \overline{v}t)] \exp\left[-\frac{(x-\overline{v}t)^2}{2\kappa_x(t)}\right]}{\sqrt{2\pi\kappa_x(t)^3}}, \tag{8.25}$$

where the apparent dispersion coefficient $\mathcal{D}_x(t)$ is defined by

$$\mathcal{D}_x(t) = \frac{1}{2}\frac{d\kappa_x(t)}{dt}. \tag{8.26}$$

The mean first passage time is given by $\mu_t(x) = x/\overline{v}$. For the variance of the first passage time we obtain

$$\kappa_t(x) \propto \frac{\sigma_v^2 \tau_D}{\overline{v}^2}\frac{x}{\overline{v}} \begin{cases} \left(\frac{x}{\overline{v}\tau_D}\right)^{1/2} & d = 2 \\ \ln\left(\frac{x}{\overline{v}\tau_D}\right) & d = 3 \\ 1 & d > 3, \end{cases} \tag{8.27}$$

see Appendix I.

Figure 8.4 shows the full temporal behavior of the with first-passage time distribution obtained numerical simulations for different disorder scenarios in $d = 2$ dimensions. We make use of the velocity distribution (8.14). We observe that the distribution of first passage times broadens for decreasing δ because $\sigma_v^2/\overline{v}^2$ increases with decreasing δ as $1/(\delta + 2)$.

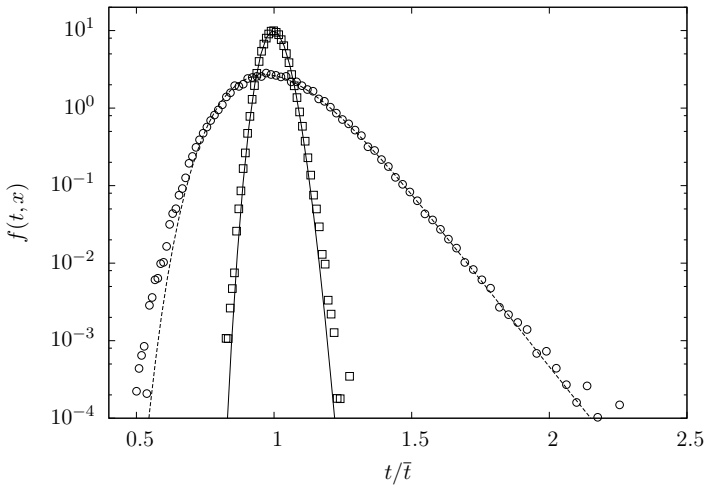

Figure 8.4: First passage time distributions for $\delta = 1/2$ (circles) and $\delta = 1.4$ (squares) in (8.14) for $d = 2$ dimensions at the control plane $x_c = 100\ell$ and $x_c = 5000\ell$, respectively. The dashed and the solid lines represent the analytical solution (8.25).

Heavy-tailed velocity distribution

We first consider the case $0 < \alpha < 1$. Using expression (8.15) in relation (8.22) between the first passage time and particle distributions, we find

$$f(t,x) = \frac{x}{\eta(t)^2}\frac{d\eta(t)}{dt}F_\alpha[\eta(t)/x], \tag{8.28}$$

where we defined $F_\alpha(y) = g_\alpha(1/y)$; $g_\alpha(x)$ is a one-sided stable density. For $\alpha = 1/2$, $g_{1/2}(x)$ is a Lévy distribution. Thus we obtain the exact expression

$$f(t,x) = \frac{\eta(t)^{-1/2}}{x^{1/2}}\frac{d\eta(t)}{dt}\frac{a\exp\left[-a^2\eta(t)/2x\right]}{\sqrt{2\pi}}, \tag{8.29}$$

with a a constant. For general $0 < \alpha < 1$, $F_\alpha(y)$ behaves at large y as a stretched exponential (Uchaikin and Zolotarev, 1999; Koren et al., 2007),

$$F_\alpha(y) \sim \frac{(y\alpha)^{\frac{1-\alpha/2}{1-\alpha}}\exp\left[-c_\alpha^2(1-\alpha)(y\alpha)^{\frac{\alpha}{1-\alpha}}\right]}{\sqrt{2\pi(1-\alpha)\alpha}} \tag{8.30}$$

with c_α a constant that depends on the details of the heavy-tailed velocity distribution. The full behavior of $f(t,x)$ for $\alpha = 1/2$ is shown in Figure 8.5 for $d < 3$ and $d = 3$ dimensions, which is in agreement with the analytical prediction (8.29). The behavior of the mean first passage time $\mu_t(x)$ with distance

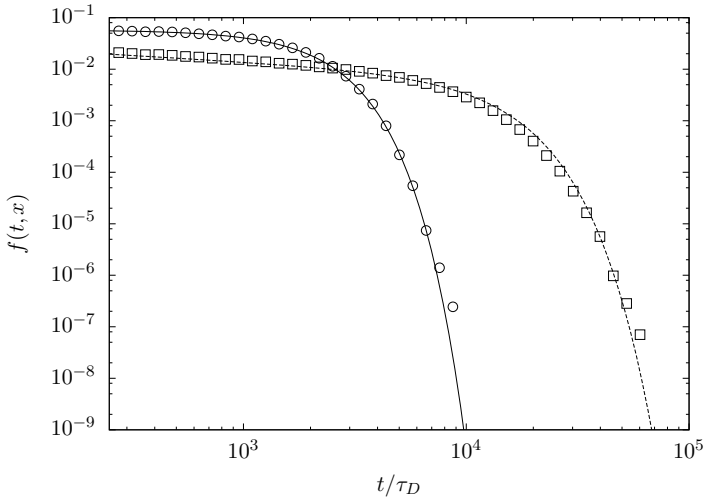

Figure 8.5: First passage time distributions at the control plane $x = 10^4$ for $\alpha = 1/2$ in $d = 2$ (squares) and $d = 3$ (circles). The solid and dashed lines represent Eq. (8.29) for $d = 2$ and $d = 3$ dimensions.

depends on the spatial dimension. Inserting expression (8.28) in (8.23) and using (8.17), we obtain the following scaling behaviors for the mean first passage time with distance,

$$\mu_t(x) \propto \begin{cases} x^{2\alpha/(1+\alpha)} & d = 2 \\ x^{\alpha} \ln(x)^{1-\alpha} & d = 3 \\ x^{\alpha} & d > 3. \end{cases} \tag{8.31}$$

The mean first passage time evolves sublinearly with distance, but faster with decreasing dimension because of increasing correlation of subsequent (low) velocities. Note that the mean first passage time is related to the harmonic mean velocity, which is dominated by low velocities. The scaling of the variance $\kappa_t(x)$ of first passage times is obtained analogously by inserting (8.28) in (8.24) and using (8.17),

$$\kappa_t(x) \propto \mu_t(x)^2 \tag{8.32}$$

For $1 < \alpha < 2$ we use expression (8.15) in (8.22) in order to obtain

$$f(t,x) = \frac{\overline{v}\eta(t) + (x - \overline{v}t)\frac{d\eta(t)}{dt}}{\eta(t)^2} g_\alpha \left[\frac{x - \overline{v}t}{\eta(t)} \right], \tag{8.33}$$

where $g_\alpha(x)$ is an extreme stable density. The long-time behavior of $f(t,x)$ is obtained by noting first that $t/\eta(t)$ increases with time because $\eta(t)$ evolves sublinearly for $1 < \alpha < 2$. Thus, the asymptotic behavior of $f(t,x)$ is obtained from the behavior of $g_\alpha(x)$ for $x \to -\infty$, which is given by (Uchaikin and Zolotarev, 1999)

$$g_\alpha(x) \sim \frac{\left(\frac{|x|}{\alpha}\right)^{\frac{1-\alpha/2}{\alpha-1}} \exp\left[-c_\alpha^2(\alpha-1)\left(\frac{|x|}{\alpha}\right)^{\frac{\alpha}{\alpha-1}}\right]}{\sqrt{2\pi(1-\alpha)\alpha}}. \tag{8.34}$$

Thus, $f(t,x)$ behaves at long times as a stretched exponential and all first passage time moments exist. In this case and in general for velocity distributions with $\overline{v} < \infty$, the mean first passage time is given by $\mu_t(x) = x/\overline{v}$. The variance of the first passage times for $1 < \alpha < 2$ scales as

$$\kappa_t(x) \propto \begin{cases} x^{(5-\alpha)/2} & d = 2 \\ x^{3-\alpha} \ln(x)^{\alpha-1} & d = 3 \\ x^{3-\alpha} & d > 3, \end{cases} \tag{8.35}$$

see Appendix I.

The behavior of the mean first passage time and the analytical scalings are shown in Figure 8.6 for $d = 2$ and $d = 3$ dimensions for $\alpha = 1/2$ and $\alpha = 1.4$. As discussed above, for $0 < \alpha < 1$, the mean first passage time at a control plane is larger in $d = 2$ than in $d = 3$ as a consequence of stronger persistence of low velocities.

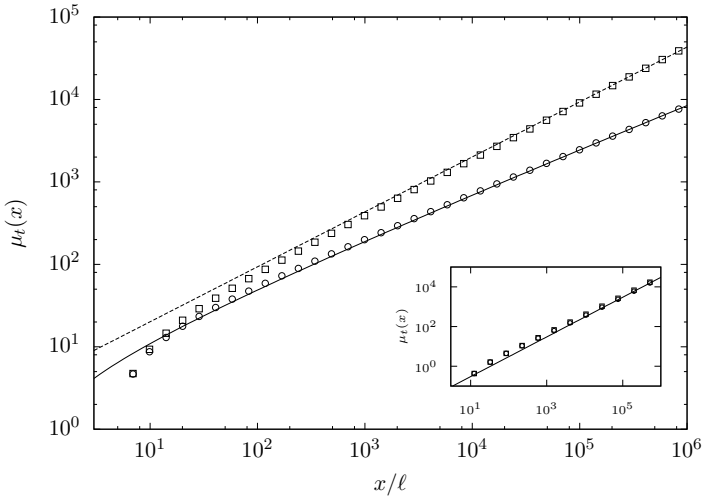

Figure 8.6: (Main) Mean first passage time for $\alpha = 1/2$ for $d = 2$ (squares) and $d = 3$ (circles). (Inset) Mean first passage time for $\alpha = 1.4$ for $d = 2$ and $d = 3$. Lines represent the asymptotic scalings (8.31).

8.3 Random retardation model

We contrast the behaviors observed in the previous section to dispersion under spatially random retardation. Here particle motion is ruled by the Langevin equation

$$dx(t) = \frac{v_0 dt}{\theta[\mathbf{z}(t)]}, \qquad d\mathbf{z}(t) = \sqrt{\frac{2Ddt}{\theta[\mathbf{z}(t)]}}\boldsymbol{\zeta}(t), \tag{8.36}$$

where the retardation factor $\theta(\mathbf{z})$ is distributed according to $p_\theta(\theta)$. Note that unlike in the Matheron-de Marsily model, disorder here acts also on diffusion in transverse direction, which affects disorder sampling. We define the operational time through $dt(s) = \theta[\mathbf{z}(s)]ds$ and transform $t \to s$ in (8.36) to obtain

$$dx(s) = v_0 ds, \qquad d\mathbf{z}(s) = \sqrt{2Dds}\boldsymbol{\zeta}(s). \tag{8.37}$$

This subordinated process describes a biased Brownian motion. In order to determine the large scale particle motion, we coarse grain (8.37) so that each step corresponds to a change in θ, which occurs whenever a particle diffuses to a contiguous channel, this means for $\|\Delta\mathbf{z}(s)\| = \ell$. The (operational) time σ needed for this transition is given by the diffusive first passage time, which is exponentially distributed with mean τ_D. Diffusion depends on the local retardation coefficient. Therefore, the coarse grained equations read as

$$x_{n+1} = x_n + v_0\sigma_n \qquad t_{n+1} = t_n + \theta_n\sigma_n, \tag{8.38}$$

where we set $\theta_n \equiv \theta(\mathbf{z}_n)$. The numerical simulations reported in the following are based on this TDRW. For the derivations of the average dispersion behavior, in the following, we approximate the operational time σ_n needed for single step by its mean τ_D. Thus, the transition length for a single step in this approximation is constant and equal to $\Delta x = v_0\tau_D$. The transition time is $\tau = \theta\tau_D$, which is distributed according to

$$\psi(t) = \frac{1}{\tau_D} p_\theta(t/\tau_D). \tag{8.39}$$

As above, transverse particle motion describes a random walk on a d_w–dimensional hyperlattice, and, as a consequence, the $\{\theta_n\}$ and thus the transition times $\{\tau_n\}$ form correlated random series. Unlike in the Matheron-de Marsily model, here the disorder affects the temporal increments. The particle time t_n can be renormalized into families of independent increments as

$$t_n = \gamma_n \sum_{i=1}^{S_n} \theta_i \tau_D. \tag{8.40}$$

Note the duality of the particle motions given by (8.6)–(8.8) in the Matheron-de Marsily model and (8.38)–(8.40) here.

8.3.1 First passage times

The first passage time distribution here is given by

$$f(t,x) = \sum_{n=0}^{\infty} \overline{\delta(t - t_{n_x})}, \tag{8.41}$$

where $n_x = x/v_0\tau_D$. The particle time t_{n_x} is according to (8.40) the sum of independent random variables. Note the duality with expression (8.9) for the particle density in the Matheron-de Marsily model.

Finite disorder variance

We first consider the case of finite disorder variance. Exploiting the duality between (8.41) and (8.9), we obtain from (8.11) that $f(t,x)$ follows at large $x \gg v_0\tau_D$ the Gaussian distribution

$$f(t,x) = \frac{\exp\left[-\frac{(t - x\overline{\theta}/v_0)^2}{2\kappa_t(x)}\right]}{\sqrt{2\pi\kappa_x(t)}}, \tag{8.42}$$

where the mean first passage time is $x\overline{\theta}/v_0$ and the variance of the first passage time is

$$\kappa_t(x) = \sigma_\theta^2 \tau_D \frac{x}{v_0} \begin{cases} \left(\frac{x}{v_0\tau_D}\right)^{1/2} & d = 2 \\ \ln\left(\frac{x}{v_0\tau_D}\right) & d = 3 \\ 1 & d > 3. \end{cases} \tag{8.43}$$

For dimensions $d < 4$, the variance of the first-passage time scales superdiffusively with distance.

Heavy-tailed disorder distribution

We now consider heavy-tailed distributions of the retardation coefficient which for $\theta \gg 1$ behave as $p_\theta(\theta) \sim \theta^{-1-\beta}$ with $0 < \beta < 2$. The generalized central limit theorem indicates that the first passage time distribution converges towards a stable law for $S_n \gg 1$ because (8.40) is the sum of independent increments. Thus, we obtain in analogy to the particle distributions (8.15) in the random velocity model

$$f(t,x) = \begin{cases} g_\beta[t/\hat{\eta}(x)]/\hat{\eta}(x) & 0 < \beta < 1 \\ g_\beta[(t - x\overline{\theta}/v)/\hat{\eta}(x)]/\hat{\eta}(x) & 1 < \beta < 2. \end{cases} \tag{8.44}$$

For $0 < \beta < 1$, $g_\beta(t)$ is a one-sided stable density, for $1 < \beta < 2$ it is an extreme stable density (Uchaikin and Zolotarev, 1999). The scaling functions behaves as $g_\beta(t) \propto t^{-1-\beta}$ at times $t \gg \tau_D$. The scaling variable $\hat{\eta}(x)$ is given by $\hat{\eta}(x) = \eta(x/v_0\tau_D)$, where $\eta(t)$ is defined by (8.16).

The power-law tailing is not affected by the correlation of transition times, which impacts, however, the scaling of the maximum $f_m(x)$ of the first-passage time distribution according to $f_m(x) \propto 1/\hat{\eta}(x)$. For $\alpha < 1$ the time $\tau_m(x)$ of maximum arrival scales as $\tau_m(x) \propto \hat{\eta}(x)$. This is illustrated in Figure 8.7, which compares the first passage time distributions obtained from numerical random walk simulations with the derived scalings. Note that Figure 8.7 corresponds to Figure 8.3 for the particle distribution. The numerical time-domain random walk simulations are performed using the following Pareto distribution for the retardation coefficient θ

$$p_\theta(\theta) = \frac{\beta}{\theta_0}\left(\frac{\theta}{\theta_0}\right)^{-1-\beta} \tag{8.45}$$

with $\theta > \theta_0$.

8.3.2 Spatial density and moments

The average particle density is given by

$$c(\mathbf{x},t) = \sum_{n=0}^{\infty} \overline{\langle \delta(x - x_n)\delta(\mathbf{z} - \mathbf{z}_n)\delta_{n,n_t}\rangle}. \tag{8.46}$$

Transverse particle motion is equivalent to an unbiased random walk in the presence of quenched random traps (Bouchaud and Georges, 1990; Russian et al., 2017). Thus, the mean displacement in transverse direction is $\overline{\mathbf{z}(t)} = \mathbf{0}$ and the mean squared displacement is $\kappa_z(t) = \overline{\mathbf{z}(t)^2} = \ell^2\overline{n_t}$. The longitudinal particle

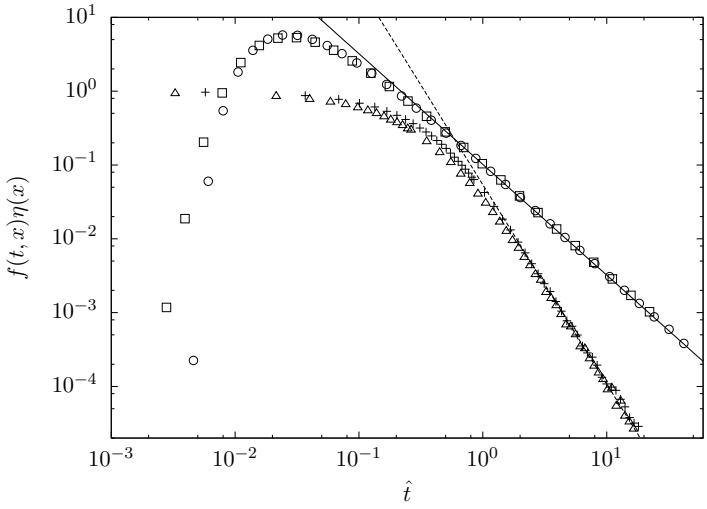

Figure 8.7: First passage time distributions for $\beta = 1/2$ (circles and squares) and $\beta = 1.7$ (triangles and crosses) in $d = 3$ dimensions at the control plane $x_c = 10^2\ell$ and $5 \cdot 10^2\ell$ rescaled by $\eta(x)$ versus $\hat{t} = t/\eta(x)$ for $\beta < 1$ and $\hat{t} = (t - \overline{\theta}x/v)/\eta(x)$ for $1 < \beta < 2$. The dashed and solid lines represent the scaling $t^{-1-\beta}$ for $\beta = 1/2$ and $\beta = 1.7$, respectively.

particle position is here given by $x(t) = n_t v_0 \tau_D$. Note that we set the operational time $\sigma = \tau_D$ for the analytical derivations. Thus, the particle density is

$$c(x,t) = \sum_{n=0}^{\infty} \overline{\delta(x - nv_0\tau_D)\delta_{n,n_t}}, \tag{8.47}$$

which is of the same form as the first passage time distribution (8.20) in the Matheron-de Marsily model. Thus, in analogy with (8.22), mass conservation gives the following relation between the first passage time distribution and the particle distribution

$$c(x,t) = \frac{\partial}{\partial x} \int_t^{\infty} dt' f(t',x). \tag{8.48}$$

The mean displacement and the displacement variance are given by

$$\mu_x(t) = \int dx x c(x,t) = v_0 \tau_D \overline{n_t} \tag{8.49}$$

$$\kappa_x(t) = \int dx [x - \mu_x(t)]^2 c(x,t) = v_0^2 \tau_D^2 (\overline{n_t^2} - \overline{n_t}^2). \tag{8.50}$$

Note that the mean displacement in longitudinal direction is proportional to the transverse mean squared displacement $\mu_x(t) \propto \kappa_z(t)$.

Finite disorder variance

For $\overline{\theta^2} < \infty$, the transverse mean squared displacement evolves diffusively as $\kappa_z(t) = 2d_w Dt/\overline{\theta}$ (Russian et al., 2017), this means transverse disorder sampling is effectively diffusive as for the Matheron-de Marsily model. As a result, the longitudinal mean displacement evolves linearly with time as $\mu_x(t) = v_0 t/\overline{\theta}$, and the displacement variance behaves as

$$\kappa_x(t) \propto v_0^2 \tau_D \frac{\sigma_\theta^2}{\overline{\theta}^2} \frac{t}{\overline{\theta}} \begin{cases} \left(\frac{t}{\overline{\theta}\tau_D}\right)^{1/2} & d = 2 \\ \ln\left(\frac{t}{\overline{\theta}\tau_D}\right) & d = 3 \\ 1 & d > 3, \end{cases} \tag{8.51}$$

see Appendix I. These expressions correspond to (8.27) for the moments of the first passage time in the Matheron-de Marsily model. Using the duality between the Matheron-de Marsily model and the random retardation model, we see immediately from (8.25) that the spatial particle distribution is given by

$$c(x,t) = \frac{\left[\kappa_t(x)\frac{\overline{\theta}}{v_0} + \mathcal{D}_t(x)\left(t - \frac{x\overline{\theta}}{v_0}\right)\right] \exp\left[-\frac{\left(t - \frac{x\overline{\theta}}{v_0}\right)^2}{2\kappa_t(x)}\right]}{\sqrt{2\pi\kappa_t(x)^3}}, \tag{8.52}$$

where $2\mathcal{D}_t(x) = d\kappa_t(x)/dx$.

Heavy-tailed disorder distribution

Transverse particle motion here is subdiffusive (Russian et al., 2017), which affects the efficiency of disorder sampling across strata or channels, which in turn affects the longitudinal particle motion. For $0 < \beta < 1$, we obtain from (8.48) in analogy with (8.28)

$$c(x,t) = \frac{t}{\hat{\eta}(x)^2} \frac{d\hat{\eta}(x)}{dx} F_\beta[\hat{\eta}(x)/t], \tag{8.53}$$

where $F_\beta(y) = g_\beta(1/y)$. It behaves at large y as the stretched exponential (8.29). Along the same lines, we obtain for $1 < \beta < 2$

$$c(x,t) = \frac{\frac{\overline{\theta}\hat{\eta}(x)}{v_0} + \left(t - \frac{x\overline{\theta}}{v_0}\right)\frac{d\hat{\eta}(x)}{dx}}{\hat{\eta}(x)^2} g_\beta\left[\frac{t - \frac{x\overline{\theta}}{v_0}}{\eta(t)}\right], \tag{8.54}$$

with $g_\beta(x)$ an extreme stable density. The behavior of $c(x,t)$ at large distances corresponds to the behavior of $g_\beta(x)$ as $x \to -\infty$, which is given by the stretched exponential (8.34).

For $d \leq 3$ dimensions, particle motion is CTRW-like, characterized by correlation in subsequent time increments, which is quantified by the renormalization of the particle time according to (8.40) and encoded in (8.53) and (8.54) by

$\hat{\eta}(x)$. For $0 < \beta < 1$, we obtain by inserting the scaling form (8.53) into definitions (8.49) and (8.50) for the displacement mean and variance the quasi-ballistic scaling behaviors

$$\kappa_x(t) \propto \mu_x(t)^2 \propto \begin{cases} t^{4\beta/(1+\beta)} & d = 2 \\ t^{2\beta} \ln(t)^{2-2\beta} & d = 3. \end{cases} \tag{8.55}$$

This behavior is caused by the long residence times in individual channels or strata, which on one hand slows the mean displacement down and on the other hand leads to the quasi-ballistic scaling.

For $1 < \beta < 2$, the retardation in individual channels is weaker and the mean displacement is given by $\mu_x(t) \propto v_0 t/\overline{\theta}$ for all dimensions, while the variance scales as

$$\kappa_x(t) \propto \begin{cases} t^{(5-\beta)/2} & d = 2 \\ t^{3-\beta} \ln(t)^{\beta-1} & d = 3, \end{cases} \tag{8.56}$$

see Appendix I. While dispersion in the absence of diffusion is ballistic, the observed behaviors here are entirely due to the diffusive disorder sampling across channels of equal retardation properties. Particle motion is only CTRW-like because the quenched nature of the underlying disorder is inherited through the correlation of subsequent θ_n.

For $d > 3$, particles describe a CTRW in longitudinal direction because of the efficient diffusive transverse sampling through which the disorder experienced by the particles assumes an annealed character. Thus, displacement mean and variance show the scaling known from uncorrelated CTRW (Shlesinger, 1974; Margolin and Berkowitz, 2002), this means

$$\mu_x(t) \propto t^{\beta} \qquad \kappa_x(t) \propto t^{2\beta} \tag{8.57}$$

for $0 < \beta < 1$ and

$$\mu_x(t) \propto t \qquad \kappa_x(t) \propto t^{3-\beta} \tag{8.58}$$

for $1 < \beta < 2$.

Figures 8.8 and 8.9 show the temporal evolution of the mean and the variance of particle displacements in $d = 2$ and $d = 3$ dimensions for power-law distributed retardation coefficients with exponents $\beta = 1/2$ and $\beta = 1.7$, respectively. We observe ballistic behavior at times shorter than τ_D, which is the characteristic time for the onset of transverse disorder sampling. For times larger than τ_D, the moments evolve towards their respective asymptotic scalings, which depend on the heterogeneity and the dimensionality of the medium.

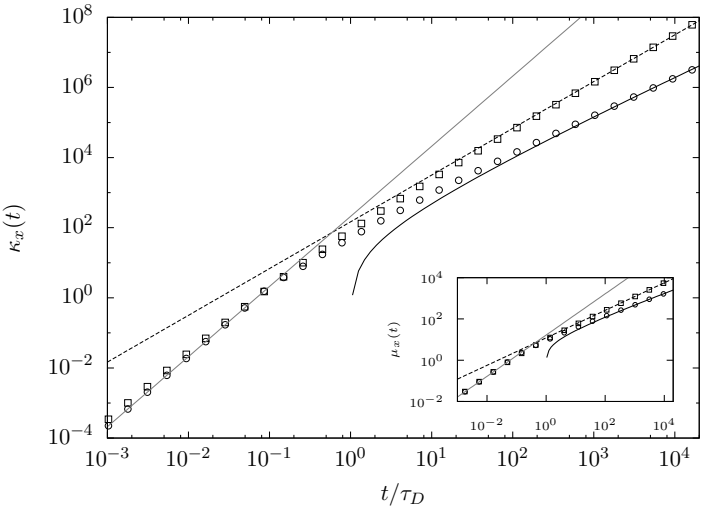

Figure 8.8: (Main) Longitudinal variance of particle displacements for $\beta = 1/2$ and for $d = 2$ (squares) and $d = 3$ (circles). Black lines are analytical scalings, the gray line is ballistic. (Inset) Mean position, black lines denote the analytical scalings, the gray line linear scaling.

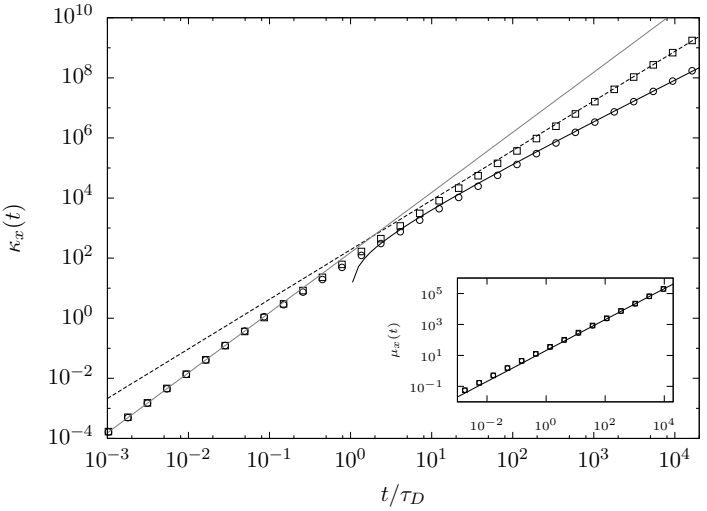

Figure 8.9: (Main) Longitudinal variance of particle displacements for $\beta = 1.7$ and for $d = 2$ (squares) and $d = 3$ (circles). Black lines are analytical scalings, the gray line is ballistic. (Inset) Mean position, the gray line denotes linear scaling.

8.4 Conclusions

In conclusion we have analyzed the impact of diffusion on anomalous transport in stratified and fibrous disordered media, for which transport is otherwise ballistic. We have shown how diffusive disorder sampling changes the nature of average transport depending on the microscopic transport mechanisms, disorder distribution, and dimensionality of space. Transverse diffusion acts differently on longitudinal transport properties and on the first passage time distributions depending on the disorder model. There is complete duality in spatial and temporal features between the random velocity model and the random retardation model. The quenched nature of the underlying disorder is inherited by the average particle motion in $d \leq 3$ dimensions, for which we discover correlated Lévy flights in the case of the Matheron-de Marsily model with heavy tailed velocities and correlated biased continuous time random walks for the random retardation model with heavy tailed retardation distribution. For $d > 4$ the disorder particles experience assumes an annealed character, which leads to Lévy flight dynamics in the random velocity and biased CTRW behavior in the random retardation model. These results shed light on the pivotal role of diffusion for the prediction and interpretation of anomalous transport behaviors and signal transmission in disordered structures.

9

Summary and conclusions

This section concludes the thesis by summarizing the main results. We first provide a general summary, in which we recall the key messages of the thesis. Next, we proceed to the detailed summaries and conclusions for each chapter. Finally, we give an outlook on further research challenges that we consider of significant interest.

Summary and general conclusions

We have studied non-Fickian transport in heterogeneous porous media by investigating the mechanisms that lead to its occurrence and by quantifying their impact on transport features. A general framework that allows to describe and predict anomalous transport behavior has been proposed. Remarkably, the parameterization of the proposed models does not require previous knowledge of transport features, as it is carried out in terms of medium and flow attributes only.

Throughout the thesis, we have focused our attention on the heterogeneity of the advective field, which is known to play a pivotal role on transport's behavior. Its impact has been quantified through the study of different disorder scenarios, which include random velocity fields as well as Darcian fields obtained through the solution of flow in random hydraulic conductivity fields. Alongside with heterogeneous advection, we have considered different processes that induce anomalous transport. These include solute trapping, spatial correlation of the advective field and retardation processes. In addition, we have studied the role of diffusion as a process that promotes the sampling of the heterogeneity, thus mitigating the effect of spatial correlation. An important improvement in the understanding of non-Fickian transport refers to the investigation of different injection conditions, since we have shown that transport stationarity depends on the nature of solute injection. Each chapter of this thesis is dedicated to the study of different processes, whose impact has been evaluated in combination

with the heterogeneity of the advective field, which is the common denominator of all chapters.

We have shown that the time domain random walk and the more general continuous time random walk are valid frameworks for the upscaling of transport. Their effectiveness lies in their capability to capture non-Fickian features such as the non-linear growth of the variance of particles displacements, the non-Gaussian spatial profiles and the heavy-tailed breakthrough curves. Remarkably, within this framework it is possible to account for the different processes that give rise to anomalous transport in a systematic way. This means that it is possible to parameterize the TDRW and the CTRW, i.e. the joint PDF of transition times and lengths, in terms of transport-independent quantities, which are related to flow and to the geometric and hydraulic properties of the porous medium. Note that no detailed knowledge of the flow field and of the geometry is required. In contrast, the parameterization is carried out through average quantities or their distributions. In fact, in the CTRW framework the distribution of transition times is mapped onto the steady-state distribution of s-Lagrangian velocity, which is obtained from the Eulerian velocity magnitude PDF through flux-weighting. In Chapters 5-7 we have shown that in non-stationary conditions, the knowledge of the velocity PDF at the injection is also required. The transition length distribution is parameterized in terms of the characteristic length scale, if it exists. In the CTRW framework, the latter is given by the distance at which velocities de-correlate, as we showed in Chapters 3, 5, 6 and 7. In some cases, e.g. for stratified media (see Chapter 8), the characteristic length scale emerges directly from the geometric properties of the medium. If a characteristic length scale does not exist and we are in presence of strongly-correlated advective fields as those described in Chapter 4, we have to use a general CTRW model in which the transition lengths are distributed and their statistics is mapped onto a distributions of correlation scales. The PDF of transition times is generally parameterized in terms of the velocity distribution. It also accounts for trapping processes, as we showed in Chapter 3 through the distribution of return times and for diffusion through the distribution of crossing times (see Chapter 8). In principle, although the task is often non-trivial, these parameters can be measured or inferred from laboratory or field experiments.

Specific conclusions

In the following, we resume the main conclusions of each chapter.

- In Chapter 3, we have shown that the TDRW framework accounts for mass transfer processes through a trapping rate and a distribution trapping times that we parameterize in terms of the return times by diffusion in semi-infinite media. We have identified two time scales characterizing the trapping process, which define regimes of distinct transport behaviors. In the early time regime, no trapping event occurs and transport is ruled by the heterogeneity of the advective field. In the pre-asymptotic regime, as

some of the particles get trapped, a chromatographic stretching of the solute plume occurs. This stretching is due to increasing distance between trapped and mobile particles and it reflects itself in the super-linear growth of the variance of particles displacements. Finally, in the asymptotic regimes, particles have spent more time in the immobile than in the mobile phase. Therefore, transport behavior in the long time limit is governed by the trapping process.

- In Chapter 4, we have studied anomalous transport induce by heterogeneous advection and correlation. We have proposed a coupled CTRW approach, in which the heterogeneity of the flow field is mapped onto a distribution of velocities and the spatial correlation is accounted for through a distribution of transition lengths. Although in some cases it is not possible to decouple the transition PDF, in general the stronger process governs the behavior of the displacement variance. We have shown that different mechanisms can lead to the same anomalous behavior of the variance of particle displacements. Thus, in order to discriminate the mechanisms underlying non-Fickian transport it is necessary to also consider the spatial density and the breakthrough curves.

- In Chapter 5 we have derived the relationships between flow and transport attributes and we have quantified the impact of different injection conditions on transport. We have found the relationship between Eulerian and Lagrangian velocities. Specifically, one can distinguish between t-Lagrangian velocities sampled isochronally and s-Lagrangian velocities sampled equidistantly along streamlines. We have show that the PDFs of t- and s-Lagrangian velocities are linked through flux-weighting. The stationarity of the Lagrangian velocities depends on the injection conditions. Specifically, t-Lagrangian velocities are stationary for resident injection, while s-Lagrangian velocities are stationary for flux-weighted injection. Based on these results, we have developed a CTRW model for the evolution of Lagrangian velocities. This CTRW is defined through a Markov velocity process based on stochastic relaxation which is parameterized in terms of the steady-state velocity PDF and the correlation length along streamlines. Within this framework, we have studied the impact of strongly heterogeneous advective fields on transport under different injection conditions. We have shown that the non-Fickian behavior of the dispersion coefficient is fully determined by the flux-weighted Eulerian PDF and by the correlation length.

- In Chapter 6 we have studied the organization of velocities in Darcian flows and we have investigated the relationship between Eulerian and Lagrangian velocities statistics by using Markovian velocity models. To this end, we have considered Darcy flows in random hydraulic conductivity fields characterized by a multi-Gaussian structure and broad distribution of point values. Different injection conditions are tested, so that non-stationary transport

conditions are considered. In order to reproduce the evolution of the velocity PDF, we use an Ornstein-Uhlenbeck process which is parameterized in terms of the velocity correlation length. We show that the correlated CTRW model based on the OU process is able to reproduce the velocity PDF evolution, as well as the evolution of the mean and the variance of Lagrangian velocity that we observe in Monte Carlo numerical simulations.

- In Chapter 7, we have proposed a large-scale transport framework that is parameterized in terms of medium and flow properties and that allows for the description and the prediction of anomalous transport features. We have studied the impact of different disorder configurations, enhancing advective heterogeneity and different injection conditions on transport in Darcy fields. We have used the Markovian models for the evolution of the mean and the variance of Lagrangian velocities that we presented in the previous chapter and we have combined them with the CTRW approach to derive the moments of particles displacement, the spatial particle density and the first passage time distribution. We have distinguished two temporal regimes which are defined by a characteristic time scale of advection, which represents the time needed by a particle to explore the flow heterogeneity. We have observed that at early times the mean and the variance of particle displacement are fully determined by the injection conditions. In the asymptotic regime, while the mean displacement is governed by the stationary velocity PDF only, the variance keeps memory of the injection conditions. This memory effect is also observed in the first passage time distributions, whose tails are fully determined by the slowest particles, according to the single big (temporal) jump principle.

- In Chapter 8 we have quantified the impact of transverse diffusion as sampling process on anomalous transport in correlated heterogeneous advective fields. Specifically, we consider stratified or fibrous media where particles move by advection along the layers orientation and diffusively in transverse directions. Within a CTRW framework, we have considered two different quenched disorder configurations that affect the diffusion process in different ways. These configurations are the random velocity model, which is an extension of the well-known model by Matheron and de Marsily and the random retardation model, which accounts for spatially-varying retardation properties that are mapped onto a distribution of retardation coefficients. We have shown that the impact of diffusion on transport depends on the specific disorder model, as well as on the dimensionality of space. Specifically, we have found that there is perfect duality in space and time between the random velocity and the random retardation model. In $d \leq 3$ dimensions, transport dynamics is described by a correlated Lévy flight for the random velocity model and by a correlated biased CTRW for random retardation. In $d > 4$ dimensions, the vanishing return probability makes particles experience an annealed disorder, despite the intrinsic quenched nature of the system. As a consequence, particles dynamics describes a

Lévy flight in the random velocity model and a CTRW in the random retardation model.

With this thesis, we have shed some new light onto the understanding of the mechanisms underlying non-Fickian transport and we have performed the transport upscaling by means of the CTRW framework.

Outlook

To deepen the understanding of non-Fickian transport in heterogeneous porous media and the impact of the underlying physical mechanisms, the various aspects would deserve some efforts. Among them, we suggest

- to study the impact of diffusion in Darcian flows. Diffusion shortens the correlation scales by promoting mass transfer across streamlines. It is still not clear, however, how to account for this mechanism in the proposed correlated CTRW approach;
- to consider the impact of disorder and correlation on transport in non multi-Gaussian conductivity fields, e.g. in binary fields, connected and disconnected fields;
- to apply the correlated CTRW model to real field data, for instance those of the MAcroDispersion Experiment (MADE) site;
- to further study the relationship between medium and flow properties in order to parameterize the CTRW model in terms of geometric and hydraulic properties only.

APPENDIX A

Trapping Time Scales

The mass exchange process exhibits two distinct time scales. The first one is given by the inverse of the trapping rate $\tau_\gamma = \gamma^{-1}$. This time scale represents the time at which, on average, particles undergo the first trapping event. Moreover, it is also the average time that the particles spend in the mobile phase. For times larger than τ_γ, advection ceases to be the only process that governs transport.

The second time scale represents the moment at which particles start spending on average more time trapped than in the mobile phase. In order to determine this scale, we need to compare the average time spent mobile, which is given by τ_γ to the the average time spent immobile at a given time t. Note that the average trapping of the stable distribution (3.37) does not exist. Thus, in order to determine the characteristic trapping time after n trapping event, we first consider the mean number $\nu(t_f) \equiv \langle n_{t_f} \rangle$ of trapping times needed to arrive at a given total trapping time $t_{f,n} = \sum_{i=1}^{n} \tau_{f,i}$, which is given by the renewal theorem as

$$\nu(t_f) = 1 + \int_0^{t_f} dt' \nu(t_f - t') p_f(t'). \tag{A.1}$$

This equation is solved for the Laplace transform of $\nu(t_f)$ as

$$\nu^*(\lambda) = \frac{1}{\lambda} \frac{1}{1 - p_f^*(\lambda)}. \tag{A.2}$$

Using the stable distributions (3.37) for small $\lambda\tau_g$ gives $\nu^*(\lambda) \approx \tau_g (\lambda\tau_g)^{-1-\delta}$, from which we obtain in time

$$\nu(t_f) \approx \left(\frac{t}{\tau_g} \right)^{\delta}. \tag{A.3}$$

The latter gives us a relation between the total trapping time and number of trapping events. We can use this relation to define a total mean trapping time as

a function of step number by setting $\nu(\langle t_f \rangle) = n$, which gives $\langle t_f(n) \rangle = \tau_g n^{1/\delta}$. Thus an average trapping time after n steps is simply $\langle \tau_f(n) \rangle = \langle t_f(n) \rangle / n$, which gives

$$\langle \tau_f(n) \rangle = \tau_g n^{\frac{1-\delta}{\delta}}. \tag{A.4}$$

Notice that the latter is not strictly an average trapping time because for the stable distributions (3.37) the mean does not exist. It is rather a characteristic trapping time after n trapping events.

APPENDIX B

Moments of the spatial distribution

B.1 Weak advective heterogeneity

In the following we will derive the expressions for the scaling of the moments and the variance of particle displacements in both the longitudinal and transverse directions in the pre-asymptotic and in the asymptotic time regimes. In particular, we will consider all the possible cases corresponding to different choices of the distribution of trapping times. For the derivation of the moments, we will make use of the inverse Gamma distribution for δ in $(1, 2)$ and of stable distribution for δ in $(0, 1)$. This choice has as a consequence the fact that the Laplace transform of the distribution of immobile times in the asymptotic limit ($\lambda \to 0$) can be approximated for $\lambda\tau_g \ll 1$ as

$$p_f^*(\lambda) \approx 1 - (\lambda\tau_g)^\delta. \tag{B.1}$$

By inserting equation (B.1) into equation (3.18), we get the expression for the distribution of transit times

$$\psi^*(\lambda) \approx \frac{1}{1 + \lambda\tau_0 + \gamma\tau_0(\lambda\tau_g)^\delta} \tag{B.2}$$

From equation (B.2) we identify the trapping time scale τ_e as follows. The second term in the denominator dominates for $\lambda \ll \gamma(\gamma\tau_g)^{\frac{\delta}{1-\delta}}$ and analogously for times $t \gg \tau_\gamma(\gamma\tau_g)^{\frac{\delta}{\delta-1}} \equiv \tau_e$.

We first derive the scalings of the moments in the pre-asymptotic time regime. Under this conditioned, the PDF of transition times can be expanded and approximated with

$$\psi^*(\lambda) \approx 1 - \lambda\tau_0\,. \tag{B.3}$$

By inserting equation (B.3) into the equations for the first moment (3.43) and for the second moment (3.44) in this time regime and by considering the leading term in λ, we obtain

$$m_1^*(\lambda) \propto \lambda^{-2}, \qquad m_{11}^*(\lambda) \propto \lambda^{-3} + \lambda^{-2}, \qquad m_{22}^*(\lambda) \propto \lambda^{-2}. \tag{B.4}$$

We recall that the first moment in the transverse direction is always null. By applying the Tauberian theorems, we calculate the scaling in time from the expressions in the Laplace domain of equation (B.4). Thus, we find

$$m_1(t) \propto t, \qquad m_{11}(t) \propto t^2 + t, \qquad m_{22}(t) \propto t. \tag{B.5}$$

These results are valid for $\delta \in (0, 2)$. The variance is computed using equation (3.42). Note that the term proportional to t^2 in equation (B.5) will cancel out with the square of the first moment. Therefore, we get for the variance

$$\kappa_{11}(t) \propto t, \qquad \kappa_{22}(t) \propto t\,. \tag{B.6}$$

The procedure here described will be adopted to calculate all the scalings of the first moment and the variance in the following.

At long times, i.e. in the asymptotic time regime the PDF of transition times can be approximated with

$$\hat{\psi}(\lambda) \approx 1 - \tau_0 \gamma (\tau_g \lambda)^\delta\,. \tag{B.7}$$

By substituting this expression into equations (3.43) and (3.44), we get the scalings of the moments in the Laplace space. The mean value in the longitudinal direction behaves asymptotic as

$$m_1^*(\lambda) \propto \lambda^{-1-\delta} \tag{B.8}$$

By making use of the Tauberian theorems, we derive the asymptotic behavior of the variance in the temporal domain and we get

$$m_1(t) \propto t^\delta \tag{B.9}$$

This procedure is repeated to calculate all the scalings of the moments. In the transverse direction, as we have already pointed out before, the first moment in the transverse directions is always null $m_2 = 0$. For the spatial variances we obtain

$$\kappa_{11}(t) \propto t^{2\delta}, \qquad \kappa_{22}(t) \propto t^\delta. \tag{B.10}$$

B.2 Strong advective heterogeneity

We derive here the scalings of the moments for the case of strong advective heterogeneity. The latter is mapped onto heavy-tailed distributions of the mobile transition times. In particular, we will refer to inverse Gamma distributions

for β in $(1, 2)$. Therefore, the Laplace transform of ψ_m at long times can be approximated with

$$\psi_m(\lambda) \approx 1 - \alpha_1 \lambda \tau_v + \alpha_2 (\lambda \tau_v)^\beta \,. \tag{B.11}$$

where α_1 and α_2 are constants. By inserting this expression into equation (3.18), we get the Laplace transform of the PDF of the compound process

$$\psi^*(\lambda) \approx 1 - \alpha_1 \tau_v (\lambda + \gamma[1 - p_f^*(\lambda)]) + \alpha_2 (\tau_v \lambda + \tau_v \gamma[1 - p_f^*(\lambda)])^\beta \,. \tag{B.12}$$

The Laplace transform of the distribution of trapping times at long times is approximated by equation (B.1). By substituting the latter into equation (B.12) we get the distribution of total transition times in the Laplace space

$$\psi^*(\lambda) \approx 1 - \alpha_1 \left[\lambda \tau_v + \gamma \tau_v (\lambda \tau_g)^\delta\right] + \alpha_2 \left[\lambda \tau_v + \gamma \tau_v (\lambda \tau_g)^\delta\right]^\beta \,. \tag{B.13}$$

We now follow the same procedure described in appendix B.1 to derive the scaling of the moments in the pre-asymptotic and asymptotic limit for different choices of the parameters β and δ. In the pre-asymptotic limit, the mean value of particle displacements scales linearly with time

$$m_1(t) \propto t \tag{B.14}$$

in the longitudinal direction, while in the transverse directions the mean is zero $m_2(t) = 0$.
For the mean squared displacement, we find

$$\kappa_{11}(t) \propto t^{3-\beta} \tag{B.15}$$

in the direction of advection, while in the transverse direction the variance scales linearly

$$\kappa_{22}(t) \propto t \,. \tag{B.16}$$

Unlike the previous case, late behavior is strongly conditioned by the trapping properties of the medium and, as a consequence, the scalings of the moments will in general depend on the distribution of times that the particles spend in the immobile phase. In particular, the first moment in the longitudinal direction scales as

$$m_1(t) \propto t^\delta \,, \tag{B.17}$$

while in the transverse directions the mean value is always null $m_2(t) = 0$.
The scaling of the mean squared displacement along the direction in which advection occurs is given by

$$\kappa_{11}(t) \propto t^{2\delta} \,, \tag{B.18}$$

while in the transverse direction we get

$$\kappa_{22}(t) \propto t^\delta \,. \tag{B.19}$$

APPENDIX C

First passage time distribution

Here we will derive the scaling of the FPTD in the asymptotic and pre-asymptotic regimes for both weak and strong advective heterogeneity. The derivation will be performed for the same scenarios discussed in the previous section.

C.1 Weak advective heterogeneity

We will derive the expressions for the asymptotic regime. It has been previously shown that the distribution of transition times is given by equation (B.2). For $\lambda\tau_e \ll 1$, we obtain

$$\psi^*(\lambda) \approx 1 - \gamma\tau_0(\lambda\tau_g)^\delta \,. \tag{C.1}$$

Inserting the latter into (3.50) and using (3.48) gives for the Laplace transform of the FPTD

$$f^*(\lambda, x_c) = \exp[-\langle n_c\rangle\gamma\tau_0(\lambda\tau_g)^\delta], \tag{C.2}$$

which is again a stable distribution characterized by the exponent δ. This gives directly the scaling $f(t, x_c) \propto t^{-1-\delta}$ for $t \gg \tau_e$.

C.2 Strong advective heterogeneity

Inserting (B.13) in (3.50) gives for $f^*(\lambda, x_c)$

$$\begin{aligned} f^*(\lambda, x_c) \approx \exp\Big[-\langle n_c\rangle \Big(&\alpha_1\left[\lambda\tau_v + \gamma\tau_v(\lambda\tau_g)^\delta\right] \\ &+\alpha_2\left[\lambda\tau_v + \gamma\tau_v(\lambda\tau_g)^\delta\right]^\beta\Big)\Big] \,. \end{aligned} \tag{C.3}$$

For $\lambda \ll \gamma$, we approximate

$$f^*(\lambda, x_c) \approx \exp\left[-\langle n_c \rangle \alpha_1 \gamma \tau_v (\lambda \tau_g)^\delta\right], \tag{C.4}$$

which gives $f(t, x_c) \propto t^{-1-\delta}$ for $t \gg \tau_\gamma$. For $\lambda \gg \gamma$, we have

$$f^*(\lambda, x_c) \approx \exp\left(-\langle n_c \rangle \left[\alpha_1 \lambda \tau_v + \alpha_2 (\lambda \tau_v)^\beta\right]\right), \tag{C.5}$$

which gives the preasymptotic scaling $f(t, x_c) \propto t^{-1-\beta}$ for $t \ll \tau_\gamma$.

APPENDIX D

Eulerian and s-Lagrangian velocity PDFs

Here we show the derivation of the s-Lagrangian PDF from the Eulerian PDF. The latter is defined as

$$p_e(v) = \lim_{V\to\infty} \frac{1}{V} \int_{\Omega} d\mathbf{x}\, \delta[v - v_e(\mathbf{x})]\,, \tag{D.1}$$

where V is the volume of the region Ω. We define the s-Lagrangian PDF sampled among particles as

$$p_s(v,s) = \lim_{V_0\to\infty} \frac{1}{V_0} \int_{\Omega_0} d\mathbf{a} \frac{v(\mathbf{a})}{\langle v_e \rangle} \delta\left(v - v_e[\mathbf{x}(s,\mathbf{a})]\right), \tag{D.2}$$

where $\mathbf{x}(s=0;\mathbf{a}) = \mathbf{a}$, Ω_0 is the region of space occupied by the particles at $s=0$, V_0 its volume. Expression (D.2) accounts for the flux-weighting of the initial particle injection. We apply the transformation $\mathbf{x} = \mathbf{x}(s,\mathbf{a})$ to Eq. (D.1) in order to obtain

$$p_e(v) = \lim_{V\to\infty} \frac{1}{V} \int_{\Omega_0} d\mathbf{a}\, \mathbb{J}(\mathbf{a},s) \delta\left(v - v_e[\mathbf{x}(s,\mathbf{a})]\right)\,, \tag{D.3}$$

where $\mathbb{J}(\mathbf{a},s)$ is the norm of the determinant of the Jacobian of the transformation. We notice that the following relationship holds $\frac{d}{ds}\mathbb{J} = \mathbb{J}\nabla\cdot\left(\frac{\mathbf{v}_s}{v_s}\right)$. Under the condition of incompressibility, the latter reduces to

$$\frac{d}{ds}\mathbb{J} = -\mathbb{J}\frac{\mathbf{v}_s\cdot\nabla v_s}{v_s^2}\,. \tag{D.4}$$

Since $v_s(s) = v_e[\mathbf{x}(s,\mathbf{a})] = \|\mathbf{u}[\mathbf{x}(s;\mathbf{a})]\|$, we obtain from Eq. (4.5b)

$$\frac{dv_s}{ds} = \frac{\mathbf{v}_s}{v_s}\cdot\nabla v_s. \tag{D.5}$$

Thus, Eq. (D.4) reduces to

$$\frac{d}{ds}\mathbb{J} = -\frac{1}{v_s}\frac{dv_s}{ds}\mathbb{J}\,. \tag{D.6}$$

Since for $\mathbb{J}(\mathbf{a}, 0) = 1$, corresponding to the fact that the starting points are mapped identically onto themselves for $s = 0$, integrating the differential Eq. (D.6) yields

$$\mathbb{J}(\mathbf{a}, s) = \frac{v_e(\mathbf{a})}{v_e[\mathbf{x}(s, \mathbf{a})]}. \tag{D.7}$$

By substituting the latter into Eq. (D.3), we obtain

$$p_e(v) = \lim_{V\to\infty}\frac{1}{V}\int_{\Omega_0} d\mathbf{a}\, v_e(\mathbf{a})\frac{\delta\left(v - v_e[\mathbf{x}(s, \mathbf{a})]\right)}{v_e[\mathbf{x}(s, \mathbf{a})]}. \tag{D.8}$$

We can write this expression as

$$p_e(v) = \frac{\langle v_e\rangle}{v}\lim_{V\to\infty}\frac{1}{V}\int_{\Omega_0} d\mathbf{a}\frac{v_e(\mathbf{a})}{\langle v_e\rangle}\delta\left(v - v_e[\mathbf{x}(s, \mathbf{a})]\right), \tag{D.9}$$

where we use that $v = v_e[\mathbf{x}(s, a)]$ as per the Dirac delta in the integrand. Using (D.2) to identify $p_s(v)$ on the right side gives Eq. (4.6).

APPENDIX E

Correlation functions

In this Appendix, we derive the analytical expressions of the correlation function for the geometry described in Sect. 4.2.2. To this scope, we introduce the fluctuations of the Eulerian velocity with respect to its average $v'_e(\mathbf{x}) = v_e(\mathbf{x}) - \langle v_e(\mathbf{x})\rangle$, where the mean of v'_e is null by definition. For a position in the bin (n, m, p), we set $x = x_n + \delta_x$, $y = y_n + \delta_y$ and $z = z_n + \delta_z$, where δ_x is uniformly distributed between 0 and ℓ_{n+1}, while δ_y and δ_z are uniformly distributed in $(0, d_0]$ and in $(0, h_0]$, respectively. Therefore, the fluctuations can be expressed as

$$v'_e(\mathbf{x}) = \sum_{n,m,p} v'_{e;n,m,p} \mathbb{I}(0 < \delta_x \leq \ell_{n+1}) \times \mathbb{I}(0 < \delta_y \leq d_0)\mathbb{I}(0 < \delta_z \leq h_0)\,, \tag{E.1}$$

where $v'_{e;n,m,p}$ is the value of the fluctuation in the bin labeled with (n, m, p). The covariance function $\mathcal{C}(\mathbf{x} - \mathbf{x}')$ is defined as in Eq. (4.12). Because of the stationarity of the field, the covariance function only depends on the relative positions in the medium. Since the correlation is non-zero only within the same bin, we can write

$$\mathcal{C}(\mathbf{x} - \mathbf{x}') = \sum_{n,m,p} \langle v'^2_{e;n,m,p} \mathbb{I}_{\delta_x}(n)\mathbb{I}_{\delta_y}(m)\mathbb{I}_{\delta_z}(p) \times \mathbb{I}_{\delta'_x}(n)\mathbb{I}_{\delta'_y}(m)\mathbb{I}_{\delta'_z}(p)\rangle\,. \tag{E.2}$$

where the primed deltas refer to the point $\mathbf{x}'$ and the indicator functions are 1 if the point is within the bin and 0 otherwise. The ensemble averaging is performed by integrating over the uniformly distributed variables δ_i and δ'_i, with $i = x, y, z$, as well as over the bins sizes ℓ. By defining $\mathbf{\Delta x} = \mathbf{x} - \mathbf{x}'$, the explicit calculation

leads to

$$\mathcal{C}(\mathbf{x}-\mathbf{x}') = \sigma_v^2 \int_{|\Delta x|}^{\infty} d\ell\, p_\ell(\ell) \left(1 - \frac{|\Delta x|}{\ell}\right) \times \left(1 - \frac{|\Delta y|}{d_0}\right)\left(1 - \frac{|\Delta z|}{h_0}\right), \tag{E.3}$$

and 0 for $|\Delta y| > d_0$ or $|\Delta z| > h_0$. where $\sigma_v^2 = \mathcal{C}(\mathbf{0})$ is the variance of the Eulerian velocity. The correlation function is defined by $\mathscr{C}(\mathbf{x}) = \mathcal{C}(\mathbf{x})/\sigma_v^2$. By substituting the definition into Eq. (E.3), we observe that the covariance function can be factorized into

$$\mathscr{C}(\mathbf{x}) = \mathscr{X}(x)\mathscr{Y}(y)\mathscr{Z}(z)\,, \tag{E.4}$$

where

$$\mathscr{X}(x) = \int_{|x|}^{\infty} d\ell\, p_\ell(\ell) \left(1 - \frac{|x|}{\ell}\right)$$

$$\mathscr{Y}(y) = \left(1 - \frac{|y|}{d_0}\right) H(d_0 - |\Delta y|)$$

$$\mathscr{Z}(z) = \left(1 - \frac{|z|}{h_0}\right) H(h_0 - |\Delta z|)$$

represent the correlation functions in the x, y and z directions, respectively.

APPENDIX F

Spatial moments

In the following, we derive expressions (4.43)-(4.44) for the first and second displacement moments and the asymptotic scalings of the mean and variance. To this end, we define the jth moments of $\Phi(x,t)$ and $P(x,t)$ as

$$\mu_j^{(\Phi)}(t) = \int dx^j \Phi(x,t) \tag{F.1}$$

$$\mu_j^{(P)}(t) = \int dx^j P(x,t). \tag{F.2}$$

F.1 Derivation of mean and variance

The relationship between the particle density with and without interpolation is given in the Fourier and Laplace space by Eq. (4.39). By substituting this expression into Eq. (4.42), for the Laplace transform of the first and second moment of the spatial density $c(x,t)$ we get

$$\begin{aligned} m_1^*(\lambda) = &\frac{\lambda}{1-\psi^*(\lambda)} \Big[\mu_1^{(\Phi)}(\lambda)\mu_0^{(P)}(\lambda) \\ &+\mu_1^{(P)}(\lambda)\mu_0^{(\Phi)}(\lambda)\Big] \end{aligned} \tag{F.3}$$

$$\begin{aligned} m_2^*(\lambda) = &\frac{\lambda}{1-\psi^*(\lambda)} \Big[\mu_2^{(\Phi)}(\lambda)\mu_0^{(P)}(\lambda) \\ &+ 2\mu_1^{(\Phi)}(\lambda)\mu_1^{(P)}(\lambda) + \mu_2^{(P)}(\lambda)\mu_0^{(\Phi)}(\lambda)\Big] , \end{aligned} \tag{F.4}$$

where the μs are the moments of P and Φ in Laplace space. The sub-index denotes the order of the moment and the super-index indicates the distribution. Notice that the zero-th order moment of $P(x,t)$ in Laplace space is given by $\mu_0^{(P)}(\lambda) = \tilde{P}^*(k=0,\lambda)$. By using Eq. (4.38) and by assuming an instantaneous

injection of particles at $t = 0$, we get

$$\mu_0^{(P)}(\lambda) = \lambda^{-1} \,. \tag{F.5}$$

Analogously, the first and the second moments of $P(x,t)$ are calculated by applying the expressions for the moments (4.42) to the distribution of Eq. (4.38). Thus, we get

$$\mu_1^{(P)}(\lambda) = \frac{\mu_1^*(\lambda)}{\lambda[1-\psi^*(\lambda)]} \tag{F.6}$$

$$\mu_2^{(P)}(\lambda) = \frac{1}{1-\psi^*(\lambda)} \left[2\mu_1^*(\lambda)\mu_1^{(P)}(\lambda) + \frac{\mu_2^*(\lambda)}{\lambda} \right] . \tag{F.7}$$

The zero-th moment of $\Phi(x,t)$ is defined as the integral of the distribution over the spatial domain. Integrating Eq. (4.33) yields $\mu^{(\Phi)}(t) = \int_t^\infty \psi(\tau) d\tau$, whose Laplace transform reads

$$\mu_0^{(\Phi)}(\lambda) = \frac{1-\psi^*(\lambda)}{\lambda} \,. \tag{F.8}$$

Finally, the first moment of Φ is

$$\mu_1^{(\Phi)}(\lambda) = \frac{1}{\lambda^2} \int_0^\lambda d\lambda' \, \mu_1^*(\lambda') - \frac{1}{\lambda}\mu_1^*(\lambda) \,, \tag{F.9}$$

while the second moment is given by

$$\mu_2^{(\Phi)}(\lambda) = \frac{2}{\lambda^3} \int_0^\lambda d\lambda' \lambda' \mu_2^*(\lambda') - \frac{\mu_2^*(\lambda)}{\lambda} \,. \tag{F.10}$$

By substituting Eqs. (F.5), (F.6), (F.8) and (F.9) into Eq. (F.3) we get Eq. (4.43) for the Laplace transform of the first moment of particle density. Analogously, by substituting Eqs. (F.5), (F.6), (F.7), (F.8), (F.9) and (F.10) into Eq. (F.4), we get Eq. (4.44) for the Laplace transform of the second moment.

F.2 Asymptotic scalings

In this section we derive explicitly the asymptotic scalings of the first and second centered moment of particle density for each scenario presented in Sect. 4.4.

F.2.1 Distribution-induced anomalous diffusion

We first show that $\psi(t)$ scales asymptotically as $t^{-1-\beta}$. By definition, $\psi(t) = \int_{-\infty}^{\infty} dx \psi(x,t)$. By using Eq. (4.27), the distributions of bins lengths (4.16) and

the distribution of velocities (4.11), we get that the j-th moment of $\psi(x,t)$ scales at long times as

$$\mu_j(t) \propto t^{-1-\beta} \int_0^\infty dx\, x^{j+\beta} e^{-x/\ell_0}, \tag{F.11}$$

where $\mu_0(t) = \psi(t)$. For $t \to \infty$ the integral converges to $\Gamma(\beta + j + 1)$. Thus, from Eq. (F.11) we conclude that asymptotically $\mu_j(t) \propto t^{-1-\beta}$ for $j = 0, 1, 2$. By making use of Tauberian theorems, we obtain that the Laplace transform of quantities that scale asymptotically as $t^{-1-\beta}$ behaves for small λ as $1 - a_1\lambda^\beta$ for $\beta \in (0,1)$ and as $1 - a_1\lambda + a_2\lambda^\beta$ for $\beta \in (1,2)$. Finally, if $\beta = 1$, the scaling is $1 - a_1\lambda + a_3\lambda \ln \lambda$. Thus, we get

$$\mu_j^*(\lambda) \propto \begin{cases} 1 - a_1\lambda^\beta & \beta \in (0,1) \\ 1 - a_1\lambda + a_3\lambda \ln \lambda & \beta = 1 \\ 1 - a_1\lambda + a_2\lambda^\beta & \beta \in (1,2). \end{cases} \tag{F.12}$$

The real coefficients $\{a_i\}_{i=1,..,3}$ depend on the specific distribution. By substituting the corresponding scalings into Eq. (4.43) and by taking the leading orders in λ we get the asymptotic scalings in the Laplace domain of the first moment of particle density

$$m_1^*(\lambda) \propto \begin{cases} \lambda^{-1-\beta} & \beta \in (0,1) \\ \frac{\lambda^{-2}}{\ln \lambda} & \beta = 1 \\ \lambda^{-2} & \beta \in (1,2]. \end{cases} \tag{F.13}$$

The asymptotics in real time are obtained by the application of the Tauberian theorems, which provides the results listed in Table F.1. Analogously, we calculate the second moment by substituting the scalings of Eq. (F.12) into Eq. (4.44) and we get, in Laplace space

$$m_2^*(\lambda) \propto \begin{cases} \lambda^{-1-2\beta} & \beta \in (0,1) \\ \frac{\lambda^{-3}}{\ln^3 \lambda} & \beta = 1 \\ \lambda^{-3} + \lambda^{\beta-4} & \beta \in (1,2]. \end{cases} \tag{F.14}$$

The application of the Tauberian theorems provides the following scalings in the time domain

$$m_2(t) \propto \begin{cases} t^{2\beta} & \beta \in (0,1) \\ \frac{t^2}{\ln^3 t} & \beta = 1 \\ t^2 + t^{3-\beta} & \beta \in (1,2]. \end{cases} \tag{F.15}$$

Recall that the second centered moment is given by $\kappa(t) = m_2(t) - m_1^2(t)$. By taking the leading orders in t, we obtain the results that are listed in Table F.1.

	$\beta \in (0,1)$	$\beta = 1$	$\beta \in (1,2]$
$m_1(t)$	t^β	$\frac{t}{\ln(t)}$	t
$\kappa(t)$	$t^{2\beta}$	$\frac{t^2}{\ln^3(t)}$	$t^{3-\beta}$

Table F.1: Distribution-induced anomalous diffusion: asymptotic scalings of first moment and variance.

F.2.2 Correlation-induced anomalous diffusion

As we did in the previous section, we start by deriving the scaling of $\psi(t)$. By using the PDF of transition times and lengths of Eq. (4.27), the distribution of bins sizes (4.18) and the velocity PDF (4.9), we get that the j-th moment of $\psi(x,t)$ is given by

$$\mu_j(t) = \frac{\alpha \ell_0^\alpha}{t\sqrt{2\pi\sigma_e^2}} \int_{\ell_0}^{\infty} dx\, x^{j-1-\alpha} \times \exp\left(-\frac{[\ln(x/t) - \mu_s]^2}{2\sigma_e^2}\right). \tag{F.16}$$

We introduce the change of variable $y = x/t$. With this substitution, Eq. (F.16) simplifies to

$$\mu_j(t) = \frac{\alpha \ell_0^\alpha t^{j-1-\alpha}}{\sqrt{2\pi\sigma_e^2}} \int_{\ell_0/t}^{\infty} dy\, y^{j-1-\alpha} \times \exp\left[-\frac{(\ln y - \mu_s)^2}{2\sigma_e^2}\right]. \tag{F.17}$$

For $t \to \infty$ the integral converges to a constant value. Thus, by applying Tauberian theorems in the long time limit we get for $j = 0$

$$\psi^*(\lambda) \propto \begin{cases} 1 - a_1\lambda^\alpha & \alpha \in (0,1) \\ 1 - a_1\lambda + a_3\lambda\ln\lambda & \alpha = 1 \\ 1 - a_1\lambda + a_2\lambda^\alpha & \alpha \in (1,2)\,. \end{cases} \tag{F.18}$$

Analogously, we find that the first moment of $\psi(x,t)$ scales in Laplace space as

$$\mu_1^*(\lambda) \propto \begin{cases} \lambda^{\alpha-1} & \alpha \in (0,1) \\ 1 + a_3\ln\lambda & \alpha = 1 \\ 1 - a_1\lambda^\alpha & \alpha \in (1,2), \end{cases} \tag{F.19}$$

while for the second moment we get

$$\mu_2^*(\lambda) \propto \begin{cases} \lambda^{\alpha-2} & \alpha \in (0,1] \\ \lambda^{\alpha-1} & \alpha \in (1,2). \end{cases} \tag{F.20}$$

By substituting the scalings of Eqs. (F.18) and (F.19) into Eq. (4.43), we find

$$m_1^*(\lambda) \propto \begin{cases} \lambda^{-2} & \alpha \in (0,1) \\ \frac{\lambda^{-2}}{\ln \lambda} & \alpha = 1 \\ \lambda^{-2} & \alpha \in (1,2]. \end{cases} \tag{F.21}$$

By applying the Tauberian theorems, we find the scalings in the time domain that are listed in Table F.2. The scalings of the second moments are obtained in Laplace space by substituting Eqs. (F.18),(F.19) and (F.20) into Eq. (4.44), which gives

$$m_2^*(\lambda) \propto \begin{cases} \lambda^{-3} & \alpha \in (0,1) \\ \frac{\lambda^{-3}}{\ln \lambda} & \alpha = 1 \\ \lambda^{-3} + \lambda^{\alpha-4} & \alpha \in (1,2]. \end{cases} \tag{F.22}$$

The application of Tauberian theorems provides the following scalings in the time domain

$$m_2(t) \propto \begin{cases} t^2 & \alpha \in (0,1) \\ \frac{t^2}{\ln t} & \alpha = 1 \\ t^2 + t^{3-\alpha} & \alpha \in (1,2]. \end{cases} \tag{F.23}$$

Finally, by using these scalings for the calculation of the second centered moment and by taking the leading orders in t, we get the scalings that are listed in table F.2.

	$\alpha \in (0,1)$	$\alpha = 1$	$\alpha \in (1,2]$
$m_1(t)$	t	$\frac{t}{\ln t}$	t
$\kappa(t)$	t^2	$\frac{t^2}{\ln t}$	$t^{3-\alpha}$

Table F.2: Correlation-induced anomalous diffusion: asymptotic scalings of first moment and variance.

F.2.3 Anomalous diffusion induced by distribution and correlation

In this scenario the distribution of step lengths is given by (4.18), while the distribution of velocities is (4.11). By substituting these expressions into Eq.

(4.27) and by calculating the spatial moments, we get

$$\mu_j(t) \propto t^{-1-\beta} \int_{\ell_0}^{\infty} dx\, x^{j+\beta-\alpha-1} \exp\left(-\frac{x}{v_{\max} t}\right). \tag{F.24}$$

By using the change of variable $y = \frac{x}{v_{\max} t}$ we get

$$\mu_j(t) \propto t^{j-\alpha-1} \int_{\frac{\ell_0}{v_{\max}}}^{\infty} dy\, y^{j+\beta-\alpha-1} \exp(-y). \tag{F.25}$$

For different values of α and β very different asymptotic behaviors arise. In particular, we get

$$\mu_j(t) \propto \begin{cases} t^{j-1-\alpha} & \alpha < \beta + j \\ t^{-1-\omega} \ln t & \alpha = \beta + j \\ t^{-1-\beta} & \alpha > \beta + j, \end{cases} \tag{F.26}$$

where $\omega = \min(\alpha, \beta)$. Recall that the range of the parameters does not allow the possibility $\alpha \geq \beta + 2$. Therefore, a unique expression for the scaling of the second moment of $\psi(x,t)$ is found. Namely, we get $\mu_2(t) \propto t^{1-\alpha}$. In the following, we will treat four different scenarios, neglecting the cases in which $\alpha = \beta$ because of their unlikelihood. Nevertheless, those cases are reported in Table F.3 for completeness.

Case $\alpha, \beta \in (0,1); \alpha \neq \beta$ By using Tauberian theorems into Eq. (F.26), we find that the distribution of transition times admits the following expansion for large times in Laplace domain

$$\psi^*(\lambda) \propto 1 - a_1 \lambda^{\omega}. \tag{F.27}$$

The first moment, given by Eq. (F.26) for $j = 1$, scales in Laplace space as $\mu_1^*(\lambda) \propto \lambda^{\alpha-1}$, while the second moment scales as $\mu_2^*(\lambda) \propto \lambda^{\alpha-2}$. By substituting the so-obtained scalings into Eq. (4.43) and (4.44), we get for the first and the second moment of particles density

$$m_1^*(\lambda) \propto \lambda^{-1-\nu} \qquad\qquad m_2^*(\lambda) \propto \lambda^{-1-\mu} + \lambda^{-1-\epsilon}, \tag{F.28}$$

where $\nu = \min(1, \beta - \alpha + 1)$ and $\epsilon = \min(2, 2 + \beta - \alpha)$. By applying the Tauberian theorems, we find the scalings summarized in Table F.4.

Case $\alpha, \beta \in (1,2); \alpha \neq \beta$ In this case, for long times Eq. (F.26) can be expanded in Laplace space as

$$\psi^*(\lambda) \propto 1 - a_1 \lambda + a_2 \lambda^{\omega}, \tag{F.29}$$

while the first and the second moments of $\psi(x,t)$ scale as $\mu_1^*(\lambda) \propto \lambda^{\alpha-1}$ and as $\mu_2^*(\lambda) \propto \lambda^{\alpha-2}$, respectively. By applying the usual methodology, we get

$$m_1^*(\lambda) \propto \lambda^{-2} \qquad\qquad m_2^*(\lambda) \propto \lambda^{-3} + \lambda^{\omega-4}, \tag{F.30}$$

After applying the Tauberian theorems and by using $\kappa(t) = m_2(t) - m_1^2(t)$, for the first and second centered moment of particle displacements, we get the scalings listed in table F.4.

Case $\alpha \in (0,1), \beta \in (1,2)$ For this scenario, by using Eq. F.26 and Tauberian theorems, we get again the scaling of Eq. (F.27) for $\psi^*(\lambda)$ while the first and the second moment scale as $\mu_1^*(\lambda) \propto \lambda^{\alpha-1}$ and $\mu_2^*(\lambda) \propto \lambda^{\alpha-2}$, respectively (note that here $\alpha < \beta + 1$). In this case, we get from Eqs. (4.43) and (4.44)

$$m_1^*(\lambda) \propto \lambda^{-2} \qquad\qquad m_2^*(\lambda) \propto \lambda^{-3}. \tag{F.31}$$

The corresponding scalings in time domain are listed in Table F.5.

Case $\alpha \in (1,2), \beta \in (0,1)$ In this last scenario, we get from Eq. (F.26) and from the Tauberian theorems

$$\psi^*(\lambda) \propto 1 - a_1 \lambda^{\beta}, \tag{F.32}$$

while the second moment of $\psi(x,t)$ scales as $\mu_2^*(\lambda) \propto \lambda^{\alpha-2}$, respectively. The first moment, given by Eq. (F.26) for $j = 1$, scales as

$$\mu_1^*(\lambda) \propto \begin{cases} \lambda^{\alpha-1} & \alpha < \beta + 1 \\ 1 - a_1 \lambda^{\beta} & \alpha > \beta + 1. \end{cases} \tag{F.33}$$

By substituting the scalings here derived into Eqs. (4.43) and (4.44) we get in Laplace space

$$m_1^*(\lambda) \propto \lambda^{-1-\beta} \qquad\qquad m_2^*(\lambda) \propto \lambda^{-1-2\beta}. \tag{F.34}$$

The scalings in time domain are obtained through the application of Tauberian theorems and are listed in Table F.5.

	$\alpha = \beta \in (0,1)$	$\alpha = \beta = 1$	$\alpha = \beta \in (1,2)$
$m_1(t)$	$\frac{t}{\ln(t)}$	$\frac{t}{\ln^2 t}$	t
$\kappa(t)$	$\frac{t^2}{\ln(t)}$	$\frac{t^2}{\ln^2 t}$	$t^{3-\alpha}\ln(t)$

Table F.3: Anomalous transport induced by distribution and correlation: asymptotic scaling of the first moment and variance.

	$\alpha \neq \beta$, $\alpha, \beta \in (0,1)$	$\alpha \neq \beta$, $\alpha, \beta \in (1,2)$
$m_1(t)$	t^{ν}	t
$\kappa(t)$	t^{ε}	$t^{3-\omega}$

Table F.4: Anomalous transport induced by distribution and correlation: asymptotic scaling of the first moment and variance.

	$\alpha \in (0,1), \beta \in (1,2)$	$\alpha \in (1,2), \beta \in (0,1)$
$m_1(t)$	t	t^{β}
$\kappa(t)$	t^2	$t^{2\beta}$

Table F.5: Anomalous transport induced by distribution and correlation: asymptotic scaling of the first moment and variance.

APPENDIX G

Uncorrelated s-Lagrangian velocities

The one-point t-Lagrangian velocity PDF (5.25) can be expanded as

$$\hat{p}_t(v,t) = \int_0^t dt' \sum_{n=0}^{\infty} \langle \delta(v - v_n)\delta(t' - t_n)\delta_{n,n_t}\rangle, \tag{G.1}$$

where δ_{ij} denotes the Kronecker-delta. Note that $\delta_{n,n_t} \equiv \mathbb{I}(t_n \leq t < t_{n+1})$. Thus, we can write (G.1) as

$$\begin{aligned}\hat{p}_t(v,t) = &\int_0^t dt' \sum_{n=0}^{\infty} \langle \delta(v - v_n)\delta(t' - t_n)\rangle \\ &\times \mathbb{I}(0 \leq t - t' < \ell_c/v),\end{aligned} \tag{G.2}$$

where we used that t_n is independent of v_n, and that per the Dirac-delta, the v_n in the indicator function is set equal to v. We further obtain

$$\begin{aligned}\hat{p}_t(v,t) &= \int_{t-\ell_c/v}^{t} dt' \sum_{n=0}^{\infty} \langle \delta(v - v_n)\rangle\langle\delta(t' - t_n)\rangle \\ &\equiv p_s(v) \int_{t-\ell_c/v}^{t} dt' \sum_{n=0}^{\infty} R_n(t').\end{aligned} \tag{G.3}$$

for $t > \ell_c/v$; $R_n(t)$ is the PDF of t_n. As t_n is a Markov process in step number, we have the Chapman-Kolmogorov equation for the conditional PDF $R_{n,n'}(t|t')$

$$R_{n+1,n'}(t|t') = \int_{t'}^{t} dz \psi(t - z) R_{n,n'}(z|t'). \tag{G.4}$$

As the process is homogeneous in n and in t, we have that $R_{n'+m,n'}(t|t') \equiv R_m(t-t')$. The sum over $R_n(t)$,

$$R(t) = \sum_{n=0}^{\infty} R_n(t') \tag{G.5}$$

satisfies the integral equation (5.27).

For the two-point PDF, we obtain in analogy to (G.3)

$$\begin{aligned}\hat{p}_t(v,t;v',t') &= p_s(v)p_s(v') \\ &\times \int\limits_{t-\ell_c/v}^{t} dz \int\limits_{t'-\ell_c/v'}^{t'} dz' \sum_{n=0}^{\infty}\sum_{n'=0}^{\infty} R_{n,n'}(z,z'),\end{aligned} \tag{G.6}$$

where $R_{n,n'}(z,z')$ is the joint density of t_n and $t_{n'}$, which can be written as

$$R_{n'+m,n'}(z,z') = R_m(z-z')R_{n'}(z'). \tag{G.7}$$

We used the stationarity of the conditional PDF discussed above. Thus, we obtain now

$$\begin{aligned}\hat{p}_t(v,t;v',t') &= p_s(v)p_s(v') \\ &\times \int\limits_{t-\ell_c/v}^{t} dz \int\limits_{t'-\ell_c/v'}^{t'} dz' \sum_{m=0}^{\infty}\sum_{n'=0}^{\infty} R_m(z-z')R_{n'}(z'), \\ &\equiv p_s(v)p_s(v') \int\limits_{t-\ell_c/v}^{t} dz \int\limits_{t'-\ell_c/v'}^{t'} dz' R(z-z')R(z').\end{aligned} \tag{G.8}$$

Shifting $z \to t-z$ and $z' \to t'-z'$ gives

$$\begin{aligned}\hat{p}_t(v,t;v',t') &= p_s(v)p_s(v')\times \\ &\int\limits_{0}^{\ell_c/v} dz \int\limits_{0}^{\ell_c/v'} dz' R(t-t'+z'-z)R(t'-z').\end{aligned} \tag{G.9}$$

Using now expression (5.26) gives (5.30).

APPENDIX H

Correlated s-Lagrangian velocities

The Master equation (5.47) for $R(v,t,s)$ follows from the Chapman-Kolmogorov equation (5.46) in the limit $\Delta s \to 0$. In fact, inserting (5.33b) and (5.33f) gives

$$R(v,t,s+\Delta s) = \exp(-\Delta s/\ell_c) R(v,t-\Delta s/v,s) + [1-\exp(-\Delta s/\ell_c)] p_s(v) \int_0^\infty dv' R(v',t-\Delta s/v',s). \tag{H.1}$$

Expanding the left hand right side for small Δs gives

$$R(v,t,s) + \Delta s \frac{\partial R(v,t,s)}{\partial s} + \cdots = R(v,t,s) - \frac{\Delta s}{v}\frac{\partial R(v,t,s)}{\partial t} - \frac{\Delta s}{\ell_c} R(v,t,s) + \frac{\Delta s}{\ell_c} p_s(v) \int_0^\infty dv' R(v',t,s) + \ldots, \tag{H.2}$$

where the dots denote higher order contributions in Δs. Dividing by Δs and taking the limit $\Delta s \to 0$ gives (5.47).

We now derive the solution of Equation (5.48). To this end, we perform the Laplace transform, which gives

$$\lambda \hat{p}_t^*(v,\lambda) = -\frac{v}{\ell_c}\hat{p}_t^*(v,\lambda) + p_s(v) \int_0^\infty dv' \frac{v'}{\ell_c}\hat{p}_t^*(v',\lambda). \tag{H.3}$$

This is a Fredholm equation of the second kind with degenerate kernel (Polyanin and Manzhirov, 1998). It can be written as

$$\hat{p}_t^*(v,\lambda) = g_0^*(v,\lambda)p_0(v) + g_0^*(v,\lambda)p_s(v)\int_0^\infty dv' \frac{v'}{\ell_c}\hat{p}^*(v',\lambda). \tag{H.4}$$

where we defined

$$g_0^*(v,\lambda) = \frac{1}{\lambda + v/\ell_c}. \tag{H.5}$$

The solution of (H.4) has the form

$$\hat{p}_t^*(v,\lambda) = g_0^*(v,\lambda)\left[p_0(v) + p_s(v)A(v,\lambda)\right]. \tag{H.6}$$

Inserting the latter into (H.4) gives for $A(v,\lambda)$

$$A(v,\lambda) = \frac{\psi_0^*(\lambda)}{1-\psi_s^*(\lambda)} \tag{H.7}$$

where we defined

$$\psi_i^*(\lambda) = \int_0^\infty dv' g_0^*(v',\lambda)\frac{v'}{\ell_c}p_i(v) \tag{H.8}$$

with $i = 0, s$. Inserting (H.7) into (H.6) and setting $p_s(v) = vp_e(v)/\langle v_e\rangle$ gives (5.49).

APPENDIX I

Moments of displacement and first passage time

Here we derive the asymptotic scalings of the moments of the first passage time distribution for the Matheron-de Marsily model with the velocity distribution (8.18) and the displacement moments for the random retardation model with the distribution (8.45) of the retardation coefficient. As we discuss in the main text, the random velocity model and the random retardation model are dual. The first passage time distribution (8.20) of the Matheron-de Marsily model corresponds to the particle distribution (8.47) in the random retardation model. The first passage time in the random velocity model is given by

$$t(x) = n_x \tau_D \tag{I.1}$$

and the position in the random retardation model by

$$x(t) = n_t v_0 \tau_D. \tag{I.2}$$

Thus, mean and variance of first-passage time and displacement can be written as

$$\mu_\theta(\xi) = \theta_0 \overline{n_\xi} \qquad \kappa_\theta(x) = \theta_0^2 \left(\overline{n_\xi^2} - \overline{n_\xi}^2 \right), \tag{I.3}$$

where $\xi = t$, $\theta = x$ and $\theta_0 = v_0 \tau_D$ for the displacement moments and $\xi = x$ and $\theta = t$ and $\theta_0 = \tau_D$ for the first passage time moments. Note that the asymptotic scalings depend only on the moments of the renewal process n_ξ. The derivation of the behavior of the moments of n_ξ can be found in Ref. Russian et al. (2017) for the power-law distribution $\psi_\xi \sim (\xi/\xi_0)^{-1-\nu}$ with $0 < \nu < 2$. Note that $\nu = \alpha$ for the random velocity and $\nu = \beta$ for the random retardation model. For the convenience of the reader, in the following, we provide the derivation for the case of $1 < \nu < 2$.

The distribution of n_ξ is given by

$$p_n(\xi) = \overline{\delta_{n,n_\xi}}. \tag{I.4}$$

Its ith moments are defined by

$$h_k(\xi) = \sum_{n=0}^{\infty} n^k p_n(\xi) \tag{I.5}$$

The Laplace transform of (I.4) can be written for large n as (Russian et al., 2017)

$$p_n^*(\lambda) = -\frac{1}{\lambda}\frac{d}{dn} f_n^*(\lambda). \tag{I.6}$$

where we defined

$$f_n^*(\lambda) = \psi^*(\gamma_n \lambda)^{S_n}. \tag{I.7}$$

Likewise, we write the Laplace transform of the moments (I.5) as

$$h_k^*(\lambda) = -\frac{1}{\lambda}\int_0^\infty dn n^k \frac{d}{dn} f_n^*(\lambda), \tag{I.8}$$

for which we obtain by integration by parts

$$h_k^*(\lambda) = \frac{1}{\lambda} k \int_0^\infty dn n^{k-1} f_n^*(\lambda), \tag{I.9}$$

As outlined above, we consider the case $\psi_\xi(\xi) \propto (\xi/\xi_0)^{-1-\nu}$ and focus on the case $1 < \nu < 2$. The Laplace transform of $\psi_\xi(\xi)$ is for $\lambda\xi_0 \ll 1$ given by

$$\psi_\xi^*(\lambda) = 1 - \overline{\xi}\lambda + a_\nu \lambda^\nu, \tag{I.10}$$

where the constant a_ν depends on the specific form of the distribution $\psi_\xi(\xi)$. For $\nu > 2$, we set $\nu = 2$ in (I.10) and a_ν is equal to $\overline{\xi^2}/2$. Using this expansion, we can write (I.7) as

$$f_n^*(\lambda) = \exp\left[S_n \ln\left(1 - \overline{\xi}\gamma_n\lambda + a_\nu \gamma_n^\nu \lambda^\nu\right)\right]. \tag{I.11}$$

Expansion of the exponent gives

$$f_n^*(\lambda) = \exp\left(-\overline{\xi} S_n \gamma_n \lambda + A_\nu S_n \gamma_n^\nu \lambda^\nu\right), \tag{I.12}$$

where $A_\nu = a_\nu$ for $1 < \nu < 2$ and $A_\nu = \sigma_\xi^2/2$ for $\nu > 2$ with $\sigma_\xi^2 = \overline{\xi^2} - \overline{\xi}^2$. Further expanding the exponential, we obtain in leading order

$$f_n^*(\lambda) \approx \exp\left(-n\overline{\xi}\lambda\right)\left(1 + S_n^{1-\nu} n^\nu A_\nu \lambda^\nu\right), \tag{I.13}$$

where we used that $\gamma_n = n/S_n$.

For $d = 2$, this means $d_w = 1$, we obtain for the moments

$$h_k^*(\lambda) = \frac{1}{\lambda} k \int_0^\infty dn n^{k-1} \exp\left(-n\bar{\xi}\lambda\right) + \frac{1}{\lambda} k \int_0^\infty dn n^{k+\frac{\nu-1}{2}} A_\nu \lambda^\nu \exp\left(-n\bar{\xi}\lambda\right), \quad \text{(I.14)}$$

Scaling of $n \to n\bar{\xi}\lambda$ gives

$$h_k^*(\lambda) = \frac{\lambda^{-1-k}}{\bar{\xi}^k} k\Gamma(k) + \frac{1}{\lambda} (\lambda\bar{\xi})^{-k-\frac{1-\nu}{2}} A_\nu k\Gamma\left[1 + k + (\nu-1)/2\right]. \quad \text{(I.15)}$$

Inverse Laplace transform gives

$$h_k(\xi) = (\xi/\bar{\xi})^k + B_{2k}(\xi/\bar{\xi})^{k-\frac{\nu-1}{2}}, \quad \text{(I.16)}$$

with

$$B_{2k} = \frac{A_\nu}{\bar{\xi}^\nu} \frac{k\Gamma\left[1 + k + (\nu-1)/2\right]}{\Gamma\left[1 + k - (\nu-1)/2\right]}. \quad \text{(I.17)}$$

Specifically, we obtain for the mean and variance of n_ξ in leading order

$$\overline{n_\xi} = \xi/\bar{\xi}, \quad \text{(I.18)}$$

$$\overline{n_\xi^2} - \overline{n_\xi}^2 \propto \frac{A_\nu}{\bar{\xi}^\nu} (\xi/\bar{\xi})^{2-\frac{\nu-1}{2}}. \quad \text{(I.19)}$$

For $d = 3$, this means $d_w = 2$, we derive along the same lines that

$$h_k(\xi) = (\xi/\bar{\xi})^k + B_{3k}(\xi/\bar{\xi})^{1+k-\nu} \ln(\xi/\bar{\xi})^{\nu-1}, \quad \text{(I.20)}$$

with $B_{3k} \propto A_\nu/\bar{\xi}^\nu$ a constant. Mean and variance of n_ξ are given by

$$\overline{n_\xi} = \xi/\bar{\xi}, \quad \text{(I.21)}$$

$$\overline{n_\xi^2} - \overline{n_\xi}^2 \propto \frac{A_\nu}{\bar{\xi}^\nu} (\xi/\bar{\xi})^{3-\nu} \ln(\xi/\bar{\xi})^{\nu-1}. \quad \text{(I.22)}$$

For $d > 3$, this means $d_w > 2$, we find

$$h_k(\xi) = (\xi/\bar{\xi})^k + B_{4k}(\xi/\bar{\xi})^{1+k-\nu}, \quad \text{(I.23)}$$

with $B_{4k} = A_\nu/\bar{\xi}^\nu$ a constant. Thus, we obtain for the mean and variance of n_ξ

$$\overline{n_\xi} = \xi/\bar{\xi}, \quad \text{(I.24)}$$

$$\overline{n_\xi^2} - \overline{n_\xi}^2 \propto \frac{A_\nu}{\bar{\xi}^\nu} (\xi/\bar{\xi})^{3-\nu}. \quad \text{(I.25)}$$

APPENDIX J

Flow statistics in Ln K-fields

For the particle tracking simulations, we assume steady Eulerian properties. Since boundary conditions impact Eulerian velocities, we explore empirically the "biased belt", in which Eulerian velocity are not steady. For the most heterogeneous case, we find steady Eulerian velocity statistics (variance) inside a belt with a thickness of aoubt 20 correlation length (Figure: J.1).

To verify the accuracy of our numerical simulations, we compared our results to other numerical references (de Dreuzy et al., 2007; Gotovac et al., 2009). Figure J.2 shows the good agreement between our numerical setting and these references. For consistency, we computed the correlation function along the mean flow direction to illustrate how the Eulerian velocity correlation decreases for increasing heterogeneity. This decrease in correlation is related to the increase of flow channeling. Our results are consistent with the study of Gotovac et al. (2009) (see their Figure 7a, p.12/24).

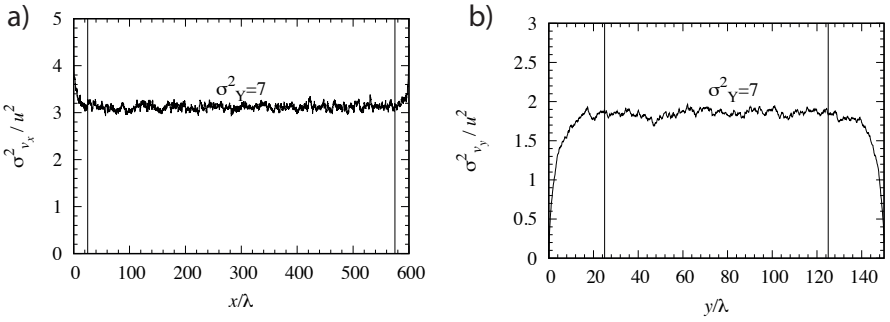

Figure J.1: Variance of Eulerian velocity in the direction (a) longitudinal and (b) transverse to the mean flow. Vertical lines indicates where the variance becomes stationary and the inner boundaries used for particle tracking simulations.

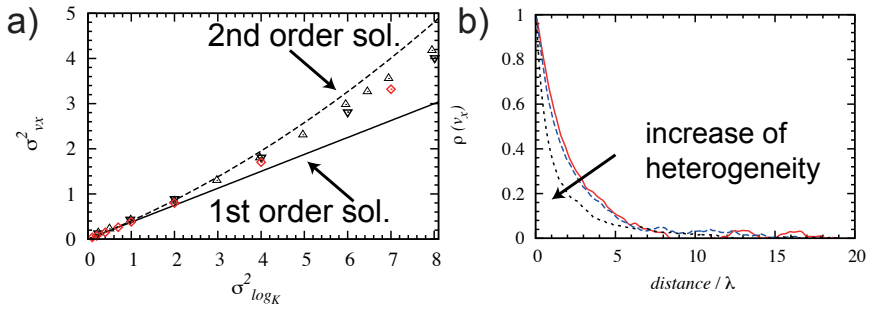

Figure J.2: Variance (a) and correlation function (b) of the velocity component along the mean flow direction for $\ln_K$ fields. The variance of the Eulerian velocity along the mean flow direction increases non linearly with increasing variance of the $\ln_K$ field. Our simulations (red diamond) agrees with references from the literature: upward triangles from de Dreuzy et al. (2007) and downward triangles from Gotovac et al. (2009). The 1st and 2nd-order approximations provides accurate estimates for $\sigma^2_{\ln_K} < 1$ and $\sigma^2_{\ln_K} < 2$ respectively. For increasing heterogeneity, the correlation length of the Eulerian velocity decreases as a result of flow channeling.

APPENDIX K

Ornstein-Uhlenbeck process

We consider the Kolmogorov equation for the process (6.30), which reads in discrete s

$$w(s+\Delta s) = w(s) - \frac{\Delta s}{\ell_c} w(s) + \sqrt{2\kappa \Delta s}\eta(s), \tag{K.1}$$

where $\eta(s)$ is a Gaussian random variable of 0 mean and unit variance. The Kolmogorov equation for the PDF of velocity is

$$p_w(w, s+\Delta s) = \int ds' p(w', s) f(w - w'; w'), \tag{K.2}$$

where we defined

$$f(w - w'; w') = \langle \delta[w - w' + w'\Delta s/\ell_c - \sqrt{2\kappa\Delta s}\eta(s)]\rangle. \tag{K.3}$$

Kramers-Moyal expansion and scale limit $\Delta s \to 0$ gives the Smoluchowski equation. Note that

$$\int dw (w - w') f(w - w'; w') = w'\Delta s/\ell_c \tag{K.4}$$

$$\int dw (w - w')^2 f(w - w'; w') = 2\kappa\Delta s. \tag{K.5}$$

We rewrite (K.2) as

$$p_w(w, s+\Delta s) = \int ds' p(w - w', s) f(w'; w - w'), \tag{K.6}$$

and expand the integrand as

$$\begin{aligned} p_w(w - w', s) f(w'; w - w') = p_w(w, s) f(w'; w) - \frac{\partial}{\partial w} p_w(w, s) w' f(w'; w) \\ + \frac{1}{2}\frac{\partial^2}{\partial w^2} p_w(w, s) w'^2 f(w'; w) \end{aligned} \tag{K.7}$$

Inserting the latter into (K.6) and using (K.4) and (K.5) gives

$$p_w(w, s + \Delta s) = p_w(w, s) + \Delta s \frac{\partial}{\partial w} \frac{w}{\ell_c} p_w(w, s) + \Delta s \kappa \frac{\partial^2}{\partial w^2} p_w(w, s) + \ldots, \quad \text{(K.8)}$$

where the dots denote contributions of order Δs^2. In the limit $\Delta s \to 0$ gives the Smoluchowski equation

$$\frac{\partial p_w(w, s)}{\partial s} = \frac{\partial}{\partial w} \frac{w}{\ell_c} p_w(w, s) + \kappa \frac{\partial^2}{\partial w^2} p_w(w, s). \quad \text{(K.9)}$$

Its steady state distribution is obtained from

$$\frac{\partial}{\partial w} \frac{w}{\ell_c} p_w(w, s) + \kappa \frac{\partial^2}{\partial w^2} p_w(w, s) = 0. \quad \text{(K.10)}$$

The latter can be integrated to give

$$p_w(w) = \frac{\exp\left(-\frac{w^2}{2\kappa \ell_c}\right)}{\sqrt{2\pi\kappa\ell_c}} \quad \text{(K.11)}$$

This implies that the w–increment

$$\begin{aligned} w(s + \Delta s) - w(s) = w(0) \exp(-s/\ell_c)[\exp(-\Delta s/\ell_c) - 1] \\ + \int_s^{s+\Delta s} ds' \exp[-(s - s')/\ell_c] \sqrt{2\kappa} \xi(s), \end{aligned} \quad \text{(K.12)}$$

is Gaussian distributed at large $s \gg \ell_c$, for which

$$w(s + \Delta s) - w(s) \approx \int_s^{s+\Delta s} ds' \exp[-(s - s')/\ell_c] \sqrt{2\kappa} \xi(s). \quad \text{(K.13)}$$

K.1 Parameter estimation in Ornstein-Uhlenbeck process

This section describes the procedure to estimate the velocity correlation parameter ℓ_c of the OU-model. This estimation is uses the map of the evolution of the ensemble mean s-Lagrangian velocity to the mean of the w process. It is convenient to estimate the correlation value of the latter process since it can be described analyticaly. In short, estimation of ℓ_c is done with the analytical solution that describes the evolution of the Gaussian random variable w in the Ornstein-Uhlenbeck model.

Empirical w are obtained by DNS through the map of s-Lagrangian velocities to w and averaging over particles and over realizations. The first step of the map consits in computing the probability (score) of the s-Lagrangian velocity with the cumulative density function of the steady-state s-Lagrangian distribution

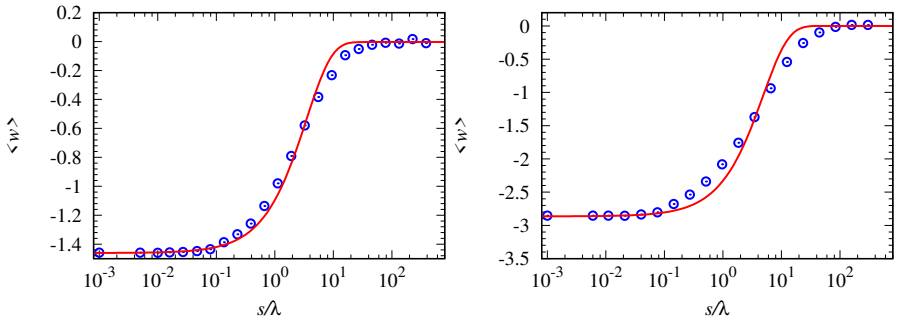

(a) Lognormal (b) Gamma

Figure K.1: Spatial evolution of the w process obtained by DNS (dots) and fitted analytical solution (blue line) for the two most 'heterogeneous' K field, left: $\sigma^2_{\ln_K} = 7$, $\ln_K$-field and right $\alpha = 0.1$, γ_K-field. The fitted correlation length are: $\ell_c = 3.472\lambda$ (+/-0.08) and $\ell_c = 4.853\lambda$ (+/- 0.1961).

(here, the flux-weighted Eulerian velocity distribution). The second step of the map is to use this probability to obtain a random value from a unit-Gaussian distribution. These steps are repeated over a given number of distances along streamlines, particles and flow realizations. Averages are computed for each step (over particles) and then, over realizations (ensemble average).

In the OU-model, the evolution of the mean for a unit Gaussian distribution is given by:

$$\langle\ w(s)\ \rangle = (\mu_0 - \mu)\exp(-\gamma s) + \mu \tag{K.14}$$

in which $\gamma^{-1} = \ell_c$, and μ_0 and μ are the initial and steady-state mean after mapping to the unit Gaussian respectively.

Figure K.1 shows an example of the spatial evolution of the empirical ensemble $\langle w \rangle$ process that stems from DNS of transport in heterogeneous $\ln_K$-fields, with $\sigma^2_{\ln_K=7}$. In addition, the figure shows the fitted analytical solution for the OU process. The analytical solution plots over the empirical data of $\langle\ w\ \rangle$, confirming the good agreement between the model and the data. The fit is obtained for $\ell_c = 3.472\lambda$. This estimates is similar but smaller (i.e. 3.472 vs 5.2λ) than the correlation length estimated for the Bernoulli model.

APPENDIX L

Publications and conference presentations

Publications in scientific journals

- **Comolli, A.**, Hidalgo, J. J., Moussey, C., and Dentz, M. (2016). Non-fickian transport under heterogeneous advection and mobile-immobile mass transfer. *Transport in Porous Media*, 115(2):265-289.

- Dentz, M., Kang, P. K., **Comolli, A.**, Le Borgne, T., and Lester, D. R. (2016). Continuous time random walks for the evolution of lagrangian velocities. *Physical Review Fluids*, 1(7):074004.

- **Comolli, A.** and Dentz, M. (2017). Anomalous dispersion in correlated porous media: a coupled continuous time random walk approach. *The European Physical Journal B*, 90(9):166.

- **Comolli, A.** and Dentz, M. (*submitted*) Impact of diffusion on anomalous dispersion in structured disordered media: From correlated Levy flights to continuous time random walks.

Presentations in conferences

2018

- **Comolli, A.**, Hakoun, V. and Dentz, M. - Darcy-scale anomalous transport in heterogeneous porous media: a continuous time random walk approach. CMWR - Saint Malo (France).

- Hakoun, V., **Comolli, A.** and Dentz, M. - Evolution of Lagrangian velocities in steady Darcy flow fields and impact on solute transport. CMWR - Saint Malo (France).

- **Comolli, A.**, Hakoun, V. and Dentz, M. - Spatial Markov models for non-Fickian transport in heterogeneous porous media. EGU General Assembly 2018 - Vienna (Austria).

- Hakoun, V., **Comolli, A.** and Dentz, M. - Modeling macrodispersive behaviors of solutes in a heterogeneous alluvial aquifer with spatial Markov models for velocities. EGU General Assembly 2018 - Vienna (Austria).

2017

- Hakoun, V., **Comolli, A.** and Dentz, M. - From medium heterogeneity to flow and transport: A time-domain random walk approach. AGU Fall Meeting 2017 - New Orleans (USA).

- **Comolli, A.** and Dentz, M.- Non-Fickian transport in heterogeneous media: the role of disorder and spatial correlation. GHS Seminar - Barcelona (Spain).

- **Comolli, A.**, Hakoun, V. and Dentz, M. - The mechanisms of anomalous transport in heterogeneous media: From medium structure to stochastic particle motion. SIAM GS 2017 - Erlangen (Germany).

- **Comolli, A.**, Hidalgo, J.J., Moussey, C. and Dentz, M. - A continuous time random walk model for transport in heterogeneous porous media. Interpore 2017 - Rotterdam (The Netherlands).

- Hakoun, V., **Comolli, A.** and Dentz, M. - From unstationary to stationary Lagrangian velocities in heterogeneous Darcian flow and the impact on solute dispersion. Interpore 2017 - Rotterdam (The Netherlands).

- **Comolli, A.**, Hakoun, V. and Dentz, M. - A continuous time random walk model for Darcy-scale anomalous transport in heterogeneous porous media. EGU General Assembly 2017 - Vienna (Austria).

- Hakoun, V., **Comolli, A.** and Dentz, M. - Lagrangian velocities evolution in steady Darcian flow, the impact on solute dispersion and an application to the MADE tracer test. EGU General Assembly 2017 - Vienna (Austria).

2016

- **Comolli, A.** and Dentz, M. - Anomalous transport under heterogeneous advection and mobile-immobile mass transfer. 2nd Meeting of young researchers of IDAEA- Barcelona (Spain).

- **Comolli, A.** and Dentz, M. - Lévy walk dynamics of anomalous transport in quenched random velocity fields. 614. WE-Heraeus Seminar - Bad Honnef (Germany).

- **Comolli, A.**, Hidalgo, J.J., Moussey, C. and Dentz, M. - Modelling transport in media with heterogeneous advection properties and mass transfer with a continuous time random walk approach. EGU General Assembly 2016 - Vienna (Austria).

- **Comolli, A.**, Hidalgo, J.J., Moussey, C. and Dentz, M. - Non-Fickian transport under heterogeneous advection and solute trapping. GHS Seminar - Barcelona (Spain).

2015

- **Comolli, A.** and Dentz, M. - Coupled continuous time random walks for anomalous transport in media characterized by heterogeneous mass transfer properties. AGU Fall Meeting 2015 - San Francisco (USA).

- **Comolli, A.** and Dentz, M. - Characterization of anomalous transport in quenched random velocity fields. 1st Meeting of young researchers of IDAEA - Barcelona (Spain).

- **Comolli, A.** and Dentz, M. - Quantification of anomalous transport in correlated heterogeneous media using coupled continuous time random walks. AGU Chapman Conference - Valencia (Spain).

- **Comolli, A.** and Dentz, M. - Characterization of anomalous transport in quenched random velocity fields. 3rd Cargèse Summer School on flow and transport in porous and fractured media - Cargèse (France).

Bibliography

Aarnes, J. E., Gimse, T., and Lie, K.-A. (2007). An introduction to the numerics of flow in porous media using matlab. In *Geometric modelling, numerical simulation, and optimization*, pages 265–306. Springer.

Abramowitz, M. and Stegun, I. A. (1972). *Handbook of Mathematical Functions*. Dover Publications, New York.

Adams, E. E. and Gelhar, L. W. (1992). Field study of dispersion in a heterogeneous aquifer, 2. Spatial moment analysis. *Water Resour. Res.*, 28(12):3293–3308.

Akimoto, T., Barkai, E., and Saito, K. (2016). Universal fluctuations of single-particle diffusivity in a quenched environment. *Phys. Rev. Lett.*, 117:180602.

Attinger, S., Dentz, M., and Kinzelbach, W. (2004). Exact transverse macro dispersion coefficient for transport in heterogeneous media. *Stoch. Environ. Res. Risk Assess.*, 18:9–15.

Banks, D. S. and Fradin, C. (2005). Anomalous diffusion of proteins due to molecular crowding. *Biophysical journal*, 89(5):2960–2971.

Barenblatt, G., Zheltov, I. P., and Kochina, I. (1960). Basic Concepts in the Theory of Seepage of Homogeneous Liquids in Fissured Rocks [Strata]. *PMM*, 24(5):825–864.

Barkai, E., Garini, Y., and Metzler, R. (2012). Strange kinetics of single molecules in living cells. *Phys. Today, No. 8, 65, 29 (2012).*, 8:29–35.

Barthelemy, P., Bertolotti, J., Vynck, K., Lepri, S., and Wiersma, D. S. (2010). Role of quenching on superdiffusive transport in two-dimensional random media. *Phys. Rev. E*, 82:011101.

Barthelemy, P., Bertolotti, J., and Wiersma, D. S. (2008). A Lévy flight for light. *Nature*, 453:495–498.

Baule, A. and Friedrich, R. (2005). Joint probability distributions for a class of non-markovian processes. *Phys. Rev. E*, 71:026101.

Bear, J. (1972). *Dynamics of fluids in porous media*. American Elsevier, New York.

Becker, M. W. and Shapiro, A. M. (2003). Interpreting tracer breakthrough tailing from different forced-gradient tracer experiment configurations in fractured bedrock. *Water Resour. Res.*, 39:1024.

Bellin, A., Salandin, P., and Rinaldo, A. (1992). Simulation of dispersion in heterogeneous porous formations: Statistics, first-order theories, convergence of computations. *Water Resources Research*, 28(9):2211–2227.

Benke, R. and Painter, S. (2003). Modeling conservative tracer transport in fracture networks with a hybrid approach based on the boltzmann transport equation. *Water Resour. Res.*, (39):1324.

Benson, D. A. and Meerschaert, M. M. (2009). A simple and efficient random walk solution of multi-rate mobile/immobile mass transport equations. *Adv. Wat. Res.*, 32 (4):532–539.

Benson, D. A., Meerschaert, M. M., and Revielle, J. (2013). Fractional calculus in hydrologic modeling: A numerical perspective. *Advances in water resources*, 51:479–497.

Benson, D. A., Schumer, R., Meerschaert, M. M., and Wheatcraft, S. W. (2001). Fractional dispersion, lévy motion, and the made tracer tests. In *Dispersion in heterogeneous geological formations*, pages 211–240. Springer.

Benson, D. A., Wheatcraft, S. W., and Meerschaert, M. M. (2000). Application of a fractional advection-dispersion equation. *Water Resources Research*, 36(6):1403–1412.

Berkowitz, B. (2002). Characterizing flow and transport in fractured geological media: A review. *Adv. Water Resour.*, 25:861–884.

Berkowitz, B., Cortis, A., Dentz, M., and Scher, H. (2006). Modeling non-fickian transport in geological formations as a continuous time random walk. *Rev. Geophys.*, 44:RG2003.

Berkowitz, B., Emmanuel, S., and Scher, H. (2008). Non-fickian transport and multiple-rate mass transfer in porous media. *Water Resour. Res.*, 44:W03402.

Berkowitz, B., Klafter, J., Metzler, R., and Scher, H. (2002). Physical pictures of transport in heterogeneous media: Advection-dispersion, random-walk, and fractional derivative formulations. *Water Resour. Res.*, 38(10):1191.

Berkowitz, B., Kosakowski, G., Margolin, G., and Scher, H. (2001). Application of continuous time random walk theory to tracer test measurements in fractured and heterogeenous porous media. *Groundwater*, 39 (4):593–604.

Berkowitz, B. and Scher, H. (1995). On characterization of anomalous dispersion in porous and fractured media. *Water Resour Res*, 31(6):1461–1466.

Berkowitz, B. and Scher, H. (1997). Anomalous transport in random fracture networks. *Phys. Rev. Lett.*, 79(20):4038–4041.

Berkowitz, B. and Scher, H. (1998). Theory of anomalous chemical transport in fracture networks. *Phys. Rev. E*, 57(5):5858–5869.

Bijeljic, B. and Blunt, M. J. (2006). Pore-scale modeling and continuous time random walk analysis of dispersion in porous media. *Water Resour. Res.*, 42:W01202.

Bijeljic, B., Mastaghimi, P., and Blunt, M. J. (2011a). Signature of non-fickian solute transport in complex heterogeneous porous media. *Phs. Rev. Lett.*, 107:204502.

Bijeljic, B., Mostaghimi, P., and Blunt, M. J. (2011b). Signature of non-Fickian solute transport in complex heterogeneous porous media. 107:204502.

Bijeljic, B., Raeini, A., Mostaghimi, P., and Blunt, M. J. (2013). Predictions of non-fickian solute transport in different classes of porous media using direct simulation on pore-scale images. *Phys. Rev. E*, 87:013011.

Boggs, J., Beard, L., Waldrop, W., Stauffer, T., MacIntyre, W., and Antworth, C. (1993). Transport of tritium and four organic compounds during a natural-gradient experiment (made-2). Technical report, Electric Power Research Inst., Palo Alto, CA (United States); Tennessee Valley Authority, Norris, TN (United States). Engineering Lab.; Air Force Engineering and Services Center, Tyndall AFB, FL (United States).

Bouchaud, J. P. and Georges, A. (1990). Anomalous diffusion in disordered media: Statistical mechanisms, models and physical applications. *Phys. Rep.*, 195(4,5):127–293.

Bouchaud, J. P., Georges, A., Koplik, J., Provata, A., and Redner, S. (1990). Superdiffusion in random velocity fields. *Phys. Rev. Lett.*, 64:2503.

Brenner, H. and Edwards, D. (1993). *Macrotransport Processes*. Butterworth-Heinemann, MA, USA.

Brockmann, D. and Geisel, T. (2003). Lévy flights in inhomogeneous media. *Phys. Rev. Lett.*, 90:170601.

Brown, C., Liebovitch, L. S., and Glendon, R. (2006). Lévy flights in dobe ju/'hoansi foraging patterns. *Human Ecology*, 35 (1):129–138.

Carrera, J., Sánchez-Vila, X., Benet, I., Medina, A., Galarza, G., and Guimerà, J. (1998). On matrix diffusion: formulations, solution methods, and qualitative effects. *Hydrogeology Journal*, 6:178–190.

Caspi, A., Granek, R., and Elbaum, M. (2000). Enhanced diffusion in active intracellular transport. *Physical Review Letters*, 85(26):5655.

Checkin, A., Hoffmann, M., and Sokolov, I. M. (2009). Continuous-time random walk with correlated waiting times. *Phys, Rev, E*, 80:031112.

Chevrollier, M., Mercadier, N., Guerin, W., and Kaiser, R. (2010). Anomalous photon diffusion in atomic vapors. *The European Physical Journal D-Atomic, Molecular, Optical and Plasma Physics*, 58(2):161–165.

Christakos, G. (1992). *Random Field Models in Earth Sciences*. Academic Press.

Cirpka, O. A. and Kitanidis, P. K. (2000). An advective-dispersive streamtube approach for the transfer of conservative tracer data to reactive transport. *Water Resour. Res.*, 36:1209–1220.

Comolli, A. and Dentz, M. (2017). Anomalous dispersion in correlated porous media: a coupled continuous time random walk approach. *The European Physical Journal B*, 90(9):166.

Comolli, A., Hidalgo, J. J., Moussey, C., and Dentz, M. (2016). Non-fickian transport under heterogeneous advection and mobile-immobile mass transfer. *Transport in Porous Media*, 115(2):265–289.

Cortis, A. and Berkowitz, B. (2004). Anomalous transport in "classical" soil and sand columns. *Soil Science Society of America Journal*, 68(5):1539–1548.

Cortis, A., Chen, Y., Scher, H., and Berkowitz, B. (2004). Quantitative characterization of pore-scale disorder effects on transport in "homogeneous" granular media. *Phys. Rev. E*, 70:041108.

Cushman, J. H. and Ginn, T. R. (1993). Nonlocal dispersion in media with continuously evolving scales of heterogeneity. *Transp. Porous Media*, 13(1):123–138.

Cushman, J. H. and Ginn, T. R. (2000). Fractional advection-dispersion equation: A classical mass balance with convolution–Fickian flux. *Water Resour. Res.*, 36:3763–3766.

Cushman, J. H., Hu, X., and Ginn, T. R. (1994). Nonequilibrium statistical mechanics of preasymptotic dispersion. *J. Stat. Phys.*, 75(5/6):859–878.

Cushman, J. H., O'Malley, D., and Park, M. (2009). Anomalous diffusion as modeled by nonstationary extensions of brownian motion. *Phys. Rev. E*, 79:032101.

Cvetkovic, V., Cheng, H., and Wen, X.-H. (1996). Analysis of nonlinear effects on tracer migration in heterogeneous aquifers using Lagrangian travel time statistics. *Water Resour. Res.*, 32(6):1671–1680.

Cvetkovic, V., Dagan, G., and Shapiro, A. (1991). An exact solution of solute transport by one-dimensional random velocity fields. *Stochastic Hydrology and Hydraulics*, 5(1):45–54.

Cvetkovic, V., Fiori, A., and Dagan, G. (2014). Solute transport in aquifers of arbitrary variability: A time-domain random walk formulation. *Water Resources Research*, 50(7):5759–5773.

Dagan, G. (1984). Solute transport in heterogenous porous formations. *J. Fluid Mech.*, 145:151–177.

Dagan, G. (1989). *Flow and transport in porous formations*. Springer, New York.

Dagan, G. (1994). The significance of heterogeneity of evolving scales to transport in porous formations. *Water Resour. Res.*, 30(12):3327–3336.

Dagan, G. (2017). Solute plumes mean velocity in aquifer transport: Impact of injection and detection modes. *Advances in Water Resources*, 106:6–10.

Dagan, G. and Bressler, E. (1979). Solute dispersion in unsaturated soil at field scale, i, theory. *Soil Sci. Soc. Am. J.*, 43:461–466.

de Anna, P., Le Borgne, T., Dentz, M., Tartakovsky, A. M., Bolster, D., and Davy, P. (2013). Flow intermittency, dispersion and correlated continuous time random walks in porous media. *Phys. Rev. Lett.*, 110:184502.

de Dreuzy, J.-R., Beaudoin, A., and Erhel, J. (2007). Asymptotic dispersion in 2d heterogeneous porous media determined by parallel numerical simulations. *Water Resources Research*, 43(10).

de Marsily, G. (1986). Quantitative hydrogeology: groundwater hydrology for engineers. Technical report.

Delay, F., Ackerer, P., and Danquigny, C. (2005). Simulating solute transport in porous or fractured formations using random walk particle tracking. *Vadose Zone J.*, 4:360–379.

Delay, F., Porel, G., and Sardini, P. (2002). Modelling diffusion in a heterogeneous rock matrix with a time-domain lagrangian method and an inversion procedure. *Comptes Rendus Geoscience*, 334(13):967–973.

Dentz, M. and Berkowitz, B. (2003). Transport behavior of a passive solute in continuous time random walks and multirate mass transfer. *Water Resour. Res.*, 39(5):1111.

Dentz, M. and Berkowitz, B. (2005). Exact effective transport dynamics in a one-dimensional random environment. *Phys. Rev. E*, 72(3):031110.

Dentz, M. and Bolster, D. (2010). Distribution- versus correlation-induced anomalous transport in quenched random velocity fields. *Phys. Rev. Lett.*, 105:244301.

Dentz, M. and Castro, A. (2009). Effective transport dynamics in porous media with heterogeneous retardation properties. *Geophys. Res. Lett.*, 36:L03403.

Dentz, M., Cortis, A., Scher, H., and Berkowitz, B. (2004). Time behavior of solute transport in heterogeneous media: transition from anomalous to normal transport. *Adv. Water Resour.*, 27(2):155–173.

Dentz, M., Gouze, P., and Carrera, J. (2011). Effective non-local reaction kinetics for transport in physically and chemically heterogeneous media. *J. Cont. Hydrol.*, 120:222–236.

Dentz, M., Gouze, P., Russian, A., Dweik, J., and Delay, F. (2012). Diffusion and trapping in heterogeneous media: an inhomogeneous continuous time random walk approach. *Adv. Wat. Res.*, 49:13–22.

Dentz, M., Kang, P. K., Comolli, A., Le Borgne, T., and Lester, D. R. (2016a). Continuous time random walks for the evolution of lagrangian velocities. *Physical Review Fluids*, 1(7):074004.

Dentz, M., Kang, P. K., and Le Borgne, T. (2015a). Continuous time random walks for non-local radial solute transport. *Adv. Wat. Res.*, 82:16–26.

Dentz, M., Le Borgne, T., and Carrera, J. (2008a). Effective transport in random shear flows. *Phys. Rev. E*, 77:020101.

Dentz, M., Le Borgne, T., Lester, D. R., and de Barros, F. P. J. (2015b). Scaling forms of particle densities for Lévy walks and strong anomalous diffusion. *Phys. Rev. E*, 92:032128.

Dentz, M., Lester, D. R., Borgne, T. L., and de Barros, F. P. J. (2016b). Coupled continous time random walks for fluid stretching in two-dimensional heterogeneous media. *Physical Review E*.

Dentz, M., Russian, A., and Gouze, P. (2016c). Self-averaging and ergodicity of subdiffusion in quenched random media. *Physical Review E*, 93(1):010101.

Dentz, M., Scher., H., Holder, D., and Berkowitz, B. (2008b). Transport behavior of coupled continuous-time random walks. *Phys. Rev. E*, 78:041110.

Eames, I. and Bush, J. (1999). Longitudinal dispersion by bodies fixed in a potential flow. In *Proceedings of the Royal Society of London A: Mathematical, Physical and Engineering Sciences*, volume 455, pages 3665–3686. The Royal Society.

Eaton, J. W. (2002). *GNU Octave Manual*. Network Theory Limited.

Edery, Y., Guadagnini, A., Scher, H., and Berkowitz, B. (2014). Origins of anomalous transport in heterogeenous media: Structural and dynamic control. *Water Resour Res*, 50 (2):1490 – 1505.

Eftekhari, A. A. (2015). Fvtool: a finite volume toolbox for matlab (version v0.11). zenodo. http://doi.org/10.5281/zenodo.18156. Technical report.

Fernàndez-Garcia, D., Llerar-Meza, G., and Gómez-Hernández, J. (2009). Upscaling transport with mass transfer models: Mean behavior and propagation of uncertainty. *Water Resour. Res.*, 45:W10411.

Fiori, A., Jankovic, I., Dagan, G., and Cvetkovic, V. (2007). Ergodic transport through aquifers of non-gaussian log conductivity distribution and occurence of anomalous behavior. *Water Resour. Res.*, 43:W09407.

Frampton, A. and Cvetkovic, V. (2009). Significance of injection modes and heterogeneity on spatial and temporal dispersion of advecting particles in two-dimensional discrete fracture networks. 32(5):649–658.

Galassi, M., Davies, J., Theiler, J., Gough, B., Jungman, G., Alken, P., Booth, M., Rossi, F., and Ulerich, R. (2015). Gnu scientific library reference manual , isbn 0954612078. *Library available online at http://www. gnu. org/software/gsl*.

Gardiner, C. W. (1986). Handbook of stochastic methods for physics, chemistry and the natural sciences. *Applied Optics*, 25:3145.

Gelhar, L. W. (1993). *Stochastic subsurface hydrology*. Prentice Hall.

Gelhar, L. W. and Axness, C. L. (1983). Three-dimensional stochastic analysis of macrodispersion in aquifers. *Water Resour. Res.*, 19(1):161–180.

Gelhar, L. W., Welty, C., and Rehfeldt, K. R. (1992). A critical review of data on field-scale dispersion in aquifers. *Water Resour. Res.*, 28(7):1955–1974.

Gentle, J. E. (2006). *Random number generation and Monte Carlo methods*. Springer Science & Business Media.

Ginn, T. R., Simmons, C. S., and Wood, B. D. (1995). Stochastic-convective transport with nonlinear reaction: Biodegradation with microbial growth. *Water Resour. Res.*, 31(11):2689–2700.

Gjetvaij, F., Russian, A., Gouze, P., and Dentz, M. (2015). Dual control of flow field heterogeneity and immobile porosity on non-fickian transport in berea sandstone. *Water Resour. Res.*, 51.

Gotovac, H., Cvetkovic, V., and Andricevic, R. (2009). Flow and travel time statistics in highly heterogeneous porous media. *Water resources research*, 45(7).

Gouze, P., Le Borgne, T., Leprovost, R., Lods, G., Poidras, T., and Pezard, P. (2008a). Non-Fickian dispersion in porous media: 1. multi-scale measurements using single well injection withdrawal tracer tests at the ses sitjoles/aliance test site (spain). *Water Resources Research*, 44:W06426.

Gouze, P., Melean, Z., Le Borgne, T., Dentz, M., and Carrera, J. (2008b). Non-fickian dispersion in porous media explained by heterogeneous microscale matrix diffusion. *Water Resour. Res.*, 44:W11416.

Guadagnini, A. and Neuman, S. P. (1999). Nonlocal and localized analyses of conditional mean steady state flow in bounded, randomly nonuniform domains: 1. theory and computational approach. *Water Resources Research*, 35(10):2999–3018.

Guadagnini, A. and Neuman, S. P. (2001). Recursive conditional moment equations for advective transport in randomly heterogeneous velocity fields. *Transport in Porous Media*, 42(1-2):37–67.

Haggerty, R., Fleming, S. W., Meigs, L. C., and McKenna, S. A. (2001). Tracer tests in a fractured dolomite: 2. analysis of mass transfer in single-well injection-withdrawal tests. *Water Resources Research*, 37(5):1129–1142.

Haggerty, R. and Gorelick, S. M. (1995). Multiple-rate mass transfer for modeling diffusion and surface reactions in media with pore-scale heterogeneity. *Water Resour. Res.*, 31(10):2383–2400.

Haggerty, R., McKenna, S. A., and Meigs, L. C. (2000). On the late time behavior of tracer test breakthrough curves. *Water Resour. Res.*, 36(12):3467–3479.

Hakoun, V., Comolli, A., and Dentz, M. (2018). Unpublished.

Harvey, C. F. and Gorelick, S. M. (1995). Temporal moment-generating equations: Modeling transport and mass transfer in heterogeneous aquifers. *Water Resour. Res.*, 31(8):1895–1911.

Haslauer, C., Guthke, P., Bárdossy, A., and Sudicky, E. (2012). Effects of non-gaussian copula-based hydraulic conductivity fields on macrodispersion. *Water Resources Research*, 48(7).

Hatano, Y. and Hatano, N. (1998). Dispersive transport of ions in column experiments: An explanation of long-tailed profiles. *Water Resour Res*, 34 (5):1027–1033.

Holzner, M., Morales, V. L., Willmann, M., and Dentz, M. (2015). Intermittent lagrangian velocities and accelerations in three-dimensional porous medium flow. *Phys. Rev. E*, 92:013015.

Hsu, K., Zhang, D., and Neuman, S. P. (1996). Higher-order effects on flow and transport in randomly heterogenous porous media. *Water Resour. Res.*, 32:571–582.

Hyman, J. D., Painter, S. L., Viswanathan, H., Makedonska, N., and Karra, S. (2015). Influence of injection mode on transport properties in kilometer-scale three-dimensional discrete fracture networks.

Jeon, J.-H., Javanainen, M., Martinez-Seara, H., Metzler, R., and Vattulainen, I. (2016). Protein crowding in lipid bilayers gives rise to non-gaussian anomalous lateral diffusion of phospholipids and proteins. *Phys. Rev. X*, 6:021006.

Jeon, J.-H., Tejedor, V., Burov, S., Barkai, E., Selhuber-Unkel, C., Berg-Sørensen, K., Oddershede, L., and Metzler, R. (2011). In vivo anomalous diffusion and weak ergodicity breaking of lipid granules. *Physical review letters*, 106(4):048103.

Kang, P. K., de Anna, P., Nunes, J., Bijeljic, B., Blunt, M. J., and Juanes, R. (2014). Pore-scale intermittent velocity structure underpinning anomalous transport through 3-d porous media. *Geophys. Res. Lett.*, 41 (17):6184–6190.

Kang, P. K., Dentz, M., Le Borgne, T., and Juanes, R. (2011). Spatial markov model of anomalous transport through random lattice networks. *Phys. Rev. Lett.*, 107:180602.

Kang, P. K., Dentz, M., Le Borgne, T., and Juanes, R. (2015a). Anomalous transport on regular fracture networks: impact of conductivity heterogeneity and mixing at fracture intersections. *Phys. Rev. E*, 92(2):022148.

Kang, P. K., Dentz, M., Le Borgne, T., Lee, S., and Juanes, R. (2016). Anomalous transport in disordered fracture networks: Evolution of the lagrangian velocity distribution and ctrw model for arbitrary injection modes. *under review.*

Kang, P. K., Dentz, M., Le Borgne, T., Lee, S., and Juanes, R. (2017). Anomalous transport in disordered fracture networks: Spatial markov model for dispersion with variable injection modes. *Adv. Water Resour.*

Kang, P. K., Le Borgne, T., Dentz, M., Bour, O., and Juanes, R. (2015b). Impact of velocity correlation and distribution on transport in fractured media: field evidence and theoretical model. *Water Resour. Res.*, 51:940–959.

Kenkre, V. M., Montroll, E. W., and Shlesinger, M. F. (1973). Generalized master equations for continuous-time random walks. *J. Stat. Phys.*, 9(1):45–50.

Kinzelbach, W. (1988). The random-walk method in pollutant transport simulation. *NATO ASI Ser.*, C(224):227–246.

Klafter, J., Blumen, A., Zumofen, G., and Shlesinger, M. F. (1990). Lévy walk approach to anomalous diffusion. *Phys. A*, 168:637.

Klafter, J. and Silbey, R. (1980). Derivation of continuous-time random-walk equations. *Phys. Rev. Lett.*, 44(2):55–58.

Klafter, J. and Sokolov, I. (2005). Anomalous diffusion spreads its wings. *Phys. World*, 18(8):29–32.

Klafter, J. and Sokolov, I. M. (2011). *First steps in random walks: from tools to applications.* Oxford University Press.

Koch, D. L. and Brady, J. F. (1988). Anomalous diffusion in heterogeneous porous media. *Phys. Fluids A*, 31:965–1031.

Kohlbecker, M. V., Wheatcraft, S. W., and Meerschaert, M. M. (2006). Heavy-tailed log hydraulic conductivity distributions imply heavy-tailed log velocity distributions. *Water resources research*, 42(4).

Koren, T., Lomholt, M. A., Chechkin, A. V., Klafter, J., and Metzler, R. (2007). Leapover lengths and first passage time statistics for lévy flights. *Physical review letters*, 99(16):160602.

Kou, S. C. and Sunney Xie, X. (2004). Generalized langevin equation with fractional gaussian noise: Subdiffusion within a single protein molecule. *Phys. Rev. Lett.*

Kubo, R., Toda, M., and Hashitsume, N. (1991). *Statistical Physics II, Non-Equilibrium Statistical Mechanics*. Springer Verlag Berlin Heidelberg.

Kutner, R. and Masoliver, J. (2017). The continuous time random walk, still trendy: fifty-year history, state of art and outlook. *Eur. Phys. J. B*, 90:50.

Le Borgne, T., Bolster, D., Dentz, M., de Anna, P., and Tartakovsky, A. M. (2011). Effective pore-scale dispersion upscaling with a correlated continuous time random walk approach. *Water Resour Res*, 47:W12538.

Le Borgne, T., de Dreuzy, J. R., Davy, P., and Bour, O. (2007). Characterization of the velocity field organization in heterogeneous media by conditional correlation. *Water Resour. Res.*, 43:2006WR004875.

Le Borgne, T., Dentz, M., and Carrera, J. (2008a). A lagrangian statistical model for transport in highly heterogeneous velocity fields. *Phys. Rev. Lett.*, 101:090601.

Le Borgne, T., Dentz, M., and Carrera, J. (2008b). Spatial markov processes for modeling lagrangian particle dynamics in heterogeneous porous media. *Phys. Rev. E*, 78:041110.

LeBlanc, D. R., Garabedian, S. P., Hess, K. M., Gelhar, L. W., Quadri, R. D., Stollenwerk, K. G., and Wood, W. W. (1991). Large-scale natural gradient tracer test in sand and gravel, cape cod, massachusetts: 1. experimental design and observed tracer movement. *Water Resources Research*, 27(5):895–910.

Levy, M. and Berkowitz, B. (2003). Measurement and analysis of non-fickian dispersion in heterogeneous porous media. *J. Cont. Hydrol.*, 64:203–226.

Mackay, D., Ball, W., and Durant, M. (1986). Variability of aquifer sorption properties in a field experiment on groundwater transport of organic solutes: Methods and preliminary results. *Journal of contaminant hydrology*, 1(1-2):119–132.

Magdziarz, M., Weron, A., Burnecki, K., and Klafter, J. (2009). Fractional Brownian motion versus continuous time random walk: a simple test for subdiffusive dynamics. *Phys. Rev. Lett.*, 103:180602.

Maloszewski, P. and Zuber, A. (1985). On the theory of tracer experiments in fissured rocks with a porous matrix. *J. Hydrol.*, 79:333.

Manzo, C., Torreno-Pina, J. A., Massignan, P., Lapeyre, G. J., Lewenstein, M., and García-Parajo, M. F. (2015). Weak ergodicity breaking of receptor motion in living cells stemming from random diffusivity. *Phys. Rev. X*, 5:011021.

Margolin, G. and Berkowitz, B. (2002). Spatial behavior of anomalous transport. *Phys. Rev. E*, 65(031101):1–11.

Margolin, G., Dentz, M., and Berkowitz, B. (2003). Continuous time random walk and multirate mass transfer modeling of sorption. *Chem. Phys.*, 295:71–80.

Massignan, P., Manzo, C., Torreno-Pina, J., Garcia-Parajo, M., Lewenstein, M., and Lapeyre, J. G. (2014). Nonergodic subdiffusion from brownian motion in an inhomogeneous medium. *Phys. Rev. Lett.*, 112:150603.

Matheron, G. (1967). Eléments pour une théorie des milieux poreux.

Matheron, M. and de Marsily, G. (1980). Is transport in porous media always diffusive? *Water Resour. Res.*, 16:901–917.

Meerschaert, M. M., Benson, D. A., and Baumer, B. (1999). Multidimensional advection and fractional dispersion. *Phys. Rev. E*, 59(5):5026–5028.

Meerschaert, M. M., Nane, E., and Xiao, Y. (2009). Correlated continuous time random walks. *Stat. Prob. Lett.*, 79:1194–1202.

Meroz, Y. and Sokolov, I. M. (2015). A toolbox for determining subdiffusive mechanisms. *Phys. Rep.*, 573:1.

Metzler, R., Jeon, J. H., Cherstvy, A. G., and Barkai, E. (2014). Anomalous diffusion models and their properties: non-stationary, non-ergodicity, and ageing at the centenary of single particle tracking. *Phys. Chem. Chem. Phys.*, 16:24128.

Metzler, R. and Klafter, J. (2000a). The random walk's guide to anomalous diffusion: a fractional dynamics approach. *Phys. Rep.*, 339(1):1–77.

Metzler, R. and Klafter, J. (2000b). The random walk's guide to anomalous diffusion: a fractional dynamics approach. *Phys. Rep.*, 339(1):1–77.

Metzler, R. and Klafter, J. (2004). The restaurant at the end of the random walk: recent developments in the description of anomalous transport by fractional dynamics. *J. Phys. A: Math. Gen.*, 37:161–208.

Meyer, D. W. and Saggini, F. (2016). Testing the markov hypothesis in fluid flows. *Phys. Rev. E.*, 93:053103.

Miyaguchi, T. and Akimoto, T. (2011). Intrinsic randomness of transport coefficient in subdiffusion with static disorder. *Phys. Rev. E*, 83:031926.

Montroll, E. W. and Weiss, G. H. (1965). Random walks on lattices, 2. *J. Math. Phys.*, 6(2):167.

Morales, V. L., Dentz, M., Willmann, M., and Holzner, M. (2017). Stochastic dynamics of intermittent pore-scale particle motion in three-dimensional porous media: Experiments and theory. *Geophysical Research Letters*, 44(18):9361–9371.

Morales-Casique, E., Neuman, S. P., and Guadagnini, A. (2006). Nonlocal and localized analyses of nonreactive solute transport in bounded randomly heterogeneous porous media: Theoretical framework. *Adv. Water Resour.*, 29(8):1238–1255.

Moroni, M. and Cushman, J. (2001). Statistical mechanics with three-dimensional particle tracking velocimetry experiments in the study of anomalous dispersion. ii. experiments. *Phys. Fluids*, 13:81–91.

Neuman, S. and Zhang, Y. (1990). A quasi-linear theory of non-fickian and fickian subsurface dispersion 1. theoretical analysis with application to isotropic media. *Water Resour. Res.*, 26(5):887–902.

Noetinger, B. and Estebenet, T. (2000). Up-scaling of double porosity fractured media using continuous-time random walks methods. *Transport in Porous Media*, 39(3):315–337.

Noetinger, B., Roubinet, D., Russian, A., Le Borgne, T., Delay, F., Dentz, M., De Dreuzy, J.-R., and Gouze, P. (2016). Random walk methods for modeling hydrodynamic transport in porous and fractured media from pore to reservoir scale. *Transport in Porous Media*, pages 1–41.

Painter, S. (1996). Evidence for non-gaussian scaling behavior in heterogeneous sedimentary formations. *Water Resources Research*, 32(5):1183–1195.

Painter, S. and Cvetkovic, V. (2005). Upscaling discrete fracture network simulations: An alternative to continuum transport models. *Water Resources Research*, 41(2).

Painter, S. L., Cvetkovic, V., and Pensado, O. (2008). Time-domain random-walk algorithms for simulating radionuclide transport in fractured porous rock. *Nuclear Technology*, 163(1):129–136.

Pearson, K. (1905). The problem of the random walk. *Nature*, 72 (1865):294.

Pollock, D. (1988). Semianalytical computation of path lines for finite-difference models. *Ground Water*, 26 (6):743–750.

Polyanin, A. D. and Manzhirov, A. V. (1998). *Handbook of Integral Equations*. CRC Press.

Pope, S. B. (2000). *Turbulent Flows*. Cambridge University Press.

Puyguiraud, A., Dentz, M., and Gouze, P. (2017). Flow and transport in digitized images of berea sandstone: ergodicity, stationarity and upscaling. In *AGU Fall Meeting Abstracts*.

Ramos-Fernández, G., Mateos, J. L., Miramontes, O., Cocho, G., Larralde, H., and Ayala-Orozco, B. (2004). Lévy walk patterns in the foraging movements of spider monkeys (ateles geoffroyi). *Behavioral ecology and Sociobiology*, 55(3):223–230.

RCoreTeam et al. (2013). R: A language and environment for statistical computing.

Rebenshtok, A., Denisov, S., Hänggi, P., and Barkai, E. (2014). Infinite densities for Lévy walks. *Phys. Rev. E*, 90:062135.

Rehfeldt, K. R., Boggs, J. M., and Gelhar, L. W. (1992). Field study of dispersion in a heterogeneous aquifer: 3. geostatistical analysis of hydraulic conductivity. *Water Resources Research*, 28(12):3309–3324.

Roth, K. and Jury, W. A. (1993). Linear transport models for adsorbing solutes. *Water Resour. Res.*, 29(4):1195–1203.

Rubin, Y. (1990). Stochastic modeling of macrodispersion in heterogenous porous media. *Water Resour. Res.*, 26:133–141.

Rubin, Y. (2003). *Applied stochastic hydrogeology*. Oxford University Press, New York.

Russian, A., Dentz, M., and Gouze, P. (2016). Time domain random walks for hydrodynamic transport in heterogeneous media. *Water Resources Research*.

Russian, A., Dentz, M., and Gouze, P. (2017). Self-averaging and weak ergodicity breaking of diffusion in heterogeneous media. *Physical Review E*, 96(2):022156.

Saffman, P. (1959). A theory of dispersion in a porous medium. *Journal of Fluid Mechanics*, 6(03):321–349.

Salamon, P., Fernàndez-Garcia, D., and J., G.-H. J. (2006). A review and numerical assessment of the random walk particle tracking methods. *J. Cont. Hydrol.*, 87:277–305.

Salandin, P. and Fiorotto, V. (1998). Solute transport in highly heterogeneous aquifers. *Water resources research*, 34(5):949–961.

Sanchez-Vila, X. and Carrera, J. (2004). On the striking similarity between the moments of breakthrough curves for a heterogeneous medium and a homogeneous medium with a matrix diffusion term. *Journal of Hydrology*, 294(1-3):164–175.

Sanchez-Vila, X., Guadagnini, A., and Carrera, J. (2006). Representative hydraulic conductivities in saturated groundwater flows. *Rev. Geophys.*, 44:RG3002.

Scher, H. and Lax, M. (1973). Stochastic transport in a disordered solid. I. Theory. *Phys. Rev. B*, 7(1):4491–4502.

Scher, H., Margolin, G., Metzler, R., Klafter, J., and Berkowitz, B. (2002). The dynamical foundation of fractal stream chemistry: the origin of extremely long retention times. *Geophys. Res. Lett.*, 29:1061.

Scher, H. and Montroll, E. W. (1975). Anomalous transit-time dispersion in amorphous solids. *Phys. Rev. B*, 12 (6):2455–2477.

Schlather, M., Malinowski, A., Menck, P. J., Oesting, M., Strokorb, K., et al. (2015). Analysis, simulation and prediction of multivariate random fields with package randomfields. *Journal of Statistical Software*, 63(8):1–25.

Schumer, R., Benson, D. A., Meerschaert, M. M., and Bauemer, B. (2003). Fractal mobile/immobile solute transport. *Water Resour Res*, 39(10):1296.

Seymour, J. D., Gage, J. P., Codd, S. L., and Gerlach, R. (2004). Anomalous fluid transport in porous media induced by biofilm growth. *Phys. Rev. Lett.*, 93:198103.

Shlesinger, M. (1974). Asymptotic solutions of continuous-time random walks. *J. Stat. Phys.*, 10 (5):421–434.

Shlesinger, M. (2017). Origins and applications of the montroll-weiss continuous time random walk. *Eur. Phys. J. B*, 90:93.

Shlesinger, M. F., Klafter, J., and Wong, Y. M. (1982). Random walks with infinite spatial and temporal moments. *J. Stat. Phys.*, 27 (3):499–512.

Shlesinger, M. F., West, B. J., and Klafter, J. (1987). Lévy dynamics of enhanced diffusion: Application to turbulence. *Phys. Rev. Lett.*, 58:1100–1103.

Silva, O., Carrera, J., Dentz, M., Kumar, S., Alcolea, A., and Willmann, M. (2009). A general real-time formulation for multi-rate mass transfer problems. *Hydrology and Earth System Sciences*, 13(8):1399–1411.

Sokolov, I. M. (2012). Models of anomalous diffusion in crowded environments. *Soft Matter*.

Stanley, H. E. (1984). Application of fractal concepts to polymer statistics and to anomalous transport in randomly porous media. *Journal of Statistical Physics*, 36(5-6):843–860.

Sudicky, E. A. (1986). A natural gradient experiment on solute transport in a sand aquifer: Spatial variability of hydraulic conductivity and its role in the dispersion process. *Water Resources Research*, 22(13):2069–2082.

Swanson, K. R., Bridge, C., Murray, J., and Alvord, E. C. (2003). Virtual and real brain tumors: using mathematical modeling to quantify glioma growth and invasion. *Journal of the neurological sciences*, 216(1):1–10.

Szymanski, J. and Weiss, M. (2009). Elucidating the origin of anomalous diffusion in crowded fluids. *Phys. Rev. Lett.*, 103:038102.

Tecklenburg, J., Neuweiler, I., Carrera, J., and Dentz, M. (2016). Multi-rate mass transfer modeling of two-phase flow in highly heterogeneous fractured and porous media. *Advances in water resources*, 91:63–77.

Tejedor, V., Bénichou, O., Voituriez, R., Jungmann, R., F., S., Selhuber-Unkel, C., Oddershede, L. B., and Metzler, R. (2010). Quantitative analysis of single particle trajectories: mean maximal excursion methods. *Biophys. J.*, 98:1364–1372.

Thalabard, S., Krstulovic, G., and Bec, J. (2014). Turbulent pair dispersion as a continuous-time random walk. *J. Fluid Mech.*, 755:R4.

Toivonen, M. S., Onelli, O. D., Jacucci, G., Lovikka, V., Rojas, O. J., Ikkala, O., and Vignolini, S. (2018). Anomalous-diffusion-assisted brightness in white cellulose nanofibril membranes. *Advanced Materials*.

Tyukhova, A., Dentz, M., Kinzelbach, W., and Willmann, M. (2016). Mechanisms of anomalous dispersion in flow through heterogeneous porous media. *Physical Review Fluids*, 1(7):074002.

Uchaikin, V. V. and Zolotarev, V. M. (1999). *Chance and stability: stable distributions and their applications*. Walter de Gruyter.

Vineyard, G. H. (1963). The number of distinct sites visited in a random walk. *J. Math. Phys.*, 4:1191–1193.

Viswanathan, G. M., Afanasyev, V., V., B. S., Murphy, E. J., Prince, P. E., and Stanley, H. E. (1996). Lévy flight search patterns of wandering albatrosses. *Nature*, 381:413.

Wang, P. P., Zheng, C., and Gorelick, S. M. (2005). A general approach to advective–dispersive transport with multirate mass transfer. *Advances in Water Resources*, 28(1):33–42.

Weiss, G. H. (1994). *Aspects and Applications of the Random Walk*. Elsevier North-Holland.

Willmann, M., Carrera, J., and Sanchez-Vila, X. (2008). Transport upscaling in heterogeneous aquifers: What physical parameters control memory functions? *Water Resour. Res.*, 44:W12437.

Yu, S. R., Burkhardt, M., Nowak, M., Ries, J., Petrášek, Z., Scholpp, S., Schwille, P., and Brand, M. (2009). Fgf8 morphogen gradient forms by a source-sink mechanism with freely diffusing molecules. *Nature*, 461(7263):533.

Zaburdaev, V., Denisov, S., and Klafter, J. (2015). Lévy walks. *Reviews of Modern Physics*, 87(2):483.

Zhang, D. and Benson, D. A. (2008). Lagrangian simulation of multidimensional anomalous transport at the made site. *Geophys. Res. Lett.*, 35:L07403.

Zhang, Y., Green, C. T., and Baeumer, B. (2014). Linking aquifer spatial properties and non-fickian transport in alluvial settings. *J. Hydrol.*, 512:315–331.

Zheng, C., Bianchi, M., and Gorelick, S. M. (2011). Lessons learned from 25 years of research at the made site. *Groundwater*, 49(5):649–662.

Zinn, B., Meigs, L. C., Harvey, C. F., Haggerty, R., Peplinski, W. J., and Freiherr von Schwerin, C. (2004). Experimental visualization of solute transport and mass transfer processes in two-dimensional conductivity fields with connected regions of high conductivity. *Environ. Sci. Technol.*, 38:3916–3926.

Zumofen, G., Klafter, J., and Blumen, A. (1991). Trapping aspects in enhanced diffusion. *Journal of statistical physics*, 65(5):991–1013.